University of Lorraine   Institute of Fundamental Technological Research   C2MP Doctoral School
of the Polish Academy of Sciences

<u>THESE</u>

Présentée et soutenue publiquement pour l'obtention du titre de

DOCTEUR DE l'UNIVERSITE DE LORRAINE

Mention:« SCIENCES DES MATERIAUX »

Par **Tomasz LIBURA**

Etude de la tenue à l'impact après vieillissement en fatigue, des composites stratifiés à base d'acrylique

Study of the impact resistance of laminated composites based on Elium acrylic matrix subjected to prior fatigue aging

Soutenue publiquement le 9 novembre 2022 à Metz

Membres du jury:

Rapporteurs :	**Nadia BAHLOULI**	**Professeur, Université de Strasbourg, Strasbourg**
	Tomasz A. ŁODYGOWSKI	**Professeur, Poznan University of Technology, Poznan**
Examinateurs :	**Marion MARTINY**	**Professeur, Université de Lorraine, Metz**
	Jerzy MALACHOWSKI	**Professeur, Military University of Technology, Warsaw**
	Zdzisław NOWAK	**Professeur, IPPT PAN, Warsaw**
Membres invités :	**Pierre GERARD**	**Dr, R&D Engineer, ARKEMA, Lacq**
Directeur de thèse :	**Alexis RUSINEK**	**Professeur, Université de Lorraine, Metz**
Co-Directeur de thèse :	**Zbigniew L. KOWALEWSKI**	**Professeur, IPPT PAN, Warsaw**
Co-Directeur de thèse	**Rodrigue MATADI BOUMBIMBA**	**Maître de conférences – HDR, Université de Lorraine, Metz**

Acknowledgments

preparation, dynamic tests and microscopy observations.

Many thanks to Mr. Andrzej CHOJNACKI and Mr. Łukasz CICHACKI for their help in preparing the unique elements of testing stands as well as to Mr. Mirosław WYSZKOWSKI and Mr. Adam BRODECKI from IPPT PAN for their help with thermomechanical characterization and fatigue tests of composites.

Finally, I thank all my friends, my parents, my sister and my wife Marta who have been always with me.

Contents

List of Figures

List of Tables

Abbreviations

PMC   Polymer-based composites

FRP   Fiber Reinforced Polymer

CFRA   Continuous Fiber Reinforced Acrylic -matrix

CFRP   Carbon fibers reinforced polymer

GFRP   Glass Fiber Reinforced Polymer

GFRE   Glass Fibers Reinforced Elium

UD   Unidirectional

TP   Thermoplastic matrix

TS   Thermoset matrix

PMMA Poly[Methyl Methacrylate]

ABS   Acrylonitrile Butadiene Styrene

LCF   Low Cyclic Fatigue

HCF   High Cyclic Fatigue

SEM   Scanning Electron Microscopy

CT   Computed Tomography

TGA   Thermogravimetric Analysis

LCM   Liquid Composite Molding

SHPB   Split Hopkinson Pressure Bar

EPD   Energy Profile Diagram

CBT   Classical Beam Theory

DCB   Double Cantilever Beam

ENF   End-Notched Flexure

General introduction

Nowadays, the automobile manufacturers try to build cars using novel materials; lighter, stronger and cheaper. For this purpose, thermoplastic polymer elements, as well as thermoset resin based laminated composites have been introduced to the construction of vehicles. They are 30% and 50% lighter than aluminum and steel alloy [1], respectively. Feldmann evaluated in 2008 [2], that the metal elimination from the construction of cars would decrease the demand for energy by 26%. Therefore, the usage of polymers is necessary, since an average weight of the modern cars produced in Europe increases continuously, e.g. in 1995, the average mass of car was 950 kg, while today it is around 1350 kg [2].

At the same time, the newest international carbon dioxide emission standards emphasize reduced energy use, and additionally promote the application of organic matrix composites in the transportation industry [3]. The global automotive plastics market is predicted to rise from USD 32.8 billion in 2021 to USD 51.9 billion by 2026, registering a compound annual growth rate (CAGR) of about 13.5% during the foreseen period of 2021-26 [4]. Taking into account such increase in plastic production, a new reinforced laminates with recyclable resins have begun to play an increasingly important role. It is expected that by 2035 most of thermoset organic polymers used in composite materials will be replaced by fully recyclable thermoplastic composites [2,4].

Therefore, with the perspective of environmental protection in the background, the fully recyclable thermoplastic resin, termed ELIUM has been developed by ARKEMA engineers and proposed for its application in automotive industry. Among the basic advantages of Elium acrylic thermoplastic liquid resin, the most important seem to be its compatibility with a large panel of existing ancillaries, mold construction and mixing machines previously used for the fabrication of laminated composites with a thermosetting resin. This reduces significantly the cost of its introduction, and thus, accelerates application in different areas, especially in the automotive industry.

Since 2011, three laboratories; LEMTA, LCPM, LMOPS and two manufacturers: IRT M2P and ARKEMA, have been working together within 2 projects: "Perfect resin" and "COACH". The first one was focused on optimization of the manufacturing process and improvement of

mechanical properties of the glass fiber/Elium acrylic woven laminates. In turn, the second project was devoted to the production opportunities of laminated thermoplastic composite structures in extremely short time without the loss of their excellent properties. As a consequence, a repeatable and automated process has been developed to enable the mass production of composite laminates based on Elium, that significantly reduced their production costs and made them attractive to automotive manufacturers.

Until now a large number of studies related to Elium were performed. Boufaida et al. [5] and Kinvi-Dossou et al. [6] conducted classical macroscopic mechanical tests, e.g., tensile, bending and shear tests, and revealed that the continuous glass fiber reinforced acrylic resin Elium (CFRA) composite ensures the same thermomechanical properties as the thermoset-based composites, leading to its wider industrial applications. Obande et al. [7] and Cadieu et al. [8] evaluated the viscoelastic and dynamic properties of the GFRE composites, containing Elium 150. Matadi Boumbimba et al. [9] tested the hardened composite plates by adding various amounts of the acrylic tri-block copolymers (Nanostrength®). They were subjected to low velocity impact tests under different levels of the impact energy and temperature. The results revealed that the structural response of the new developed thermoplastic composite is highly dependent on the microstructure of the material as well as on the interface between both copolymer and Elium acrylic phases. Low velocity impact results obtained for various levels of energy and temperature showed that the impact resistance in terms of maximum force, absorbed energy and threshold penetration, were improved in the presence of copolymers. In the study of Kinvi-Dossou et al. [6], detailed fracture and damage analysis of the impacted specimens showed that the effect of loading rate on the structural response of glass/Elium (stiffness, dissipated energy) is comparable to that of the non-recyclable thermosetting composites.

It is well known that material properties can be also affected by damage and fracture kinetics that often occur during exploitation of structures. Therefore, in order to study how the long-term mechanical processes may change material properties, in 2018, Freund et al. [10], evaluated the exposition of the material in question to moisture cycles. The results allowed them to distinguish between two aging effects: (i) the composite yielding induced by the presence of water molecules within the polymer network and (ii) the structural damage by weakening the fiber/matrix interface. In turn, the effect of temperature and moisture

content on the damage scenario in acrylic-matrix and CFRA composite under quasi-static tensile loading was studied by Boissin et al. [11]. The authors presented how significantly these factors affected the relationship between transverse cracks in composite and given work conditions.

It should be emphasized that the composites belong to the specific group of materials that can endure some assumed initial stiffness loss generated during their exploitation [12]. Therefore, following the objectives of the COACH project, in this thesis a fatigue aging was selected as the process that can affect the internal structure of the CFRA, and as a consequence, deteriorate its impact properties. As it is well known, the impact resistance is one of the most important features which manufacturers of vehicle parts are considering. It determines the lifetime of the element and its safety as well. In order to fully assess a scale of the stiffness loss caused by cyclic fatigue loading and accompanying drop of energy dissipation capacity of glass fiber/Elium acrylic woven laminates subjected to low and high velocity impact, an extensive study is required, as this is a complex and multi-step process. On the one hand, it is necessary to consider such factors as: type of reinforcing phase, number of layers and their orientation as well. On the other hand, an application of various stress levels during the aging processes for every considered fiber orientation is desired. Taking into account a demand of the potential users of the laminated structures, a plain weave fabric made of the glass fibers was chosen as the reinforcing phase in this thesis. Such material guarantees the best distribution of stress in the main directions of the laminate. Since the composite containing this type of reinforcement has the identical properties in the warp and weft directions, only two orientations representing two different cases were selected in this study. The first one, with the fibers arranged along the main axes, and the second one oriented at an angle of 45 degrees with regard to that of fibers one, named "on-axis" (GFRE $[0°/90°]_4$) and "off-axis" (GFRE $[45°/45°]_4$), the strongest and weakest toughness of the studied material, respectively. The force applied during the fatigue aging process to laminated composites with off-axis reinforcement orientation is not transmitted through the fibers, so their fatigue response depends mainly on the stiffness and strength of the matrix itself and the quality of the fibers/matrix interface. In turn, the cyclic fatigue loading applied to laminated composites with on-axis reinforcement orientation is carried out along the fibers, that have a much higher elastic modulus than the matrix. As a result, a fatigue damage takes place usually in the transvers yarns, which does not lead to a significant

decrease of stiffness and accompanying drop of impact resistance. ***Thus, the main goal of this thesis is devoted to the verification of the hypotheses that:***

- laminates based on thermoplastic resin with yarns oriented in on-axis direction, subjected to the tensile uniaxial cyclic loading, and then to low velocities impacts, preserve their high impact resistance. This is valid especially for the laminated composites aged under the stress level lower than the yield stress.

- aged specimens containing strain rate sensitive Elium, reinforced with the glass woven fibers oriented in on-axis direction are characterized by a higher ballistic response than the aged specimens containing Elium reinforced with the glass woven fibers oriented in the off-axis direction.

Fatigue damage impact assessment through the applied impact methods in this thesis, is of particular importance, as the obtained results may contribute to the replacement of epoxy or polyester matrices-based composites by acrylic Elium based thermoplastic laminates.

In order to achieve this purpose, the study was conducted within the framework of international collaboration. The following institution were engaged: University of Lorraine (LEM3), Institute of Fundamental Technological Research Polish Academy of Sciences (IPPT PAN), Motor Transport Institute, Military University of Technology, as well ARKEMA and Institute for Technological Research Materials Metallurgy and Processes (IRTm2p). The data obtained are presented in five chapters that are briefly summarized below.

In the first chapter, a general knowledge on the polymer matrix based laminated composites, including their structure (especially different types of reinforcing phases and resins), mechanical properties as well as application in the automotive industry are presented. Then, the behaviour of composite laminates subjected to fatigue loading, as well as the resulting damage, and accompanying stiffness and strength variations are described in detail. In order to assess an influence of fatigue aging on impact resistance of glass fiber/Elium acrylic woven laminates, the selected methods are presented. Finally, in order to model the behaviour of the woven laminates subjected to low and high velocity impact, the typical failure criteria were discussed for the different damage modes.

Second chapter is devoted to the thermomechanical characterization of the elastic and plastic behaviour of the four-layer laminated glass fiber/acrylic composite through series of

static experimental tests. In addition, the fabric pattern geometry and total volume fraction of the fibers in the composite are carefully analysed for each tested orientations (0°/90° and 45°/45°). Subsequently, dynamic properties of the pure and reinforced acrylic resin Elium are studied using Split Hopkinson Pressure Bar (SHPB) at different temperatures and strain rates. The results were compared to the dynamic properties of the glass fiber/epoxy laminated composite tested at the same temperatures and strain rates. All parameters determined in this section, such as the failure limits and the shear and Young's moduli were subsequently applied for the simulation of micromechanical response of selected GFRE on the low and high velocity impacts.

In the third chapter, an experimental work dedicated to assessment of the effect of the cyclic loading (fatigue aging) on the glass fiber/Elium acrylic woven laminate was presented. In order to fully understand a fatigue response, two groups of specimens with a special shape and dimensions were considered: first one (GFRE [0°/90°]$_4$), with the fibers arranged along the main axes, and the second one (GFRE [45°/45°]$_4$) oriented at an angle of 45 degrees with regard to that of fiber one. As already mentioned, the aim of this work was to verify how the process of aging may affect the elastic properties of the material in question, and as a consequence, its impact resistance. Therefore, the experiments were carried out under the values of stress higher (LCF) and lower (HCF) than the yield stress. The fatigue response of all tested materials was evaluated and presented in terms of the stiffness variation analysis. Finally, in order to combine a fatigue damage and accompanying loss of stiffness, a damage parameter based on the theory introduced by Khachanov was presented. Determination of damage parameter enabled to identify the pre-critical state and to interrupt the fatigue aging process of specimens at the given level of degradation.

Chapter four shows the low velocity impact response of three groups of specimens of the thermoplastic based laminated composites: (i) non-aged, (ii) aged at the stress lower than the yield point (HCF), and (iii) aged at the stress higher than the yield point (LCF)). The impact resistance of all materials was presented for four values of impact energy in terms of force-displacement and time-energy characteristics. In turn, the penetration threshold was assessed using energy profile diagram and the relationship between elastic energy and impact energy. In order to assess an influence of the fatigue aging on the impact properties of glass fiber/Elium acrylic woven laminate, the impact resistance of non-aged and aged

specimens was compared. In order to better understand mechanism of defects generation induced by impact and fatigue, the results of tomographic analyses and microscopic observations of selected non-aged and aged specimens were performed and presented in this chapter. In order to study damage caused by low velocity impact, a three-dimensional intralaminar damage model was also developed based on a computational algorithm. A finite element model was implemented in a VUMAT user subroutine in Abaqus/Explicit. The impact responses of non-aged GFRE $[0°/90°]_4$ laminates, subjected to impact energies of 10 J, 30 J and 50 J, were quantified using the developed numerical approach and compared with the experimental results.

It is well known, that the mechanical behaviour of materials containing polymer resins is strain rate and temperature dependent. To fully understand the effect of those factors on the non-aged and aged glass fibers/acrylic laminated composites, the adequate methods for analysis of mechanical response of the tested materials under high velocity impact are presented in chapter five. In order to define the ballistic limits, the series of perforation tests were performed on non-aged and aged glass fibers/acrylic plates. The analytical law proposed by Recht and Ipson [13] was applied to model the ballistic curve. In addition, an evolution of the absorbed energy with impact velocity was studied. In order to assess the influence of fatigue aging on the ballistic properties of composites tested, the high velocity impact responses of non-aged and aged specimens were compared. To better understand phenomena occurring during the perforation of impacted specimens, the tomographic analysis and microscopic observations were carried out. Finally, a ballistic response of the tested laminates was predicted under high velocity impact. The same model as that presented in chapter four was applied. Experimentally and numerically determined ballistic limits and energy dissipation were compared for the non-aged GFRE $[0°/90°]_4$ 1.8 mm thick specimens.

It is worth emphasizing, that it would be not possible to study the effect of fatigue aging on dynamic properties of GFRE, without development and implementation of a new, innovative and original elements of the testing stand. It enabled preparation and performance of series of unique tests carried out on the tested materials, and finally, verification of the hypotheses is assumed. One can conclude, that the results of the study, especially its experimental part, may be of interest to the automotive industry.

Chapter 1. Polymer based laminated composites under fatigue and impact – an overview of the research to date

In this chapter, selected issues and challenges related to the laminated composites usage in the automotive industry are discussed. Special attention is focused on mechanical properties of the glass woven fabric reinforced polymer matrix laminates. The fatigue behaviour and damage development in these materials are presented on the basis of the available literature. Selected methods of low-velocity impact resistance evaluation and ballistic performance of CFRA are also studied. Finally, a review of failure mechanism is presented that enables effective physically based modelling of mechanical behaviour of such composites subjected to the impact at low and high values of velocity.

1.1 Laminated Composite Materials

Composite is a material made of two or more constituent materials with significantly different physical or chemical properties. Their combination enables to create the light and very strength elements of high stiffness. The choice of material composition is always determined by the requirements of manufacturers and needs of users. From the user point of view, costs related to purchase, maintenance and usage are important on one hand, and safety, reliability, comfort and design on the other. In turn, the car manufacturers have to cope with restrictions resulting from international regulations and strong market competition. For these reasons, the laminated composites consisting of the plain-woven glass fiber and thermoplastic acrylic resin are ideally suited for applications in the automotive industry, as well as in civil infrastructures [1]. The specific structure of polymer based laminated composites has been intensively studied in recent years. Nevertheless, for their use on a massive scale, further studies on their composition, reinforcement geometry, as well the influence of various external conditions on their static and dynamic mechanical properties are still necessary.

1.1.1 Laminated Composite Materials – basic data

The laminated composites consist of several layers with different fiber orientations. The individual components such as glass woven fabric and thermoplastic resin remain separated within the finished structure. Usually, the resin is a tackifier, which guarantees cohesion,

hardness and flexibility. In turn, the woven fabric with high-modulus serves as a reinforcing phase, and provides in-plane or bending stiffness, depending on the application. The strength of the fiber/matrix interface is equally important in determining of the composite mechanical performance [5].

There are two classification systems of composite materials. One of them is based on the matrix material (metal, ceramic, polymer) and the second is based on the reinforcing material structure. Depending on the nature of the reinforcement, one can distinguish composites with mineral, organic or vegetable fibers. In turn, considering the type of fiber geometry, the short or long unidirectional fibers (UD), and woven fabrics are used. The most common applied combinations of the components of polymer-based composite are shown in Figure 1-1.
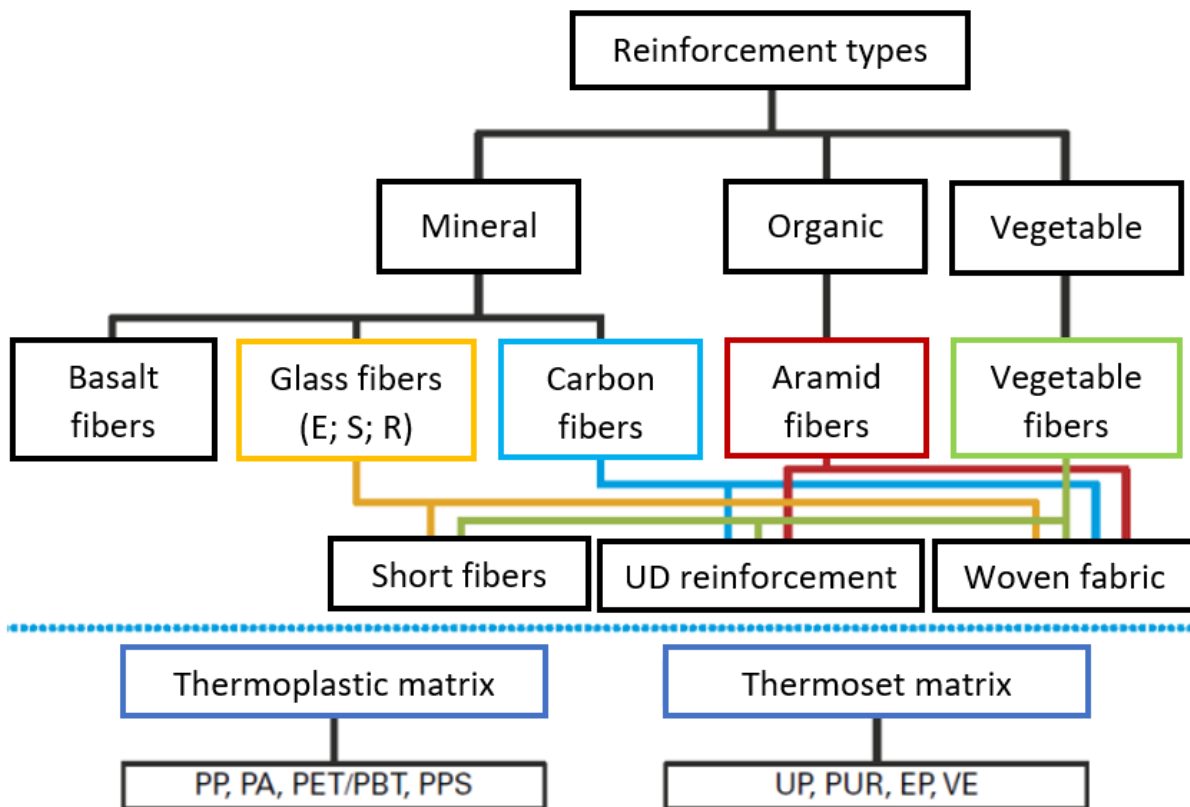
Fig. 1-1. Classification of laminated composites [14].

Depending on the types of reinforcing phase, the individual layers of laminated composite exhibit orthotropic or transversely isotropic properties. Figure 1-2 shows four types of geometric configurations in which long fiber reinforcements are implemented. The geometry and nature of reinforcement are strictly related to the intended application. In UD

composites, the fibers are uncrimped and all aligned parallel to the loading direction. As a result, they provide the highest mechanical properties in the selected direction. Flat (2D) and multidirectional (3D) fabrics are obtained by interweaving warps and wefts (Figure 1-2 (b)-(d)). Such types of geometry reduce the anisotropy of the material and increase the usability of the construction. Therefore, laminated composites consisting of 2D woven fabrics reinforcements have higher resistance to out-of-plane mechanical stresses than that of unidirectional composites and lower than that of 3D woven composites [15]. In certain situations, the depicted types of reinforcements can be mixed. The resulting hybrid composites are expensive; however, they have some unique features that provide benefits to the manufacturers and users.
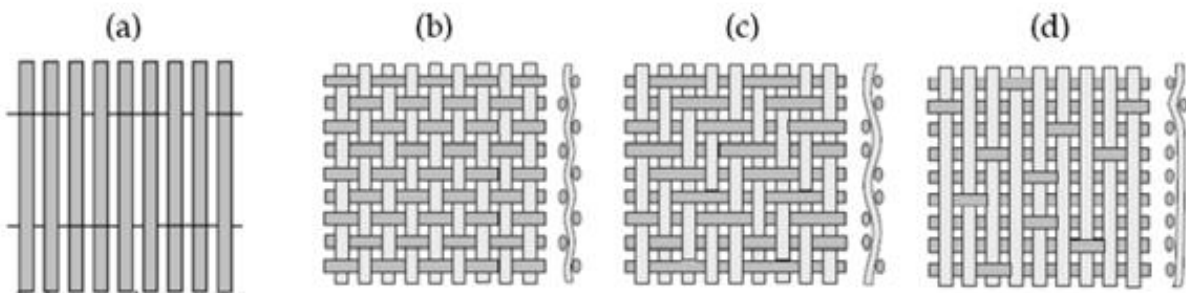
Fig. 1-2. Examples of the type of long-fiber reinforcement: (a) unidirectional, (b) plain weave, (c) twill weave and (d) satin weave [16].

A volume fraction of the reinforcing phase is usually higher than that of the resin. Such feature provides a high mechanical performance of the laminated composite. Concerning the contribution to fracture toughness of composites given by the matrix, the toughness of the matrix is partially or fully, transferred into the composite. In general, more ductile matrices are able to transfer a fraction of mechanical stresses to the fibers only, while, brittle matrices conduct all stress [17]. Beside the strong interface with the fibers, a good formability of the resins applied as well as its high resistance to the external environment are required. The most widely used resins in the polymer based laminated composites are shown in Figure 1-1. Both, thermoplastic and thermoset matrices allow to produce laminates of complex shapes. Despite the significant improvement of the thermoplastic resins' properties, the composites with thermosetting matrices offer higher mechanical resistance. In turn, the significant advantage of thermoplastic matrix is its reversibility, the ability to undergo reheating, and changing shape, while thermosetting matrix is irreversible.

Furthermore, the laminated composites based on thermoplastic resin enable the fusion bonding and recyclability. These features, as well as low cost of production, make them more attractive than the thermoset based composites and their increased application in the automotive industry.

1.1.2 Materials used in automotive production

The automotive industry uses an enormous number of materials to build cars, including iron, aluminum, steel, copper, glass, rubber, plastic and many others. These materials were modified over the decades, thus, becoming more sophisticated, better built, and safer.

More than half of the total production of modern cars consists of cast iron and steel parts (55%), plastics (11%), aluminum alloys (9%); rubber (7%) and glass (3%). The content of non-ferrous alloys (magnesium, titanium, copper and zinc) does not exceed 1%; other materials (varnishes, paints, electric wires, facing materials, etc.) make 14 %, Figure 1-3.
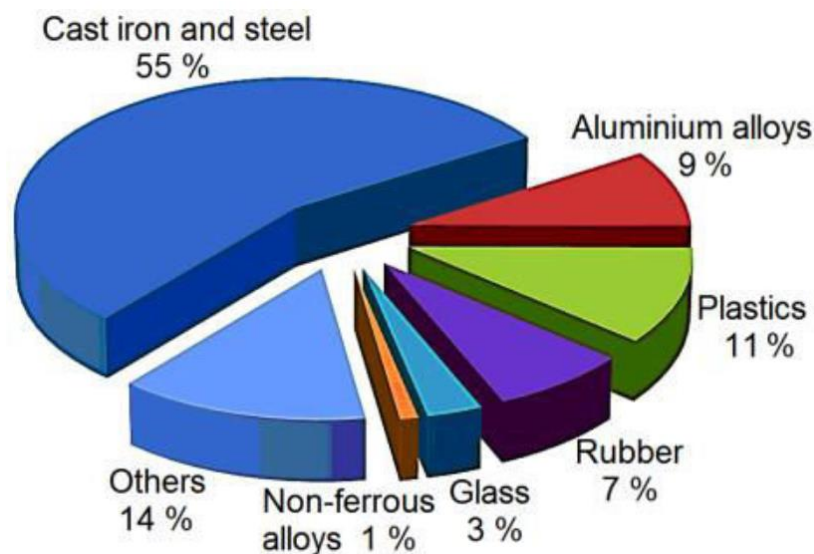
Fig. 1-3. Production volume of various types of materials used for car parts manufacturing [18].

About 80% of plastics elements used in automobiles contain: polyurethanes, polyvinyl chlorides, polypropylenes, and acrylonitrile butadiene styrene (ABS). The remaining 20% are: polyethylenes, polyamides, polyacrylates, and polycarbonates. Their common feature is almost unlimited mechanical lifetime. They exhibit an excellent corrosion, resistance and additionally, good ability to carry any static loads and vibrations. Their high strength and stiffness, resulted from addition of synthetic fibers, significantly improve the reliability and

safety of the car while reducing its weight. Since, the carbon or glass fiber reinforced polymers are especially suitable for car industry, they slowly replace steel and aluminum alloys. The only difficulty in common application of the carbon fibers in automotive industry is their very high cost of production. A part made of carbon fibers reinforced polymer is 30–40 times more expensive than that made of steel. As a result, the components produced from such materials are usually used for the tuning cars. However, application of the new manufacturing processes as well as glass fibers reinforcement, reduces a production cost of elements to the level of steel and light alloys. Figure 1-4 illustrates the usage of composites in the modern car. The outer panels of the car consisting the glass fibers reinforced polymer are marked in red.
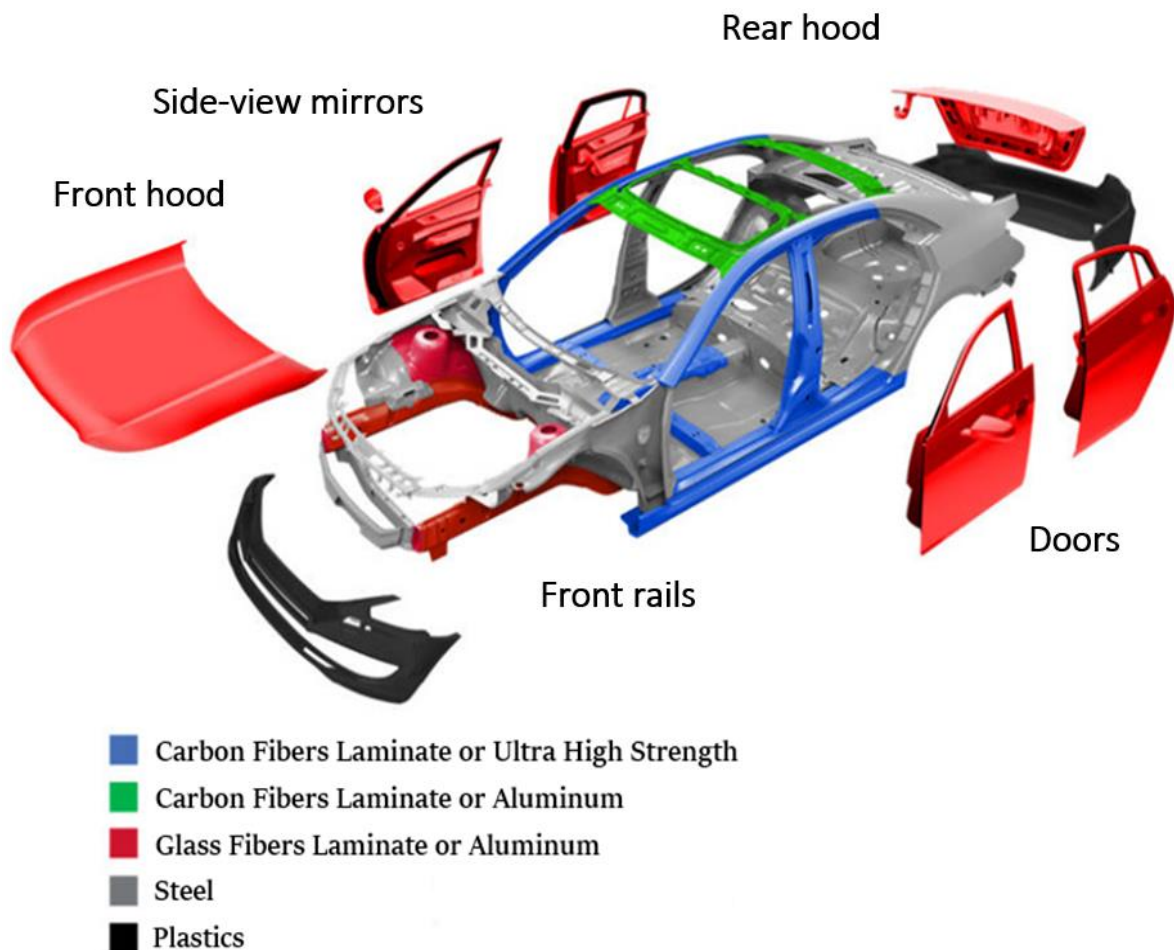
Fig. 1-4. Location of composite materials in the automotive construction [19].

Main advantages and disadvantages of using glass fibers reinforced laminates are depicted in Figure 1-5.
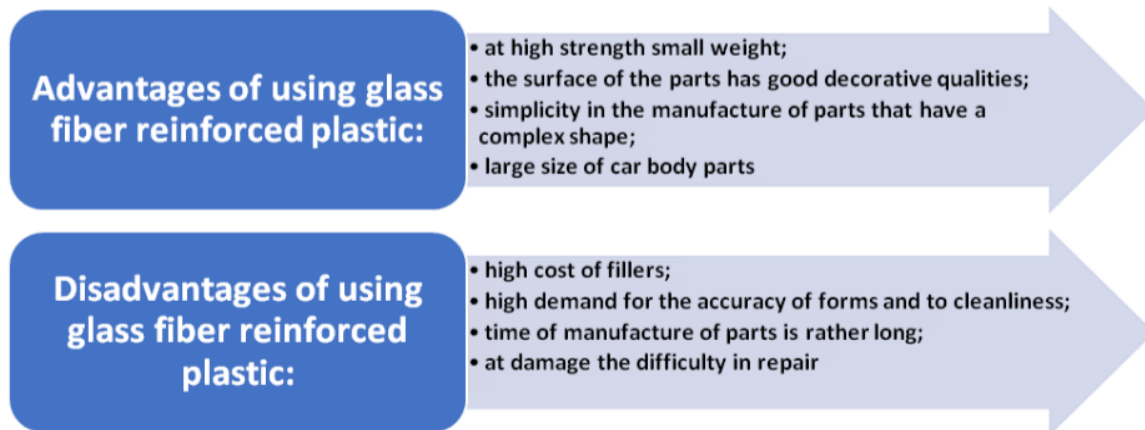
Fig. 1-5. Advantages and disadvantages of using glass fibers reinforced laminates [20].

Scientific advances and development of new polymers such as acrylic thermoplastic resin ELIUM, allow to diminish some disadvantages presented above. Introduction of modern resins facilitate the molding of laminates and significantly reduce the manufacturing time, and as a consequence, the production costs of car components. Moreover, the thermoplastic matrix of laminated composites enables the fusion bonding and remolding, thus enabling repair of the vehicle components.

1.1.3 Thermoplastic polymers-based laminated composites

The polymer-based composites attract nowadays many branches of the industry. Therefore, the key automotive companies, i.e. Renault or Stellantis Groups, are trying to increase a contribution of the thermoplastic composites in the designed vehicles. Today, the composites based on thermoplastic resins represent 37% of the world market against 63% for composites with thermosetting matrices. According to the Maximize Market Research (MMR) analysis, the thermoplastic composites industry is expected to grow at a more than 6.80% rate of CAGR by 2026 [4]. It is predicted that due to the newest European emission standards of carbon dioxide and current recycling requirements, the usage of thermoplastic matrix composites in the transportation industry will increase until the entire elimination of the thermoset in 2040.

The most widely used thermoplastic parts and components in the automotive industry are manufactured from the polyamide resins reinforced by short fibers. They are usually used as the elements working under the hood of a vehicle (injection rails, cylinder head covers,

intake manifolds, etc.) [21]. Due to their low rigidity, its application for structural or semi-structural elements are limited. In order to increase the mechanical strength and structural rigidity that come primarily from the fibers, the continuous fiber reinforcement impregnated with the acrylic resin is applied. Taking in to account the thermoplastic laminated composites, one can indicate the glass fibers as the most widely used reinforcement. According to the MMR analysis, the global glass fiber reinforced thermoplastic laminated composites market is anticipated to grow at a more than 7.80% rate of CAGR by 2026.

The thermoplastic acrylic resins are generally representing the liquid materials at room temperature which harden by the polymerization process without any heating. They have thermomechanical properties much better than those of large diffusion polymers such as polypropylene, with a lower temperature resistance (around 60-100 °C) [22]. Moreover, their unique features allow fabricating the laminated composites through processes previously reserved for thermosets (Infusion, Resin Transfer Molding (RTM), Flex-molding). From a safety point of view, the material that consists the mixture of thermoplastic resin and glass fibers ensures the same thermomechanical properties and impact resistance as that based on the thermosetting resin.

The thermoplastic acrylic resin does not damage the fibers of laminate during its manufacture and further usage. In addition, unlike thermoset, the thermoplastic acrylic resin does not have highly cross-linked bonds, that enable to remelt, and shape the composite part during manufacturing process. As a consequence, such composed laminate allows to dissolve and restore both the resin and the fibers during the recycling phase. Hence, at the end of the vehicle life, one can restore the precious fibers and resin for other applications.

1.2 Mechanical properties of the glass woven fabric reinforced polymer matrix laminates

The long fiber reinforced composite materials have a higher strength-to-density ratio and/or stiffness-to-density ratio than any other material system at moderate values of temperature. In addition, they have unique features that allow to adapt the fiber or woven fabric orientations to a given geometry, applied load and working environment. The individual layers of composites generally exhibit orthotropic or transversely isotropic properties in the plane of laminate. Due to the absence of reinforcement through-the

thickness direction, they are inherently weakest in the Z-direction (out-of-plane). There are several methods to provide reinforcement in the out-of-plane direction such as 3-D textiles, stitching, and Z-pinning. Although these approaches increase out-of-plane strength, they reduce the in-plane strength considerably [23]. In order to overcome these limits and application of the composite materials in structures where impact loading, transverse shear, and out-of-plane tensile and compressive loading appear, the laminates containing a few layers of plain woven glass fabrics reinforcement are recommended. Such a type of reinforcement ensures the in-plane high elastic properties of laminated composites on one hand, and offers good strength in out-of-plane direction on the other. Especially composites with the layers arranged in the direction of the main axes or along the applied force are the most rigid. In such case, the load applied to the material is carried out along the fibers, that have a much higher elastic modulus than the matrix. As a result, a damage takes place usually in the transversal yarns, which does not lead to a significant decrease of stiffness and accompanying drop of out-of-plane properties. An example of the laminate consisting of four layers of glass fabric, all arranged in 0°/90° orientation, is illustrated in Figure 1-6 (a). This orientation of woven fibers provides the strongest toughness in the in-plane direction of the laminate.
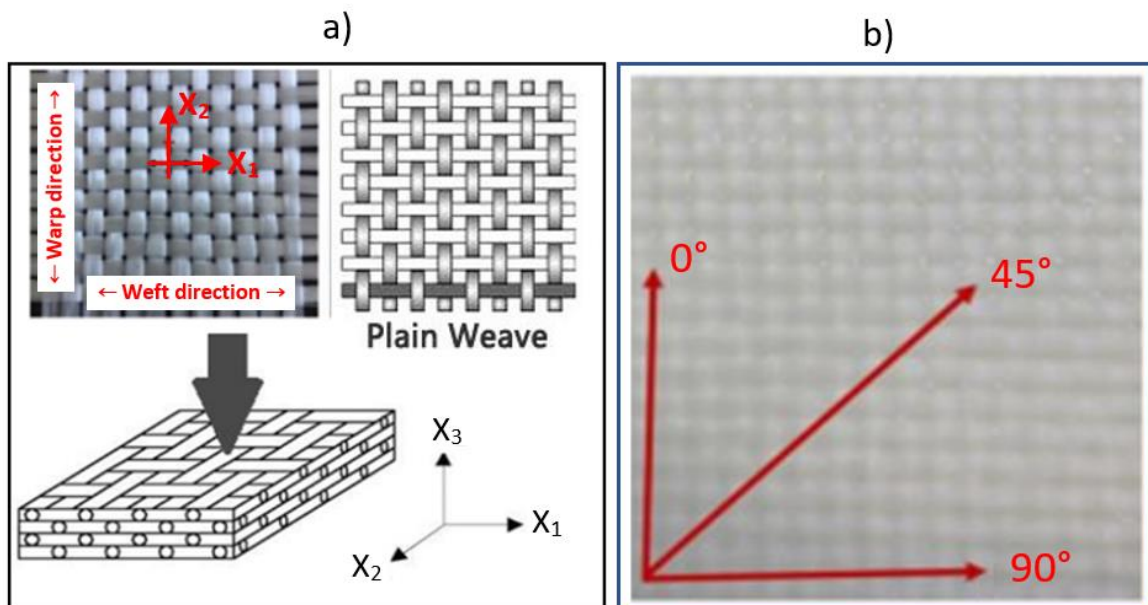
Fig. 1-6. (a) Four layers glass woven fabric configuration of [0°/90°]$_4$ orientation, (b) orientation of the yarn and direction of the applied force.

The thermomechanical behaviour of the laminated composite strongly depends on the orientation of the reinforcing phase. Therefore, regarding the laminated composites with off-axis reinforcement orientation the force applied to the material is not transmitted through the fibers. Their mechanical responses depend mainly on the quality of the fibers/matrix interface and the stiffness and strength of the matrix itself. Therefore, the laminate containing plain weave fabric, with the yarns arranged in off-axis, e.g. 45 degree, is characterized by the lower elastic limit and strength than that containing reinforcement in on-axis (along the main axes) [24]. Relation between the orientation of the yarn and direction of the applied force is illustrated in Figure 1-6 (b).

In order to describe the mechanical behaviour of the laminated composites containing the plain weave fabric, at least two orientations of fibers, representing two opposite cases are usually considered for studies. Therefore, in this work, the laminated composites containing the fibers arranged on-axis and off-axis have been studied.

1.3 Fatigue behaviour of the laminated composite

Fatigue is the progressive, localized, permanent structural change, that occurs in materials subjected to fluctuating stresses and strains that resulting in an internal damage after a given number of repetitive loading cycles. Fatigue failure is one of the most dangerous types of material damage as it can occur at low stress values (even well below the yield point of the material). The importance of cyclic loading has been recognized by the A. Wöhler (1860), who realized that cyclic stress range is more important than peak stress and introduced the concept of endurance limit (cyclic fatigue limit). Since then, many empirical methods to predict a failure have been developed.

Generally, fatigue has been classified into two types. The first one, high cycle fatigue (HCF), primarily elastic, requires more than 10^4 cycles to failure, and is generated under stress level lower than the yield point. The second one, low cycle fatigue (LCF), is induced by the stress level higher than the yield point, and is characterized by significant plasticity. During fatigue process generated either by high or low cyclic loading, one can distinguish the following three steps: (i) crack initiation, (ii) crack propagation, and (iii) ultimate failure. The most popular forms of fatigue life determination are diagrams representing relationships between:

(a) stress versus number of cycles to failure, *S-N* diagram,

(b) strain versus number of cycles to failure, $\mathcal{E}$-N *diagram*.

Fatigue behaviour of the materials is commonly characterized by *S-N* diagrams, also known as the Wöhler curves. The *S-N* curve represents a plot of the stress amplitude *(S)* versus the number of cycles to failure *(N)* on the logarithmic scale. For some iron-based and titanium alloys the *S-N* curve becomes horizontal for higher *N*, suggesting that for these materials a limit of stress amplitude can be specified below of which an infinite life is expected. Other structural metals, such as aluminium, do not have a distinct limit. Therefore, usually the fatigue strength is regarded as the value of stress amplitude to which the material can be subjected for a given number of cycles (10,000,000 cycles is the conventional used value).

The engineering structures and components are designed using the fatigue life predictions that are mainly based on *S-N* curves, in such a manner that the nominal stress amplitude remained on the level, below which inelastic deformation does not appear. When strains are no longer elastic, as occurs under certain conditions during cyclic loading of a laminated composite, the total strain can be used as an equivalent parameter instead of stress. This parameter allows to correlate the deformation and accompanying loss of stiffness with a given number of fatigue cycles. Relationship between the total strain amplitude and the number of cycles to failure is known as the strain-life ($\mathcal{E}$-N) method. In the strain-life approach the total strain amplitude $\Delta\mathcal{E}/2$ (deformation) consists of the sum of the elastic strain amplitude $\Delta\mathcal{E}e/2$ and the plastic strain amplitude $\Delta\mathcal{E}p/2$. Since 1910, the elastic part is expressed by the Basquin's law (HCF). The plastic part related to low cycle fatigue (LCF) is describing using Coffin-Manson law (1954). Based on the combination of both laws, the cyclic fatigue behaviour, is reported in form of the Manson-Coffin-Basquin curve (MCB curve). Due to the subdivided strain-life regime this curve is also called the tri-linear strain-life curve.

A type of method applied to predict fatigue life is strictly related to the external conditions and material properties, especially its internal structure and damage mode. Damage evolution under fatigue for the laminated composites are different than that in metals. Figure 1-7 illustrates typical fatigue behaviour of both types of materials as a function of the number of cycles to failure.
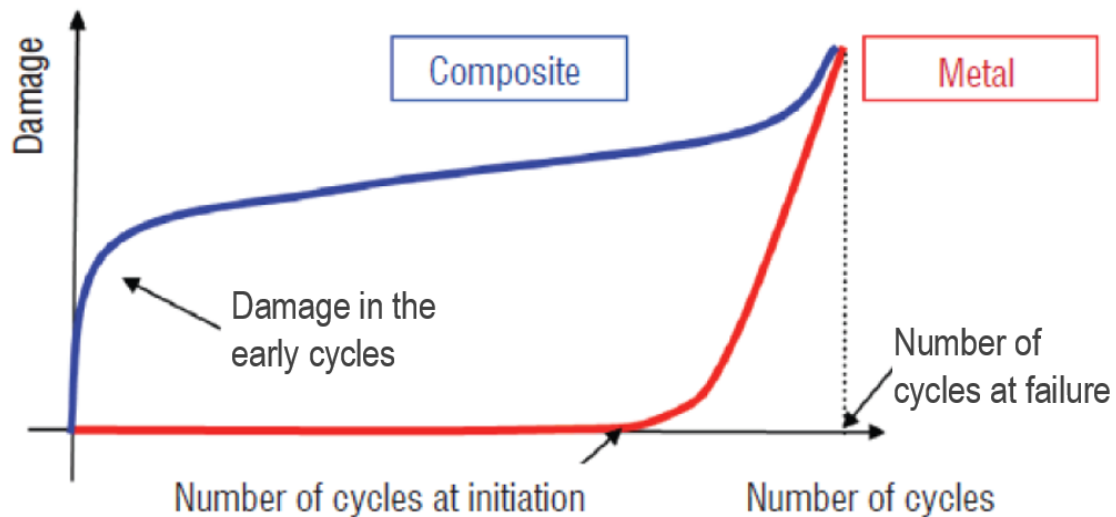
Fig. 1-7. Comparison of damage development due to fatigue for composites and metals [25].

It is clearly visible that the composites are the specific materials that can endure some assumed stiffness loss (fatigue damage) over its application [26-28]. The previous studies [12,29-30] on laminated composites indicated that inelastic deformation which occurs during cyclic loading strongly affects the fatigue life of the structure. As it increases, the small cracks in matrix or between adjacent layers appear which lead to the structural discontinuities. Since the safety of the structure is a critical factor, its influence on the fatigue strength cannot be neglected. Even a minor accumulation of such defects results in a drop of elastic properties of the laminate, and as a consequence, in a drop of the endurance limit. Therefore, in order to assess an influence of the fiber orientation and the quality of modern resins on the fatigue life of the laminated composite subjected to cyclic loading (both low and high), the extensive analyzes based on the strain-life approach are required.

1.3.1 Fatigue life prediction of the woven composite laminates

It is well known that the thermomechanical behaviour of the laminated composite strongly depends on the orientation of the reinforcing phase. Fibers orientation determines a volume fraction of the reinforcing phase, the force transmission mode, and damage evolution in the laminated composite. As a consequence, the laminated composites containing fibers arranged along the main axes (on-axis) subjected to low cyclic fatigue exhibit lower plastic deformation than those with fibers arranged at certain angle to the main axes (off-axis). Usually, there is no significant difference between the value of plastic

strain amplitude and the elastic strain amplitude of aged composites containing fibers along the main axes. Therefore, the plastic *SN*-line and elastic *SN*-line practically overlap. In turn, for the laminates containing the fibers arranged at an angle of 45° to the main axes, a difference between the plastic and elastic portion of the strain-life curve remains evident. Taking into account such aspects of physics of the laminate degradation, an extensive testing program in various loading conditions is required, for both regions of low and high cycles fatigue. Using the approaches suggested by Basquin and Coffin-Manson one can plot the elastic and plastic strain over a number of cycles to failure, and in consequence, predicts the material fatigue behaviour. An example of MCB curve is presented in Figure 1-8.
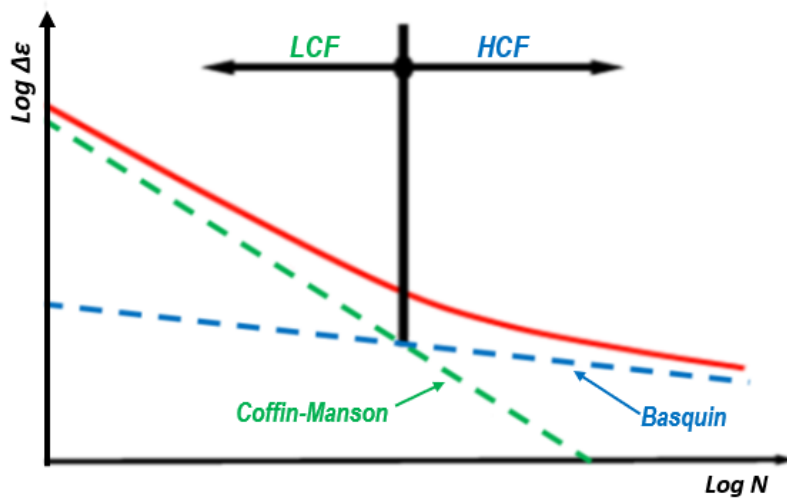
Fig. 1-8. Example of the Manson–Coffin–Basquin curve.

The elastic strain amplitude can be expressed from Basquin law (HCF):

$$\sigma_a = \frac{\Delta\sigma}{2} = \frac{\Delta\mathcal{E}_e E}{2} \tag{1-1}$$

Thus, the following equation can be obtained:

$$\frac{\Delta\mathcal{E}_e}{2} = \frac{\sigma_a}{E} = \left(\frac{\sigma'_f}{E}\right)(2N_f)^b \tag{1-2}$$

The plastic strain amplitude for low cycle fatigue (LCF) can be expressed using Coffin-Manson law:

$$\frac{\Delta\mathcal{E}_p}{2} = \frac{\sigma_a}{E} = \mathcal{E}'_f(2N_f)^c \tag{1-3}$$

Taking into account equations (1-2) and (1-3), it is possible to calculate a total strain by using the following expression:

$$\frac{\Delta \mathcal{E}_t}{2} = \frac{\Delta \mathcal{E}_e}{2} + \frac{\Delta \mathcal{E}_p}{2} = \left(\frac{\sigma'_f}{E}\right)(2N_f)^b + \mathcal{E}'_f(2N_f)^c \qquad (1\text{-}4)$$

where:

E - Young's modulus,

σ'_f - parameter that scales with tensile strength obtained by fitting experimental data,

N_f - the number of cycles to failure,

b and c - Basquin and Coffin-Manson exponents, respectively.

Based on the value of total strain calculated from equation (1-4), one can obtain the Manson – Coffin – Basquin curve.

For the long-term usage of the laminated composite, a continuously alternating loading leads to the fatigue damage accumulation, and therefore, the stiffness drops with potential destruction of the material. As far as the woven fabric composite is concerned, the main fatigue forms of damages are matrix cracking, delamination, interface debonding and fiber breakage. Depending on the degree of their evolution, a fatigue strength and stiffness of the laminated composites are decreasing [5]. Thus, it is very important to study the fatigue properties of composites under a wide range of loading conditions.

The fatigue response of laminate can be accurately described by measurement of the stiffness and strength variations, due to accumulation of internal damage caused by cyclic stress [31]. Subsequently, the residual stiffness of the tested composites can be analyzed at different stress levels for low and high number of loading cycles.
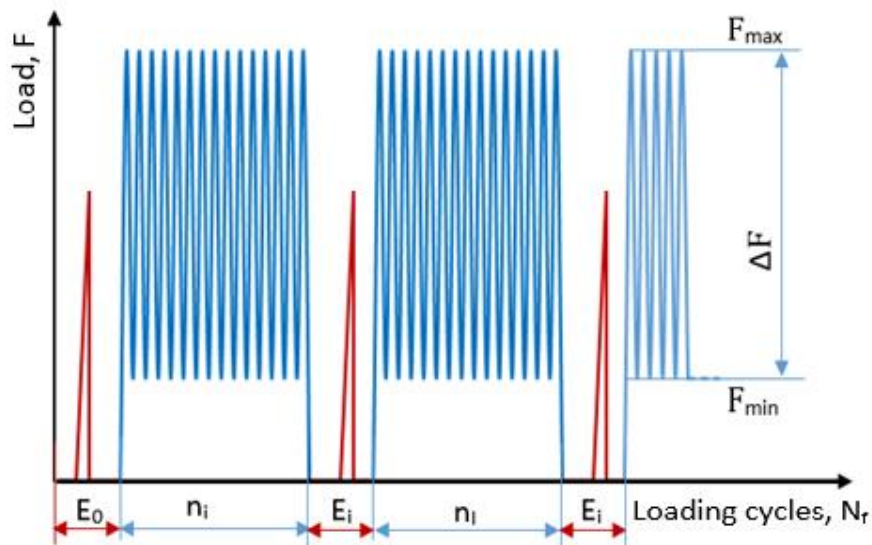
Fig. 1-9. Schematic illustration of the loading sequences.

In order to define the stiffness evolution of laminate, one can apply the same program for low and high cycle fatigue tests. Usually, the fatigue program is divided in two types of blocks denoted by blue and red, as shown in Figure 1-9. In the first block type, the elastic modulus is determined based on a simple tensile test. A maximum force during each tensile test should be lower than that corresponding to the mean loading level during fatigue aging process executed in the second block. In the second block type, a given number of uniaxial tensile cyclic loading n_i is applied. Depending on the type of test, the low cycle fatigue (LCF) or the high cycle fatigue (HCF), the values of stress amplitude are higher or lower than the yield point (σ_y), respectively. The recorded elastic modulus evolution is subsequently used to quantify the macro-scale damage.
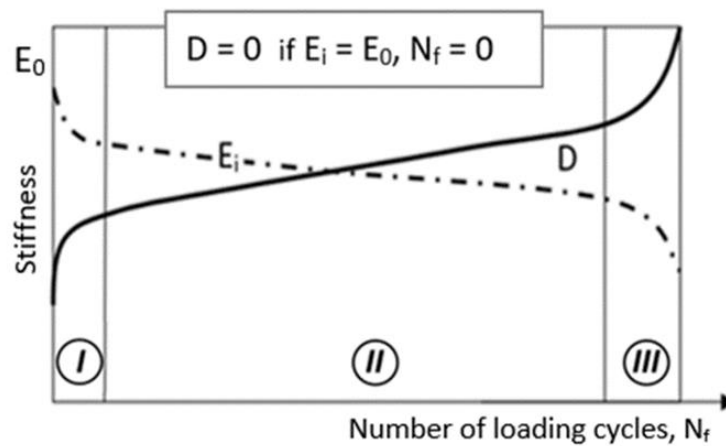
Fig. 1-10. Illustrative diagram of an evolution of damage during uniaxial tensile cyclic loading.

Based on damage evolution and accompanying loss of stiffness diagrams, a damage parameter D can be defined, as shown in Figure 1-10. By analogy to the damage definition introduced by Khachanov [31-36] or Azouaoui, et al. [12], one can find damage indicator as the loss of material stiffness. In such a case, damage can be defined by a scalar parameter D in the following way:

$$D(N_f) = 1 - \frac{E_i(N_f)}{E_0}$$

(1-5)

where:

E_0 - the initial stiffness (undamaged material),

E_i - the residual stiffness of the aged material for a given number of cycles n_i, $N_f = \sum_{i=1}^{k} n_i$.

Such defined damage parameter *D* enables one to identify either the pre-critical state or time to interrupt the cyclic loading process at a given level of stiffness loss. It has to be mentioned here, that using this method, the same level of degradation (similar stiffness loss) can be identified in all composite specimens subjected to fatigue loading. In addition, in order to relate the value of *D* parameter with evolution of damage caused by cyclic fatigue loading, the scanning electron microscope (SEM) should be used.

1.3.2 Fatigue damage development in laminated composites

The uniaxial cyclic loading process introduces in the laminated composites intralaminar and/or interlaminar mechanism of damage. Intralaminar damage is characterized by interface decohesion between the fiber and resin, which leads to cracking of the matrix. The formation of cracks in the matrix is mainly related to its rigidity and low strength. Other factors such as voids in matrix, and stress concentrations induced by fibers can increase also this type of damage. In turn, the interlaminar damage is characterized by debonding of individual layers in laminated composites. Existing low geometric diversity of singular plies, generates strong concentration of local stress caused by cyclic loading, which contributes to the growth of matrix cracks. As the microcracks increase and combine, a delamination area occurs. As it was mentioned previously, the evolution of damage in the laminated composite strongly depends on plies orientation. Figure 1-11 illustrates the processes of damage initiation and evolution under fatigue loading of 2D laminated composite with the woven fabric (warp - longitudinal yarn) arranged along the tensile fatigue direction (0°/90°).
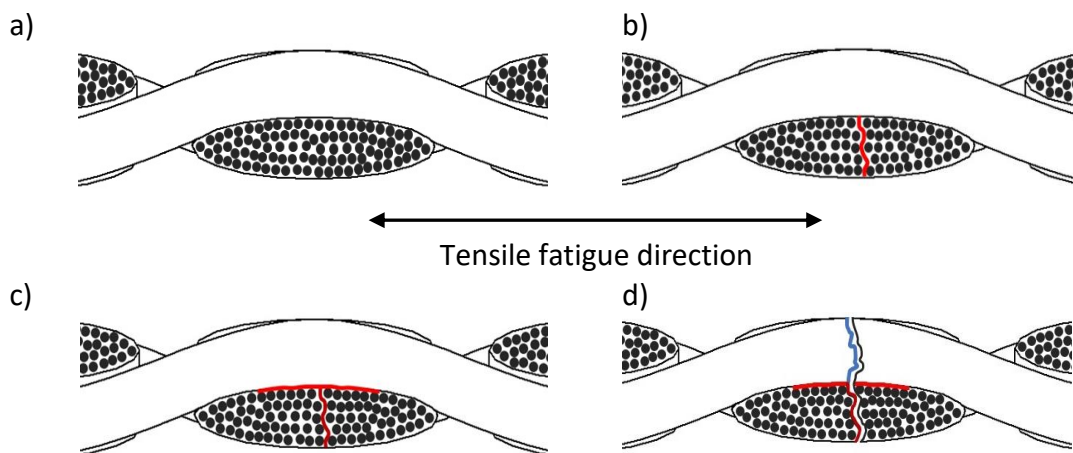
Fig. 1-11. Damage evolution induced in [0°/90°]₄ woven laminates due to fatigue loading.

The specific structure of glass woven formed by the longitudinal and transversal yarns (warp and weft, respectively) reinforcing acrylic thermoplastic resin is presented in Fig. 1-11(a). Figures 1-11(b), (c) and (d) show three types of damage appearing during fatigue aging, i.e.: (b) crack in transversal yarn which led to (c) delamination, and subsequently, (d) fracture of fibers in longitudinal yarn and yarn itself in the last cycles [37]. In turn, in the laminated composites containing woven fabric with the fibers arranged at an angle of 45 degree (45°/45°), there are no longitudinal yarns in the structural component which transfers loading force directly. The previous studies on the laminated composites with woven fabrics in this orientation [5], demonstrated that damage forms of small cavities develop mainly in the corners representing the regions rich in resin. These places are indicated in Figures 1-12 (a) and (b) by the red circles as RRA (Resin Rich Areas). Fatigue aging has the highest impact on the fiber/matrix strength in these locations, causing intralaminar damage.
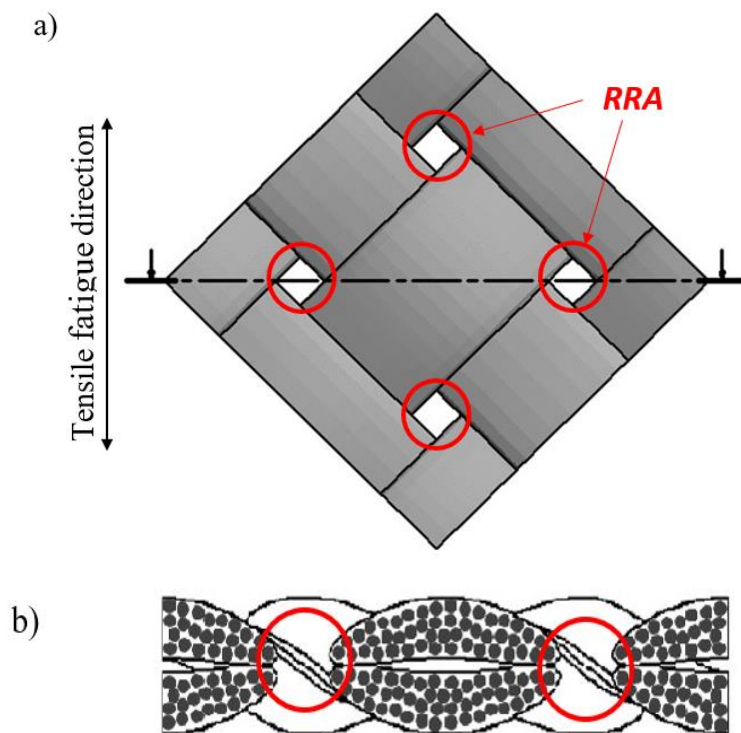
Fig. 1-12. Representative Volume Element (RVE) of the woven fabric laminated composite oriented at 45 degrees to the applied force: (a) front side, and (b) cross-section by RRA.

In order to better understand proliferation of internal changes, the scanning electron microscope (SEM) and CT scan technique are widely used. They enable a characterization of damage phenomenon in the macro and micro scales of all fiber's orientations described.

1.4 Low-velocity impact responses of CFRA

Due to the anisotropy and the heterogeneity of microstructure of laminated composites, their damage development is complex. Its evolution in laminates depends not only on the type and level of stresses, but also on the direction of applied force [15]. Usually, the out-of-plane strengths of laminate is much lower than that in the in-plane. Therefore, their application in vehicles requires knowledge on the failure progression and tolerance, especially in the direction perpendicular to the fibers layer. Since, the structural elements of a vehicle are designed to absorb the energy during crash, the ability of the material to dissipate energy of the impact is fundamental. As a consequence, the impact resistance is one of the most critical features of the composite structures, and its examination has a crucial importance. It determines the lifetime of an element, product liability and its safety as well.

A drop tower test is commonly used for evaluation of the impact properties of the acrylic matrix laminated composites. It enables one to study resistance of components at low velocity impact, according the following standards: D 7136 / D 7136 M - 07 [38], ASTM 5628-96 [39], AITM 1-0010 [40]. A simple impact test allows to find an acceleration, displacement and force evolution of the impactor during its drop on the fixed specimen. Depending on the thickness of the laminate [41], mass, shape, diameter and velocity of impactor [42-44], a partial or total perforation can be studied.

For low velocity impact test, the energy equation is given by the following formula:

$$E = mgh = \frac{1}{2}mV_0^2 \qquad (1\text{-}6)$$

where:

m - the mass,

h - the drop height,

g - the acceleration of gravity,

V_0 - the velocity at the instant of time just before the impact.

The evolution of the energy during a low velocity impact event is given by [45]:

$$E(t) = E_0 - \frac{1}{2}mV_i^2(t) = \frac{1}{2}m(V_0^2 - V_i^2(t)) \qquad (1\text{-}7)$$

where $v_i(t)$ is the velocity of impactor at time *t*, derived from the kinetic energy:

$$V_i(t) = V_0 - \frac{1}{m} \int F(t) \; dt \qquad \text{(1-8)}$$

where $F(t)$ represents the force measured by the sensor for a given time t.

Relationship between force and acceleration allows determination of the velocity at any time by a simple integration. Finally, at the end of the impact (point D in Fig. 1-13), one can calculate the absorbed energy by means of the following equation:

$$E_a = \frac{1}{2} m V_0^2 - \frac{1}{2} m V_D^2 \qquad \text{(1-9)}$$

The most common forms of the low velocity impact response presentation, and resulting damage as well, the characteristics of recorded impact histories of force-time or force-displacement. An example of the second one is shown in Figure 1-13. The impact force history at low velocity impact provides an important data regarding a damage initiation (point A in Fig. 1-13) and its further propagation [9]. A peak force (point B in Fig. 1-13) defines the maximum value of impact force (F_i) registered during the contact between the impactor head and specimen. Point C in Fig. 1-13, corresponds to the maximal deflection of laminate under low velocity impact.
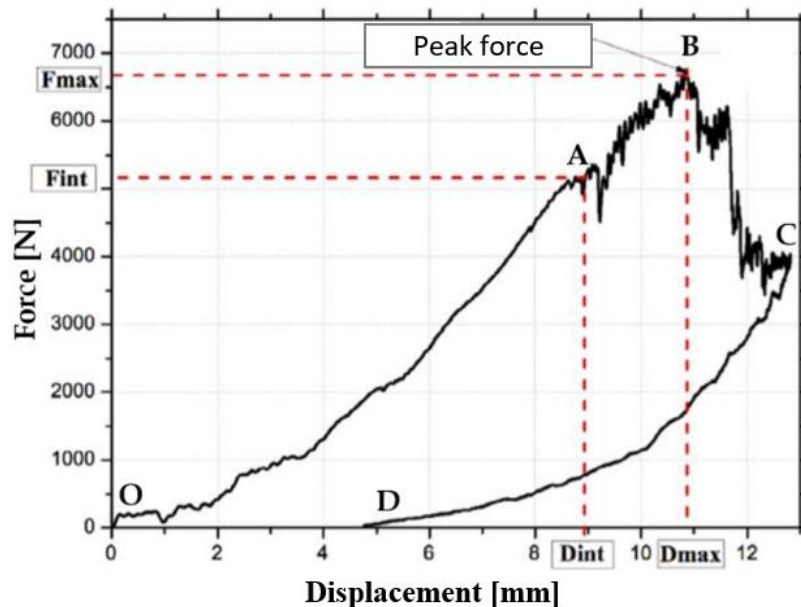
Fig. 1-13. Force versus displacement curve at low velocity impact.

In turn, an absorbed energy should be treated as the amount of energy transferred from the impactor to the specimen at the end of test. The curve representing an energy variation versus time are illustrated in Figure 1-14.
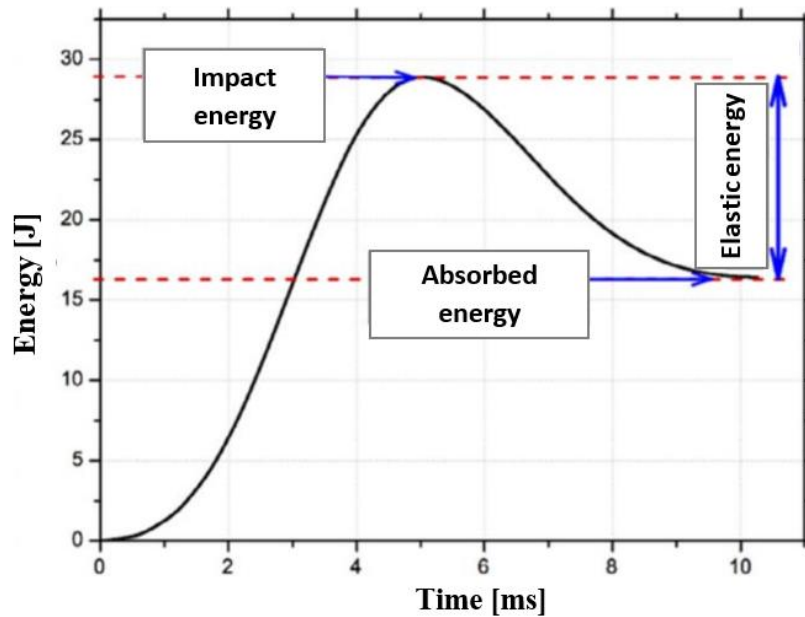
Fig. 1-14. Absorbed energy versus time curve.

The impact energy which corresponds to the peak energy on the diagram is composed of two parts, the absorbed energy (i) which generates damage in the structure of the composite, and elastic energy (ii) that serves for the impactor rebound. In the present work, the energy absorbed by the specimen is used as an indicator of damage development [9,46].

1.5 Ballistic performance evaluation of laminated composites

The safety of a structure has always been a crucial factor in the development of new materials and their applications [47,48]. Therefore, to better understand the phenomena occurring in the material during an impact, a perforation technique as well as ballistic limit are proposed. The perforation of laminated plates by impactor is a complex process which reveals such features as elastic and plastic deformation, strain rate effects, thermal softening, crack formation, delamination and fiber breakage. Besides the properties of the perforated laminate (hardness/strength, ductility, microstructure and thickness) the most important factors affecting the ballistic resistance are the impact conditions such as impact velocity, a geometry of the projectile, angle of impact and contact between the impactor and plate. Investigation of ballistic impact response of the laminated composites are usually carried out using gas gun set-up.

The applied experimental technique is presented in detail in Figure 1-15. During the tests,

the launched projectile passes through the gas gun tube. Its velocity is regulated by reduction or increase of the gas pressure accumulated in the pressure chamber. By changing the value of pressure P of the gas (air, nitrogen, etc.), an impactor with mass of 29.1 g is able to achieve the impact velocity of $V_0 = 180$ m/s. A specimen with dimensions of 100 mm x100 mm is fixed between two holders by four screws. In order to avoid the potential plastic deformation that can occur during the test, the applied holders are made of the high strength steel. During the experiment, three different states of impact can be observed. Complete perforation when the projectile passes through (i), critical perforation when the impactor stuck in the plate (ii), and no perforation (iii). In order to evaluate the high velocity impact properties, before and after the perforation of the plate, the initial velocity V_0 and residual velocity V_R, are measured using a velocity measurement system, respectively.
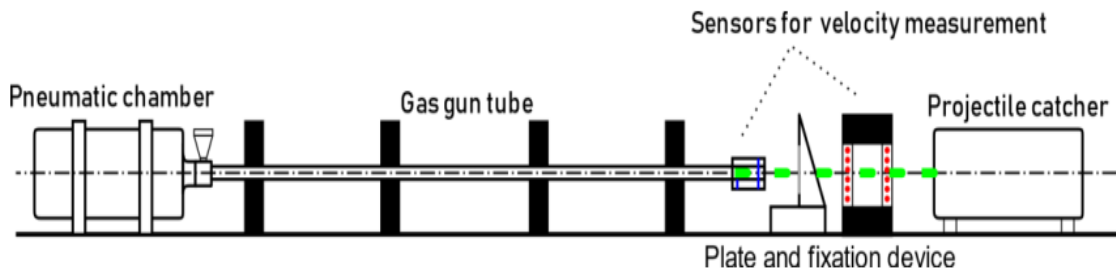
Fig. 1-15. Gas gun setup [49].

The most useful criteria to evaluate the high velocity impact resistance is the ballistic limit in terms of ballistic curves V_R–V_0. To model the ballistic curve, the analytical laws are proposed in the 1960s by Recht and Ipson [13], and Lambert-Jonas in 1976 [50]. In the present study the first one is used. This model based on consideration of momentum and energy balance. The residual velocity of the projectile V_R is calculated as a function of the initial velocity V_0 and ballistic limit velocity V_B:

$$V_R = (V_0^\kappa - V_B^\kappa)^{1/\kappa}$$

(1-10)

where K is a fitting parameter.

Another interesting method to assess the phenomena occurring during the perforation is to determine an evolution of the absorbed energy with impact velocity variation. During the perforation process, a part of the kinetic energy of the projectile is absorbed by the plate. Knowing the initial projectile velocity V_0 and residual projectile velocity V_R, energy absorbed by the plate E_d can be calculated as follows:

$$E_d = \frac{1}{2} m_p (V_0^2 - V_R^2)$$ (1-11)

where m_p is the mass of the projectile. The energy dissipation due to elastic deformation of the plate, friction between the projectile and target, and that transferred to the ejected debris are neglected, and therefore, are not taken into account in the equation (1-11).

Nowadays, one can visualize the type of damage development of the laminated composites plates induced by high velocity impact using X–ray computed tomography. This technique enables to precisely analyze the failure of fibers and resin occurring in the impacted zone. In previous studies, Gupta et al. [51] revealed that such observations allow determining the contribution of energy absorbed in fracture of fibers or absorbed during delamination under the point of impact. Usually, the failure of yarn occurs when a deflection of plate reaches the maximum level. If the maximum deflection is achieved, the fibers under the point of impact undergoes breakage due to the radial stretching of target. Tensile failure of fibers absorbs a portion of the incident energy. The total energy absorbed in tensile fracture E_{frac} can be calculated using the fallowing equation [52]:

$$E_{frac} = E_d V = E_d \pi R^2 h$$ (1-12)

where V corresponds to the volume of the composite strained up to its tensile failure. This volume is equal to the cross-sectional area of the projectile and the thickness h equal to the thickness of the composite.

In order to evaluate the ballistic performance of the laminated composites the ballistic limit and total energy dissipation criteria are used in the present work.

1.6 Failure mechanism of laminated composite structures

Woven fabric reinforced thermoplastic composites are inherently multiscale structures and can be described at three levels: microscopic, mesoscopic and macroscopic scale. The microscopic scale corresponds to their components (fiber and matrix), the mesoscopic scale consists of undulated yarns embedded in a resin, and the macroscopic one represents the laminate obtained by superposition of the layers. Such multiscale nature of the composite structures facilitates understanding of their complex behaviour by coupling different degrees of heterogeneity with the equivalent homogeneous material. As a result, one can accurately

define the relationships between the different mechanisms of deformation and damage, as well as analyse the effects of each phase on the macroscopic behaviour [53-55]. Various failure criteria for the different damage modes of laminates are proposed in the available literature. One can indicate the approaches based on: (i) damage initiation and damage propagation criteria, as well on (ii) fracture mechanics.

The approach based on damage initiation criterion is mainly applied in modeling of damage of the unidirectional (UD) fiber composites. It assumed that the failure of laminate occurs at the maximum strain or stress levels. In general, it could be divided in two main groups:

1. Failure criteria neglecting selected stress components.

2. Failure criteria considering all stress components.

Among the criteria belonging to the first group, one can indicate the ones proposed by Hoffman [56], Tsai–Wu [57], Liu–Tsai [58] and Tsai–Hill [59] theories. In general, they introduce a single inequality for each of the three in-plane stress (or strain) components. In turn, in the second group, based on criteria formulated by: Schuermann and LaRC, Hashin and Rotem [60], Chang-Chang [61], Christensen [62], Puck [63] and the generalized 3D Hashin criterion [64], the failure in one direction may be sensitive to the loads applied along other directions (including shear). Such approach allows one to combine the interactive and non-interactive conditions.

Regarding the laminated composites contained a woven fabric, Xiao et al. [65] generalized the Hashin criterion to characterize damage of a single woven ply, by taking into account the interactions between the fibers of the warp and those of the weft. In addition Juhasz et al. [66] developed a failure criterion adapted to 3D woven composites with a polymer matrix. However, the failure initiation criteria for woven composites remain to be still specified.

In the numerical model based on theories described above, the element that reach the maximum stress (or strain) level is immediately deleted, and its stiffness is reduced to zero (point A of Figure 1-16 (a)). Such material response, manifested by a sudden drop of stress and subsequent structural collapse under critical stress, is typical for the brittle laminated composites. The progressive evolution of damage (softening) needs to be taken into account in the finite-element calculation code.
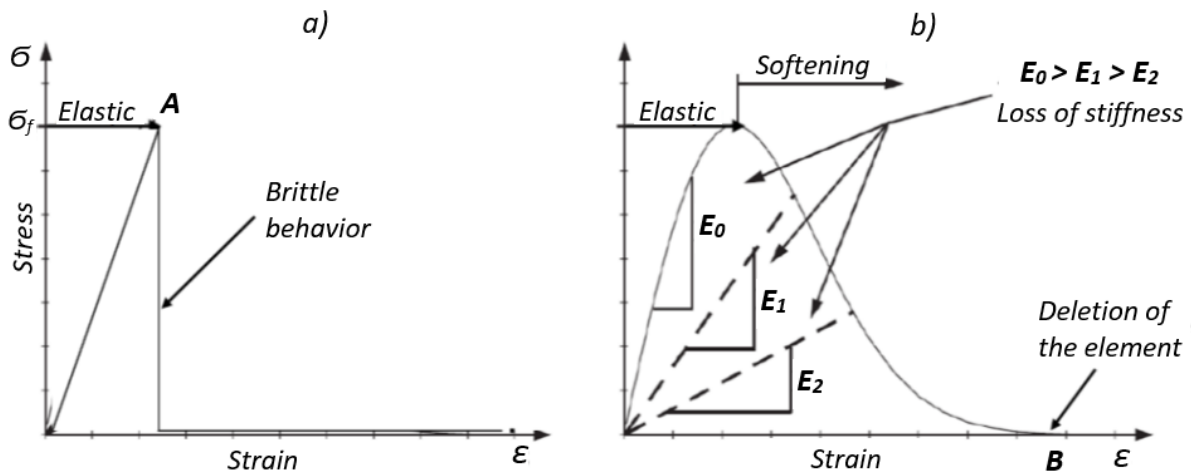
Fig. 1-16. Modeling of the damage of a laminated composite; (a) brittle behavior, (b) the progressive damage model (Matzenmiller et al. [67]).

The concept of damage mechanics was introduced by Kachanov in 1958 [68]. It is based on the assumption, that internal defects such as matrix cracks or delamination can be represented in the form of a homogeneous continuum damage fields distributed over the entire macroscopic solid domain. As they are growing, the rigidity of the material is gradually modified, that confirms the deteriorating effect of the internal damage on the mechanical properties (e.g. a growth of damage is accompanied by the progressive decrease of the Young modulus). The material degradation effects are calculated using the appropriately defined damage variables, and then, introduced into the model to simulate a progressive damage mechanism of the laminate structure. Damage variables can be presented in the scalar form (in this case, they are associated with the failure modes of the laminate) [69], or in tensor form if the orientation of the damage depends on the loading direction [70].

Continuum damage mechanics (CDM) was firstly applied for damage prediction in composites by Talreja (1985) [71]. Böhm et al. [72] developed a phenomenological damage model to describe quasi-brittle fracture behaviour in textile composites with non-crimp reinforcement. In turn, Randles and Nemes [73] developed a model using a damage variable to describe delamination identified as another critical failure mode of laminates. An important work was done by Matzenmiller et al. [67]. They proposed the anisotropic damage model to predict the strain softening behaviour (Figure 1-16 (b)) of a fiber-reinforced composite, which uses four variables of damage, and corresponds to four modes of fracture. By using the Hashin 2D criterion in plane stress state, a simple relation between

the effective stress and the nominal stress was established using 4th order damage operator. Similarly, to the anisotropic 2D damage model for long fiber composites, implemented in the Abaqus software, their model is well adapted in the standard finite element codes.

In the linear elastic fracture mechanics (MELR), the global Griffith (1921) criterion or the equivalent local Irwin (1957) criterion are taken into account in order to evaluate whether the crack is propagating or not [74]. The global approach assumes, that the propagation of cracks leads to dissipation of energy. According to Griffith's theory, the energy dissipated during crack growth is equal to the difference between the energy states of the material before and after fracture. Based on thermodynamic balance, one can consider that the fracture energy is equivalent to the new surface energy. In turn, the local criterion is based on the concept of a stress intensity factor K. It describes the intensity of the stress in the neighborhood of a crack tip as a function of the crack geometry and the loading. Based on this theory, two methods have been proposed to predict the propagation of damage in the laminated composites: the virtual crack closure technique (VCCT) and the cohesive zone model (CZM). For the evaluation of the interfacial cracking process from the crack initiation until the decohesion of interface, the second method (CZM) is more suitable. The constitutive relationships in the cohesive zone model are usually established on the basis of the relationship between the evolution of potential energy and displacement. They can be described by the bilinear law proposed by Alfano [75], parabolic linear law of Allix [76,77], or the trapezoidal and exponential laws [78]. Especially, the last law is widely used to simulate the impact behavior of the composite structures using Abaqus software.

In the present work, a macroscopic scale was taken into account in damage analysis of the quasi-transversely isotropic properties of four layers glass fiber/acrylic woven laminates. The macroscopic behavior of the response of laminated composite subject to low and high velocity impact, the failure criteria taking account interaction between different stress components have been chosen for modeling.

1.7 Conclusions

Laminated composites based on thermoplastic acrylic resin, which are the subject of research in this work, is becoming increasingly important in the automotive industry. Their specific structure allows one to reduce vehicle emissions and to achieve lightweight.

Therefore, in order to avoid their premature degradation, which can occur during exploitation, an extensive study on their mechanical behaviour is required.

In this chapter, the internal structure, as well as the mechanical properties of laminates consisting of glass plain-weave fabric composite arranged in on- and off-axis direction (0°/90° and 45°/45°, respectively) were presented. Next, a damage evolution in laminated composites subject to the low and high cyclic fatigue loading were described. In order to combine a fatigue damage and accompanying loss of stiffness, a damage parameter based on the concept introduced by Khachanov was presented.

Since, the main goal of this work, is to assess an influence of fatigue aging on the impact resistance at low and high velocity impact, the appropriate techniques to evaluate impact properties of acrylic based laminate composite, were shown. Among others, the relationship between impact force and displacement, absorbed energy, as well ballistic limit was discussed in details.

Finally, in order to model the behavior of woven laminates subjected to low and high velocity impact, the existing in the literature failure criteria for the different damage modes were analyzed. Based on the theory, in order to take into account, the through thickness stress component, the 3D Hashin modified criterion, based on four modes of damage (rupture of fibers in tension and compression, matrix cracking in tension and compression) is adopted in this work. Due to the fact that only 2D formulation of Hashin's criterion is available in Abaqus, such a 3D finite element model can be implemented through the VUMAT user subroutine using Abaqus/Explicit.

In the following chapter, the mechanical and microstructural characterizations of the glass fiber/acrylic woven laminates and pure acrylic resin ELIUM will be presented. Particular attention will be paid to the determination of its mechanical properties at different temperatures and strain rates.

Chapter 2. Thermomechanical characterization of glass fibers/Elium acrylic composite laminates

Prior to the study of fatigue aging influence on the impact resistance of glass fiber/Elium acrylic woven laminates, it is necessary to present their structure and thermomechanical properties. Therefore, in the first part of this Chapter 2, the fabrication of four-layer laminated composite plates consisting of the glass woven fabric and acrylic matrix (Elium) and pure thermoplastic resin Elium plates are presented. Then, the results of microstructural analysis of the investigated material with the yarns arranged in on- and off-axis, $[0°/90°]_4$ and $[45°/45°]_4$, respectively, are discussed. The second part of Chapter 2 is devoted to thermomechanical characterization of static and dynamic properties of the studied material for both orientations of the reinforcing phase considered. The experimental procedures, as well as the static mechanical properties, such as the failure limits and the shear and Young's moduli obtained for in-and out-of-plain direction of studied materials, are presented and discussed in details. Subsequently, the dynamic behaviour of pure and reinforced acrylic resin Elium at different temperatures and strain rates are described. All parameters determined in this chapter were subsequently applied in the three-dimensional intralaminar damage model used for the simulation of micromechanical response of selected plates subjected to the low and high velocity impact (presented in Chapter 4 and 5).

2.1 Specification of materials

The material investigated in this thesis is the glass fiber/Elium acrylic woven laminate. Elium 150 acrylic resin was developed and provided by the ARKEMA group (Lack, France). It exhibits similar mechanical properties to that of Poly(Methyl Methacrylate) (PMMA). The glass transition temperature (T_g) of Elium 150 is around 105 ∘C. In addition to the acrylic monomer (Elium), it also contains ~2.5% of the Peroxide compounds (Luperox®) that causes a polymerization reaction at ambient temperature.

A bidirectional woven glass fabric (plain weave) provided by Chomarat Textiles Industries (Le Cheylard, France) were used as the reinforcement, Figure 2-1. The material consisted of fibers intersecting themselves in the warp and weft directions. According to the datasheet, the fabric has the same properties along both of these directions. The repetition period of

the fabric pattern is T = 7.8 mm and its fabric mass area (surface density) is close to d_s = 600 g/m^2.
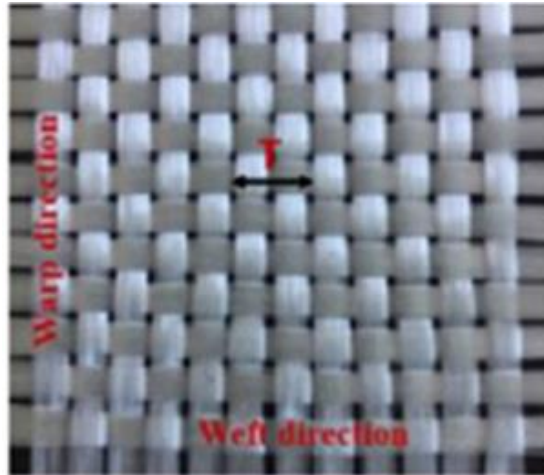
Fig. 2-1. Glass fibers plain woven fabric.

The density of the acrylic matrix and that of the fibers are indicated in Table 2-1:

Table 2-1. Density of the resin and glass fibers.

Density of the acrylic resin [kg/m^3]	Density of the glass fibers [kg/m^3]
1180	2600

2.1.1 Glass fibers based Elium acrylic laminate preparation

Composite manufacturing processes vary depending on several factors such as: the thermoplastic versus thermosetting nature of the resin, size and shape of the part, production time, as well as the expected final mechanical properties. Three steps are essential for fabrication of a composite part: (i) an impregnation of the reinforcement with the resin, (ii) shaping of the part (rheological step) and (iii) solidification step. Solidification takes place by polymerization or crosslinking in the case of thermosetting resins (at hot temperature), or by simple cooling in the case of thermoplastic resins (at ambient temperature) [79]. The processes currently used for composite manufacturing can be grouped into two main families: the draping of prepregs and liquid composite molding (LCM) [80].
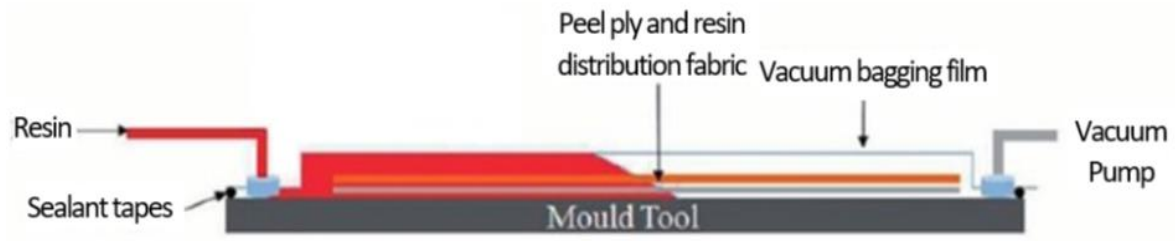
Fig. 2-2. The vacuum infusion system.

In this thesis, the vacuum infusion method was used for the laminate composite preparation, as more broadly described in [9]. This process involves the vacuum injection of a low viscosity resin into a laminate (woven), Figure 2-2. The layers of reinforcements are placed on a dry glass plate. The set is covered by a vacuum bag, which must be properly sealed. The assembly is then placed under vacuum. The vacuum allows the compaction of the laminate, while ensuring that there are no air leaks. The accelerated resin in which the peroxide catalyst (Luperox) was added, pre-mixed by blending, was introduced by means of a pot (reservoir) and a pipe (resin flow channel). The vacuum fixed by a vacuum pump enables the resin to migrate through the laminate until the upper woven is completely impregnated. Prior to the composite panel preparation, the acrylic resin was stirred and degassed in order to avoid the formation of voids during the infusion process. Four layers of the glass fabric woven identically oriented were stacking and impregnated with the Elium acrylic resin, Figure 2-3.
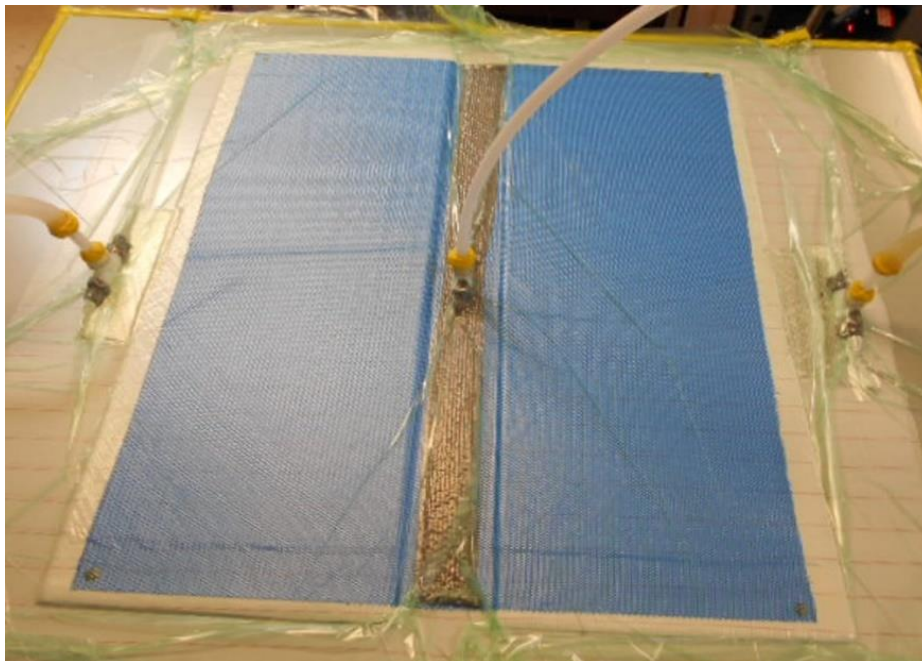
Fig. 2-3. Fabrication of GFRE by LCM.

Applying the vacuum infusion process one can fabricate large and lightweight structures with a uniform degree of consolidation. Moreover, due to very high ratio of glass or carbon fibers in the applied resin, the obtained elements are characterized by a very high strength in the in-plain direction of the laminate. Therefore, vehicle elements fabricated using vacuum infusion method are distinguished by a high quality and durability.

In order to take into account, the interlaminar damage (delamination) in the numerical modeling, the mechanical properties of pure resin Elium were determined. The material was supplied by ARKEMA in the form of plates with dimensions of 350x350 mm and thickness of about 4 mm. The plates were manufactured using the method called "Cell Casting Process", Figure 2-4. During the process, the liquid resin Elium with addition of 1 wt% of Perkadox 16 compound was introduced between 2 plates of glass. The material polymerized at temperature of about 35°C until exotherm peak was attained, then was post cured about 1h at 80°C.
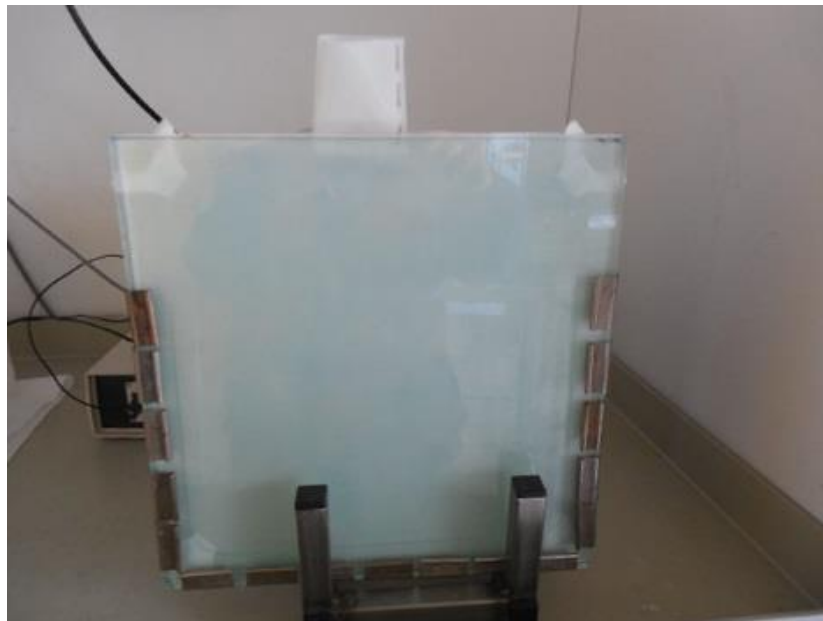
Fig. 2-4. Preparation of pure Elium150 plate by the means of cell casting process.

2.1.2 Analysis of on- and off-axis specimen's structure

An organoleptic examination of the manufactured materials in question distinguished two different surface states: a smoother surface (contact with glass) and a roughness surface (contact with bagging film). No defects were observed. Next, the optical microscope and scanning electron microscope observations were carried out on two groups of specimens.
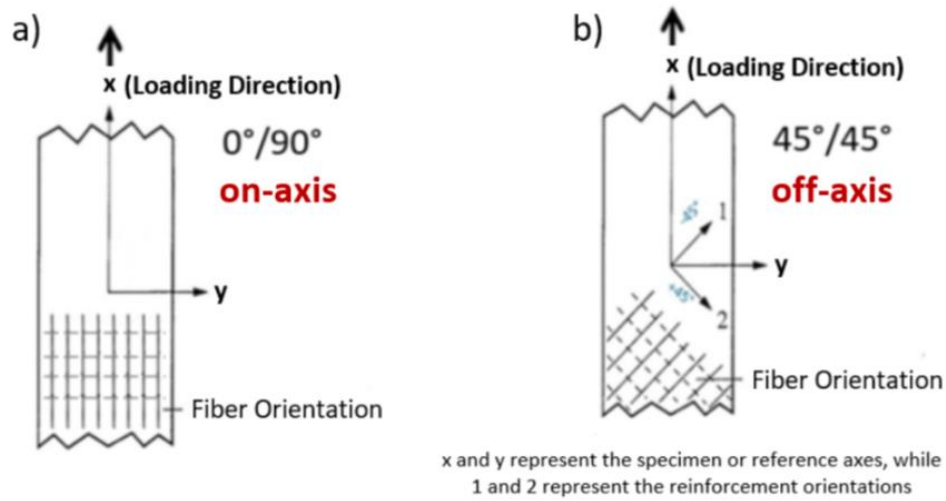
Fig. 2-5. (a) GFRE[0°/90°]₄ and (b) GFRE[45°/45°]₄.

The first group of specimens was cut out along the fibers direction (on-axis), while the second one along the direction inclined by an angle of 45° with regard to that of the fibers (off-axis). This groups were referred as GFRE[0°/90°]₄ and GFRE[45°/45°]₄, respectively. Specimens and material axes are illustrated in Figure 2-5.
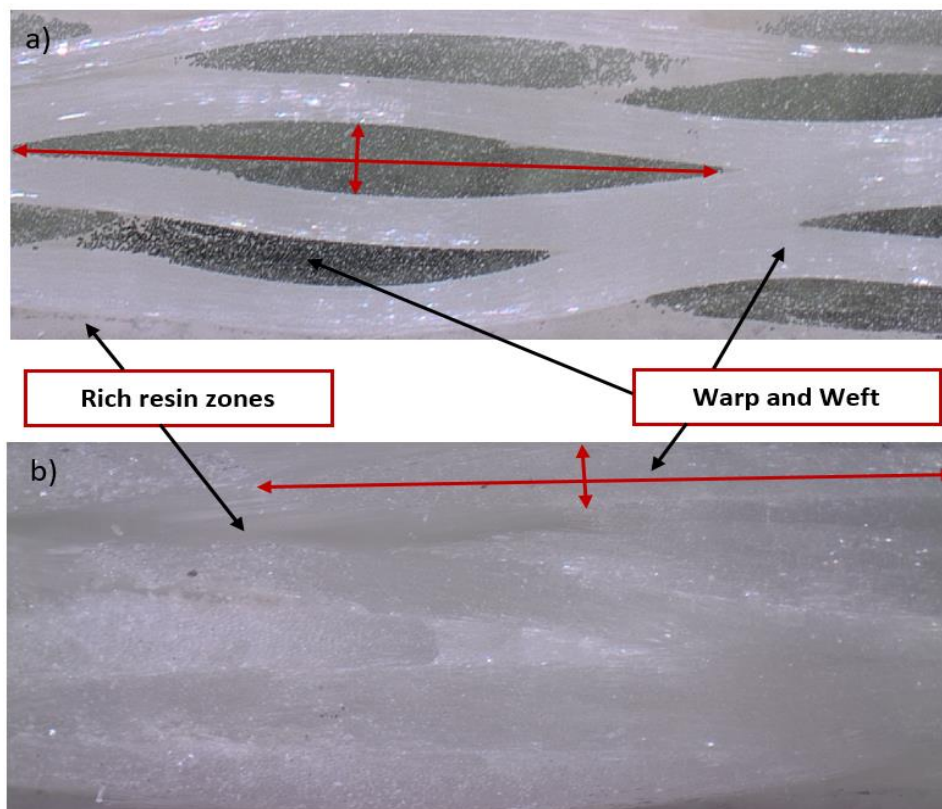
Fig. 2-6. Arrangement of fibers and resin rich areas for: (a) GFRE [0°/90°]₄ and (b) GFRE [45°/45°]₄.

Subsequently, the materials were cut using a precision cutting machine, and then mechanically polished with a diamond (final grain size close to the order of a micrometer). These operations were followed by ion polishing at 5.5 KeV.

The optical microscope observation of the fiberglass/acrylic composite (Figure 2-6 (a) and (b)) exhibited a very good consolidation of the acrylic resin. The yarns were wavy in shape with an elliptical cross-section and large and small diameters of 3.5 mm and 0.22 mm, respectively. As expected, in the case of the material oriented with an angle of 45 degree, the presence of regions rich in the acrylic resin was observed inside the structure.

SEM images (Figures 2-7 and 2-8) also confirmed a good compatibility of the acrylic resin with glass fibers. The fibers were arranged randomly in the yarns, and their diameters were in the range from 5 µm to 20 µm. The fiber holding zones (in the yarns-vein interface) and zones with low fibers density were identified.

SEM x250   SEM x700
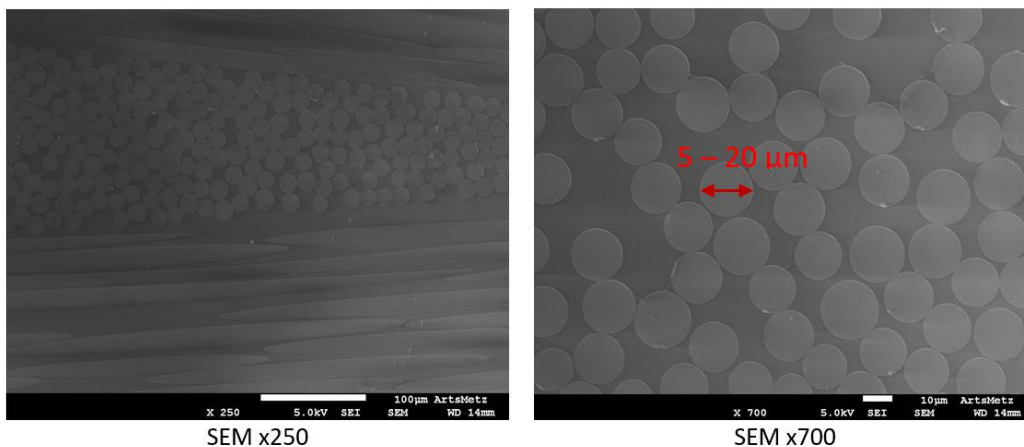
Fig. 2-7. SEM images at different magnifications showing the quality of the impregnation of the fibers in GFRE [0°/90°]₄.

SEM x 85   SEM x120
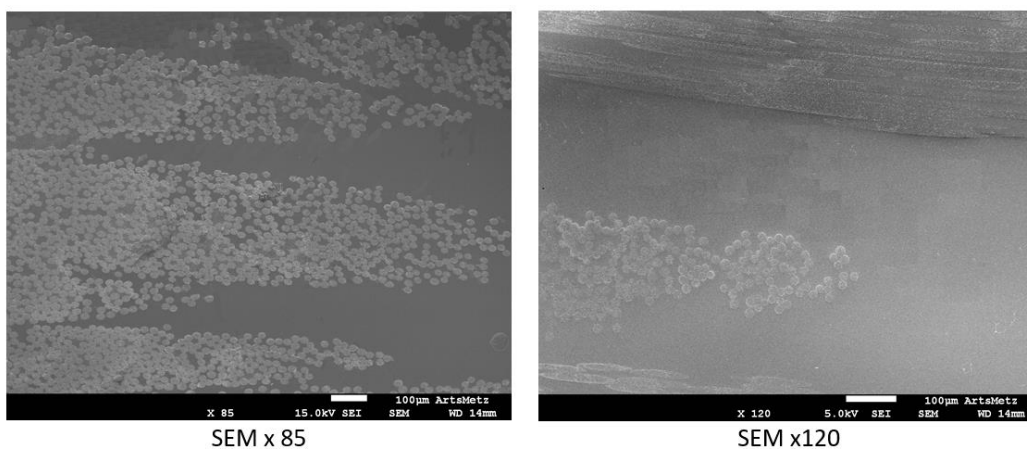
Fig. 2-8. SEM images at different magnifications showing the quality of the impregnation of the fibers in GFRE [45°/45°]₄.

The fibers content in the four layers laminated composite was determined. For this purpose, the woven fabric was weighed before and after infusion by Elium. The results of the measurements are presented in Table 2-2.

Table 2-2. Mass of ingredients used for fabrication of the laminate.

Number of layers	4 layers
Weight of the woven fabric M_w [g]	994.5
Weight of the laminated composite M_c [g]	1356.2

Assuming that there is no porosity in the material, the fiber weight fraction (f_{mf}) can be calculated using the following equation:

$$f_{mf} = M_w/M_c = 0.734 \qquad (\,2\text{-}1\,)$$

Taking into account the above result, the total fiber volume fraction was calculated in the composite:

$$V_f = \left[1 + \frac{\rho_f}{\rho_m}\left(\frac{1}{f_{mf}} - 1\right)\right]^{-1} = 0.556 \qquad (\,2\text{-}2\,)$$

The results were verified by Thermogravimetric Analysis (TGA) using Q5000IR model. The volume fraction of the E-glass fibers was about 57.0 ± 0.6% for on-axis specimens, and 59.0 ± 0.8% for off-axis specimens.

2.2 Mechanical characterization of laminated composites

As it was already mentioned, the numerical simulation of the laminated composites subjected to low and high impact velocity requires prior knowledge of its mechanical behaviour. Therefore, in order to describe the three-dimensional intralaminar damage model used in this thesis, the experimental investigations necessary to describe mechanical behaviour of glass fiber/Elium acrylic woven laminates are presented. The applied techniques allowed to determine the required failure limits, as well as the shear and Young's moduli for both in-and out-of-plain directions of the materials tested.

2.2.1 Experimental determination of elastic constants

For small deformations, the strain-displacement relationships, equilibrium and compatibility equations remain the same either for the isotropic or anisotropic composite material. In turn, the stress-strain equations of the anisotropic composite material and

isotropic material are different [81]. The general form of the Hooke's law can be expressed in the following way:

$$\sigma = C : \varepsilon^e$$

(2-3)

where:

σ - stress tensor
ε^e - elastic strain tensor
C - fourth-order tensor termed as the stiffness tensor.

Table 2-3. Different degrees of material anisotropy [82].

Materials	Stiffness matrix	Elastic constants
Orthotropic	$[C_{ij}] = \begin{bmatrix} C_{11} & C_{12} & C_{13} & 0 & 0 & 0 \\ & C_{22} & C_{23} & 0 & 0 & 0 \\ & & C_{33} & 0 & 0 & 0 \\ & & & C_{44} & 0 & 0 \\ & \text{Symmetry} & & & C_{55} & 0 \\ & & & & & C_{66} \end{bmatrix}$	9 independent E_1, E_2, E_3 V_{12}, V_{13}, V_{23} $\mu_{12}, \mu_{13}, \mu_{23}$
Quasi-transversely isotropic	$[C_{ij}] = \begin{bmatrix} C_{11} & C_{12} & C_{13} & 0 & 0 & 0 \\ & C_{11} & C_{13} & 0 & 0 & 0 \\ & & C_{33} & 0 & 0 & 0 \\ & & & C_{44} & 0 & 0 \\ & \text{Symmetry} & & & C_{55} & 0 \\ & & & & & C_{55} \end{bmatrix}$	6 independent $E_1 = E_2, E_3$ $V_{12} = V_{21}, V_{13} = V_{23}$ $\mu_{12}, \mu_{13} = \mu_{23}$
Transversely isotropic	$[C_{ij}] = \begin{bmatrix} C_{11} & C_{12} & C_{13} & 0 & 0 & 0 \\ & C_{11} & C_{13} & 0 & 0 & 0 \\ & & C_{33} & 0 & 0 & 0 \\ & \text{Symmetry} & & \frac{C_{11}-C_{12}}{2} & 0 & 0 \\ & & & & C_{55} & 0 \\ & & & & & C_{55} \end{bmatrix}$	5 independent $E_1 = E_2, E_3$ $V_{12} = V_{21}, V_{13} = V_{23}$ $\mu_{12} = \dfrac{E_1}{2(1+v_{12})}, \mu_{13} = \mu_{23}$
Cubic	$[C_{ij}] = \begin{bmatrix} C_{11} & C_{12} & C_{12} & 0 & 0 & 0 \\ & C_{11} & C_{12} & 0 & 0 & 0 \\ & & C_{11} & 0 & 0 & 0 \\ & & & C_{44} & 0 & 0 \\ & \text{Symmetry} & & & C_{44} & 0 \\ & & & & & C_{44} \end{bmatrix}$	3 independent $E_1 = E_2 = E_3 = E$ $V_{12} = V_{13} = V_{23} = V$ $\mu_{12} = \mu_{13} = \mu_{23} = \mu$
Isotropic	$[C_{ij}] = \begin{bmatrix} \lambda+2\mu & \lambda & \lambda & 0 & 0 & 0 \\ & \lambda+2\mu & \lambda & 0 & 0 & 0 \\ & & \lambda+2\mu & 0 & 0 & 0 \\ & \text{Symmetry} & & \mu & 0 & 0 \\ & & & & \mu & 0 \\ & & & & & \mu \end{bmatrix}$	2 independent E v $\mu = \dfrac{E}{2(1+v)}$

The stiffness tensor can describe any linear material, including anisotropic material such as the laminate composite. It is characterized by partial symmetries, that allow to minimize the number of stiffness matrix components. Therefore, the isotropic material can be described using only 2 components, while for the orthotropic one, 9 components are required. Examples of the degrees of material anisotropy are presented in Table 2-3.

For woven composites containing plain weave, there is no preferred direction in the in-plane of the laminate, hence, the mechanical behaviour is the same in the direction of warp and weft. As a consequence, the fourth-order tensor for the quasi-transversely isotropic material has only 6 matrix components in the three-dimensional configuration. Therefore, the stiffness tensor is defined by:

$$
\begin{Bmatrix} \sigma_{11} \\ \sigma_{22} \\ \sigma_{33} \\ \sigma_{12} \\ \sigma_{23} \\ \sigma_{31} \end{Bmatrix} = \begin{bmatrix} C_{11} & C_{12} & C_{13} & & & \\ C_{12} & C_{22} & C_{13} & & 0 & \\ C_{13} & C_{13} & C_{33} & & & \\ & & & C_{44} & 0 & 0 \\ & 0 & & 0 & C_{55} & 0 \\ & & & 0 & 0 & C_{55} \end{bmatrix} \begin{Bmatrix} \varepsilon_{11} \\ \varepsilon_{22} \\ \varepsilon_{33} \\ 2\varepsilon_{12} \\ 2\varepsilon_{23} \\ 2\varepsilon_{31} \end{Bmatrix} \qquad (2\text{-}4)
$$

In order, to describe the individual components of such stiffness tensor, the following parameters of the laminated composite are used:

− two Young's moduli: $E_{11} = E_{22}$ and E_{33}
− two Poisson's coefficients: $v_{12} = v_{21}$ and $v_{23} = v_{31}$
− two shear moduli: G_{12} and $G_{31} = G_{23}$

where orientation (3) corresponds to the direction which is perpendicular to a plane of the laminated composite.

In order to determine the material constants of a quasi-transversely isotropic laminated composite containing plain woven fabric, four types of experiments are performed:

− the uniaxial tensile test in the direction of the fibres that allows to obtain E_{11}, E_{22} and the Poisson's coefficients v_{12}
− the in-plane shear test, which gives G_{12}
− the short-beam three-point bending test, that provides G_{23}
− the out-of-plane compression test to calculate E_{33} and $v_{31,}$ v_{23}.

It should be noted that in this study, the value of shear modulus G_{23} was not determined experimentally trough the short-beam three-point bending test. This is due to the fact that the thickness of the prepared specimens of the tested material was not in accordance with the standard (D2344/D2344M). Therefore, the shear modulus G_{23} was taken from the literature, and its value was assumed to be 6.37 GPa [54].

2.2.2 Experimental investigations of mechanical properties

The tensile tests were carried out using MTS 810 uniaxial servo-hydraulic machine presented in the Figure 2-9 (a). The tensile tests were performed at room temperature under the displacement control at strain rates of 10^{-4}, 10^{-3} and 10^{-1} s^{-1}. An extensometer with the strain range of ± 0.2 was used. The loading cell was calibrated in the range of ±250 *kN*. In order to determine the Poisson's ratio, the digital image correlation (DIC) system was applied. The device was calibrated for the volume range of 190 mm×135 mm×120 mm, using the CP40-170-42201 calibration plate. Recording frequency for image capturing was constant and equal to 5 Hz. The specimens with dimensions presented in Figure 2-9 (b) were fixed by self-tightening hydraulic grips.

Determination of the elastic constants E_{11}, v_{12} - tensile tests (D3039/D3039M) [83,84]:

Orientation of the fibers has an undeniable effect on the mechanical properties of the glass fibers reinforced laminate composites. For this reason, the specimens composed of acrylic matrix and four layers of woven were cut out using a water-jet machine in two orientations, as it has been already described earlier:

-   along the fibers, GFRE [0°/90°]$_4$
-   with an angle of 45 degree with regard to that of the fibers one, GFRE [45°/45°]$_4$

The specimens with the glass woven fabric arranged along the fibers GFRE [0°/90°]$_4$ were investigated firstly.

The Young's modulus E_{11} = E_{22}, ultimate tensile strength σ_{11} = σ_{22}, maximal strain ε_{11} = ε_{22} (Figure 2-10), and Poisson's ratio v_{12} = v_{21} were determined (Figure 2-11). As it is clearly shown, the tensile response of the laminate is almost purely elastic. There is no any plastic deformation over the yield stress, which is typical for the most of the polymer-based materials reinforced with the fibers arranged along the applied force subjected to tensile loading. It should be also noted, that the ultimate tensile strength values of the material

tested exhibit strain rate dependence, which is obtained from the viscous effect of the polymer matrix. The tensile properties of tested GFRE [0°/90°]₄ are shown in Table 2-4.

a)

b)
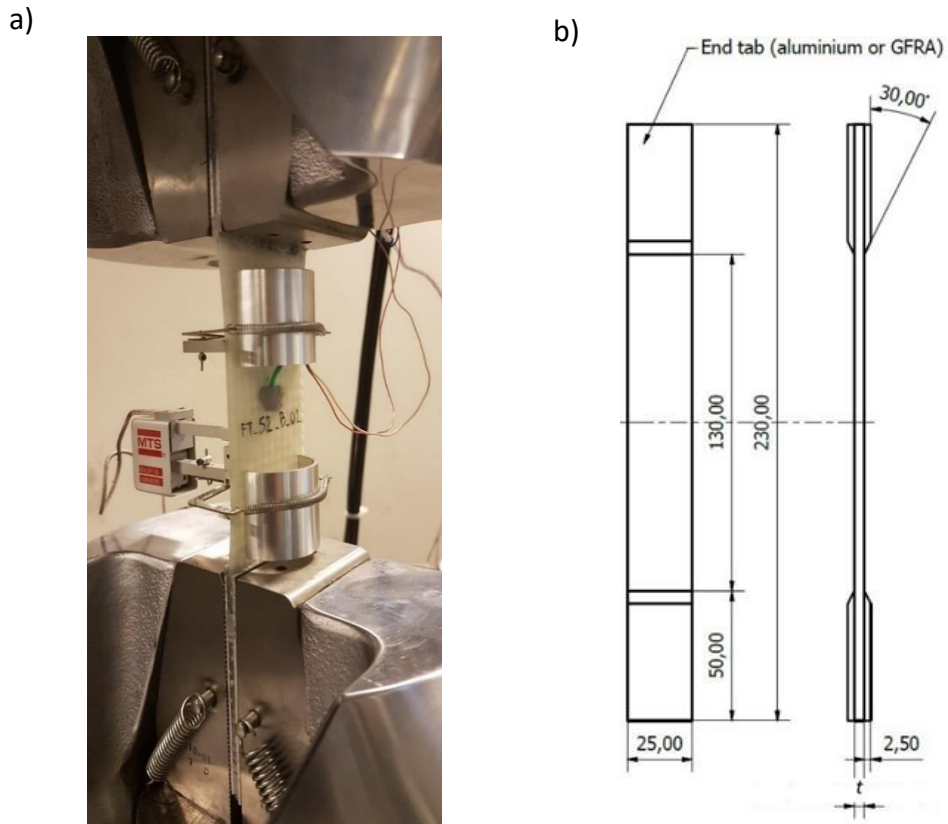
Fig. 2-9. (a) Experimental setup used for tensile tests, (b) engineering drawing of the specimen.
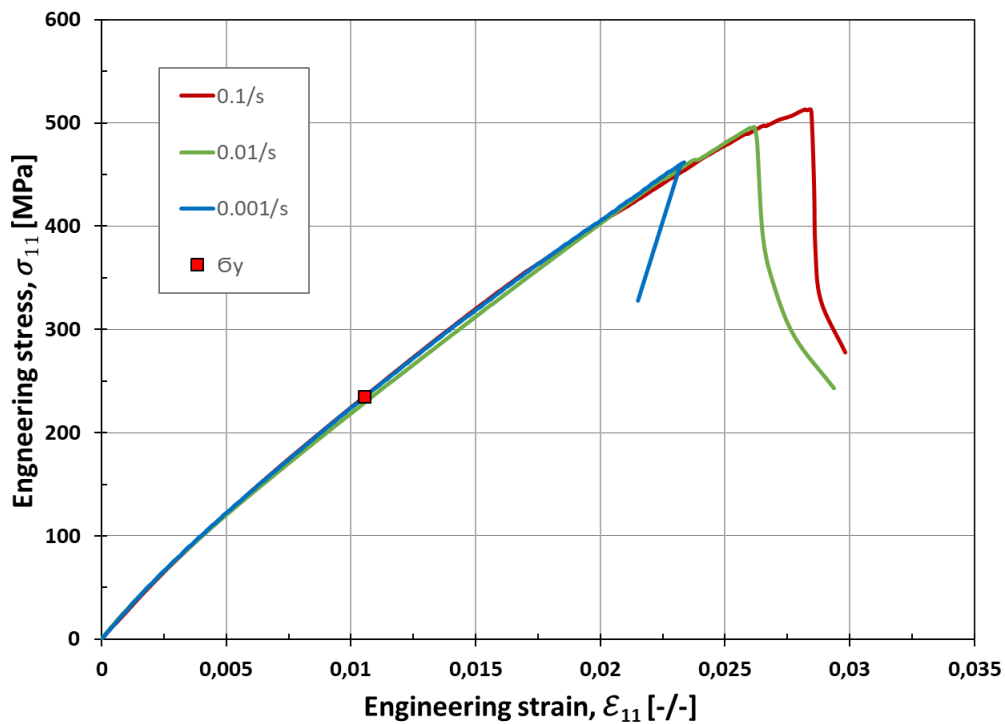
Fig. 2-10. Stress-strain curves of GFRE [0°/90°]₄ laminate.
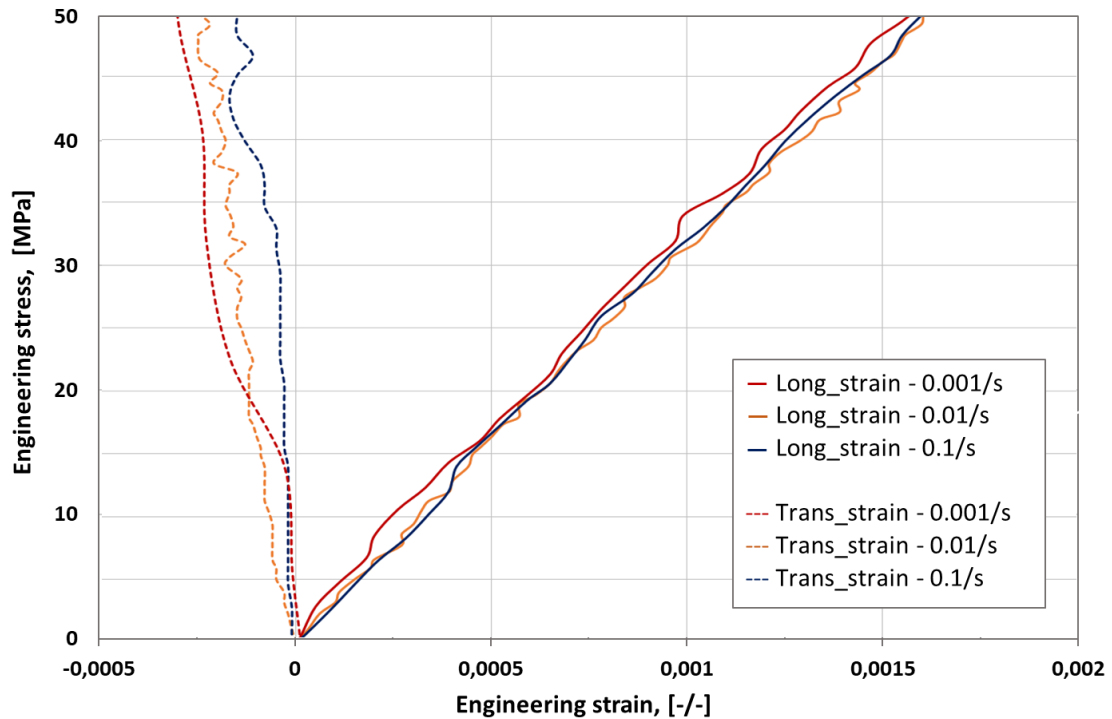
Fig. 2-11. Stress-strain curves of GFRE [0°/90°]₄ laminate for longitudinal and transversal direction.

Table 2-4. Tensile properties of GFRE [0°/90°]₄.

Strain rate	Parameter	Average value	Standard deviations
1 mm/min	E_{11}	27.4 GPa	± 1.30
	ν_{12}	0.18	± 0.06
	σ_{11}	440.0 MPa	± 36.41
	ε_{11}	0.021	± 0.002
10 mm/min	E_{11}	27.5 GPa	± 1.14
	ν_{12}	0.192	± 0.05
	σ_{11}	460.0 MPa	± 39.41
	ε_{11}	0.0235	± 0.002
100 mm/min	E_{11}	27.7 GPa	± 0.99
	ν_{12}	0.2	± 0.05
	σ_{11}	515.0 MPa	± 47.11
	ε_{11}	0.0285	± 0.002

In the next step the second group of specimens with the glass woven fabric arranged at an angle of 45 degrees with regard to that of the fibers one, GFRE [45°/45°]₄ were tested.
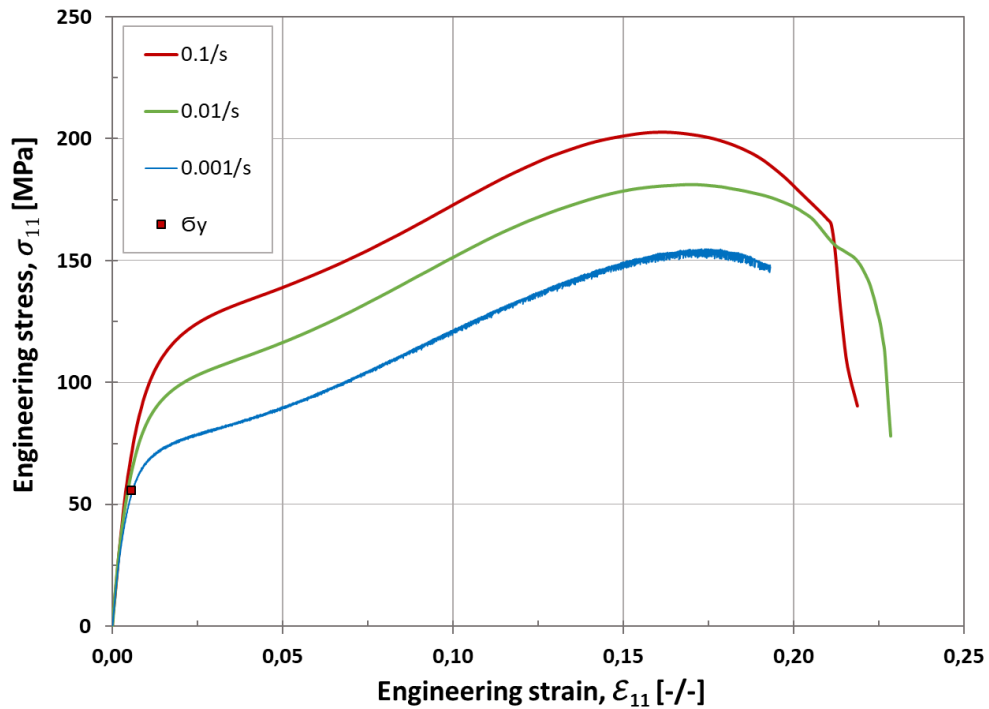
Fig. 2-12. Stress-strain characteristics for GFRE [45°/45°]₄ laminate.

In order to determine the elastic properties and failure limits, the same setup as for the on-axis test specimens was used. The tensile response in the form of the stress-strain curves, and in-plane axial and transversal stress vs strain curves of GFRE [45°/45°]₄ tested, are presented in Figures 2-12 and 2-13, respectively. All parameters determined during the experiments carried out on the off-axis laminate, are listed in Table 2-5.
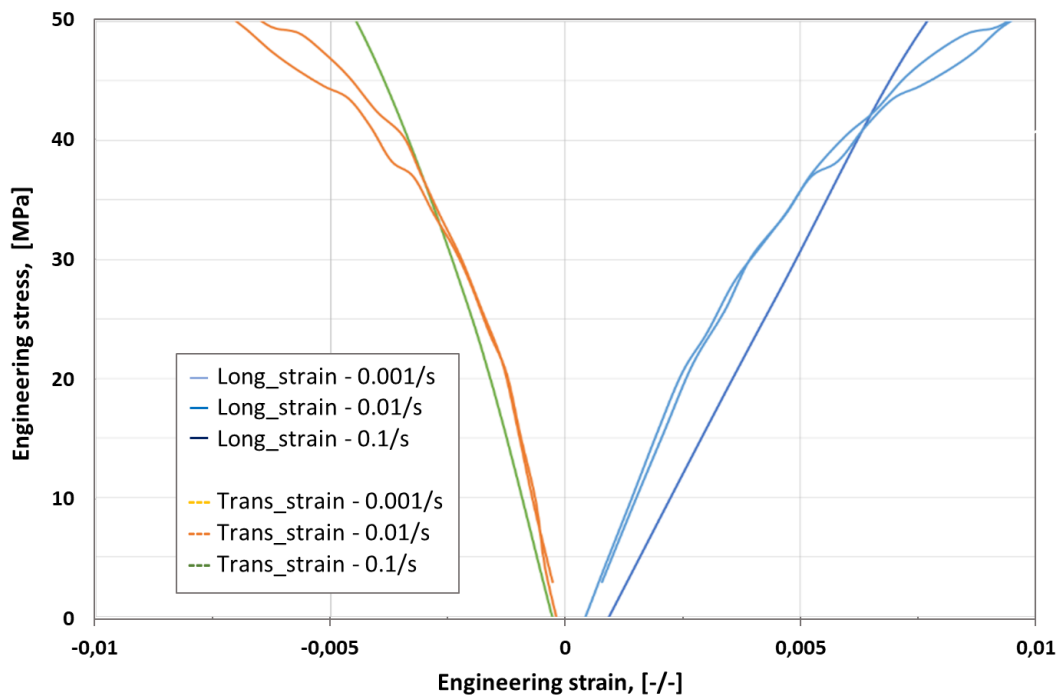
Fig. 2-13. In-plane axial and transversal stress vs strain curves of GFRE [45°/45°]₄ laminate.

Table 2-5. Tensile properties of GFRE[45°/45°]$_4$.

Strain rate	Parameter	Average value	Standard deviations
1 mm/min	E_{11}	15.9 GPa	± 1.42
	ν_{12}	0.35	± 0.08
	σ_{11}	160.0 MPa	± 10.23
	ε_{11}	0.19	± 0.012
10 mm/min	E_{11}	16.6 GPa	± 1.24
	ν_{12}	0.36	± 0.06
	σ_{11}	180.0 MPa	± 12.15
	ε_{11}	0.23	± 0.021
100 mm/min	E_{11}	17.2 GPa	± 0.93
	ν_{12}	0.38	± 0.07
	σ_{11}	205.0 MPa	± 14.36
	ε_{11}	0.215	± 0.014

Similarly as for the material containing the woven fabric arranged along the fibers (on-axis case), effect of strain-rate dependence of the strength was observed for GFRE [45°/45°]$_4$. It is typical effect occurring during the tensile loading carried out on the polymer matrix-based laminates under different values of strain rates. It has to be emphasized, that all the parameters determined till now in this section are in agreement with the results obtained by other studies reported in the literature [85,86].

Determination of the in-plane shear modulus G_{12} - Two Rail-shear test (D4255M):

In order to determine the in-plane shear properties of the fiber-reinforced composite laminates according to ASTM D4255M standard, the Rail Shear Apparatus shown in Figure 2-14 (a) was applied [87]. A special specimen was clamped between loading plates and yokes, and then, it was subjected to shear loading by compression. In order to measure shear modulus, the use of strain gauges on the specimen is required. However, one can also determine the parameter applying DIC system. Therefore, the strain component γ_{12} was determined directly by the DIC system, based on measurement frames covering area of 180 mm × 130 mm (4240 × 2824 pixels) as shown in Figure 2-14 (b). Similarly, to the tensile test, two groups of specimens were prepared. First one, with the glass woven fabric arranged

along the fibers, GFRE [0/90°]$_4$, and the second one, with reinforcement arranged at an angle of 45 degree with regard to that of the fibers one, GFRE [45°/45°]$_4$. The dimensions of standard shear specimen are shown in the Figure 2-15.
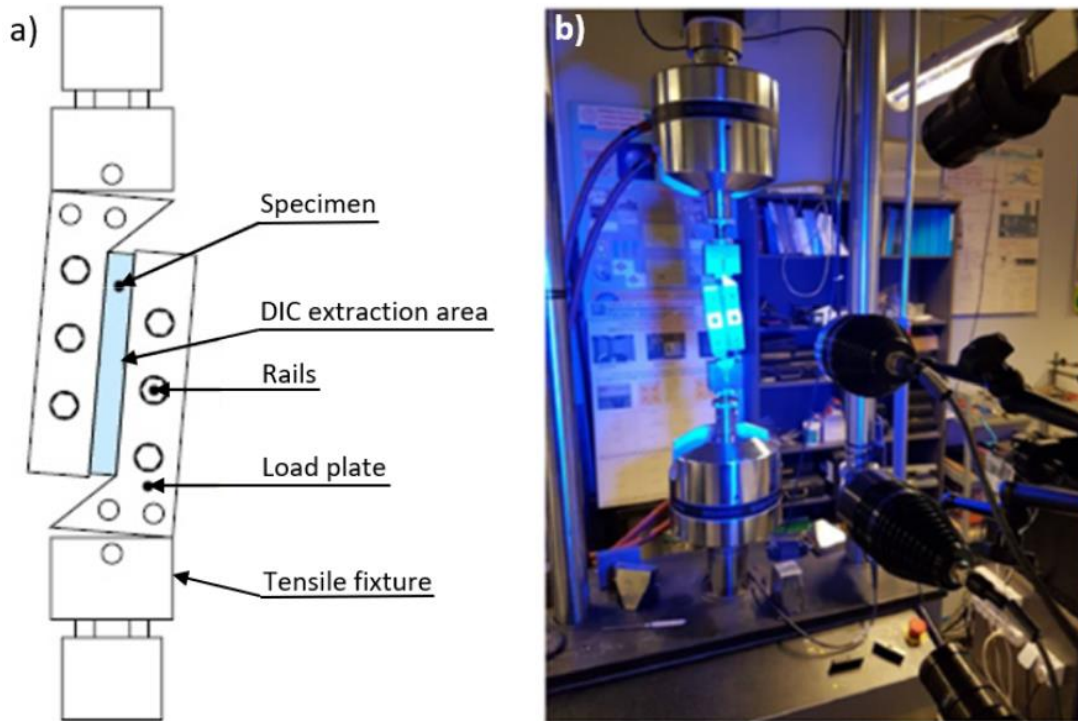
Fig. 2-14. The Rail Shear Apparatus.
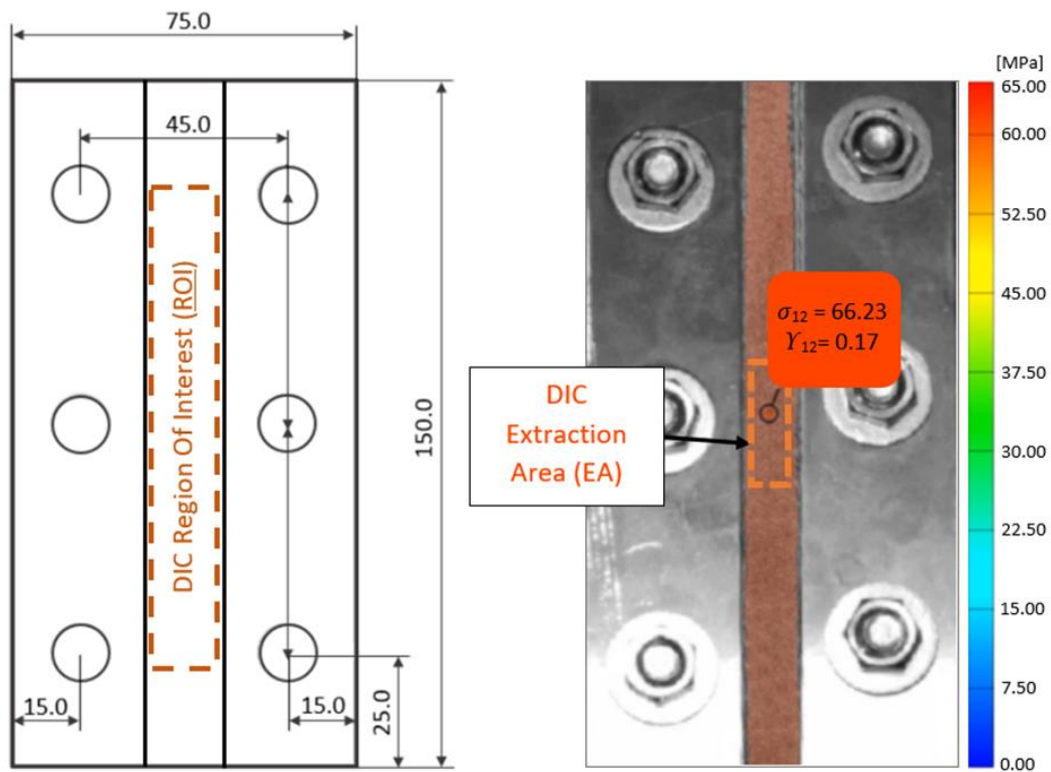
Fig. 2-15. Shape and dimensions of specimen for shear tests.

The shear stress-strain characteristics were elaborated, Figures 2-16 and 2-17. It is clearly visible, that there is an elastic region on both presented characteristics. The plastic deformation occurs only in the case of the laminate with the glass woven fabric arranged along the fibres. This is due to the specific orientation of the reinforcing phase, that is typical for the unidirectional composite laminates under shear loading. The shear properties of the tested GFRE[0°/90°]$_4$ and GFRE[45°/45°]$_4$ are shown in Tables 2-6 and 2-7, respectively.
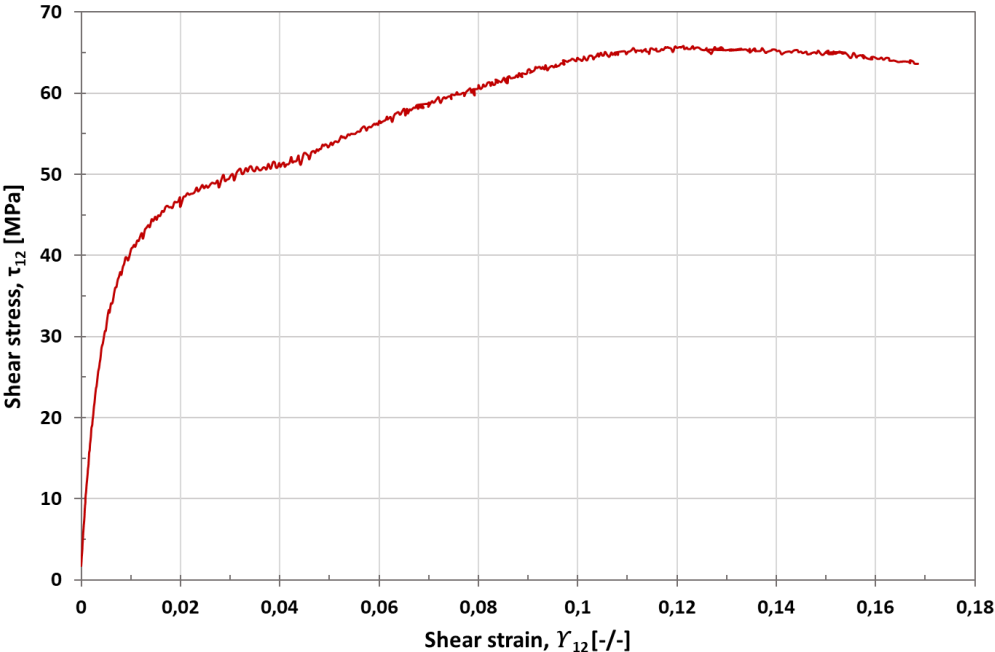
Fig. 2-16. Shear stress-strain curve for GFRE[0°/90°]$_4$ laminate.
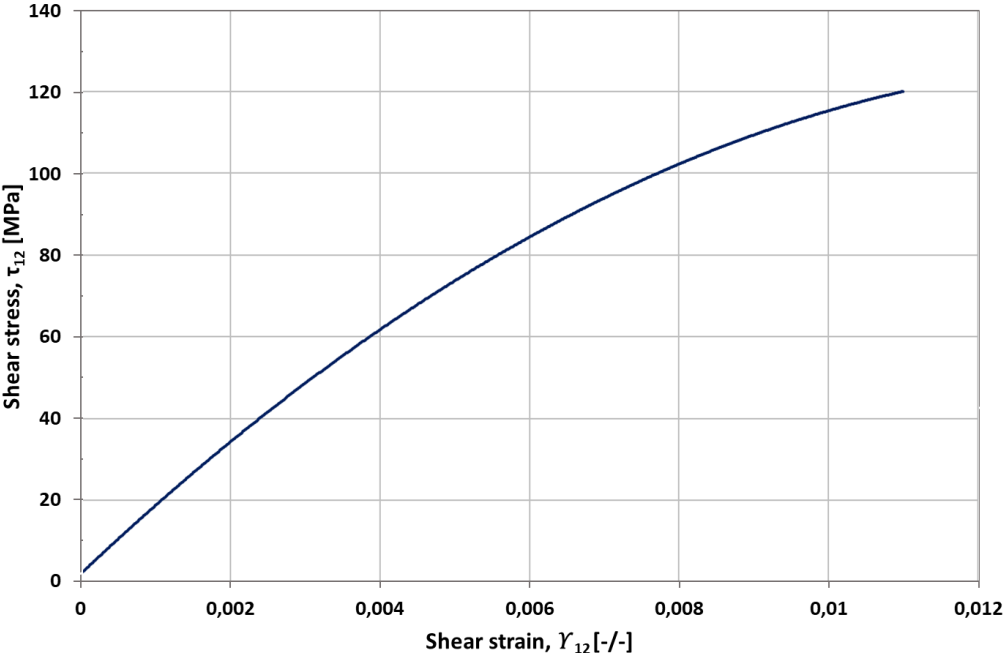
Fig. 2-17. Shear stress-strain curve for GFRE [45°/45°]$_4$ laminate.

Table 2-6. Shear properties of GFRE [0°/90°]₄.

Strain rate	Parameter	Average value	Standard deviations
1,5 mm/min	G_{12}	8.57 GPa	± 0.73
	Y_{12}	0.17	± 0.01
	τ_{12}	66.23 MPa	± 6.12

Table 2-7. Shear properties of GFRE [45°/45°]₄.

Strain rate	Parameter	Average value	Standard deviations
1,5 mm/min	G12	7.31 GPa	± 0.67
	Y_{12}	0.011	± 0.004
	τ_{12}	120.11 MPa	± 16.44

Experimental determination of the out-of-plane elastic properties - the compression test in Z direction

The aim of the compression test carried out on the cylindrical specimen with diameter of 6.5 mm, and thickness equal to 5 mm, was to determine the out-of-plane compressive modulus E_{33} and the Poisson's ratio ν_{13} of the laminated composite tested.
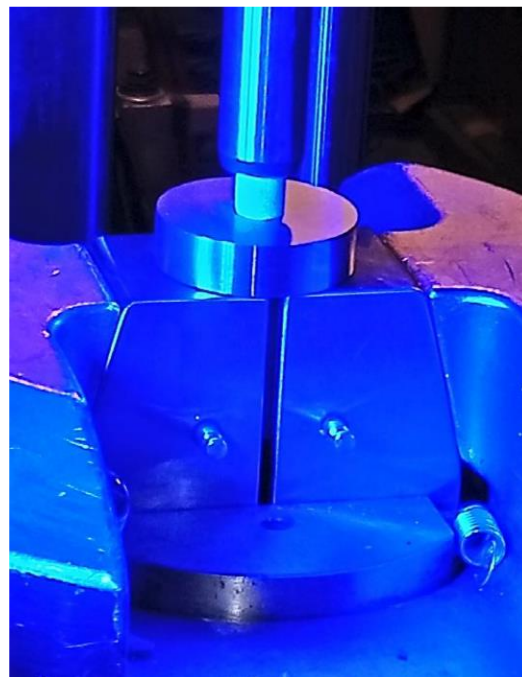
Fig. 2-18. Setup for the compression test.

The compression tests were performed under a displacement control at velocity of traverse equal to 1 mm/min at room temperature using MTS testing machine, Figure 2-18. In order to study the compressive behaviour of the glass fibre/Elium acrylic woven laminate, the DIC

system was applied. The loading cell was calibrated in the range of ±25 kN. Two groups of specimens were prepared. One cut out from the zone rich of glass fibers (F) and second one from the zone rich of thermoplastic resin (R).
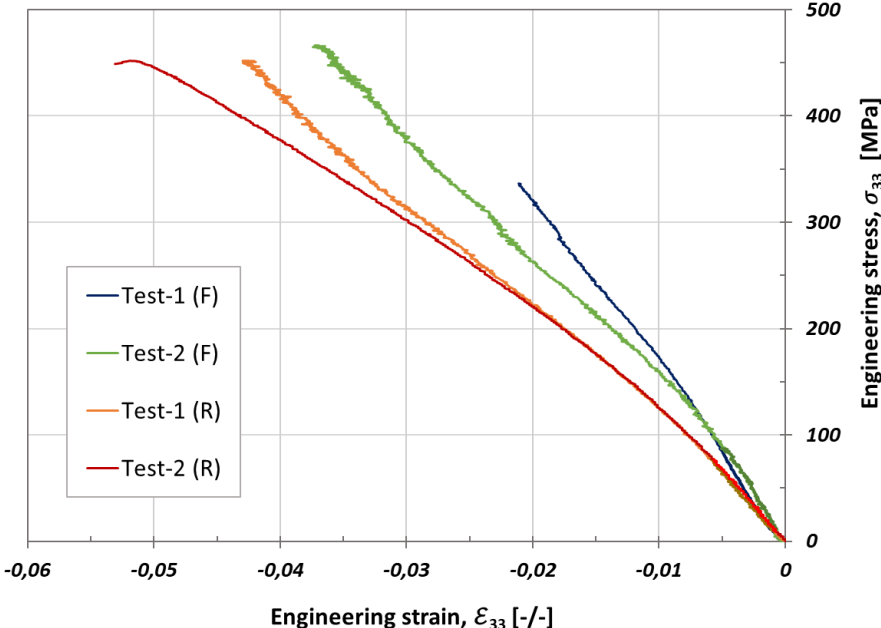
Fig. 2-19. Compressive stress-strain curves of GFRE for the case of out-of-plane.
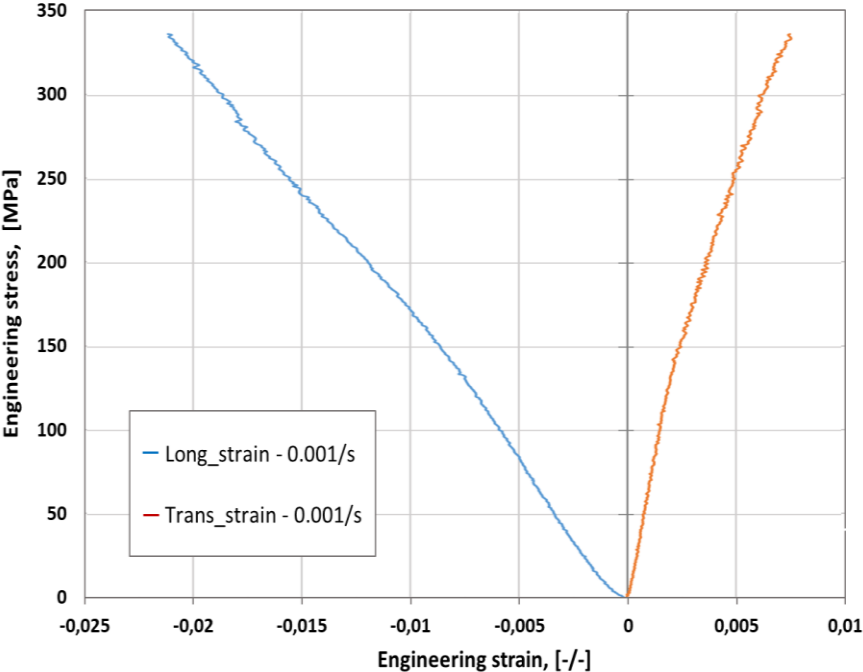
Fig. 2-20. Out-of-plane axial and transversal stress vs strain curves of the glass fibre/Elium acrylic woven laminate used for the determination of Poisson's ratio.

Based on the registered data, the compressive characteristics shown in Figures 2-19 and 2-20 were elaborated. The results indicate, that values of the Young's moduli are different for

these two selected groups. This is due to differences between the ratios of the reinforcing phase and resin content in the specimen. The specimens from the first group were cut out from the zone rich in the resin, while from the second group, from the zone rich in fibers. The compressive properties, such as the out-of-plane Young's modulus E_{33}, ultimate tensile strength σ_{33} and maximal strain ε_{33}, as well as Poisson's ratio ν_{13} of tested laminate are shown in Table 2-8.

Table 2-8. Out-of-plane properties of GFRE.

Zone	Parameter	Average value	Standard deviations
R	E_{33}	13.9 GPa	± 1.20
	ν_{13}	0.36	± 0.034
	σ_{33}	450.0 MPa	± 45.11
	ε_{33}	0.055	± 0.009
F	E_{33}	19.3 GPa	± 1.05
	ν_{13}	0.22	± 0.08
	σ_{33}	460.0 MPa	± 52.43
	ε_{33}	0.031	± 0.011

The lowest value of the Young's modulus E_{33} in out-of-plane direction (Z) was taken into account for the numerical analysis (13.9 GPa).

The experimental study of the mechanical behaviour under quasi-static loadings allowed to elaborate the stress-strain relationships for all loading directions considered. The laminated composite has an anisotropic behaviour which is strongly related to the directions of loading. Therefore, in all loading cases, the non-linearity of ply behaviour was clearly observed. The elasto-viscoplastic behaviour of acrylic resin was also well known as for most organic resins. Such behaviour was found for the woven carbon/epoxy composite by Couegnat [88] during the relaxation of the residual strain after unloading. It should be emphasized, that viscous and plastic flows are not the only processes responsible for the nonlinearity observed for laminates. The nonlinearity may also be due to damage mechanisms that occur during the loading [89].

2.2.3 Interlaminar fracture toughness characterization

Delamination is a damage phenomenon in composite materials, that occurs after significant accumulation of matrix cracks. It leads to a decohesion of the interface between

two adjacent layers. Composites subjected to low and high velocity impact are very sensitive to this type of damage. In this section the parameters of the cohesive softening law were determined, both in pure and mixed modes for a ductile thermoplastic adhesive layer. These parameters are illustrated in the Figure 2-21 [78].
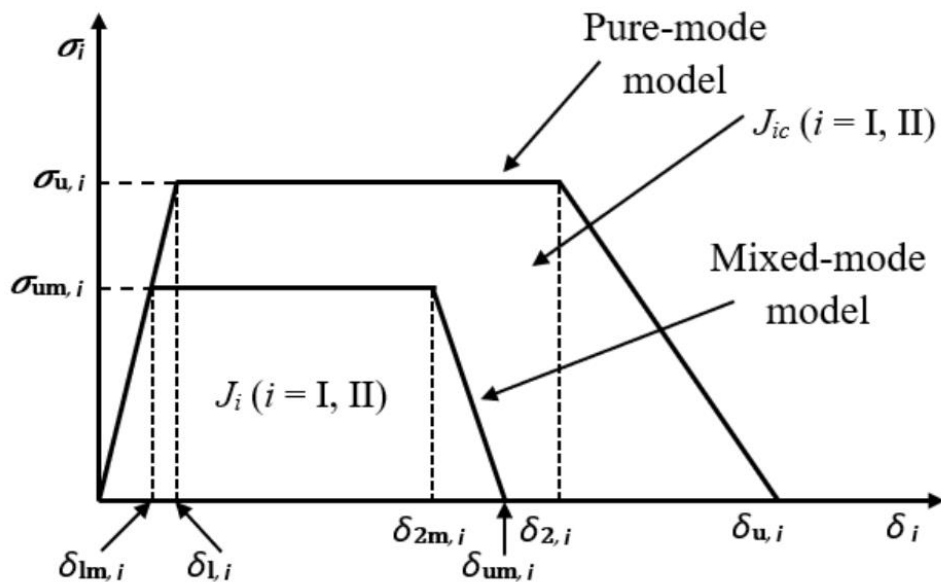
Fig. 2-21. Model of trapezoidal softening law for pure-mode and mixed-mode.

The double cantilever beam (DCB) tests were carried out under displacement control with nominal crosshead rate equal 5 mm/min using MTS tensile machine, which is shown in Figure 2-23. The loading cell was calibrated in the range of ±25 kN. In order to register a delamination process, the DIC system was applied. To avoid a bending effect of the griping part, the specimens containing 12 and 16 layers of glass woven fabric were prepared. A typical dimension of DCB specimen in agreement to the ASTM D5528 standard, is presented in Figure 2-22, [90].
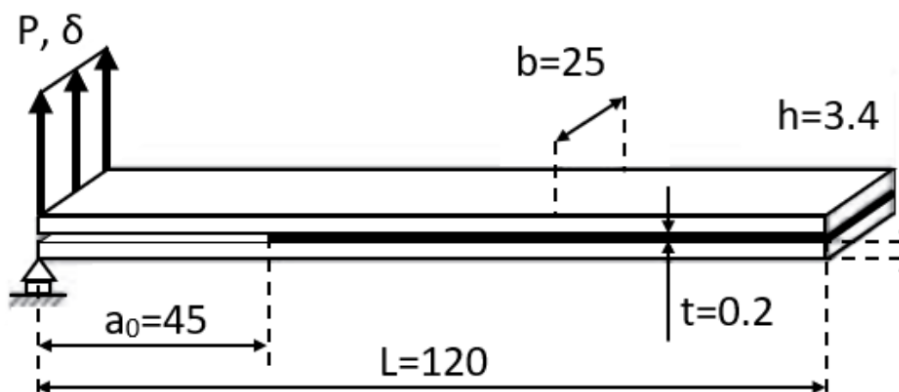
Fig. 2-22. Geometry of the DCB specimen (dimensions in mm).
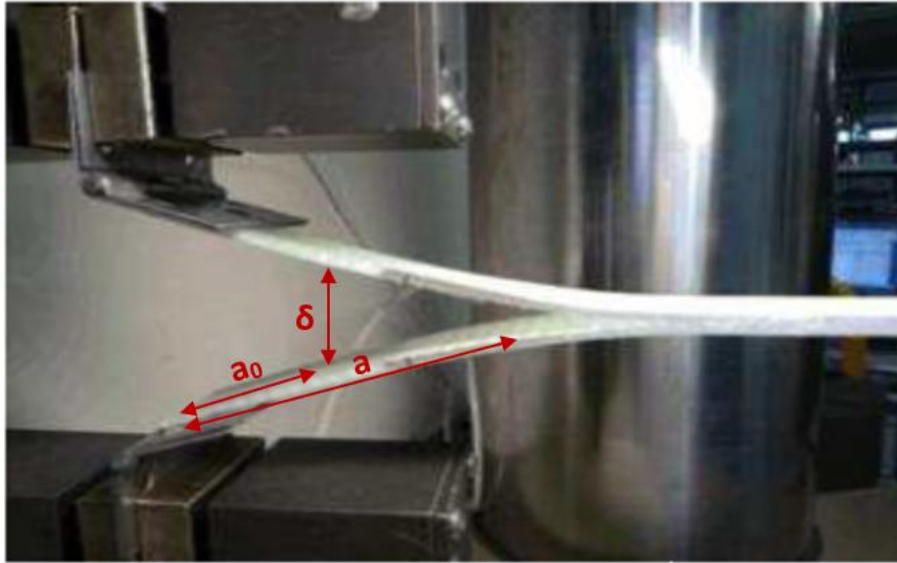
Fig. 2-23. Experimental setup of the crack propagation test in Mode I.

The displacement and force corresponding to the evolution of the length of the crack over a distance of 50 mm were measured during the tests. It was possible due to a special scale introduced on the lateral surface of specimen tested. Subsequently, the data were analyzed using a tracking software (GOM correlate). The results are shown in Figure 2-24.
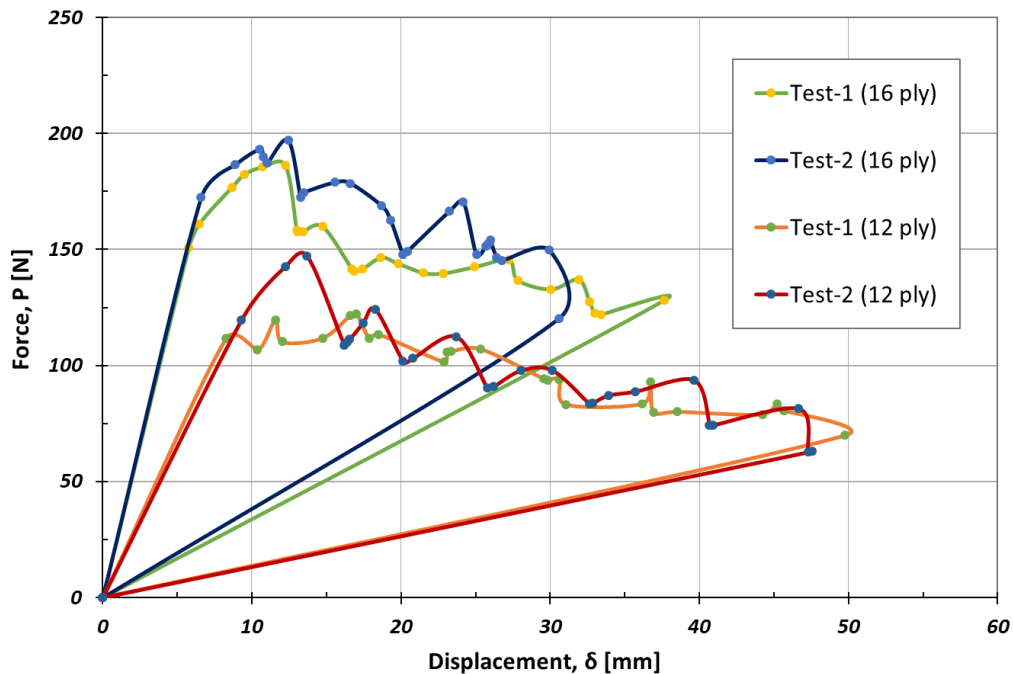
Fig. 2-24. Load-displacement curves obtained from the DCB tests for the glass/Elium with 12 and 16 layers.

The energy balance during the propagation of the crack in Mode I is described in quasi-static case by equation:

$$G_I = \frac{\partial \Pi}{b \, \partial a} \qquad (2\text{-}5)$$

where:

b - width of the specimen,

a - length of the propagated crack,

Π - crack propagation energy.

$$\Pi = \Pi_0 - \Pi_d \qquad (2\text{-}6)$$

where:

Π_0 represents the external forces,

Π_d is the strain energy.

In this work, in order to determine the energy release rate in Mode I, the most common method based on beam theory was used [91]. The classical method of beam theory (CBT: Classical Beam Theory) considers the specimen to be perfectly embedded. The rate of energy restitution is then equal to the rate of strain energy released by the beam embedded at the tip of the crack of length a (Figure 2-23):

$$G_I = \frac{3P\delta}{2ab} \qquad (2\text{-}7)$$

Based on this theory, the value of Interlaminar Fracture Toughness before crack initiation in pure Mode I was estimated, as presented in Figure 2-25. Its value was about G_{IC} = 2.1 N/mm for the tested GFRE.
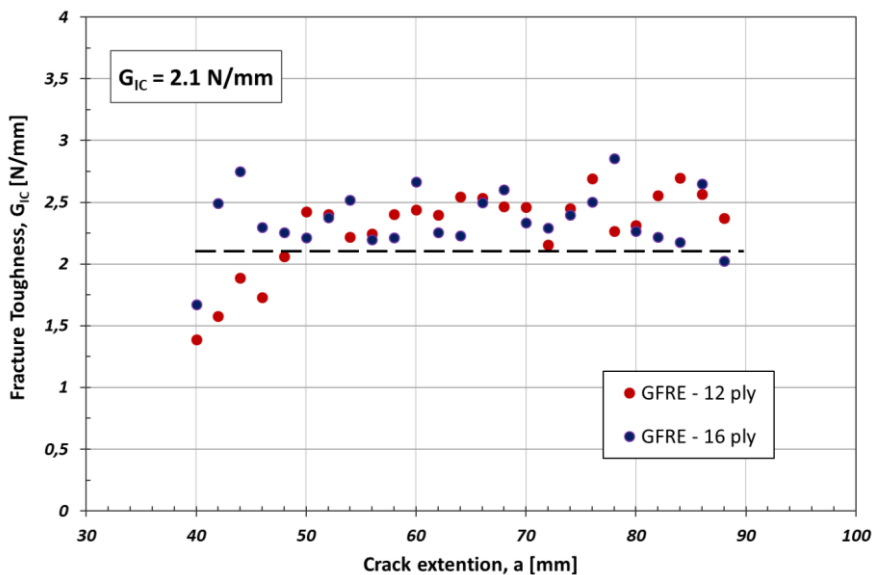
Fig. 2-25. Interlaminar Fracture Toughness (Mode I) versus cross head displacement.

In order to determine the Interlaminar Fracture Toughness in Mode II, the End-Notched Flexure (ENF) tests were conducted. However, the analysis of the specimens quality showed their disagreement to D7905 standard [92]. For this reason, the Interlaminar Fracture Toughness before crack initiation in pure Mode II was taken from the literature [54]. Its value for the tested material was equal to G_{IIC} = 3.84 N/mm.

2.3 Dynamic compressive behaviour of the laminated composites

Polymer and polymer-based composites (PMC) present material properties which are attractive for various engineering applications. Among them the high specific stiffness, strength and fatigue properties make these materials especially suitable to the automobile industries. Automotive structures in service are prone to high velocity impact from external bodies, and thus, they require to withstand various dynamic loading conditions. Hence, the understanding of the material response under dynamic loading through experimental and theoretical analysis becomes imperative. In this section different models developed by other researchers are discussed, followed by the presentation of model that seems to be mostly relevant for this thesis. Subsequently, the results of dynamic tests are described and compared to the numerical prediction.

2.3.1 Experimental results of dynamic behaviour of laminated composites

Strain rate and temperature effects of the laminated composites have been studied experimentally by many researchers: (Kumar et al., 1986); (El-Habak, 1991); (Harding, 1993); (Sierakowski & Nevill, 1971). Ochola et al. (2004) studied the strain rate and temperature sensitivity for either carbon fibers reinforced polymer (CFRP) or glass fibers reinforced polymer (GFRP). The results show that the dynamic strength for GFRP increases with increasing strain rates. The failure strain for both CFRP and GFRP was decreased with increasing strain rates. Hsiao et al. (2000) investigated the strain rate effect on material properties of thick composites and found that the stress–strain curves stiffened as the strain rate increased. Hosur et al. (2004) presented the effect of high strain rate compression loading on the off-axis satin weave carbon/epoxy composite specimens. The specimens were tested in the in-plane direction of 0°, 15°, 30°, 45°, 60°, 75°, and 90°. The results indicated, that the ultimate strength and strain varied considerably and exhibited a nonlinear stress–strain response that increased with angles up to 45° [93-95].

Several approaches have been used in order to model the stress–strain behaviour of pure thermoplastic and thermoset polymers. Recent studies [96-98] demonstrated, that dynamic behaviour of the materials can be very well described by the cooperative model developed by Richeton et al. [99]. This model takes into account an internal stress (i), physical constant (Stefan-Boltzmann constant) (ii), activation volume (iii), activation energy (iv), strain rate (v), as well as cooperative character of the yield process (vi).

It has to be emphasized however, that especially for the laminates reinforced by fiber or woven fabric made of glass or carbon, the constitutive models that capture the strain-rate effects are still very limited.

Among many models one can indicate the approach that involves examination of the mechanical properties of the constituent materials separately. According to this method, simple micromechanical relationships are developed to predict the strain rate effect of the laminated composites based on the properties of the fibers, matrix and fiber volume fraction [100]. The strain rate sensitivity of polymeric matrix can be calculated using the strain rate dependent constitutive equation developed by Goldberg et al. [101].

The second approach does not focus on the properties of each component separately, but explore a dynamic behaviour of the laminated composite as a homogeneous material. Tay et al. [102] proposed an empirical strain rate dependent constitutive equation with seven material constants for the glass fiber reinforced Epoxy composite. In order to study the dynamic tensile mechanical behaviour of a Kevlar-fiber-reinforced plastic (KFRP), Wang and Xia [103] adapted a bimodal Weibull distribution statistical model of the strain rate and temperature dependence of fibers. A test method for mechanical properties and Weibull parameters determination of fibres from the fibre yarn test was also presented. The results of simulation were in good agreement with the experimental data. Sun and co-workers [104-108] developed a series of plastic, elastic/viscoplastic and 3-D viscoplastic models to describe the mechanical properties of polymeric composites at various stain rates. However, as the composite materials do not present obvious transitions between elastic and plastic stages, these models encounter accuracy problems in describing the mechanical properties of such composites.

For the purpose of this thesis, in order to describe the inelastic behaviour of the acrylic matrix, the model suggested by Nasraoui [109] was chosen, which includes such parameters as temperature, strain rate and hydrostatic pressure. This model is based on the work of G'Sell-Jonas [110] and assumed a combination of an additive and multiplicative formulation.

2.3.2 Specimens and testing conditions

Despite many years of experience, there are still many experimental difficulties associated with the accurate characterization of the dynamic behaviour of the polymeric composites. The Split Hopkinson Pressure Bar (SHPB) test is based on one-dimensional (1-D) stress wave propagation theory with assumption that includes the dynamic stress equilibrium and nearly homogeneous deformation in the specimen should be guaranteed during an experiment. Moreover, some data at small strain rates cannot be valid because the stress in the specimen does not allow to achieve equilibrium under such small values of strain. The results usually overestimate the magnitude of the stress. Hence, a lot of experience is required for the appropriate application of this method.

The experimental set up for dynamic tests carried out in this study is shown in Figure 2-26.
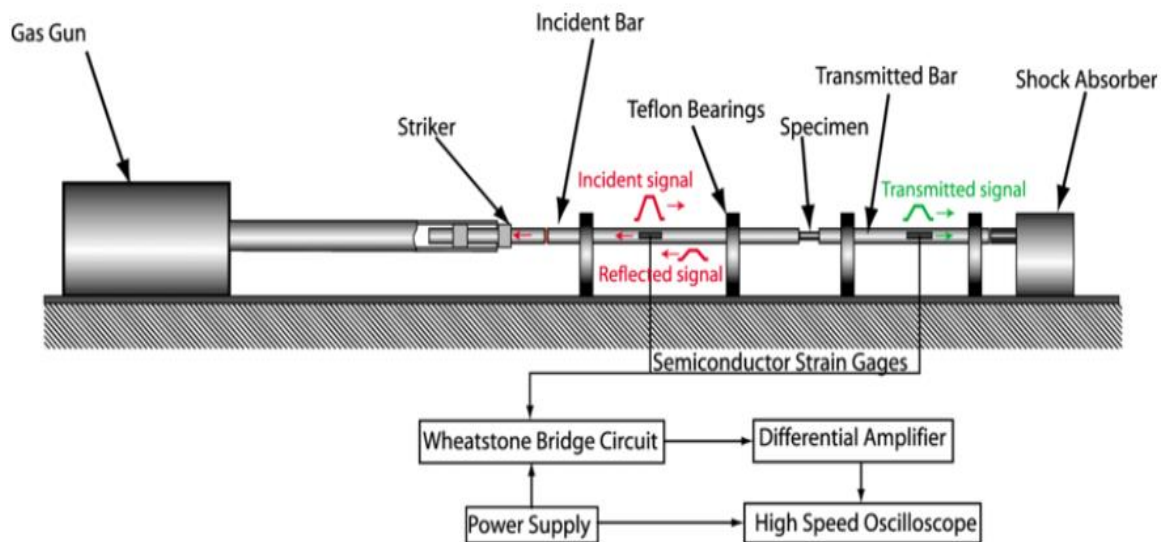
Fig. 2-26. A scheme of the Hopkinson bar device [111].

During the SHPB test, the specimen is located between incident bar and transmitter bar, when the striker impacts the incident bar, rectangular incident stress pulse ε_i is generated and travels along the incident bar until it hits the specimen. Part of the incident stress pulse

reflects from the bar/specimen interface as reflected wave ε_r and part of it transmits through the specimen because of wave impedance mismatch. The transmitted pulse ε_t emitted from the specimen travels along the transmitter bar until it hits the end of the bar, Figure 2-26.
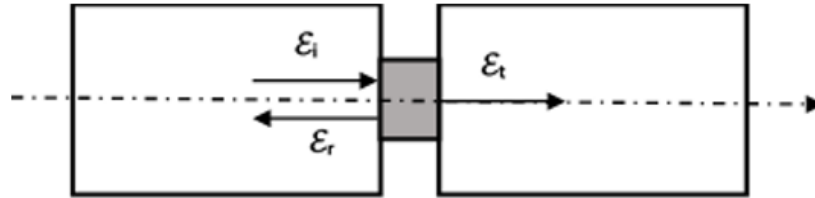
Fig. 2-27. Incident, reflected and transmitted deformation pulses at the bars/specimen interfaces.

Assuming equilibrium in short specimen, $\varepsilon_t(t) = \varepsilon_i(t) + \varepsilon_r(t)$ the strain rate, strain and stress in the specimen can be obtained by using the following equations:

$$\dot{\varepsilon}(t) = -\frac{2C_0}{L_0}\varepsilon_r(t) \qquad\qquad (\,2\text{-}8)$$

$$\varepsilon = -\frac{2C_0}{L_0}\int_0^t \varepsilon_r(t)dt \qquad\qquad (\,2\text{-}9)$$

$$\sigma = \frac{S_b}{S_0}E_0\varepsilon_t(t) \qquad\qquad (\,2\text{-}10)$$

where:

C_0 - the elastic wave velocity in the bars,

E_0 - Young's modulus of bars,

L_0 - specimen length,

S_b - cross-sectional area of the bars,

S_0 - cross-sectional area of specimen,

t - duration time.

The equations (2-10) and (2-11) enable calculation of the engineering strain. The engineering stress, the true strain and true stress are related to the engineering strain and engineering stress by:

$$\varepsilon_T(t) = -\ln(1 - \varepsilon(t)) \qquad\qquad (\,2\text{-}11)$$

$$\sigma_T(t) = \big(1 - \varepsilon(t)\big)\,\sigma(t) \qquad\qquad (\,2\text{-}12)$$

As mentioned previously, properties of the polymers and polymer based composite materials are strongly dependent on temperature. To take into account this issue, dynamic tests were performed for different temperatures, by using a warm air heating system presented in Figure 2-28.
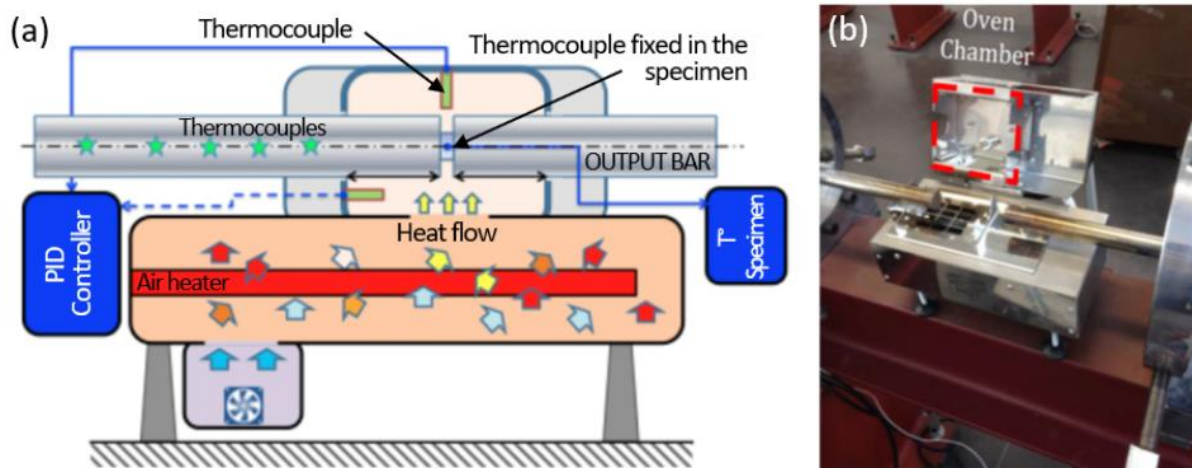
Fig. 2-28. (a) Diagram of warm air heating circuit diagram, and (b) oven chamber [96].

The device allows a uniform temperature T_0 in the volume of the specimen without generation of a gradient of temperature along the specimen as discussed by Lennon & Ramesh [96,112].

In this study, specimens of pure thermoplastic resin Elium and glass woven fabric/Elium composites were subjected to dynamic compression loading. Cylindrical specimens made of the thermoplastic pure resin Elium 150 with 10 mm diameter and about 4 mm height and specimens of ELIUM 150 reinforced with glass fibers (12 layers of glass woven fabric with dimensions of 10 x 5,5 mm representing diameter and height, respectively) were cut out in the Z direction (out-of-plane) using a water jet technique. After machining, all specimens were dried using hot air at 40°C.

Figure 2-29 shows the tested specimens and their orientation in the XYZ coordinate system. In order to study the strain rate sensitivity of these materials and the influence of the reinforcing phase located perpendicularly to the impact direction, dynamic loading experiments were conducted under strain rates ranging from 1000/s to ≈2500/s for the composites, and from 750/s to ≈2000/s for pure resin.
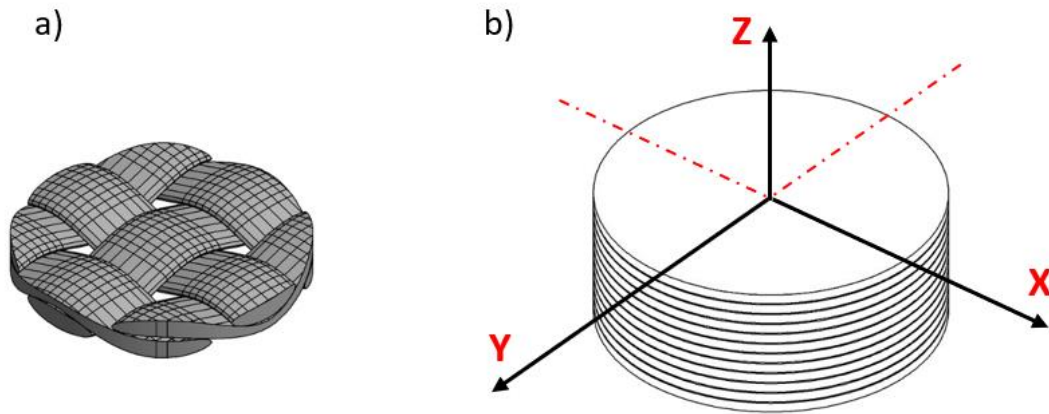
Fig. 2-29. (a) A single layer of the woven fabric, and (b) general view of the specimen.

An effect of temperature on tested materials under dynamic compression were also investigated. Besides room temperature tests both materials were also subjected to tests at 50°C and 80°C.

Finally, the stress strain characteristics of glass fiber/Elium acrylic woven laminates tested under different strain rates and temperatures were compared to the stress-strain characteristics of thermosets resin such as Epoxy containing the same number of layers of the reinforcing phase.

2.3.3 Strain rate and temperature sensitivity of the pure Elium acrylic

In the first step of the program the quasi-static compression tests were performed at room temperature by using MTS testing machine. The loading cell was calibrated in the range of ±25 kN. The DIC system was applied in order to capture the stress-strain characteristic under compression load. Based on the DIC results, the static compressive characteristics were elaborated. Then, the experimental data obtained at T = 293 K under quasi-static loading were compared with the results of the Nasraoui model [109]. The yield stress is described by the following equation in this model:

$$\sigma(\theta, \varepsilon, \dot{\varepsilon}) = \left[1 - \frac{\theta}{T_g}\right][1 - \exp(-w\varepsilon)]$$

$$[\sigma_1 \exp(-b\varepsilon)(\frac{\dot{\varepsilon}}{\dot{\varepsilon}_0})^{m_1} + \sigma_2 \exp[h_0 + h_1\left(\frac{\theta - T_{ref}}{T_{ref}}\right)\varepsilon^2][1 - (\frac{\dot{\varepsilon}}{\dot{\varepsilon}_0})^{-1}]^{-m_2}]$$

(2-13)

where:

T_{ref} - the reference temperature (298 K),

T and T_g - the absolute and glass transition temperature, respectively,

ε - true strain

$\dot{\varepsilon}_0$ - reference strain rate taken equal to 0.1 s

In equation (2-16) the term $\sigma_1 \exp(-b\varepsilon)(\frac{\dot{\varepsilon}}{\dot{\varepsilon}_0})^{m_1}$ is used to describe the yield stress and strain softening after the peak stress, whereas the second term describes the strain hardening behaviour during plastic deformation. The parameters σ_1, σ_2, h_0, h_1, w, b are intrinsic to the material and were identified in this work for pure Elium through the quasi-static and dynamic compression tests. Comparison of the experimental data with the predictions of the Nasraoui model for quasi-static loading is shown in Figure 2-30.
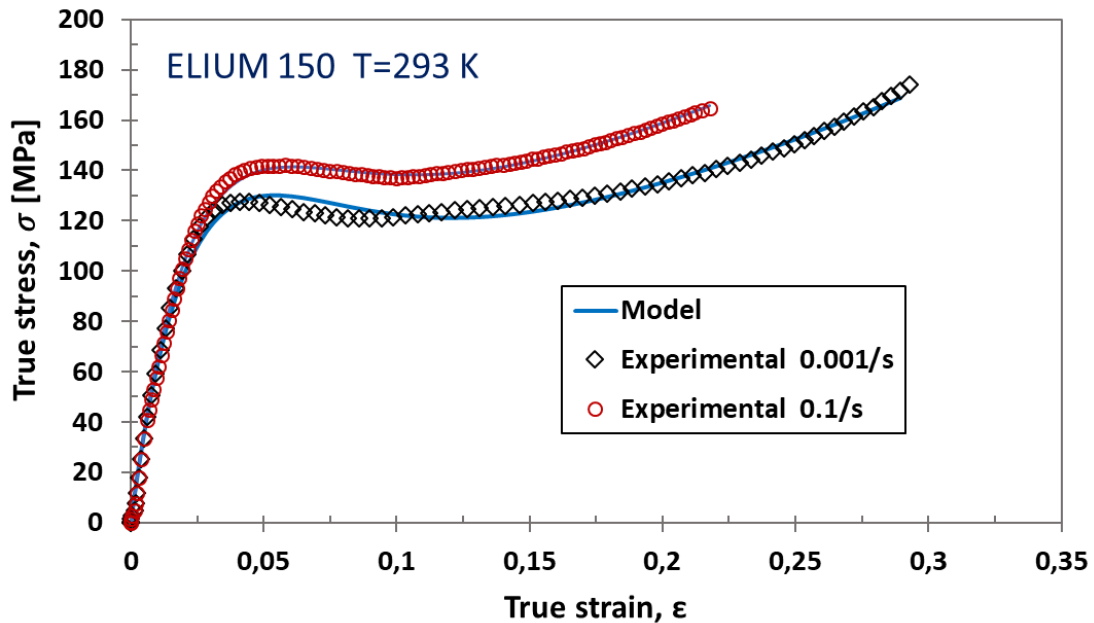
Fig. 2-30. The quasi-static out-of-plane compression characteristics of pure Elium150.

Dynamic tests using SHPB were carried out for similar dynamic loading conditions approximately: three temperatures (20°C, 50°C and 80°C) and four strain rates (1000/s, 1500/s, 2000/s and 2500/s) were taken into account.

Figure 2-31 presents all true stress versus true strain curves of the Elium 150 acrylic. According to Figure 2-31, when the temperature increases, both elastic modulus and yield stress decrease. At small strain, between 0% and around 5-6%, the Elium exhibits a viscoelastic behaviour before reaching the yield stress. At large strains, between 7 and 30%, in case of specimens tested under static loading at ambient temperature and under dynamic

loading at 80°C (about 25°C below the glass transition temperature (T_g)), the deformation developed at almost constant stress. During this stage the polymer chain segments reorganize themselves in the direction of stress, and therefore, an effect of softening can be observed.
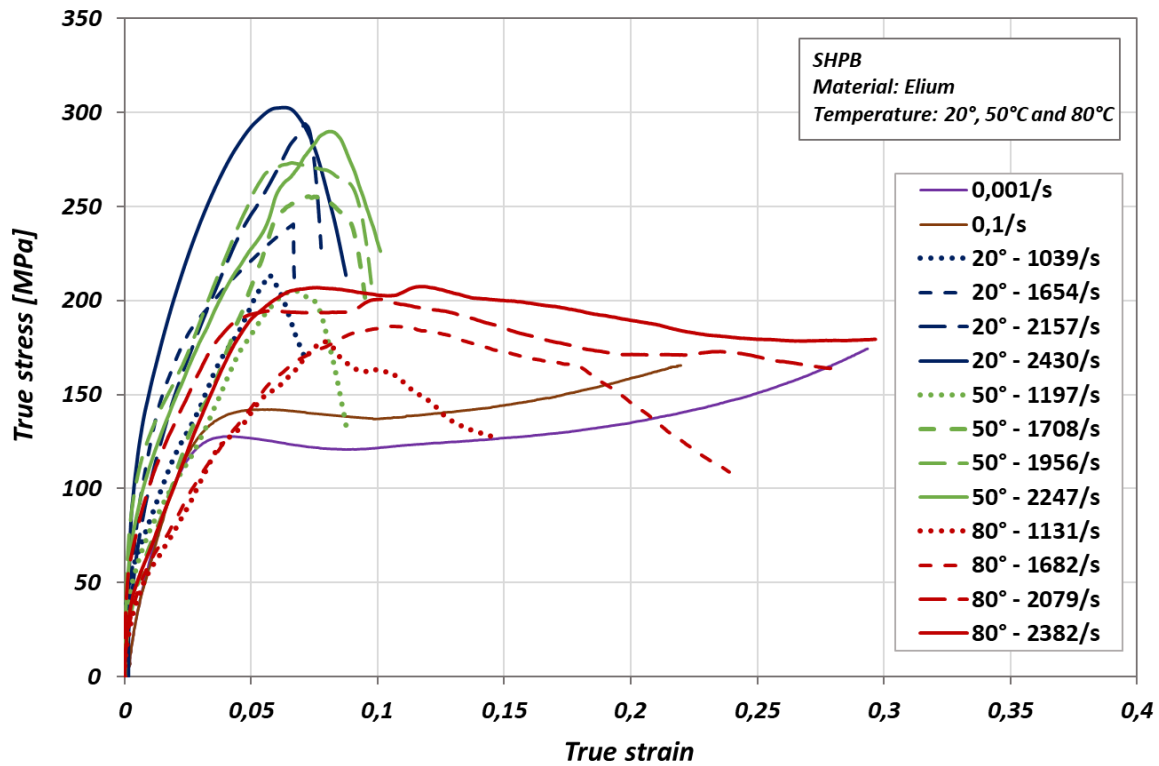
Fig. 2-31. The out-of-plane compression characteristics of pure Elium 150.
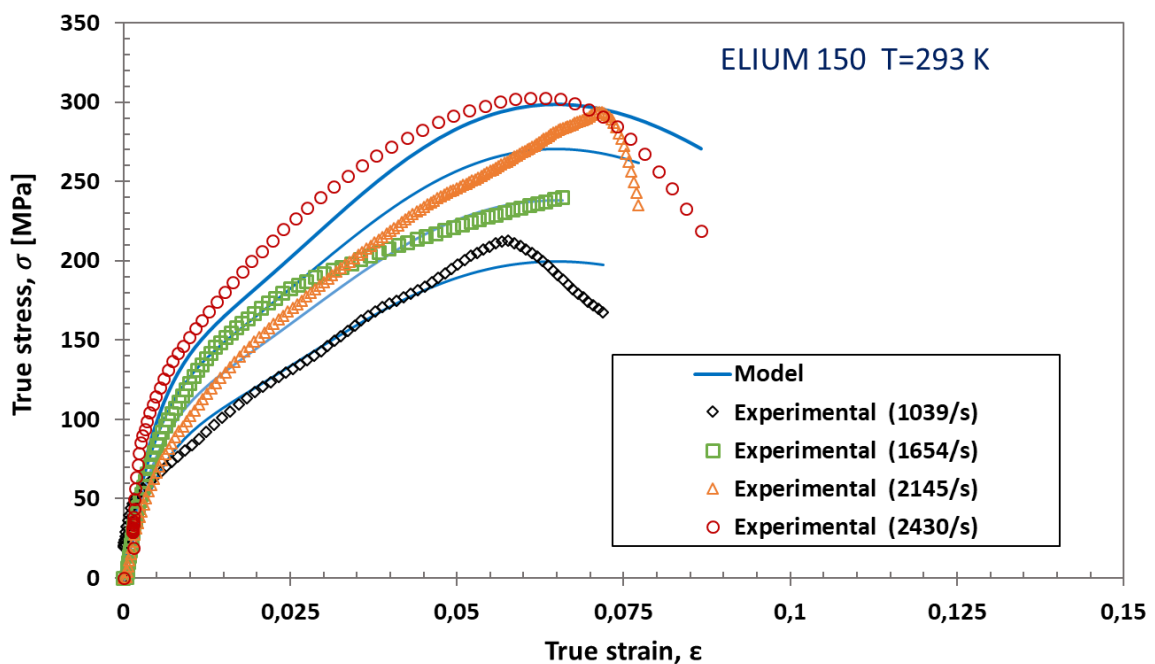
Fig. 2-32. Comparison of experimental data obtained at T = 293 K under dynamic loading with the results obtained using the Nasraoui model.

Experimental dynamic compression data were also compared with the results of the Nasraoui model predictions [109]. Parameters identified for this model are summarized in Table 2-9.

Table 2-9. Parameters for the Nasraoui [109] model identified by compression tests on pure Elium.

Tg (K)	w	σ_1 (MPa)	B	σ_2 (MPa)	h_0	h_1	$\dot{\varepsilon}_{01}$ (s^{-1})	m_1	m_2	$\dot{\varepsilon}_{02}$ (s^{-1})
378	10.58	2849	24.36	687	3.9	4.7	0.1	0.02	0.042	0.1

As it is clearly visible in Figure 2-32, this model provides a good agreement between experimental results and numerical predictions. In addition, it exhibits a good flexibility for describing the inelastic behaviour of pure Elium over a wide range of strain rate and temperature. However, the results of the numerical approach, shown in Figure 2-32, indicate that more research is needed in order to assess, and also to enhance, the predictive capabilities of the proposed model, especially in the strain hardening region described by the second component of the model.

2.3.4 Dynamic behaviour of thermoplastic and thermosetting based laminated composites at various levels of strain rate and temperature

Both Elium and Epoxy based laminated composites of 6 mm thickness, were also subjected to dynamic compression tests at three temperatures (20°C, 50°C and 80°C) and three strain rates (1000/s, 1500/s, 2000/s).
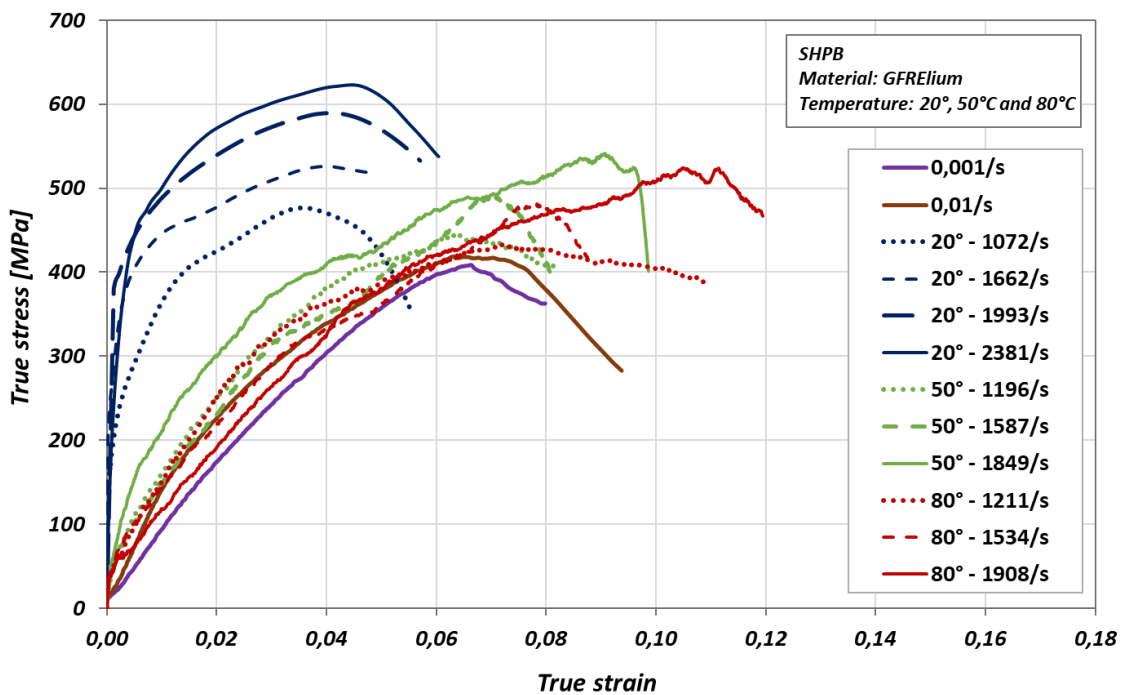
Fig. 2-33. The out-of-plane dynamic characteristics of GFRElium.

A tested GFRE, similarly to the previously tested pure resin Elium, exhibited a clear sensitivity to strain rate and temperature, Figure 2-33. However, the difference between the levels of the plastic stress obtained through the series of tests carried out at the temperature of 20°C, 50°C and 80°C are more evident than those for pure resin. Obviously, due to the addition of the reinforcing phase (glass woven fabric) the values of the ultimate stress were almost two times higher and strain range much smaller (did not exceed 10%) than that observed for pure Elium. It should be noted, that the glass fiber reinforced Elium at 50 °C seems to be more sensitive to temperature than the pure resin. This may lead to deterioration of the adhesive properties at the fiber/matrix interface caused by the increase of the temperature.

Figure 2-34 presents the dynamic curves of Epoxy based laminated composite. Glass fibers reinforced Epoxy composite seems to be less sensitive to the effects of strain rate at both temperatures 50°C and 80°C when compared to Elium. However, both materials are characterized by almost the same level of deformation under dynamic conditions.
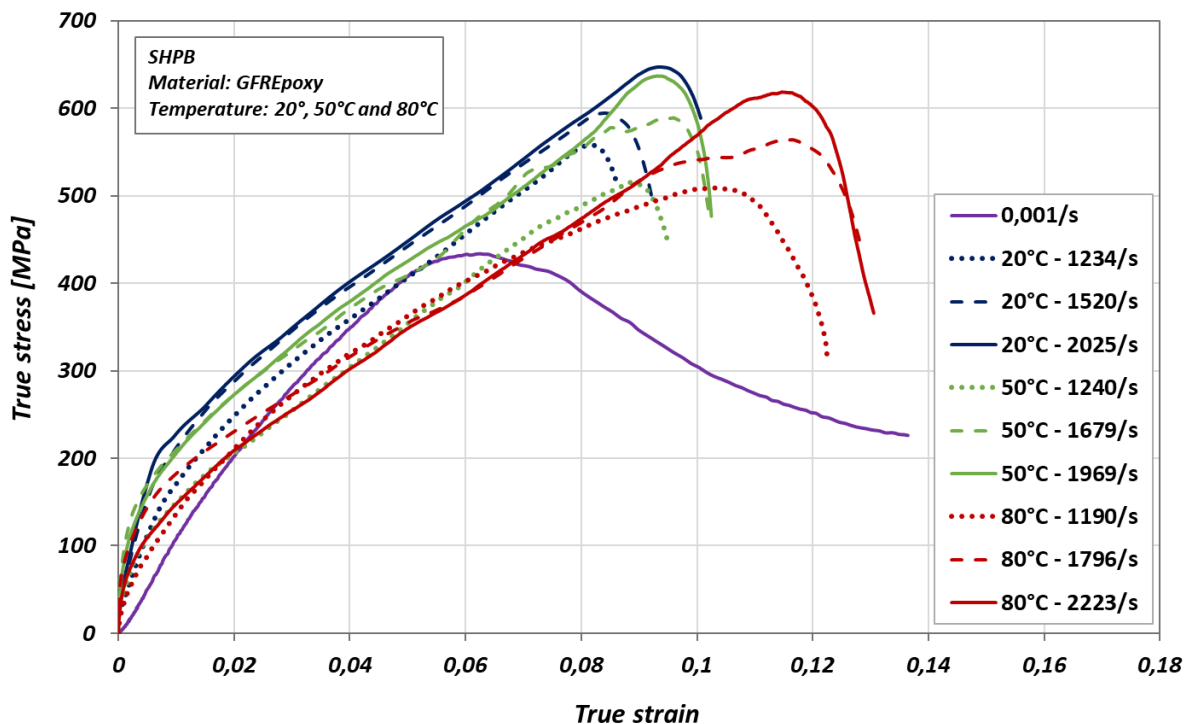
Fig. 2-34. The out-of-plane dynamic compression characteristics of GFREpoxy.

An influence of temperature on the strain rate sensitivity of tested materials under dynamic loading are presented in Figures 2-35 and 2-36. As shown in Figure 2-35, pure Elium150 is

more sensitive to temperature than the reinforced one. Moreover, its sensitivity to strain rate appears to be higher at ambient temperature than at 50°C or 80°C. An addition of the reinforcing phase significantly increases the strength and reduces the temperature effect of the tested composite, which is particularly visible at 50°C. Based on the results presented in Figure 2-36 one can conclude that the Epoxy based glass fiber laminated composite was the least sensitive material on strain rate at each temperature taken into account.
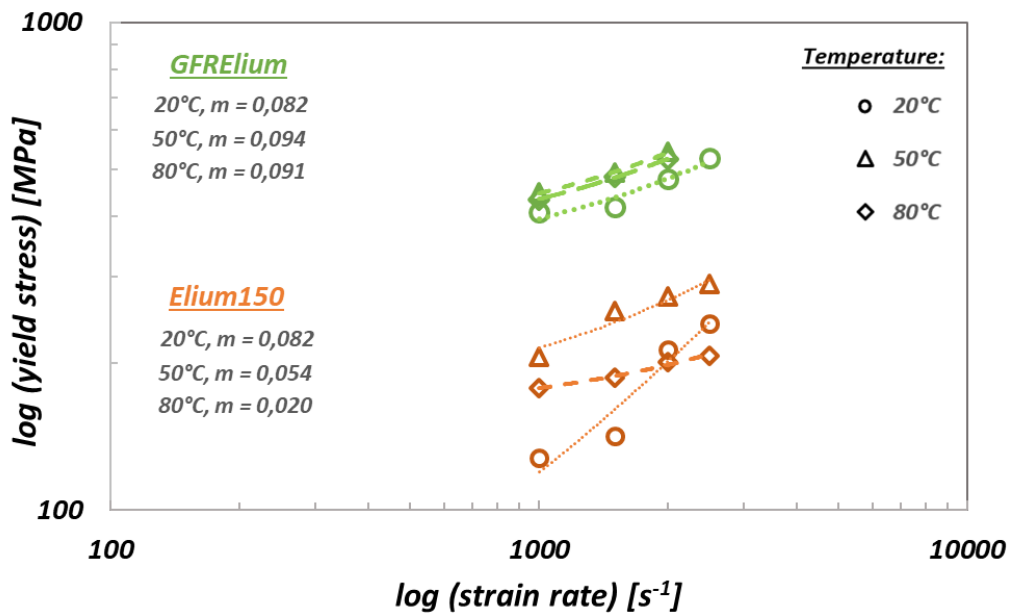
Fig. 2-35. Yield stress versus strain rate for pure and reinforced Elium 150 at 20°C, 50°C and 80°C.
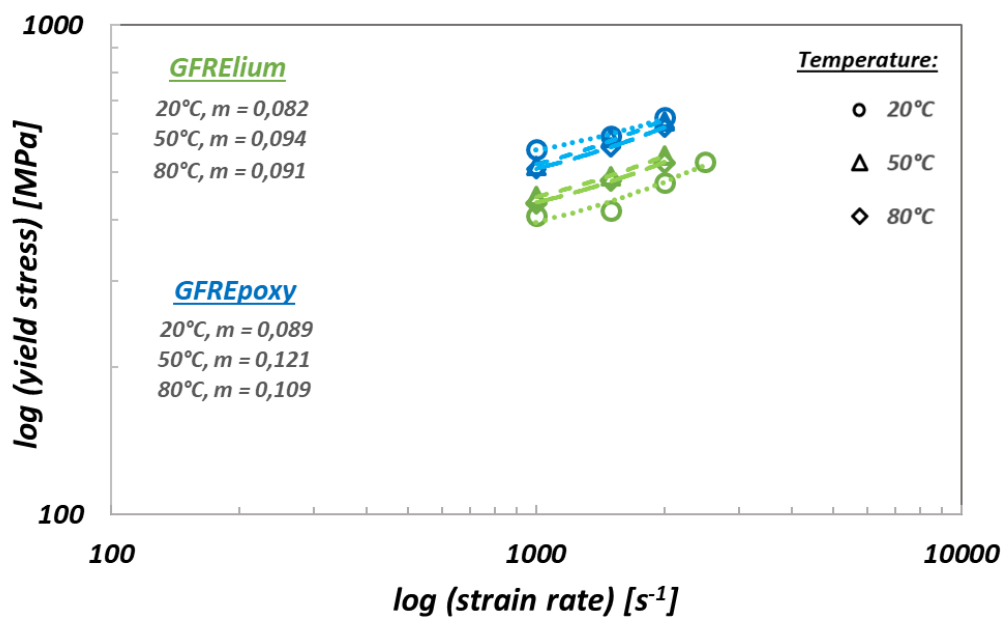
Fig. 2-36. Yield stress versus strain rate for Elium150 and Epoxy based laminated composites at 20°C, 50°C and 80°C.
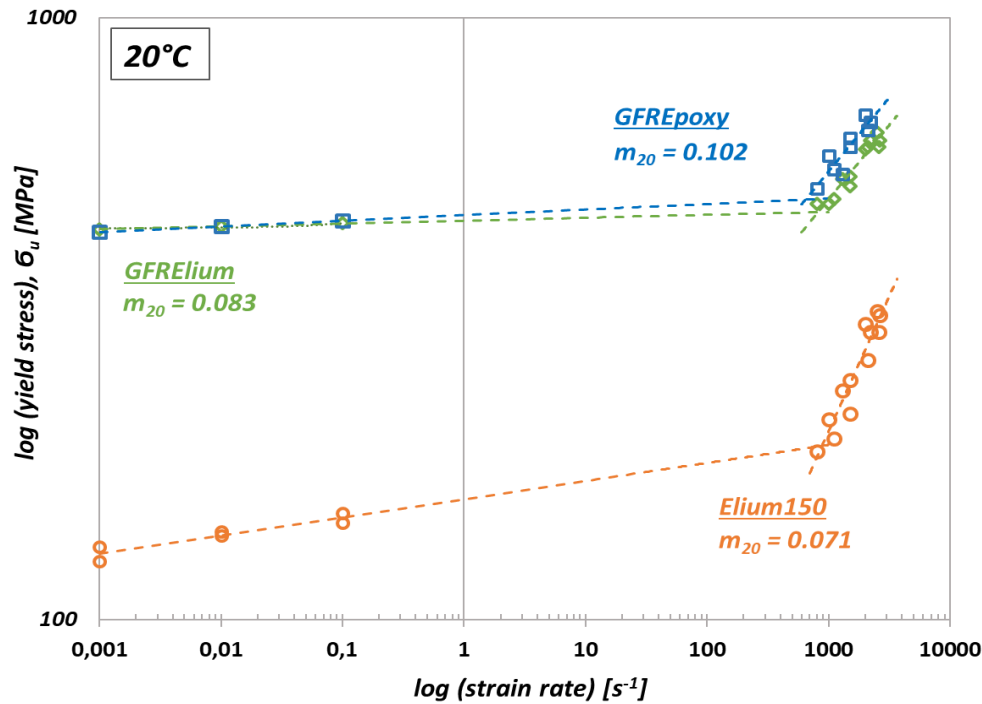
Fig. 2-37. Yield stress versus strain rate for pure Elium, Elium 150 and Epoxy based glass fibers laminated composites at 20 °C.

Figure 2-37 illustrates the sensitivity to strain rate of all tested materials at 20°C either for quasi-static or dynamic loading condition. It is clearly visible, that the materials based on thermoplastic Elium 150 resin show a higher sensitivity to temperature and strain rate, especially at high strain rates.

2.4 Conclusions

In the first part of this chapter, the manufacturing process of the materials tested was presented. Subsequently, the microstructures of all tested materials were analysed. The SEM images showed a good quality of the acrylic resin. No defects were observed at the fibers/resin interface of investigated laminated composites for both: composite with the glass woven fabric arranged along the fibers, GFRE[0/90°]$_4$, and the composite with reinforcement arranged at an angle of 45 degree with regard to that of the fibers one, GFRE[45°/45°]$_4$.

In the next step, the experimental tests were carried out to characterize the behaviour of materials under quasi-static conditions. The materials exhibited anisotropic behaviour, regardless of the loading direction. The material nonlinearity was induced by damage, elasto-viscoplastic behaviour of the matrix and woven nature of the materials.

The last part of the chapter was devoted to the analysis of dynamic properties of the pure acrylic resin and glass fibers/acrylic composite. The results were compared with those obtained for the Epoxy based glass fibers laminated composite. It was found, that materials based on thermoplastic resin showed higher sensitivity to temperature and strain rate. This effect was particularly visible for higher strain rates.

Chapter 3. Fatigue behaviour of the acrylic based glass fibers laminated composites

The aim of this part of work was to verify experimentally the effect of fatigue aging on the glass fiber/Elium acrylic woven laminate. It is particularly important for the real-life experience during exploitation of the vehicles that contain laminated composites in many of their components.

The first part of the chapter presents the geometry of the fatigue specimen with the shape adapted to the low and high velocity impact tests (that will be performed after fatigue tests). To predict the fatigue life of the studied materials the Manson-Coffin-Basquin (MCB) curves were elaborated. Based on the captured characteristics, the fatigue program designed for the Low Cyclic Fatigue (LCF) and High Cyclic Fatigue (HCF) tests was presented. Then, the analysis of stiffness evolution for the polymer-based glass fibers laminated composites under cyclic loading were described. Finally, the variation of the elastic modulus was discussed and Pre-Critical State distinguished.

3.1 Material and specimens

As discussed in Chapter 1, strain life prediction approach was chosen in the present study, in order to better understand the possible work-softening effect occurring during the cyclic loading of thermoplastic laminated composites. The shape and dimensions of the specimens used for fatigue aging tests are presented in Figure 3-1 (a). The size of the gauge part (dashed red line) was 100 × 100 mm and corresponded to the size of the specimens subsequently used for impact resistance testing. The shape and dimensions of the specimens were designed to ensure high homogeneity of the stress in the impact area. Figure 3-1 (b) shows the location of damage resulting from fatigue loading. As the composite containing the woven plain weave had the identical mechanical properties in the warp [0°] and weft [90°] (in the plane) directions, only two orientations were considered in this study. The first group of specimens was cut out along the fiber direction, while the second one along direction inclined by an angle of 45° with regard to that of the fibers one, named GFRE [0°/90°]$_4$ and GFRE [45°/45°]$_4$, respectively.
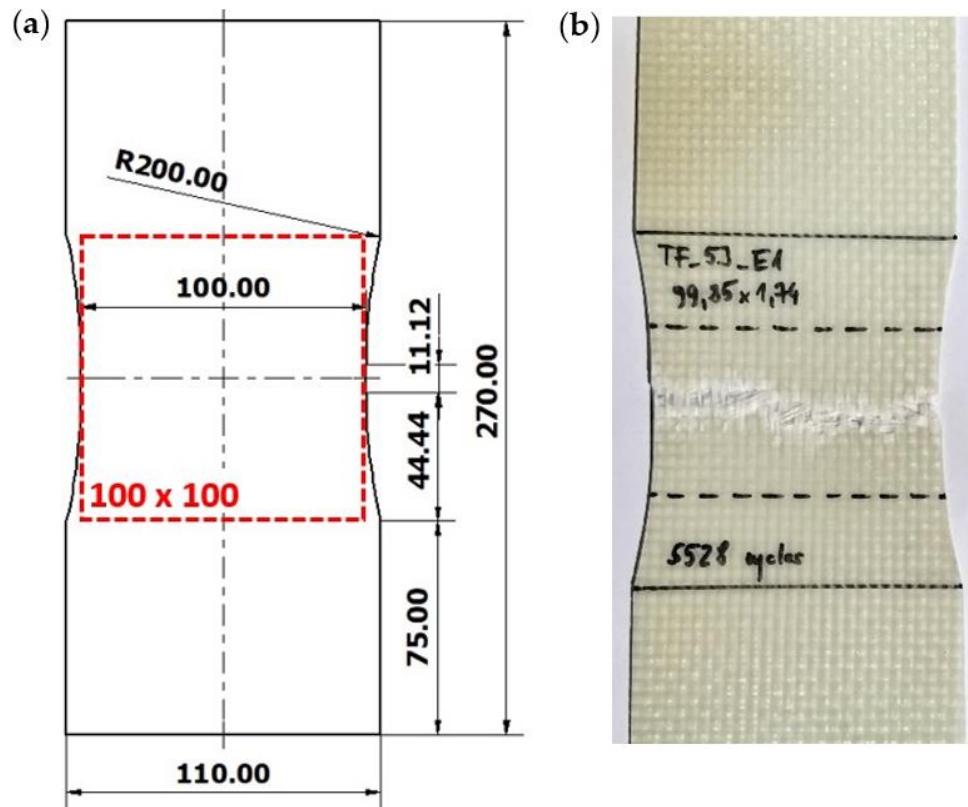
Fig. 3-1. (a) Fatigue aging specimen with the shape adapted for the low velocity impact test, (b) damage localization in GFRE [0°/90°]$_4$ specimen subjected to 5.5 × 10^3 cycles (LCF test).

3.2 Experimental investigation of the fatigue behaviour of GFRE

In order to determine the four material constants, necessary to elaborate the MCB curves, six values of stress levels were selected. Their values were selected based on the results of tensile test carried out on both materials considered. The values of stress levels taken into account for fatigue investigation are shown in Figure 3-2 and 3-3, for both tested materials, GFRE [0°/90°]$_4$ and GFRE [45°/45°]$_4$, respectively.

Three tests, were planned to be carried out below the yield point. For the rest of them, a similar program was arranged, however, under stress levels higher than the yield point. Cyclic loading was executed under force control, with the frequency of 2 Hz. Sinusoidal loading signal was selected to fulfil the following conditions $R = F_{min}/F_{max} = 0,1$. The loading cell was calibrated in the range of ± 250 kN.

Fatigue damage develops locally around imperfections, voids, inclusions, zone of delamination, matrix micro cracks and fibers accumulated in the region of minimum cross-

section where the axial stress reaches maximum value. In order to capture such changes, an extensometer with the strain range of ± 0.2 was applied during all fatigue experiments.
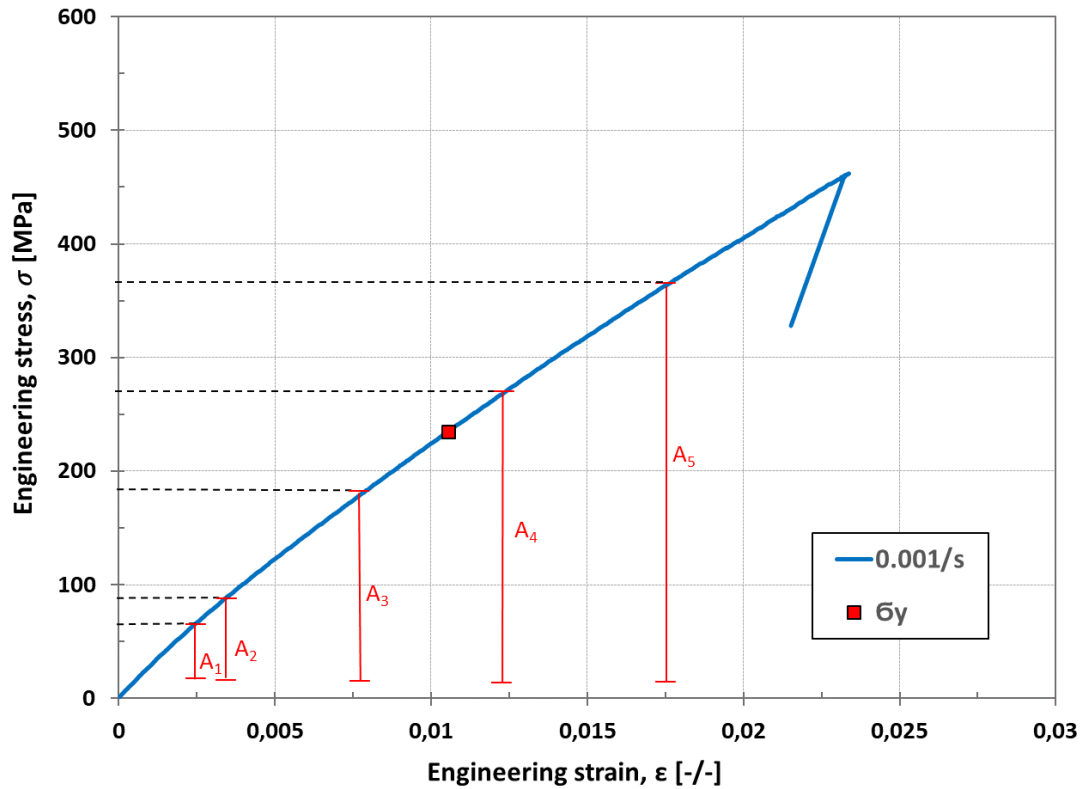
Fig. 3-2. Tensile characteristics of GFRE [0°/90°]₄.
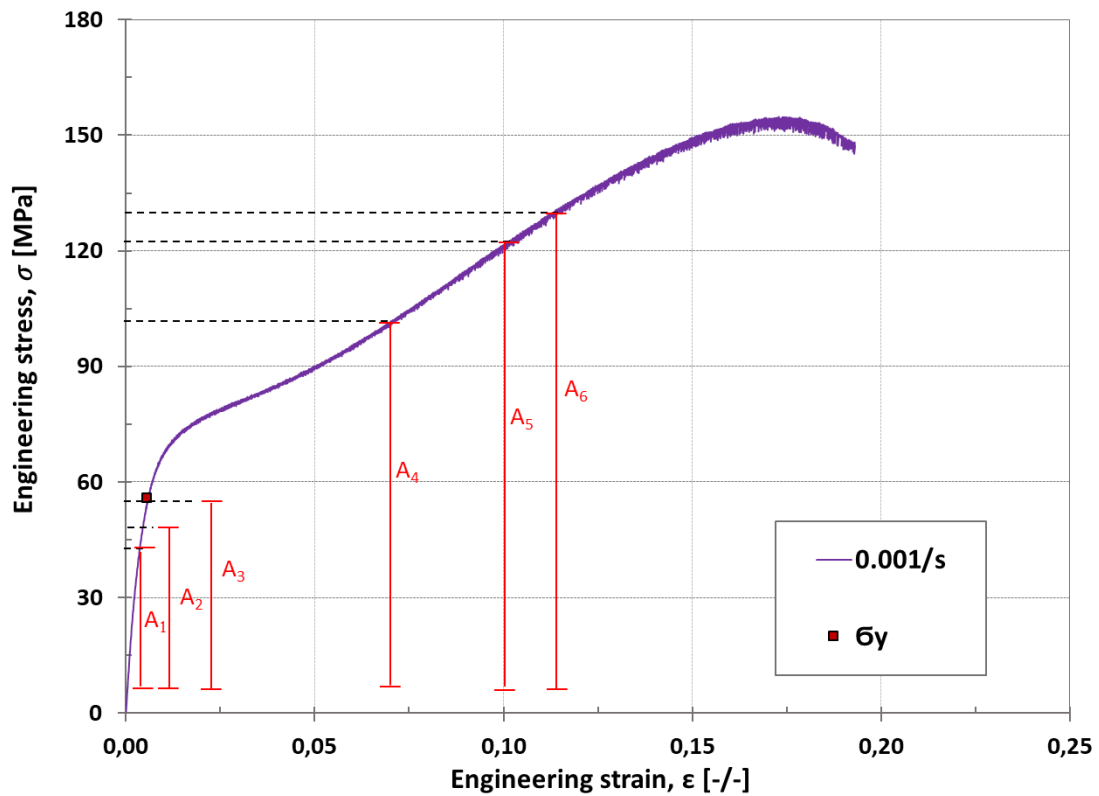
Fig. 3-3. Tensile characteristics of GFRE [45°/45°]₄.

The evolution of the hysteresis loop of the GFRP [0°/90°]₄ subjected to cyclic loading with stress amplitude lower than the yield point is presented in Figure 3-4. The first cycle is illustrated by the line denoted as (1). The second hysteresis loop registered after 500 cycles denoted as (2), moved with respect to first one (1) identifying effect of ratcheting. As it is typical for tension-tension cyclic loading, the strain increments for maximum stress were significantly greater than those obtained for the minimum ones.
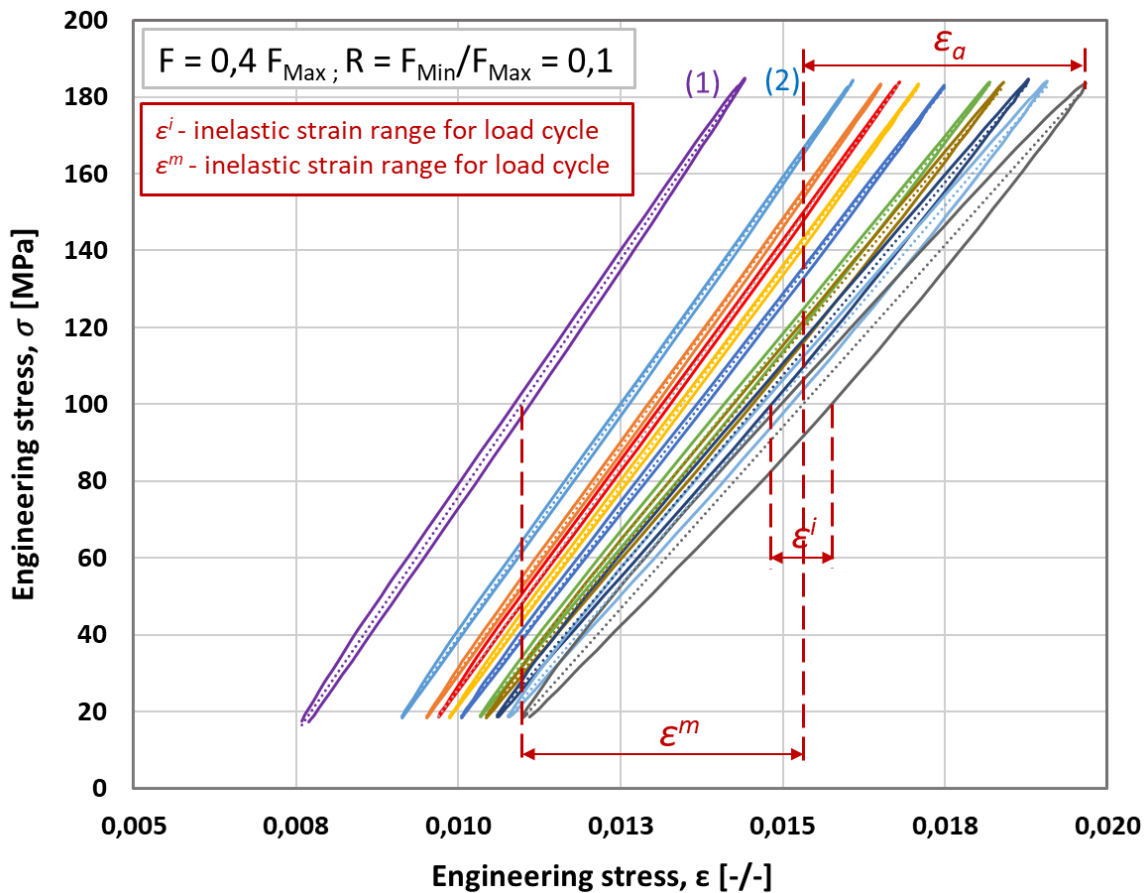
Fig. 3-4. The hysteresis loops identifying ratcheting effect for the specimen under stress amplitude lower than the yield point.

The evolution of the plastic strain amplitude for the specimen tested under stress amplitude above the yield point is shown in Figure 3-5. Intersection of the red dotted lines with a curve indicates the number of fatigue cycles that corresponds to the last stable hysteresis loop [113,114]. Based on this value and the value of total strain from equation (1-4), the Manson – Coffin – Basquin curve (presented in Figure 3-6) was elaborated to predict the fatigue life of the laminated composite for the specimens cut out along the fiber GFRE [0°/90°]₄.
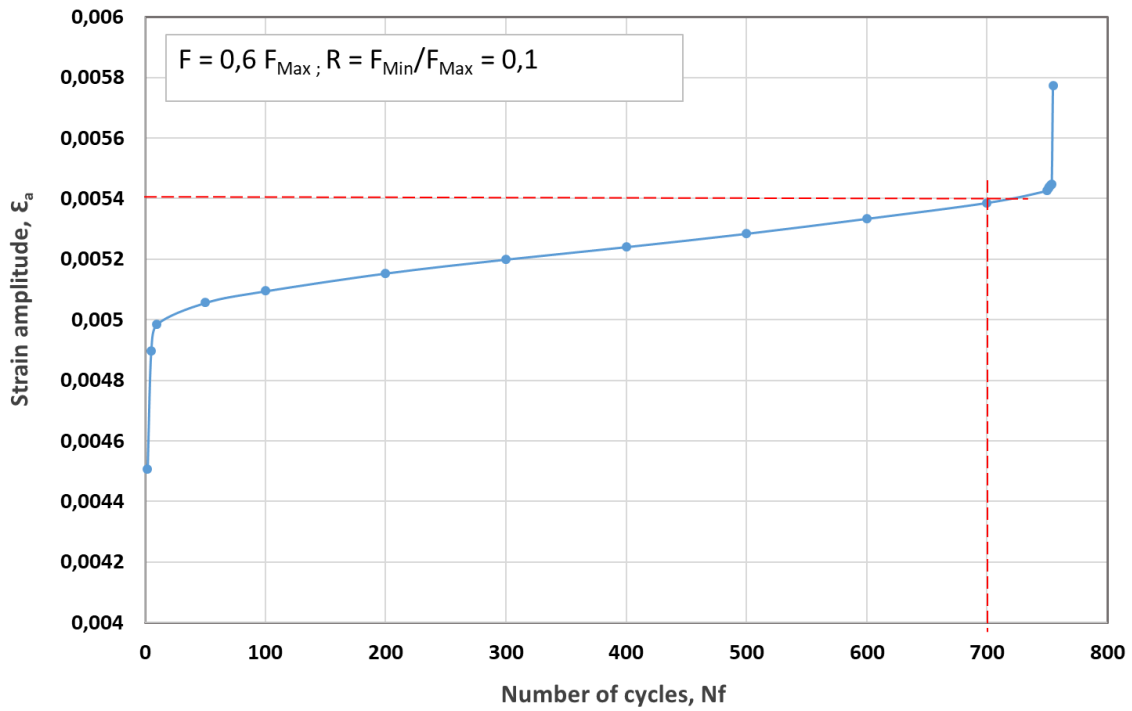
Fig. 3-5. Evolution of the plastic strain amplitude for the specimen tested under stress amplitudes above the yield point.
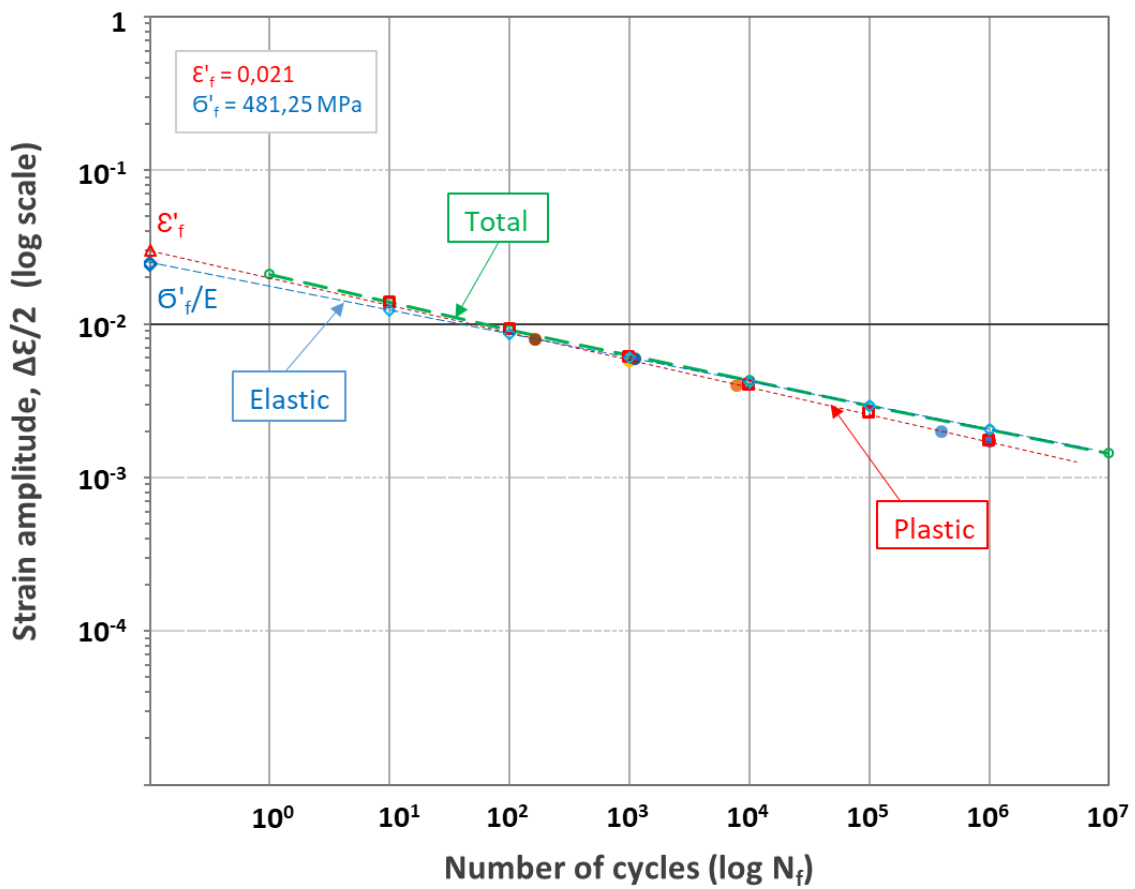
Fig. 3-6. Manson-Coffin-Basquin curve for GFRE [0°/90°]₄.

The input parameters and data collected from the experiments carried out on the specimens cut out along the fiber GFRE [0°/90°]$_4$ subjected to LCF and HCF are listed in the Table 3-1.

Table 3-1. Experimental data from tests under cyclic loading for GFRE [0°/90°]$_4$.

	σ_{max} [MPa]	σ_{min} [MPa]	R_{total}	N_f	E_n [GPa]	ε_{Max}	ε_{Min}	$\Delta\varepsilon$	$\varepsilon_a=\Delta\varepsilon/2$
LCF	366.9	36.1	0.098	163	20.59	0.0179	0.0021	0.01580	0.007904
	274.1	26.9	0.098	1100	20.49	0.0128	0.0010	0.01178	0.005893
HCF	185.0	17.37	0.097	7875	20.54	0.0184	0.0104	0.00796	0.003982
	91.11	9.27	0.102	409897	20.02	0.0051	0.0011	0.00401	0.002008
	78.50	7.92	0.101	650215	20.46	0.0041	0.0011	0.00301	0.001508

The similar program of fatigue aging was arranged for the specimens cut out with an angle of 45 degree, GFRE [45°/45°]$_4$. The results of tests carried out on the laminate under stress amplitude above the yield point (which for this fiber orientation is equal to 104.5 MPa) are presented in Figure 3-7. For this study, 650 stable cycles of hysteresis loops were recorded until the specimen failure.
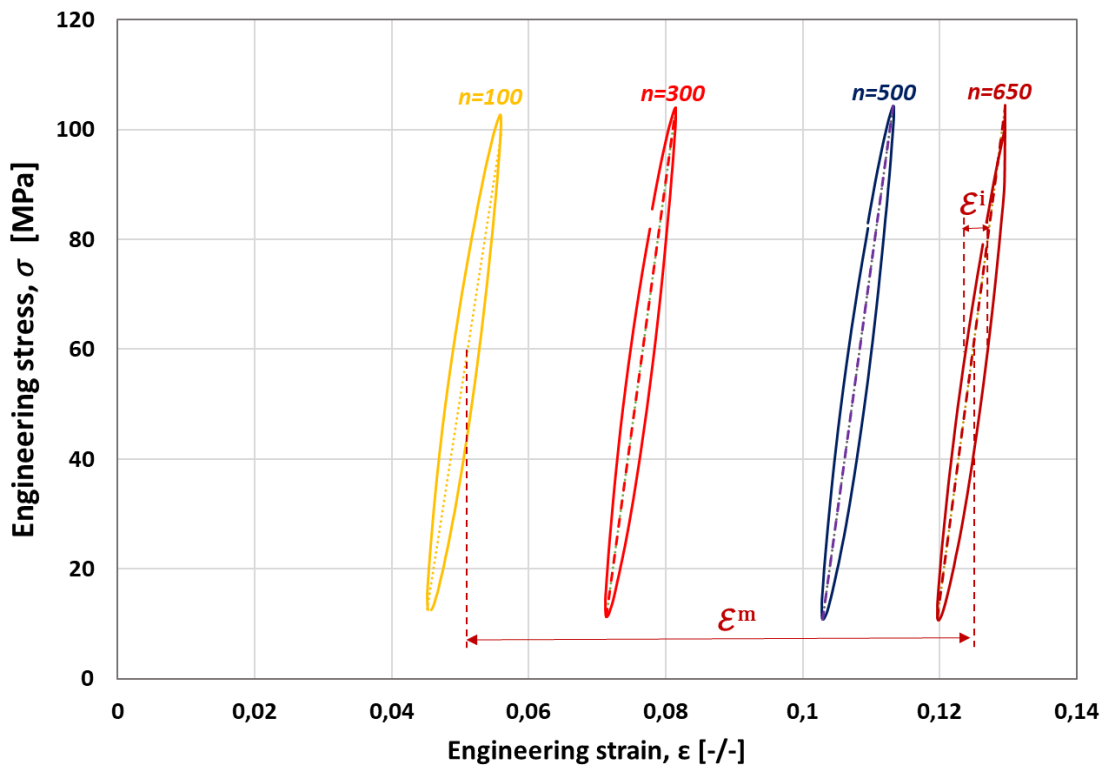
Fig. 3-7. Ratcheting effect for the specimen GFRE [45°/45°]$_4$ under stress amplitude above the yield point.

The input parameters and data collected from the experiments carried out on the specimens cut out along direction inclined by an angle of 45° with regard to that of the fibers one, GFRE [45°/45°]$_4$ subjected to LCF and HCF are presented in the Table 3-2.

Table 3-2. Experimental data from tests under cyclic loading for GFRE [45°/45°]$_4$.

	σ_{max} [MPa]	σ_{min} [MPa]	R_{total}	N_f	E_n [Gpa]	ε_{Max}	ε_{Min}	$\Delta\varepsilon$	$\varepsilon_a=\Delta\varepsilon/2$
LCF	130.2	12.96	0.099	352	5.66	0.2705	0.2495	0.20999	0.0105
	125.5	13.81	0.11	568	7.18	0.2715	0.2579	0.01362	0.00681
	104.5	10.63	0.101	731	8.82	0.1294	0.1186	0.01085	0.00542
HCF	58.88	5.98	0.101	206962	5.8	0.0573	0.0488	0.008513	0.004256
	53.62	4.94	0.092	493331	6.2	0.0381	0.0298	0.008242	0.004121
	50.65	5.01	0.099	1250346	7.52	0.3648	0.0286	0.007811	0.003905

Based on the data presented in Table 3-2 and the value of total strain calculated from equation (1-4), the Manson – Coffin – Basquin curve (presented in Figure 3-8) are elaborated to predict the fatigue life of the laminated composite for the specimens cut out along the direction inclined by an angle of 45° with respect to fibers direction, GFRE [45°/45°]$_4$.
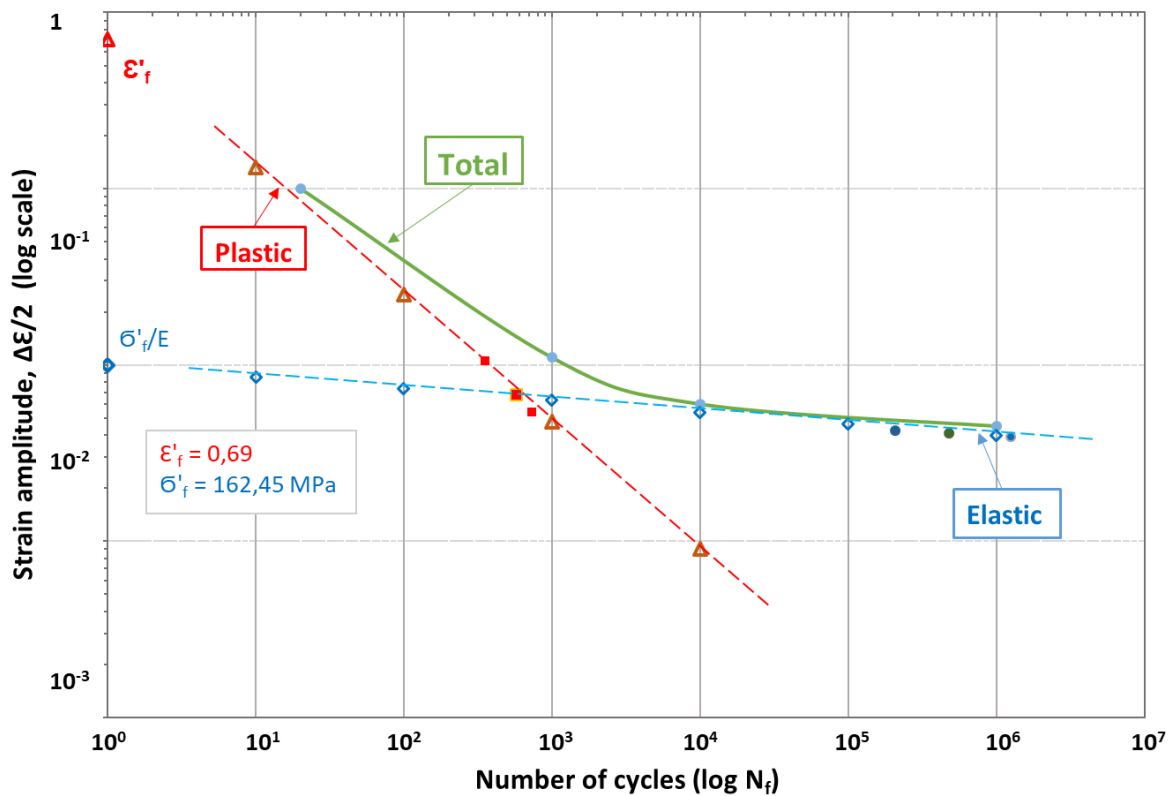
Fig. 3-8. Manson-Coffin-Basquin curve for GFRE [45°/45°]$_4$.

As observed on MCB curve presented in Figure 3-8 for the material cut out along direction inclined by an angle of 45° with regard to that of the fibers one, GFRE [45°/45°]$_4$, shows markedly a visible transition between the elastic and plastic range. This may indicate, that the glass fiber oriented at 45 degree makes the laminate less rigid, which allows deformation to be more advanced than that for the laminated composite cut out along the fiber (GFRE [0°/90°]$_4$) observed.

3.2.1 Residual stiffness examination

The MTS 810 uniaxial servo-hydraulic testing machine of the loading capacity up to 250 kN was used in all fatigue aging experiments. A special gripping system was elaborated, Figure 3-9 (a), that enabled to fix specimens in the jaws of the testing machine. In order to determine a stiffness variation during tests an MTS model 634.31F-24 longitudinal strain extensometer of the range within ±0.2 was applied. Cyclic loading was carried out under force control and frequency of 2 Hz. The sinusoidal loading mode was characterized by $R = F_{min}/F_{max} = 0.1$. A fatigue program was divided into two types of blocks distinguished by blue and red, Figure 3-9 (b). In the first type block, the elastic modulus was determined based on the simple tensile test. A maximum force during each tensile test was lower than that corresponding to the mean loading level during fatigue aging process executed in the second block. In the second type of loading block, a given number of uniaxial tensile cycles was applied. The recorded elastic modulus evolution was used either to identify the pre-critical state or to interrupt the cyclic loading process prior to total failure of the specimen.
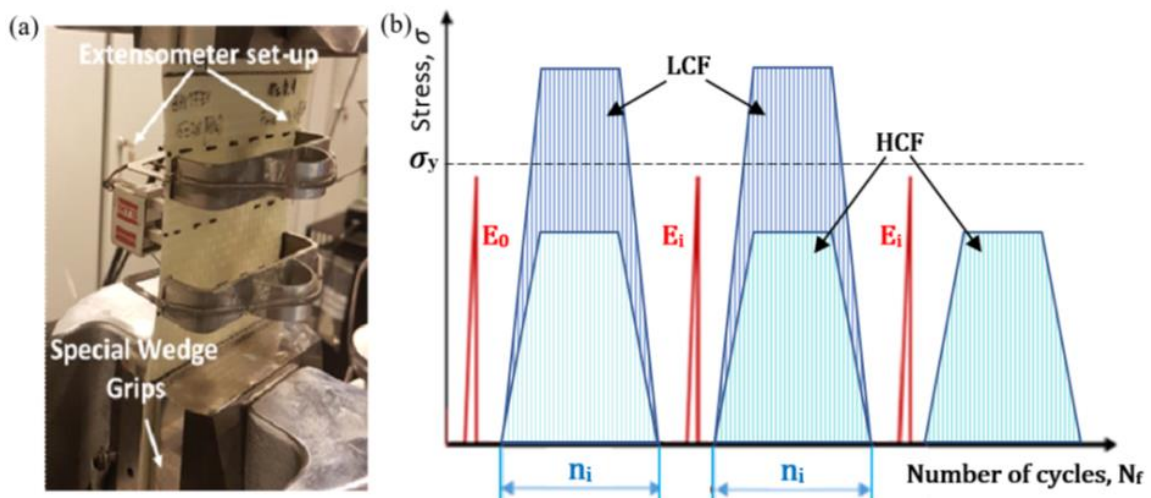
Fig. 3-9. (a) Experimental setup for fatigue aging tests, (b) schematic illustration of the loading sequences.

The fatigue aging conditions for both laminate composites tested under LCF and HCF are shown in Table 3-3.

Table 3-3. Fatigue aging conditions for both laminated composites tested under LCF and HCF.

	Specimen	σ_y (MPa)	σ_{max} (MPa)	F_{max} (kN)	F_{min} (kN)	R	f (Hz)
LCF	GFRE [0°/90°]₄	215.0 ± 7.2	250.0	43.0	4.3	0.1	2.0
	GFRE [45°/45°]₄	58.0 ± 2.8	80.0	13.7	1.3	0.1	2.0
HCF	GFRE [0°/90°]₄	215.0 ± 7.2	80.0	14.0	1.4	0.1	2.0
	GFRE [45°/45°]₄	58.0 ± 2.8	55.0	10.2	1.0	0.1	2.0

Prior to all fatigue tests, the Young's modulus (E_0) was determined, and subsequently the selected blocks of the loading cycles were executed. After the last cycle, the specimen was unloaded to zero force and the residual elastic modulus E_i was determined. Variations of the elastic modulus determined under cyclic loading for LCF and HCF tests are presented in Figures 3-10 and 3-11, respectively.
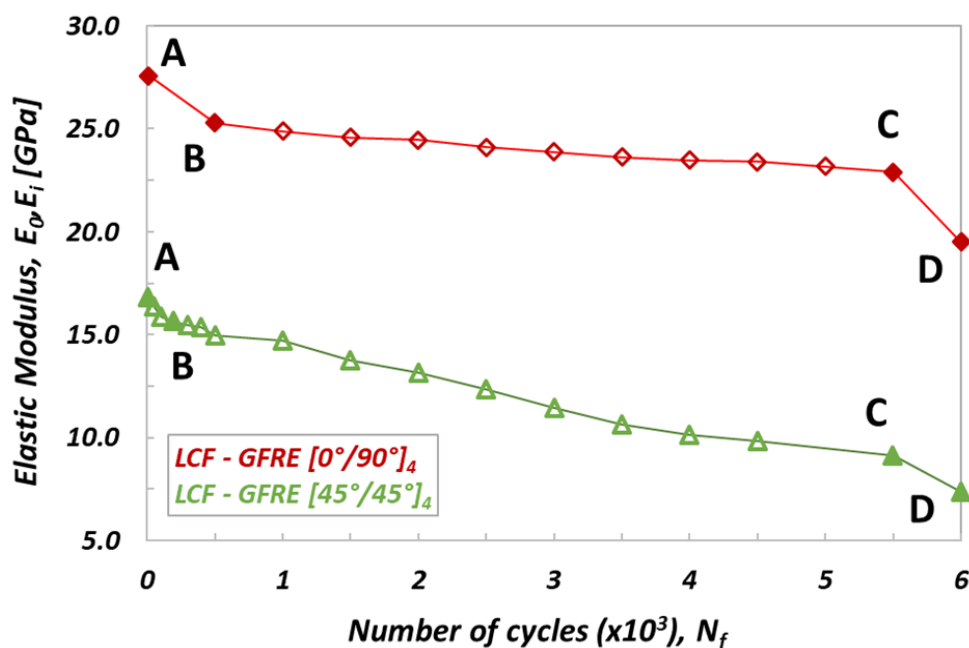
Fig. 3-10. Variation of the elastic modulus versus number of cycles for specimens of different fibers orientation obtained for LCF tests. AB—crack initiation (crack in the transverse yarn), BC—crack growth (interlaminar debonding), CD—ultimate failure (fibers breakage).

The stress levels in the LCF tests were higher than the yield point. For specimens oriented as [0°/90°]₄ the stress level was equal to 250 MPa (i.e., 35 MPa above the yield stress—see

Table 3-3). In the case of specimens oriented as ($[45°/45°]_4$) it was 80 MPa (i.e., 22 MPa above the yield stress, Table 3-3). Each block employed for reduction of the stiffness of tested material contained n_i = 500 loading cycles. As observed in Figure 3-10, the variation of stiffness with a number of cycles exhibits three clearly marked zones, for both materials in question. In the first part of the curves (up to point *B*), the stiffness drops rapidly as the result of typical fatigue feature of composite materials, in early stage of the process that mainly develops in the matrix) [28,30]. In the second stage (*BC* zone in Figure 3-10) a degradation of the matrix and delamination process are developing, however, much slower than during the first stage of fatigue. The elastic modulus decreases almost linearly, however, for GFRE $[45°/45°]_4$ more than for the GFRE $[0°/90°]_4$. In the last stage of the process, beyond point *C*, there is a relatively abrupt drop of the elastic modulus leading, as a consequence, to the fibers breakage, which takes place below point *D*.
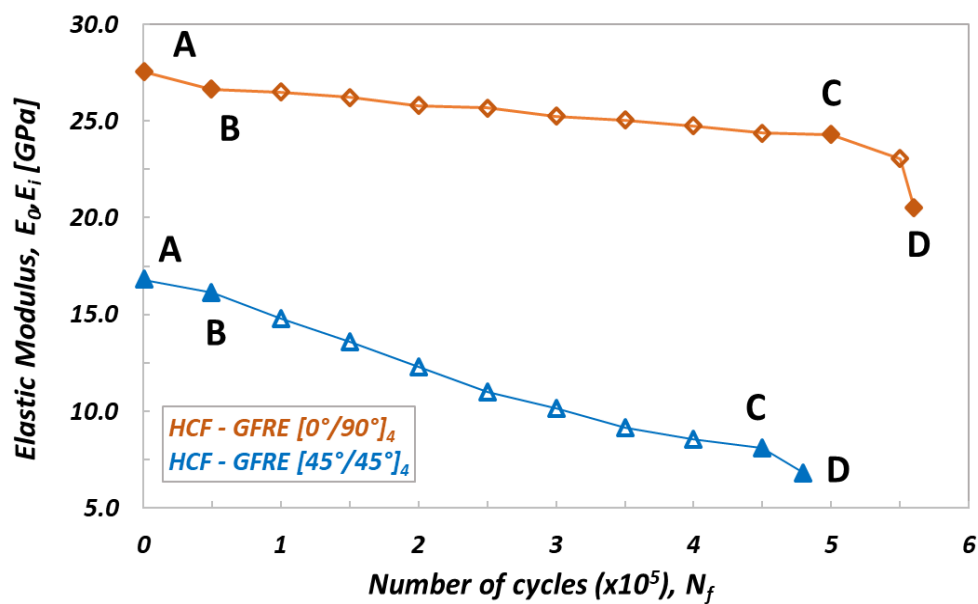
Fig. 3-11. Variation of the elastic modulus versus number of cycles for specimens of different fibers orientation obtained for HCF tests. AB—crack initiation (crack in the transverse yarn), BC—crack growth (interlaminar debonding), CD—ultimate failure (fibers breakage).

A similar program was arranged for HCF tests, however, for the stress levels lower than the yield stress. The maximum stress levels were equal to 80 and 55 MPa for $[0°/90°]_4$ and $[45°/45°]_4$ composite laminates orientations, respectively (Figure 3-11). In this case, the total number of cycles to failure N_f was about 500,000 for both orientations considered. Each of the loading blocks applied in the experimental program comprised n_i = 50,000 cycles.

Similarly, to the characteristics presented in Figure 3-10, also on curves describing an evolution of residual stiffness for HCF tests (Figure 3-11), three zones can be distinguished: *AB*, *BC* and *CD*. One can notice however, that during the HCF tests the initial stiffness decreases a bit slower (zone *AB*) than that observed for the LCF tests, and as a consequence, the curves pass smoothly to the second stage (BC zone) where the process of cyclic softening for both woven fabric orientations is practically the same as that for the specimens subjected to LCF. Finally, beyond the point *C* a similar character of the curves variations can be observed for both orientations taken into account. As it is shown in Figures 3-10 and 3-11, almost 17% reduction of the initial stiffness was obtained for the GFRE $[0°/90°]_4$ independently, whether the LCF or HCF tests were executed. In the case of GFRE $[45°/45°]_4$, the reduction of stiffness was much clearer and amounted to almost 48%.

3.2.2 Damage evolution during uniaxial tensile cyclic loading

As observed, the cyclic loading strongly affected the stiffness of the materials tested. Depending on the woven fabric orientation and number of cycles to failure, a minor or major decrease of stiffness was identified. The results are consistent with those presented in previous studies on fatigue behaviour of glass plain-weave fabric composites in on- and off-axis directions, although in this study the Elium thermoplastic resin was used as a tackifier instead of thermoset epoxy [30]. By analogy to the damage definition introduced by Kachanov [31] or Azouaoui, et al. [12], the loss of material stiffness was applied as a damage indicator. It was specified based on the value of the measured residual stiffness E_i for a given number of cycles N_f, by using equation (1-5). Its values for the specimens subjected to LCF and HCF loading are presented in Figures 3-12 and 3-13, respectively. The evolution of damage parameter D_E was used to identify the pre-critical state (i.e., the value of the maximum internal damage, at which the sample will not be destroyed) and interrupt the cyclic loading process prior to total failure of the specimen.

Taking into account evolutions of the damage parameter presented in Figures 3-12 and 3-13, one can conclude that three stages of damage can be easily noticed. In the first stage represented by a part of characteristic denoted as *0-B*, the damage parameter exhibits a significant increase and takes the values at the end of this stage of D_E = 0.085 ÷ 0.100 and D_E = 0.035 ÷ 0.040 for LCF and HCF tests, respectively. In the second stage, defects in the form

of micro cracks and delamination, generated by the fatigue aging, were increasing much faster for GFRE [45°/45°]$_4$ oriented laminate composites than that for GFRE [0°/90°]$_4$ ones. For the GFRE [0°/90°]$_4$ composite laminates, D_E parameter increases with the number of cycles to failure, only up to 0.15 and 0.10 for the LCF and HCF tests, respectively. In the case of GFRE [45°/45°]$_4$ the same parameter at the same stage of damage takes the value equal to 0.6 independently of a loading type (LCF or HCF). The third stage represents a very short final phase that covers a time to reach the failure. It appeared at N_f = 500,000 for the HCF and at N_f = 6,000 for the LCF.
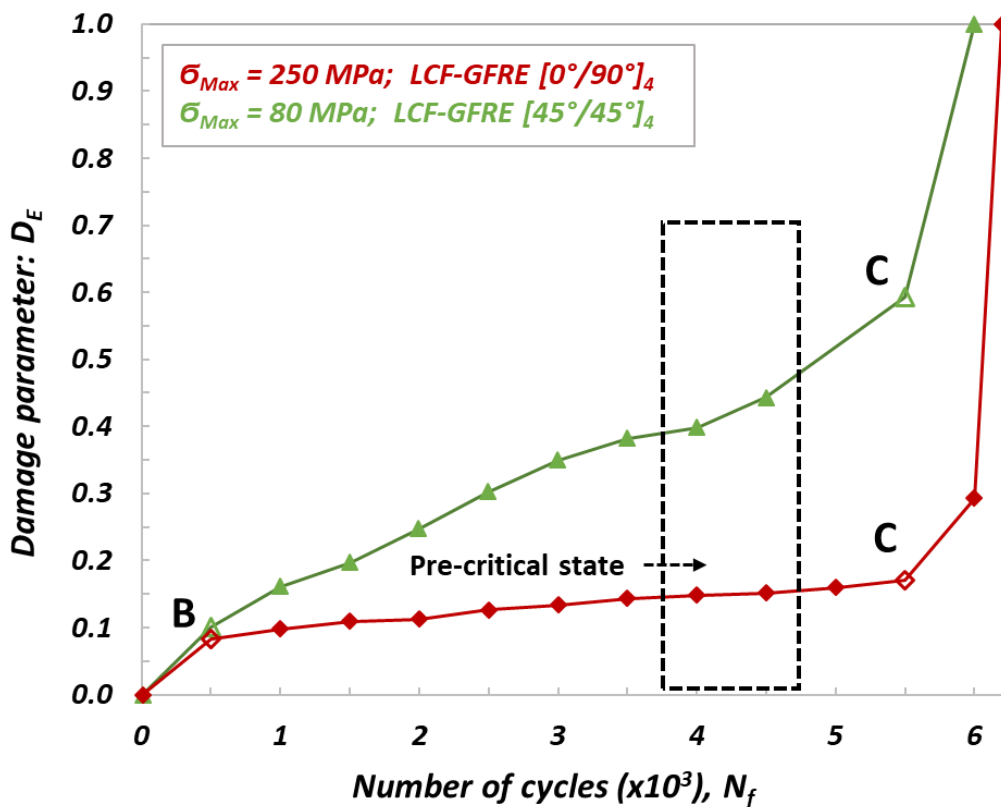
Fig. 3-12. Evolution of damage parameter D_E determined from LCF tests for GFRE [0°/90°]$_4$ and GFRE [45°/45°]$_4$.

Based on the residual stiffness E_i, and damage parameter D_E evolutions, the pre-critical states were established for all groups of the composite laminates tested. Their ranges are marked by the dotted black lines shown on Figures 3-12 and 3-13. Identification of the pre-critical states enabled to interrupt the processes of aging, induced by uniaxial cyclic loading at a given value of the stiffness loss, and to maintain a comparable character of the internal damage (micro cracks in the matrix and interlaminar debonding) for both orientations taken into account and stress levels applied.
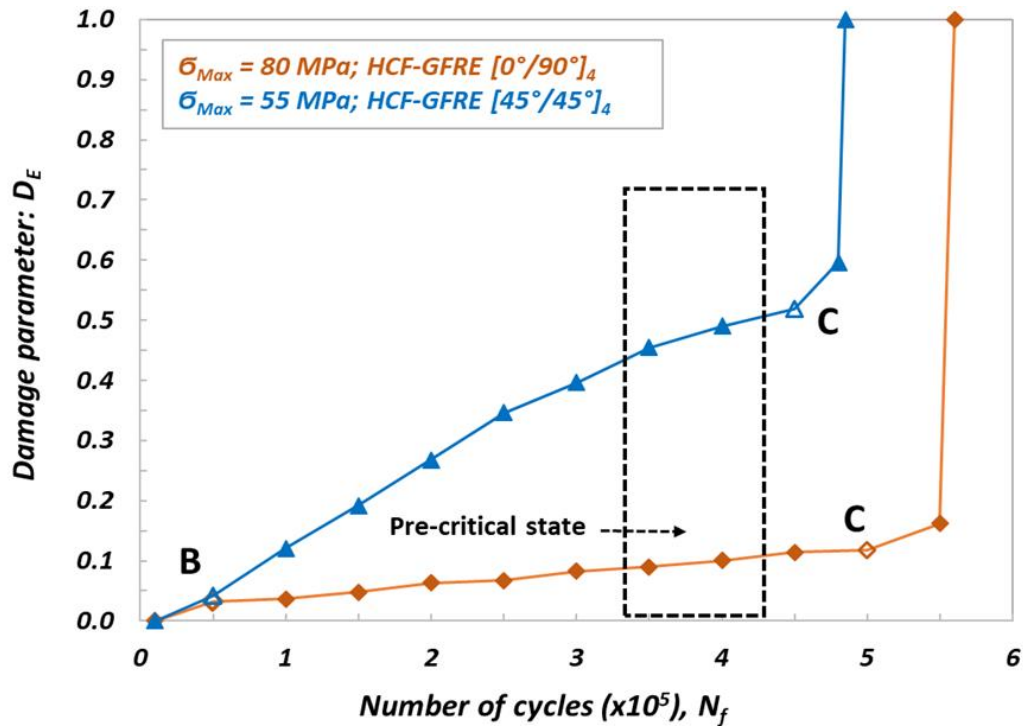
Fig. 3-13. Evolution of damage parameter D_E determined from HCF tests loading for GFRE [0°/90°]$_4$ and GFRE [45°/45°]$_4$.

Therefore, the specimens for impact tests made of the GFRE [45°/45°]$_4$ were aged until damage parameter D_E reached the value of 0.45, that corresponded to the σ_{max} = 80 MPa and N_f = 4,500 cycles for LCF tests. For the same orientation specimens subjected to HCF under σ_{max} = 55 MPa and the same value of D_E = 0.45, 350,000 cycles were necessary to reach the pre-critical phase. Regarding the material with woven fabric oriented along the force direction (GFRE [0°/90°]$_4$), the maximum safe value of the damage parameters was equal to D_E = 0.15 and D_E = 0.11, for σ_{max} = 250 MPa at LCF tests and σ_{max} = 80 MPa at HCF test, respectively. Hence, to reach the assumed value of stiffness loss the N_f = 4,000 cycles for LCF and N_f = 400,000 cycles for HCF were required.

Finally, in order to study the effect of softening generated by the fatigue aging on the impact resistance, 80 specimens for impact tests of 100 × 100 mm sizes were aged by uniaxial cyclic loading, 20 for each tested group.

3.3 Damage analysis of non-aged and aged specimens

According to the research plan, the tested specimens were not destroyed by fatigue, but only the earlier assumed damage (a given loss of stiffness) was introduced. Therefore, in

order to understand proliferation of internal changes and characterize the phenomenon of damage for both tested orientations, the cross-section surfaces were examined using a scanning electron microscope (SEM).
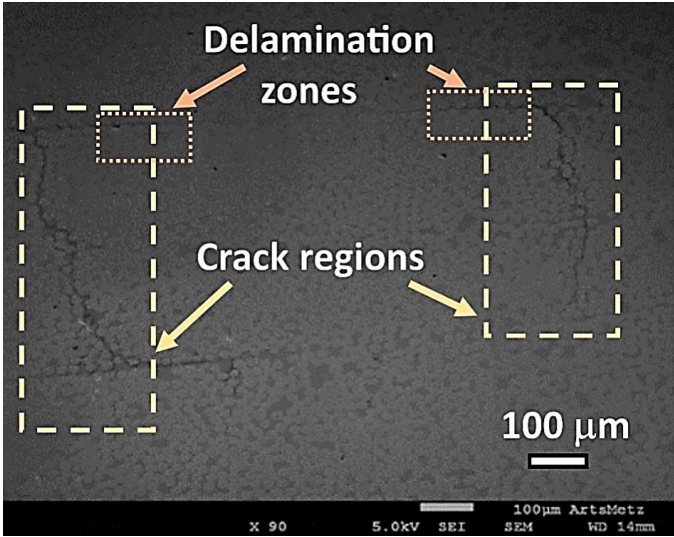
Fig. 3-14. Intralaminar and interlaminar damage (x 90) induced in GFRE [0°/90°]₄.
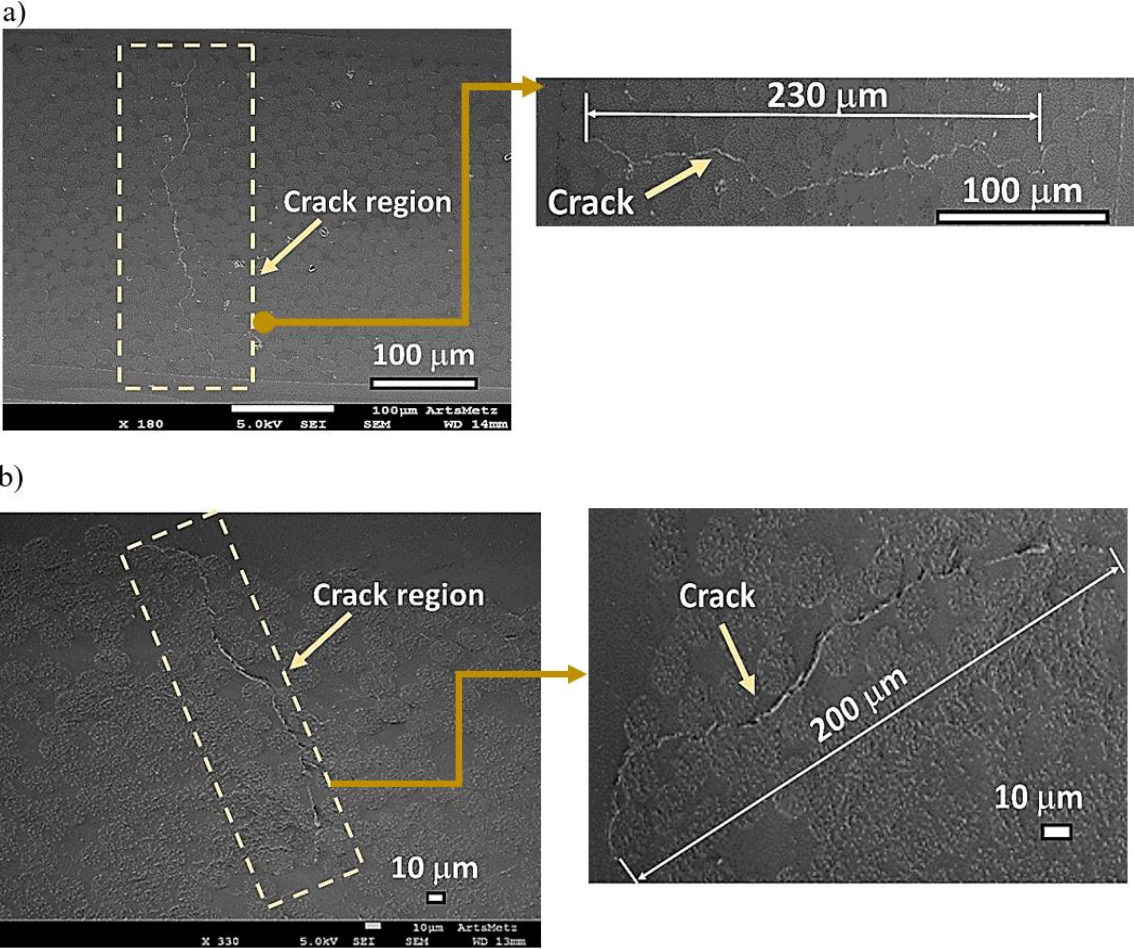
Fig. 3-15. Intralaminar (a -180x) and interlaminar damage (b – 330x) induced in [0°/90°]₄

woven laminates by fatigue loading.

Figures 3-14 and 3-15 (a) and (b), show intralaminar and interlaminar damage in the woven fabric composite with the warp oriented along the applied force - GFRE[0°/90°]$_4$ subjected to fatigue loading. There are clearly visible cracks in the transverse yarn (weft), as well as delamination between the neighbouring layers. This leads to the reduction of the stiffness in the reinforcing phase and, in consequence, decreases the strength of the composite tested.

Examination of SEM images for the specimens cut out along direction inclined by an angle of 45° with regard to that of the fibers one (GFRE [45°/45°]$_4$), Figure 3-16, confirmed that the same damage mechanisms were involved in the strain softening. Also in this case, the fracture occurred at the matrix/fiber interface. Subsequently it developed through the yarn until the border of layer, and induced delamination between the adjacent layers. It has to be mentioned however, that in a laminated composite with woven fabric oriented at 45 degrees the matrix plays a more important role in the transmission of force. Therefore, fracture in the pure resin, Figure 3-16 (a), and decohesion of fibre/matrix interface, Figure 3-16 (b), were caused by the shear transversal cracks that lead to propagate a fracture path through the resin rich areas (RRA).

a)   b)
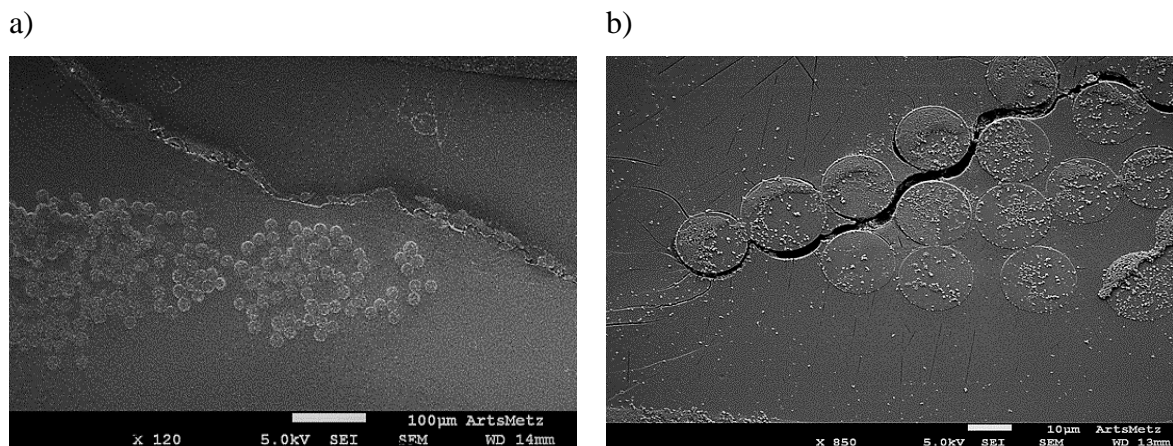
Fig. 3-16. Cracks (a – 120x) and decohesion of fiber/matrix interface (b – 850x) in the resin rich areas (RRA) - GFRE [45°/45°]$_4$.

Based on the SEM analysis one can assume that for both tested orientations of woven fabric, the matrix cracking (intralaminar damage) directly results from local tensile–shear stresses generated due to some imperfections and geometric diversity in layers which grow during the repeated uniaxial loading cycles. Then, the subsequent cycles lead to the further crack development in the transversal yarn and meta delamination. These two types of damage

strongly weaken the material, and in consequence, induce the softening of the reinforcing phase responsible for the stiffness of the composite.

3.4 Conclusions

The geometry of the fatigue specimen with the shape adapted to the low and high velocity impact tests was presented. Experimental work dedicated to the effect of damage occurring during the cyclic fatigue aging was carried out. It was observed that both tested specimens: GFRE $[0°/90°]_4$ and $[45°/45°]_4$ exhibited the visible effect of the stiffness loss during fatigue. The initial stiffness was reduced of about 17 % for the GFRE $[0°/90°]_4$, after either LCF or HCF tests. Such reduction was much more pronounced in the case of GFRE $[45°/45°]_4$ and was equal to 48 %.

Thus, it was possible to determine the damage parameter D_E that defined a number of cycles necessary to reach the pre-critical state for each group of the aged specimens under applied stress level. As a result of these measurements, the cyclic loading process was interrupted prior to the total failure of specimen at the assumed damage state. All the aged specimens acquired the same level of degradation (similar stiffness loss).

Microscopic observations carried out on the aged specimens with the fibers arranged along the applied force show that the main damage for this orientation takes a form of cracks in the transverse yarn (weft), and delamination between the neighbouring layers. In case of the specimens cut out along direction inclined by an angle of 45° with regard to that of the fibers one (GFRE $[45°/45°]_4$), the fractures occurred at the matrix/fiber interface and in the pure resin areas.

Chapter 4. Low velocity impact resistance of acrylic based glass fibers laminated composites

In the previous chapter, the attention was focused on the mechanical response of the glass fibers/acrylic laminated composite subjected to uniaxial fatigue loading.

The aim of this chapter is to evaluate the low velocity impact resistance of the previously aged and non-aged composite plates. For this purpose, the aged specimens were prepared. At first, an effect of fatigue aging on the mechanical response to the low velocity impact of the glass fibers/Acrylic composites was compared to that observed for the material non-aged. Subsequently, the damage phenomena generated during the low velocity impact were investigated for both fiber orientations of tested aged and non-aged laminated composites. Finally, for one of the studied fiber orientations, i.e. $[0/90]_4$, a numerical model was proposed in order to describe the damage process of non-aged woven laminated composite plates subjected to the low velocity impact. It enabled to compare the numerical data with the experimental results.

4.1 Specimens and testing conditions

The low impact velocity tests were performed on an Instron DYNATUP 9250HV drop weight tower. This testing stand, equipped with a thermal chamber, enabled to perform tests at room temperature of about 20 °C. The impactor used for the impact tests had a hemispherical shape with a diameter of 16 mm. The total mass, including impactor carriage and hemispherical headed impactor, was equal to 5762 ± 100 g. The square shape specimens of 100 × 100 × 2 mm dimensions were fixed in a testing stand by the special clamping system, as shown in Figure 4-1. The griping system for impact tests at low velocity consisted of a special holder and clamp to fix properly each tested specimen. The drop-weight tower device was equipped with a special transducer that contained the strain gauge/piezoelectric and infrared sensor. Its position was adjustable by means of the measuring system. A displacement was measured by this sensor with an accuracy of ±0.2 mm. In order to avoid some oscillations or signal noise induced by the voltage signal output from the force sensor, the fast Fourier transformations were applied for data filtration and

subsequent analysis. The higher frequency components were filtered, and therefore, only the harmonics of the basic frequency responses could be seen, as reported in [115,116].
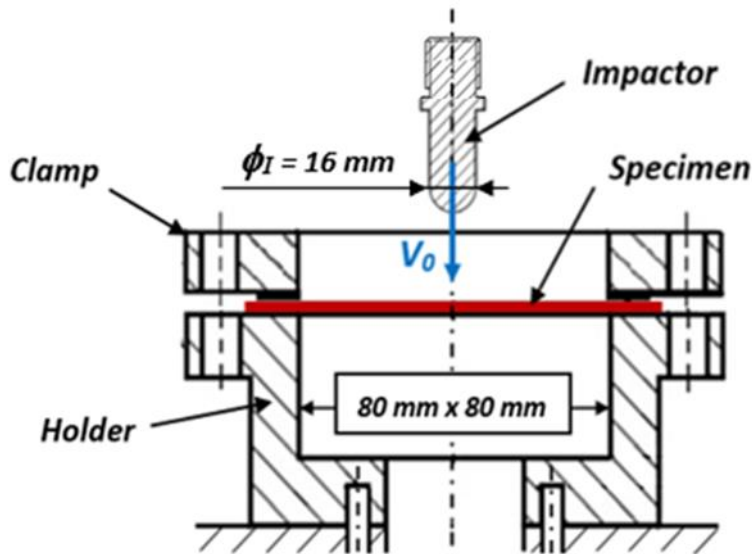
Fig. 4-1. Experimental setup used for low velocity impact tests.

Low velocity impact tests were performed on two groups of specimens, including non-aged and aged specimens. They were cut out to ensure the same orientations as those for fatigue tests. Various impact energies of 5, 10, 30 and 50 J, corresponding to impact velocities of 1.32, 1.86, 3.23 and 4.16 m/s, respectively, were used for low velocity impact tests. The tests were repeated five times for each value of impact energy in order to check the results repeatability.

Based on the force and displacement variations of the impactor, the energy changes were calculated. Such changes represent the energy transfer from the projectile to the composite specimen. The energy change history for each impact test was determined by proper integrating the velocity change plots, i.e., the area under the curve representing these changes. In the test, the absorbed energy was determined as a fraction of the energy transferred from the projectile to the composite specimen at the end of the impact, and in each case the impact energy corresponded to the kinetic energy of the projectile just before the impact. Although the maximum force, contact duration, history of force and displacement changes and energy are important characteristics of laminated composites subjected to dynamic loads, only the change in the amount of energy absorbed was the main parameter considered in the experiment. For this reason, studies were carried out on the

effect of fatigue load on impact toughness, and especially its negative effect in the form of an increase in energy dissipation due to the loss of stiffness. Impact resistance was quantified on the basis of the analysis of the maximum impact force F_i and the corresponding displacement U, as well as the absorbed energy E_a and the penetration threshold.

4.2 Effect of fatigue aging on low impact resistance of GFRE

Four groups of aged specimens were impacted. The stiffness loss introduced by fatigue was approximately equal to 12% in the group of specimens cut out along the yarns (LCF and HCF tests on GRFE [0°/90°]$_4$), and 40% for specimens with woven fabric inclined at 45° with respect to the acting force (LCF and HCF test for on GRFE [45°/45°]$_4$). In order to study the effect of the fatigue aging on the impact properties, the results were compared with those carried out on the non-aged specimens with the same woven fabric orientations. The low velocity impact test results are reported in Tables 4-1 and 4-2.

Table 4-1. Low impact velocity test results for all laminates at impact energy of 5 J and 10 J.

Specimen	5 J			10 J		
	E_a (J)	F_i (N)	U (mm)	E_a (J)	F_i (N)	U (mm)
GFRE [0°/90°]$_4$	3.7 ± 0.1	2379.5 ± 24.7	3.85 ± 0.1	5.9 ± 0.2	3731.5 ± 72.1	5.74 ± 0.1
LCF-GFRE [0°/90°]$_4$	4.2 ± 0.2	2254.2 ± 12.5	3.97 ± 0.1	7.6 ± 0.5	3494.3 ± 68.5	5.79 ± 0.2
HCF-GFRE [0°/90°]$_4$	4.0 ± 0.1	2265.9 ± 36.2	3.93 ± 0.3	6.8 ± 0.4	3344.6 ± 43.9	5.87 ± 0.5
GFRE [45°/45°]$_4$	4.0 ± 0.1	2229.5 ± 16.2	3.9 ± 0.1	7.0 ± 0.1	3594.5 ± 42.1	5.4 ± 0.1
LCF-GFRE [45°/45°]$_4$	4.4 ± 0.2	2109.5 ± 27.6	4.2 ± 0.2	8.5 ± 0.4	3150.4 ± 54.2	5.8 ± 0.2
HCF-GFRE [45°/45°]$_4$	4.3 ± 0.1	2176.7 ± 14.2	4.3 ± 0.1	7.8 ± 0.2	3235.6 ± 36.4	5.6 ± 0.2

Table 4-2. Impact test results for all the laminate composites at impact energies of 30 J and 50 J.

Specimen	30 J			50 J		
	Ea (J)	Fi (N)	U (mm)	Ea (J)	Fi (N)	U (mm)
GFRE [0°/90°]$_4$	27.6 ± 0.3	5623.8 ± 64.7	10.3 ± 0.1	-	5939.9 ± 90.2	-
LCF-GFRE [0°/90°]$_4$	29.2 ± 0.4	5125.3 ± 112	12.8 ± 0.4	-	5212.1 ± 55.4	-
HCF-GFRE[0°/90°]$_4$	28.5 ± 0.3	5116.9 ± 86.2	11.9 ± 0.2	-	5292.4 ± 116	-
GFRE [45°/45°]$_4$	28.1 ± 0.3	5750.4 ± 96.4	10.7 ± 0.2	-	6019.8 ± 67.4	-
LCF-GFRE [45°/45°]$_4$	29.7 ± 0.2	4611.6 ± 74.1	11.9 ± 0.2	-	4728.7 ± 136	-
HCF-GFRE [45°/45°]$_4$	29.1 ± 0.2	4456.8 ± 132	12.4 ± 0.3	-	4860.6 ± 185	-

4.2.1 Analysis of force-displacement and energy-time curves

The most common way to present the low velocity impact response and resulted damages is to use the recorded impact histories of force-time or force-displacement. Before

an analysis let us to define some important quantities like a peak force and adsorbed energy. Peak force corresponds to the maximum value of impact force (F_i) registered during the contact between the impactor head and specimen. Absorbed energy should be treated as the amount of energy transferred from the impactor to specimen at the end of test. The impact force history at the low impacts velocity provides important knowledge regarding a damage initiation and its further propagation [117], and therefore, a particular emphasis should be taken into account with regard to signal acquisition quality. Hence, the oscillations of higher frequency values in recorded data of force signals were filtered using the FFT techniques. As a consequence, only harmonics of responses for basic frequency level are presented on the curves. Figure 4-2 presents the force versus displacement curves for laminated composites subjected to an impact energy of 10 J.
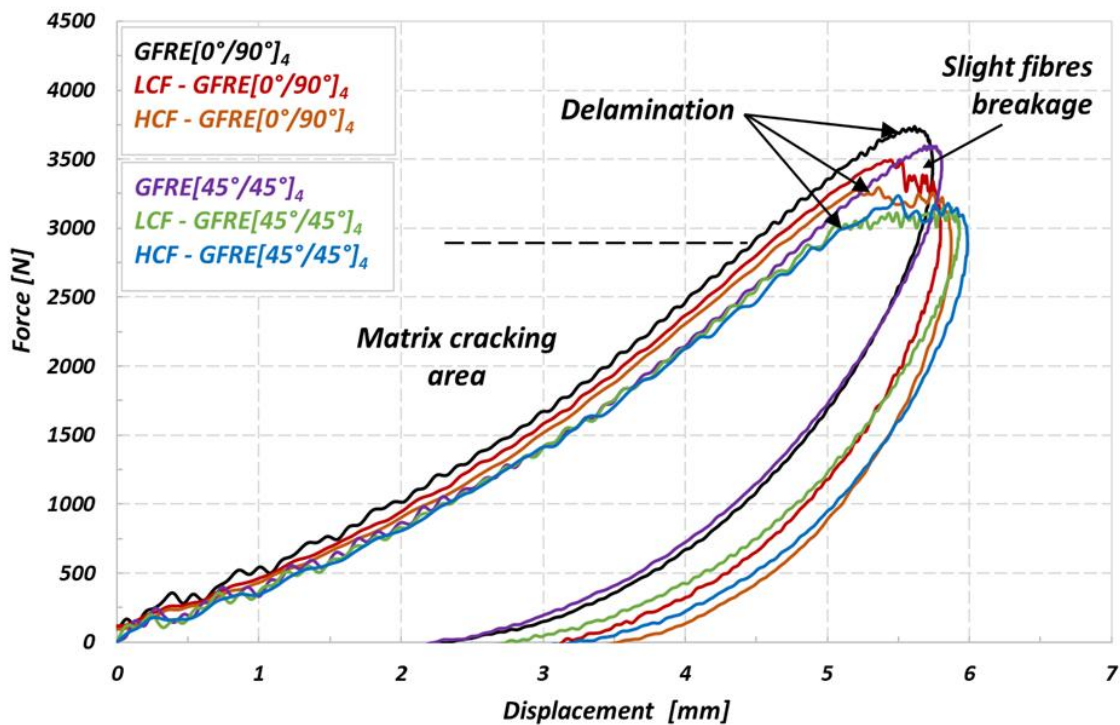
Fig. 4-2. Force–displacement curves of the non-aged and aged GFRE [0°/90°]₄ and GFRE [45°/45°]₄ due to the LCF and HCF ageing processes, the results are for an impact energy of 10 J.

The early stages of the force versus displacement curves (slope of the curve) are not the same in case of the GFRE [0°/90°]₄, indicating that fatigue aging process affected the laminate's stiffness. Subsequently, some small oscillations can be observed with force increase exhibiting a presence of matrix cracking [118]. The effect is mostly visible for GFRE

[45°/45°]₄, as a contribution of resin in the force transmission is more significant for this type of composites. It takes place for a force value of about 2200 N. Above 3000 N an effect of the force stagnation can be observed. It was due to the reduction of bending stiffness resulting from the brittle impact damage behaviour of GFRE, and moreover, from the delamination process development. The intensity of the force stagnation process was clearer for the unharmed (non-aged) specimens than that of the aged laminated composites. A decrease of the maximum impact force (F_i) was obtained for both orientations of the reinforcement considered in comparison to the non-aged composite. It was associated with an increase of the deflection, identifying material ability to dissipate more energy.

In order to better understand the effect of uniaxial fatigue aging on the low impact velocity properties and damage appearance in the material tested, the curves representing the energy variation versus time were elaborated and plotted in Figure 4-3.
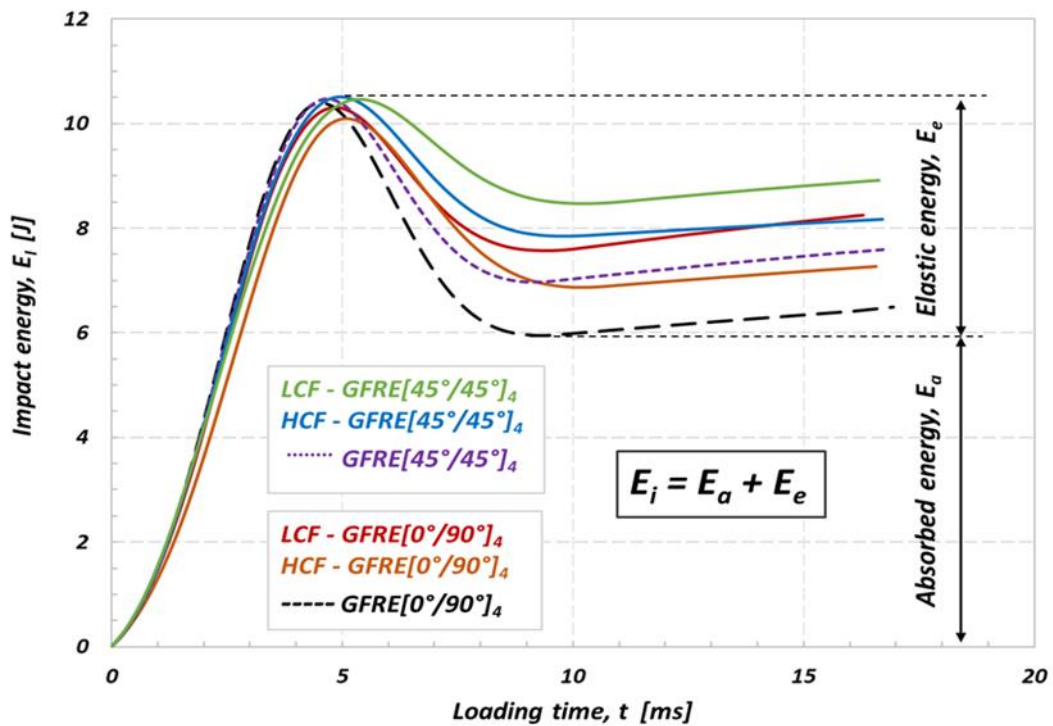
Fig. 4-3. Effect of fatigue aging on the absorbed energy of the non-aged and aged GFRE for an impact energy of 10 J at 20 °C.

The impact resistance represents the ability of the material to absorb energy without depicting too many other obvious damage indicators. The impact energy which corresponds to the peak energy on the $E_i(t)$ diagram can be decomposed into two parts, the absorbed

energy which generates damage, and elastic energy that serves for the impactor rebound. Therefore, in the present work, the energy absorbed by the specimen (E_a) is used as an indicator of the damage development [9,46]. Impact energy equal to 10 J, was insufficient to cause a complete loss of strength and penetration even for the aged specimens. However, it has to be noticed, that the laminated composites subjected to prior LCF loading exhibit much lower energy dissipation ability. The results in Figure 4-2 enable to assess a significant loss of stiffness caused by matrix cracking and interface debonding between the fibers and the matrix. The results for GFRE[45°/45°]₄ subjected to low velocity impact at 10 J showed that it was a less prone to delamination than GFRE[0°/90°]₄ and kept better impact resistance after fatigue aging. The values of absorbed energy are reported for different aging processes, in Table 4-1.

Subsequently, all groups of materials tested were subjected to the impact tests at 30 J and 50 J. Figures 4-4 and 4-5 show the evolution of the force versus displacement of the materials. All curves were obtained at room temperature (20 °C).
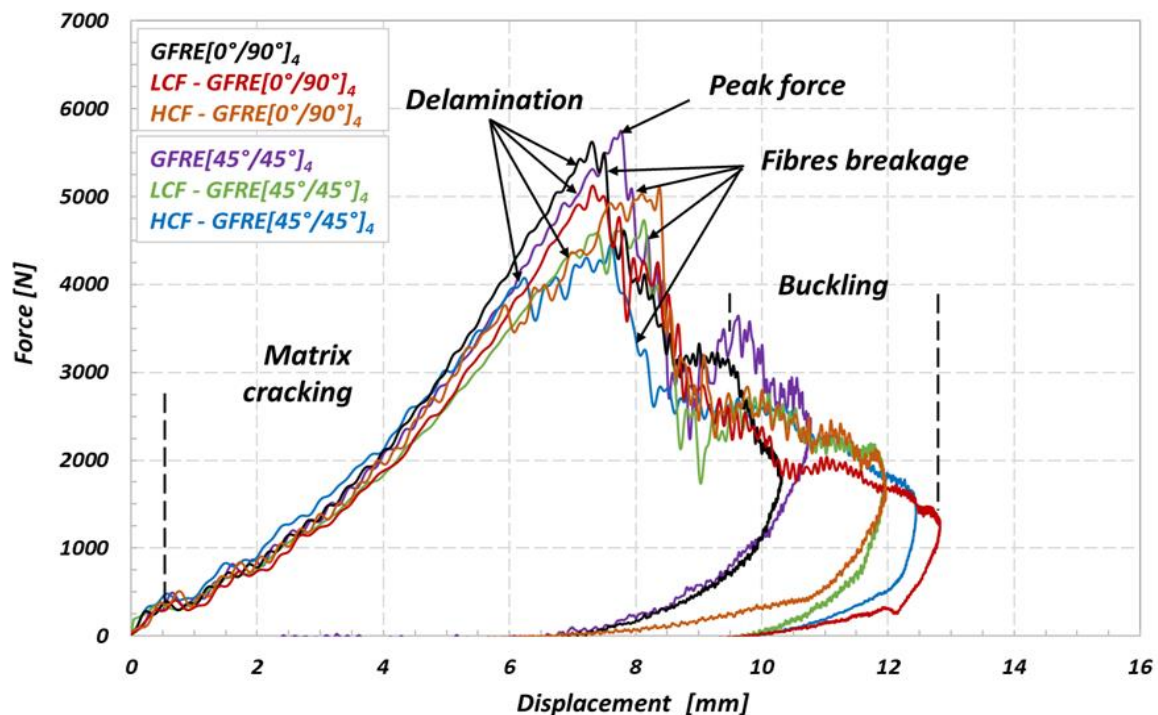
Fig. 4-4. Force–displacement curves of the non-aged and aged GFRE [0°/90°]₄ and GFRE [45°/45°]₄ under different aging processes, at 30 J.

It is clearly visible in Figure 4-4 that an initial slope of the characteristics slightly decreased due to prior in-plane uniaxial cyclic loading. This effect proves that the internal damage

induced stiffness reduction in out-of-plane direction due to matrix cracking and softening of the reinforcing phase, and as a consequence, led to partial loss of the impact dissipation ability.

The impact energy values of 30 J and 50 J were sufficient to cause a visible fracture with numerous internal cracks. Both aged and non-aged specimens did not resist to the impact at 50 J, and all of them were perforated. It should be noted that again the aged specimens representing GFRE [45°/45°]$_4$ orientation were the least resistant to impacts. In this case, the matrix cracking occurred under the force lower than that for GFRE [0°/90°]$_4$. Moreover, delamination appears during impact led to the significant reductions of the transmitted force. Hence, the peak force oscillations recorded for these specimens reached even 1000 and 1200 N approximately, for the impact tests of 30 J and 50 J, respectively.
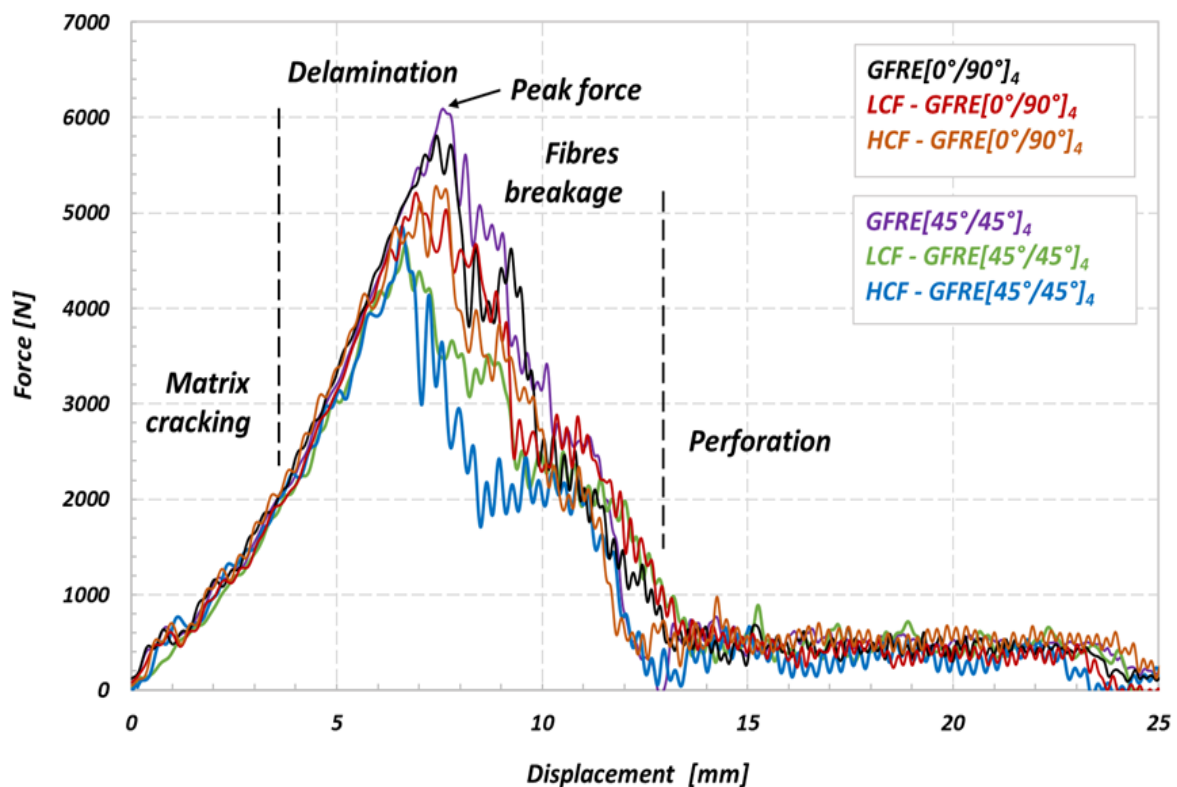
Fig. 4-5. Force–displacement curves of the non-aged and aged GFRE [0°/90°]$_4$ and GFRE [45°/45°]$_4$ under different aging processes, the results are for impact energy of 50 J.

The energy diagrams shown in Figures 4-6 and 4-7 exhibit that values of energy absorbed by GFRE [45°/45°]$_4$ subjected to prior LCF or HCF loading are considerably lower if compared to the other ones obtained in this research. Therefore, the GFRE [45°/45°]$_4$ ability to dissipate

energy is practically negligible. One can indicate such an effect looking on the course of the green line for example, that almost does not drop. In this particular case the absorbed energy is approximately equal to the impact energy, indicating that the penetration was reached. In consequence, the GFRE [45°/45°]$_4$, under LCF loading (represented by the green line in Figure 4-6) was more damaged during the impact loading expressed by relatively large delamination region.
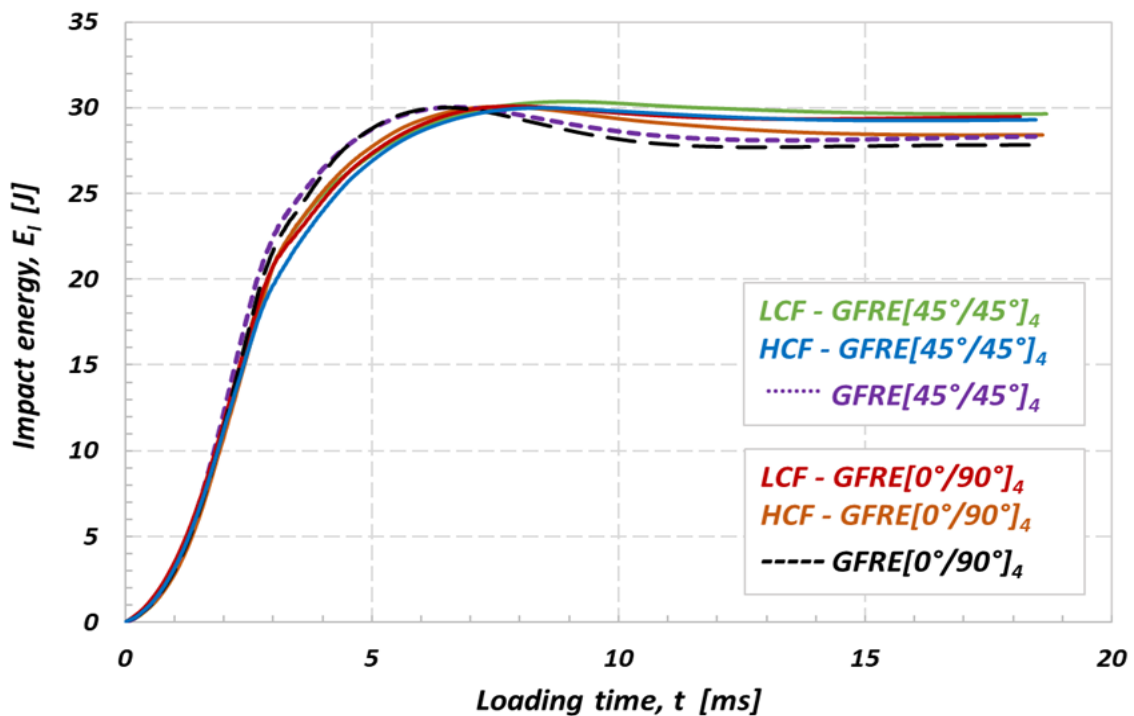
Fig. 4-6. Effect of fatigue aging on the absorbed energy of the non-aged and aged GFRE for impact energy of 30 J at 20 °C.

A comparison of the results presented in Figures 4-6 and 4-7 enabled to conclude that impact energy of 30 J may be treated as the amount of energy close to the impact strength limit for the composites tested. All energy characteristics exhibit energy peak, and further, their courses start to going down that is clear evidence of the penetration and subsequent perforation of the specimens tested. Moreover, the differences in courses of the impact energy observed for the non-aged and aged specimens directly identify an effect of fatigue aging on its impact resistance. This is an additional fact confirming previous observations, that the aged GFRE [45°/45°]$_4$ material is the weakest one among all considered in this research.
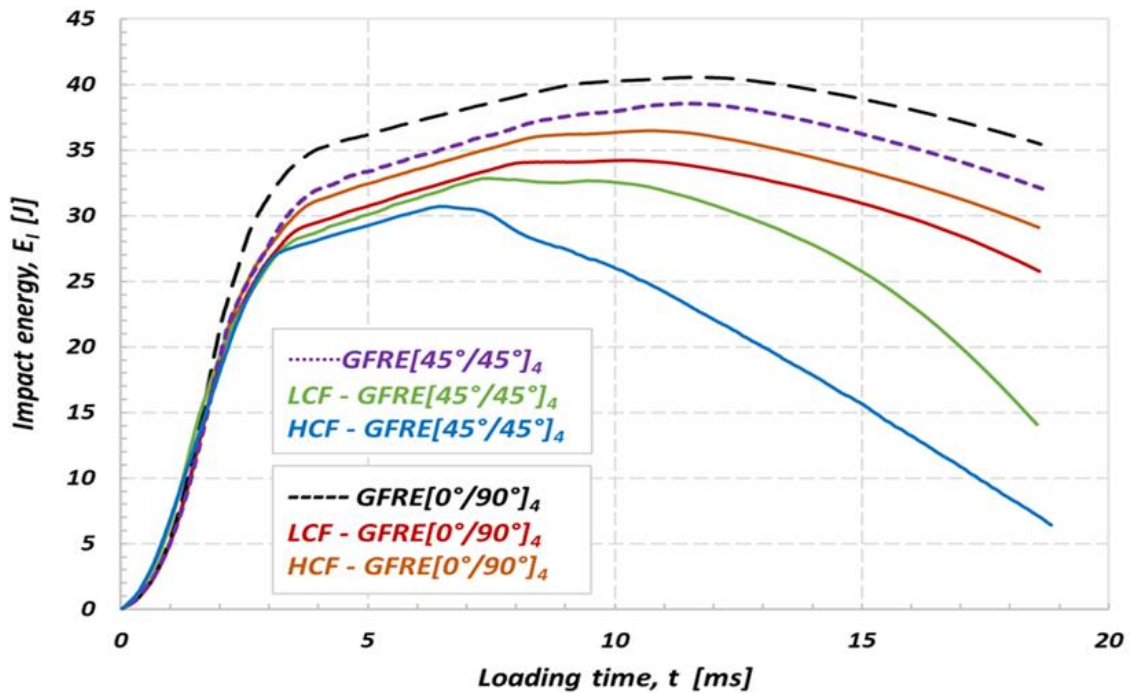
Fig. 4-7. Effect of fatigue aging on the absorbed energy of the non-aged and aged GFRE for impact energy of 50 J at 20 °C.

Having the characteristics presented in Figure 4-7 it is easy to identify the plate perforation initiation in specimens tested. In the case of non-aged material perforation started to develop when the energy level attained 40 J and 38 J, approximately, for the GFRE $[0°/90°]_4$ and GFRE $[45°/45°]_4$, respectively. Furthermore, it is clearly visible that all the groups of specimens after fatigue loading exhibited a significantly lower impact resistance. In the most undesirable case (HCF-GFRE $[45°/45°]_4$) the perforation appeared.

4.2.2 Identification of the penetration threshold

In order to assess a real influence of fatigue aging on the impact resistance of Elium acrylic based laminate composite, the penetration threshold curves were fitted for the three materials tested. In fact, it is well known that the penetration threshold belongs to the most important features, enabling better classification of the impact properties of the laminate composites [117]. This parameter determines the energy required for penetration of the laminated composite. In the present study a method defined by Reis et al. [119] and Aktas et al. [120] was applied. The authors defined an energy profile diagram (*EPD*) that is useful to compare the impact and absorbed energies, as well as to identify the penetration and

perforation thresholds. According to Aktas et al. [120], the penetration threshold can be defined as the point where the absorbed (E_a) and impact (E_i) energy are equal.

Figure 4-8 shows the *EPD* for all groups of specimens at ambient temperature. The diagram presented in Figure 4-8 summarizes the results obtained for the non-aged and aged specimens subjected to low velocity impact at energy levels equal to 5 J, 10 J and 30 J. Data points of both non-aged and aged laminate are located below the line representing the equal energy line between impact energy and absorbed energies. It means that the penetration threshold was not reached. For the highest impact energy (50 J) all the tested specimens were perforated.
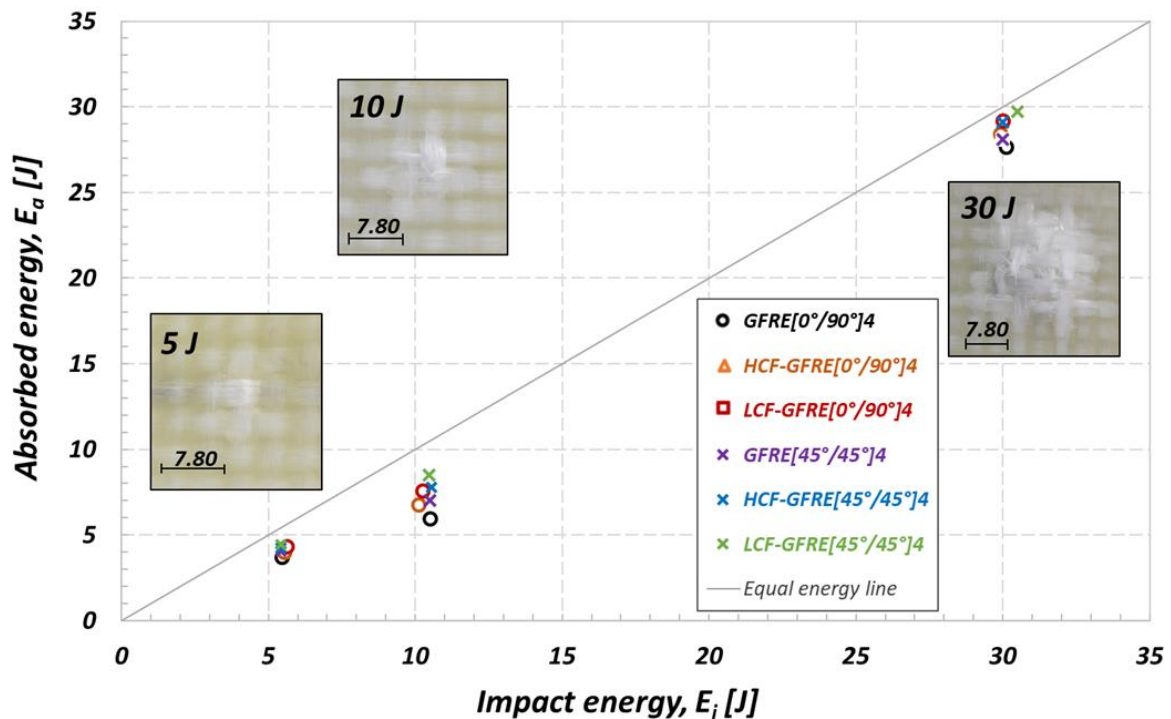
Fig. 4-8. EPD used to analysis of the effect of fatigue aging on the penetration threshold of the GFRE at 20 °C.

The results for the impact energy of 10 J and 30 J clearly show how the difference in energy absorption ability may change due to a type of reinforcement orientation and fatigue aging conditions. The prior aged laminates, under LCF loadings conditions attained practically impact resistance limit regardless of the woven fabric orientation. The highest values of absorbed energy were obtained for the GFRE [45°/45°]₄ after ageing due to LCF tests. It means that in comparison to the other considered material configurations such an oriented

material is the least suitable for applications where the impact loading is dominant. Contrary to that case, the lowest values of absorbed energy were achieved after ageing due to HCF tests for GFRE [0°/90°]₄. In order to illustrate damage occurred on the opposite side of the impacted specimens, damage images were included in Figure 4-8. They represent stages of damage for the GFRE [0°/90°]₄ in the non-aged state subjected to impact under energy equal to 5 J, 10 J and 30 J.

In this thesis another approach is also defined in which a diagram of the elastic energy versus absorbed energy is applied. The elastic energy is calculated as a difference between the impact energy (corresponding to the maximum of energy versus time curve) and absorbed energy. The roots of the corresponding second-degree polynomial equations fitting experimental data give energy values where impact energy (E_i) is equal to the absorbed energy (E_a), i.e., where $E_e = 0$. The non-zero root values indicate the penetration thresholds for laminates [9,119]. The values of the penetration thresholds for the non-aged and aged GFRE are shown in Figure 4-9.
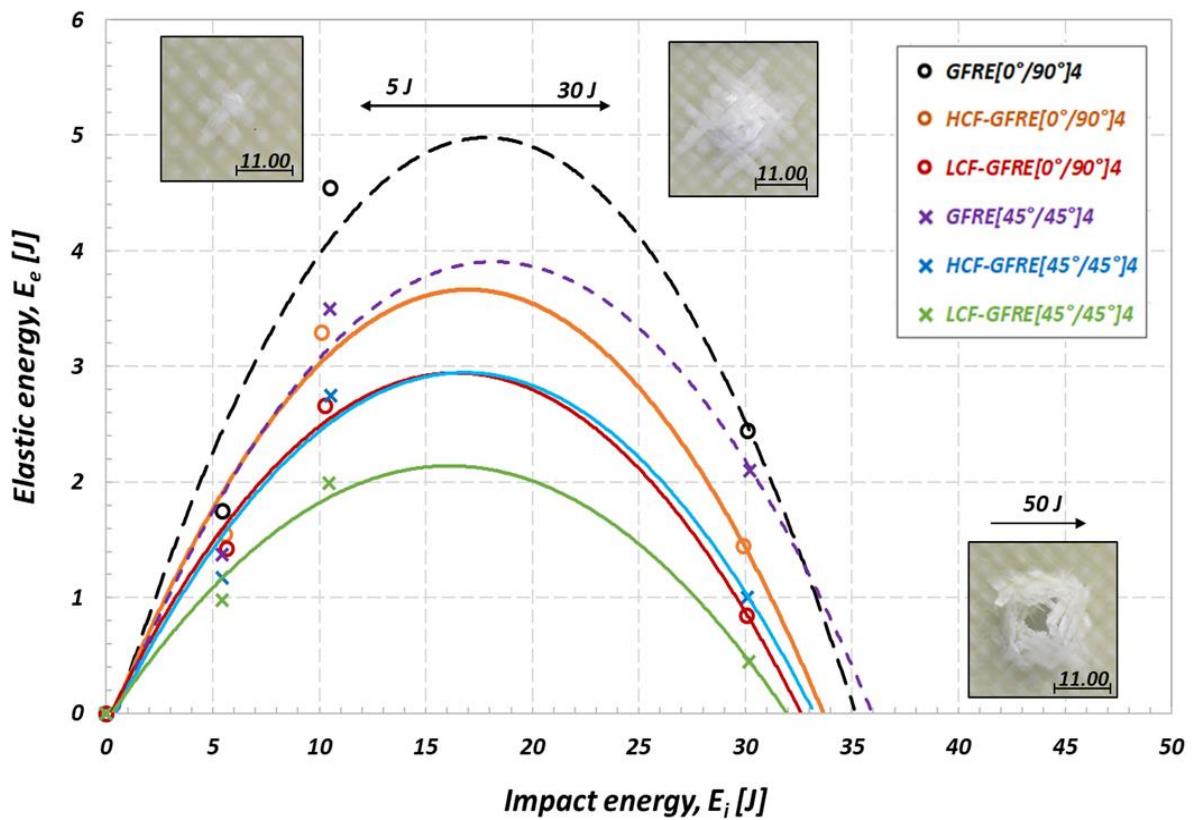
Fig. 4-9. Elastic energy versus impact energy for assessment of the effect of fatigue aging on the penetration threshold of the GFRE at 20 °C.

One can observe that the penetration thresholds calculated at 20 °C for impact energies of 5 J, 10 J and 30 J strongly depend on the internal damage introduced by fatigue aging. As expected, the non-aged composites represented materials with the best impact resistance properties. Estimated values of the impact energy at penetration thresholds were equal to 35.8 J for the GFRE [45°/45°]$_4$ and 35.1 J for GFRE [0°/90°]$_4$, respectively. In the case of the same materials after ageing due to HCF tests, the impact energies at penetration thresholds were equal to 33.2 and 33.5 J, respectively, and for the same materials after ageing due to LCF: 31.9 and 32.6 J, respectively. It is easy to notice that, the maximum difference between penetration thresholds determined is only 3.9 J. The main reason for such a small difference results directly from the limited number of data points (only 3 energy levels were used in the polynomial fitting).

Despite the limited number of data available, one can conclude that the history of the elastic energy variation due to increasing impact energy provides an effective parameter for analysis of the impact response of composites reinforced by glass fibers with different woven fabric orientations. Thanks to that, the ΔE_e, a difference between the elastic energy of the non-aged and aged composites can be easily determined. It can be observed that the difference between the elastic energy for the non-aged and aged GFRE [45°/45°]$_4$ (ΔE_e) increases with the increase of the applied impact energy. An opposite effect takes place in the case of GFRE [0°/90°]$_4$, particularly, if tests were carried out at energy values close to that corresponding to the perforation limit.

The results enable to conclude that the fatigue ageing process decreases the elastic response expressed by the stiffness reduction of both composites tested, and as a consequence, affects their toughness. It is strongly dependent on the mechanisms developing during tension on one hand, and a cohesion forces reduction between fibers and resin due to the fatigue ageing on the other. It leads to cracks generation in the transversal yarns for GFRE [0°/90°]$_4$, and either in warps or wefts for GFRE [45°/45°]$_4$.

4.2.3 Microtomographic analysis of impacted plates

Figures 4-10 and 4-11 present the back faces of the impacted composite plates for both fiber orientations tested at different energy values. At low impact energy, the damage is

localized mainly in the matrix and takes the form of numerous cracks. For tests carried out at higher impact energy, the area of damage increased significantly, revealing an occurrence of more severe forms of damages, such as delamination and fibers breakage, for example. When the composite laminates were subjected to prior fatigue aging, the obvious extent of damage area is observed, indicating as expected that low velocity impact leads to the generation of more cracks. One can indicate that the composites prestressed due to fatigue aging under the stress amplitude below the yield point were more depredated than those subjected to the same process, however, under stress amplitudes higher than the yield point. As a consequence, the mechanisms of plastic deformation were activated, which might induce some cavities and contribute to arrest propagation of cracks, when the plate is subjected to impact [49,121–122]. This effect is more obvious for the GFRE [0°/90°]4 composite laminate.
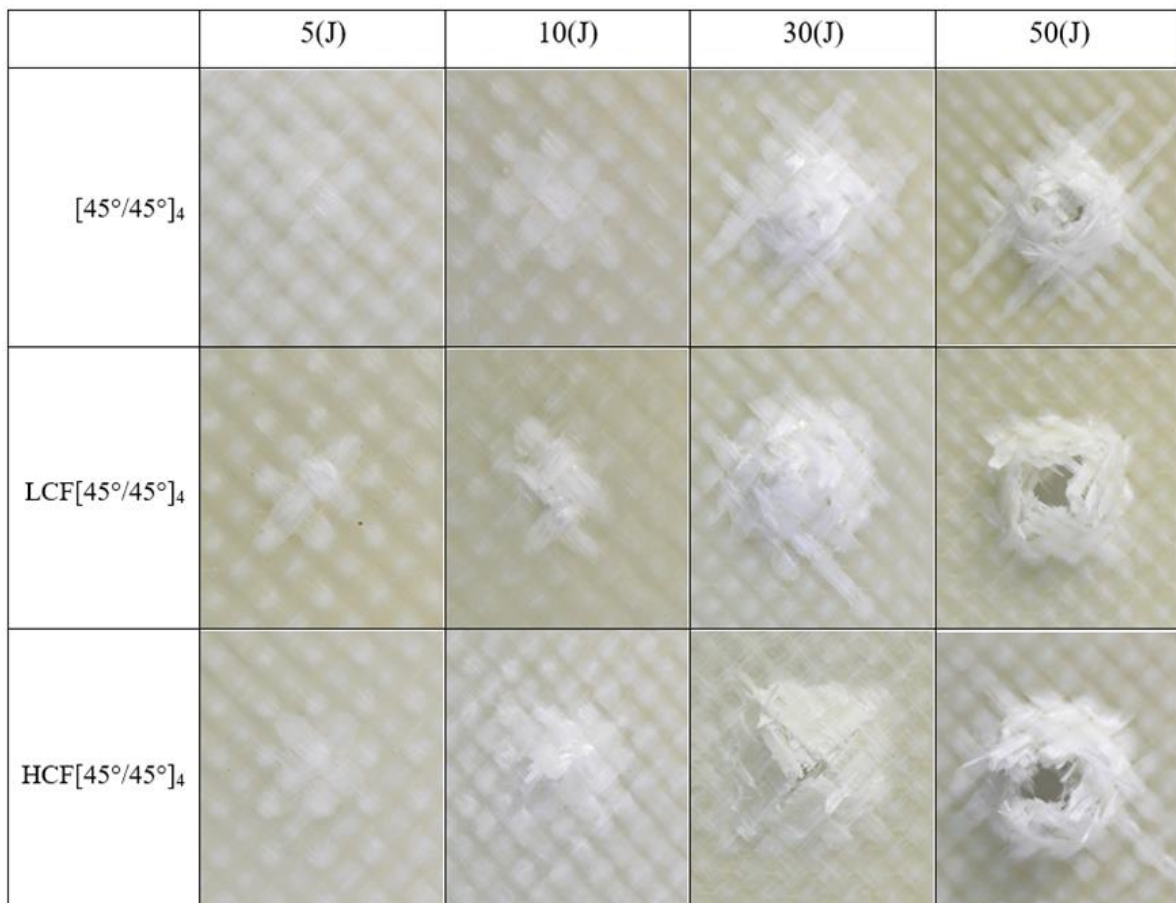
Fig. 4-10. Illustrations of damage occurred on the back face of impacted specimens for the non-aged and aged GFRE[45°/45°]$_4$ at impact energies of 5 J, 10 J, 30 J and 50 J.
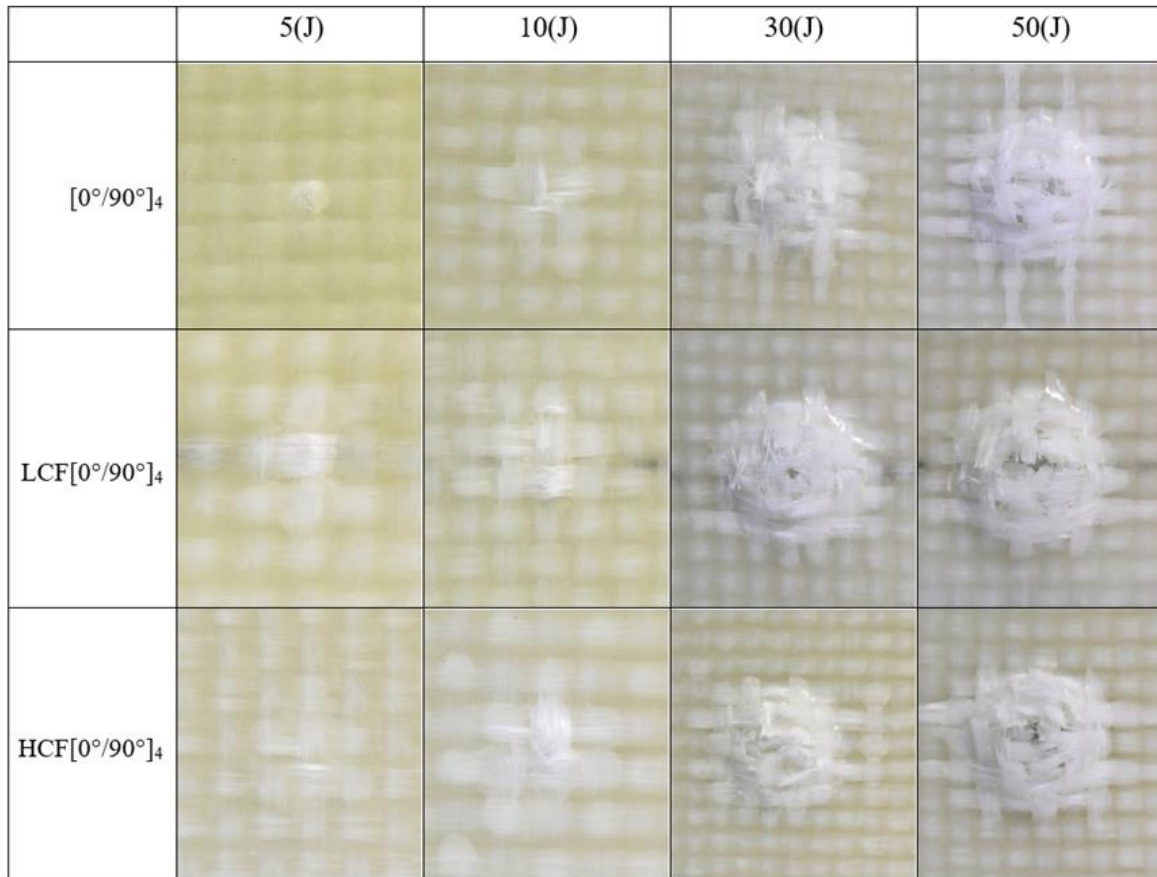
Fig. 4-11. Illustrations of damage occurred on the back face of impacted specimens for the non-aged and aged GFRE[0°/90°]₄ at impact energies of 5 J, 10 J, 30 J and 50 J.

The difference in damage that exists between the [0°/90°]₄ and [45°/45°]₄ orientations is that the two systems do not have the same glass fibers weight fractions. These observations are confirmed by the tomographic analyses performed on the specimens of [45°/45°]₄ and [0°/90°]₄ orientations, which were subjected to fatigue aging (Figures 4-12 and 4-13). An appearance of the fatigue streaks, and the severe damage that results from them, show that the matrix cracking and delamination generated during fatigue were in fact the main causes of the severely damaged areas formation.

Figure 4-12 shows intralaminar (Figure 4-12 (b), (c), (d)) and interlaminar damages (Figure 4-12 (e), (f)) in the woven fabric composite with the warps and wefts oriented with an angle of 45 degree with respect to the force direction after fatigue loading and subsequent impact. There are clearly visible some cracks in the selected yarn (weft), as well as delamination between the adjacent layers. The cracks in the warps and wefts were induced due to LCF or HCF loadings, leading to the softening of the whole structure of the composite. In

consequence, the stiffness and impact resistance were affected. Such observations are in agreement with the SEM inspections presented in the previous study of damage induced by tensile fatigue loading in composites reinforced with the glass plain-woven fabrics [37].
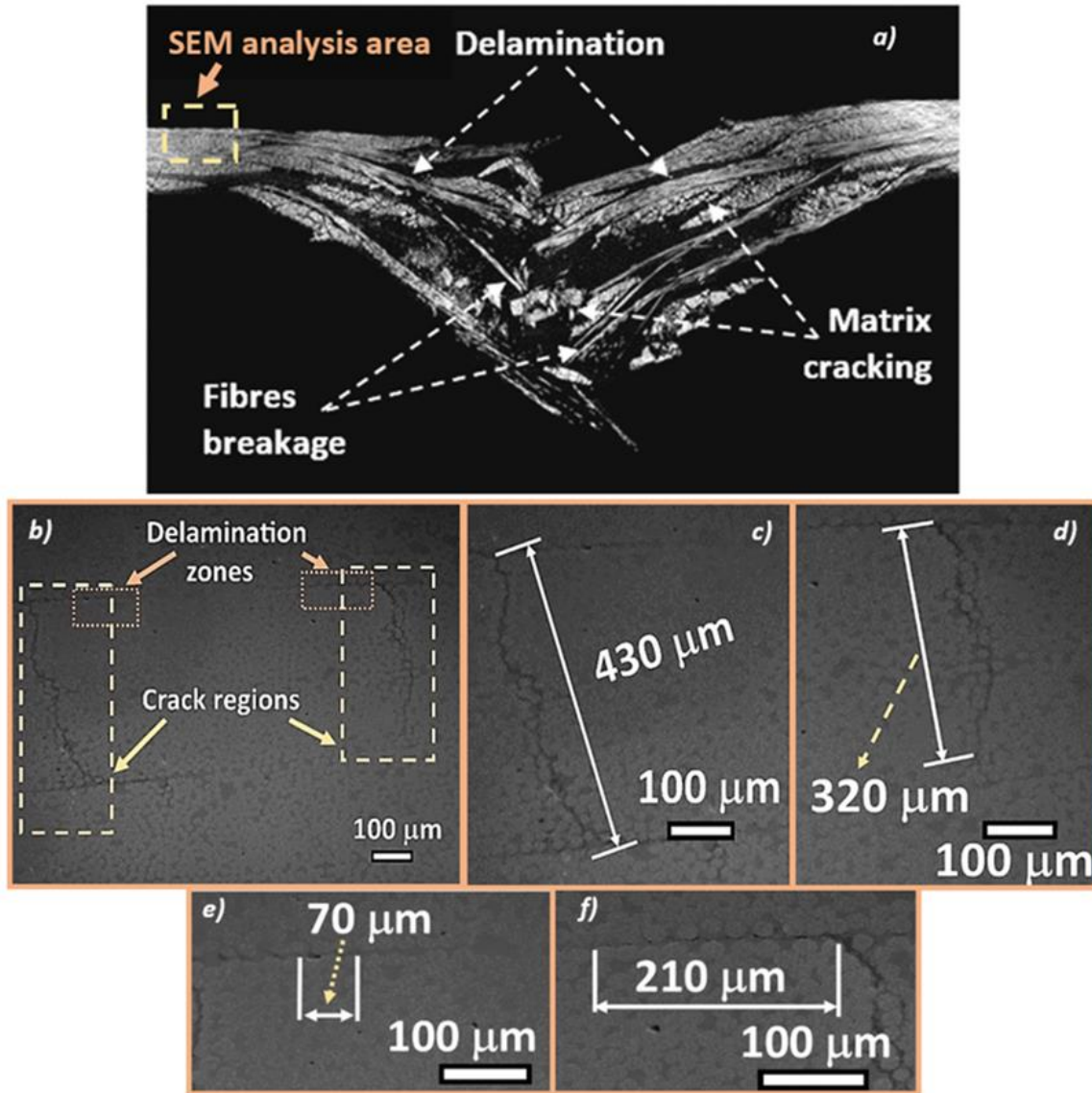
Fig. 4-12. Microtomographic and SEM analysis of the aged GFRE [45°/45°]₄, impacted at 30J for: (a) general view; (b, c, d) intralaminar defects; (e, f) interlaminar debonding.

A comparison between the non-aged and aged plates impacted at energy equal to 50 J is presented in Figure 4-13. The microtomography analysis showed that the area of matrix cracks of the non-aged laminate is smaller than that for the aged laminate plate observed. The results confirmed that the cyclic loading (aging) of the laminated composite leads to the decohesion of the fibers/matrix interface and promotes a generation of the severe delamination and matrix cracking when both tested composite laminates are impacted.
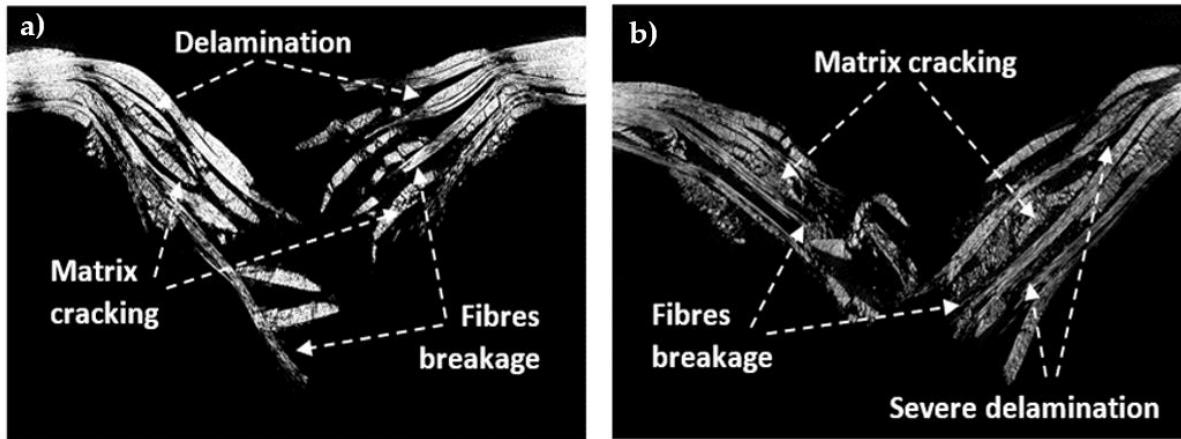
Fig. 4-13. Microtomographic analysis of the impacted GFRE [0°/90°]$_4$ at 50 J for: (a) non-aged and (b) aged composites.

4.3 Numerical simulation of low velocity impact for thin woven GFRE plates

Woven laminated composites can be analysed at three levels: microscopic, mesoscopic and macroscopic scale. It is commonly accepted that at crack initiation the major contribution is given by matrix toughness, while the difference between fracture toughness at initiation and propagation stages can be determined by the fiber bridging mechanism, which is present only during propagation [17]. Therefore, many different approaches based on the finite element method (FEM) have been proposed in the literature to simulate successfully laminate impact resistance behaviour either under quasi-static or dynamic conditions [5,6,54,123-125]. Depending on the failure mechanisms that need to be captured, the failure criteria can be two- or three-dimensional. 2D models ignore the out-of-plane effects. However, they can provide particularly good and efficient predictions, especially for low thickness laminates [64,126-127]. In turn, 3D models do not have such limitations and take into account both in-plane and out-of-plane effects. Gower et al. [128] used numerical simulations to calibrate properties such as the out-of-plane failure shear stresses. Iannucci et al. [129] developed a 3D model which introduces damage variables responsible for fiber failure in tension and compression (in-plane), and moreover, enabling analysis of the interlaminar failure leading to delamination. García-Castillo et al. [124] carried out finite element simulations on the fabric reinforced composites applying a modified Hou's criteria. Kinvi-Dossou et al. [54] proposed a meso-heterogeneous model which take into account both in-plane and out-of-plane failure modes, modifying Hashin's failure criteria. The

authors took into account influence of an effect of strain rate and temperature on the cohesive layer during the impact. All the models mentioned above show the importance of stress states analysis at out-of-plane compression or out-of-plane shear stresses for example.

In this thesis, the numerical simulations of low and high velocity impact response of plain-woven glass laminated composites were conducted at the macroscopic scale and compared with the experimental results. The macroscopic modelling approach is based on the mechanics of continuous damage to describe the intra and inter-laminar degradation occurring in the composite layers. The proposed 3D model is implemented in an explicit FEM framework for Abaqus/Explicit by a VUMAT material user-subroutine. The model consists of four layers of the glass fiber/Elium acrylic woven which represent the laminate as a homogeneous material. The phenomenon of damage, both in-plane and out-of-plane failure modes is simulated using a modified Hashin's failure criteria [54]. Usually, the laminates that contain more brittle matrices are able to transfer all their toughness into the composite while, in the case of more ductile matrices only a fraction of matrix toughness actually contributes to fracture resistance in the composite [17]. Therefore, in order to reflects delamination of layers of the glass fiber/Elium acrylic woven, thin layers of the cohesive zone (pure Elium) were introduced between the woven plies, Figure.4-14. It enables to describe the inelastic behaviour of the acrylic matrix. It should be noted that the model is based on the assumptions for the fibers that should be perfectly aligned with respect to the yarns of the warp and weft, and additionally, their undulation is neglected.
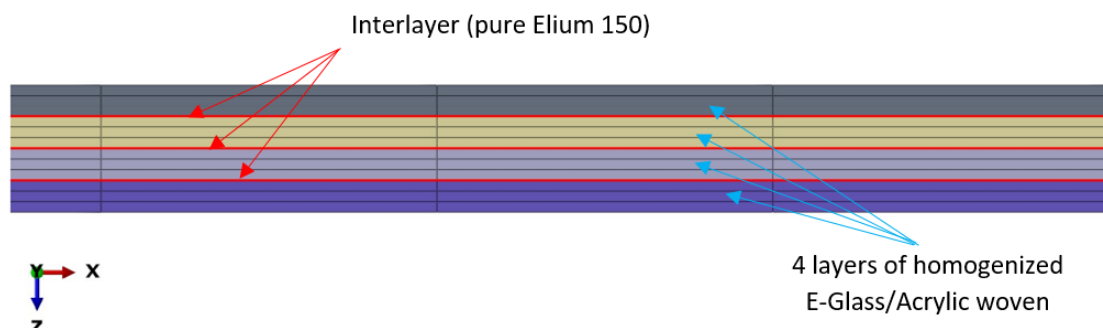
Fig. 4-14. Geometry of the laminated composite - view from its thickness side.

4.3.1 Failure criteria of reinforcing and cohesive layers

In order to reduce the number of elements of the numerical model, a material was replaced by a homogeneous equivalent of the same properties, Fig. 4-14. The elastic properties of the non-aged GFRE[0°/90°]$_4$ obtained from experimental tests on macroscopic specimens (Chapter 2.2) are summarized in Table 4-3.

Table 4-3. Elastic properties of the GFRE[0°/90°]$_4$.

Young's modulus along fiber direction: $E_{11} = E_{22}$ (GPa)	27.4
Young's modulus in the transversal direction: E_{33} (GPa)	13.9
In-plane shear modulus: G_{12} (GPa)	8.5
Out of plane shear modulus: $G_{13} = G_{23}$ (GPa)	6.4
Poisson's ratio: ν_{12}	0.192
Poisson's ratio: $\nu_{13} = \nu_{23}$	0.315

The quasi-isotropic behaviour of the laminate is based on six independent constants which formulate the following stiffness tensor:

$$\begin{pmatrix} \sigma_{11} \\ \sigma_{22} \\ \sigma_{33} \\ \sigma_{12} \\ \sigma_{31} \\ \sigma_{23} \end{pmatrix} = \begin{bmatrix} C_{11}^0 & C_{12}^0 & C_{13}^0 & & & \\ C_{12}^0 & C_{22}^0 & C_{23}^0 & & 0 & \\ C_{13}^0 & C_{23}^0 & C_{33}^0 & & & \\ & & & G_{12} & 0 & 0 \\ & 0 & & 0 & G_{31} & 0 \\ & & & 0 & 0 & G_{23} \end{bmatrix} \begin{pmatrix} \varepsilon_{11} \\ \varepsilon_{22} \\ \varepsilon_{33} \\ 2\varepsilon_{12} \\ 2\varepsilon_{31} \\ 2\varepsilon_{23} \end{pmatrix} \quad (4\text{-}1)$$

where:

$$C_{11}^0 = E_{11}^0 (1 - \nu_{23}\nu_{32})\Gamma$$
$$C_{22}^0 = E_{22}^0 (1 - \nu_{13}\nu_{31})\Gamma$$
$$C_{33}^0 = E_{33}^0 (1 - \nu_{12}\nu_{21})\Gamma$$
$$C_{12}^0 = E_{11}^0 (\nu_{21} + \nu_{31}\nu_{23})\Gamma \quad (4\text{-}2)$$
$$C_{13}^0 = E_{11}^0 (\nu_{31} + \nu_{21}\nu_{32})\Gamma$$
$$C_{23}^0 = E_{22}^0 (\nu_{32} + \nu_{12}\nu_{31})\Gamma$$
$$\Gamma = 1/(1 - \nu_{12}\nu_{21} - \nu_{31}\nu_{13} - \nu_{23}\nu_{32} - 2\nu_{21}\nu_{32}\nu_{13})$$

and C_{ij}^0 are initial stiffness matrix components calculated using the engineering constants obtained from the experiment of the undamaged laminated composite.

In order to predict the intralaminar damage of each individual ply, the failure criterion of Hashin [60] modified by Puck [63] (for the matrix) was chosen. The damage model is based on the degradation of elastic properties of the homogenized layers. To simulate damage in the plain weave fabric the failure criterion takes into account six damage variable including two for warp, and two for weft, and the other two for the matrix:

warp in tension

$$(\sigma_{11} \geq 0): \quad d_{f+} = \left(\frac{\sigma_{11}}{X_+}\right)^2 + \alpha\left(\frac{\sigma_{12}}{S_{12}}\right)^2 + \beta\left(\frac{\sigma_{13}}{S_{13}}\right)^2 = 1 \qquad (4\text{-}3)$$

warp in compression

$$(\sigma_{11} \leq 0): \quad d_{f-} = \left(\frac{\sigma_{11}}{X_-}\right)^2 = 1 \qquad (4\text{-}4)$$

weft in tension

$$(\sigma_{22} \geq 0): \quad d_{f+} = \left(\frac{\sigma_{22}}{Y_+}\right)^2 + \alpha\left(\frac{\sigma_{12}}{S_{12}}\right)^2 + \beta\left(\frac{\sigma_{23}}{S_{23}}\right)^2 = 1 \qquad (4\text{-}5)$$

weft in compression

$$(\sigma_{22} \leq 0): \quad d_{f-} = \left(\frac{\sigma_{22}}{Y_-}\right)^2 = 1 \qquad (4\text{-}6)$$

and for the matrix

$$d_m = \left(\frac{\sigma_{11}}{2X_+}\right)^2 + \left(\frac{\sigma_{22}+\sigma_{33}}{Y_+Y_-}\right)^2 + \left(\frac{\sigma_{12}}{S_{12}}\right)^2 + (\sigma_{22} + \sigma_{33})\left(\frac{1}{Y_+} + \frac{1}{Y_-}\right) = 1 \qquad (4\text{-}7)$$

where $d_m = d_{m+}$ in tension ($\sigma_{22} + \sigma_{33} \geq 0$) and $d_m = d_{m-}$ in compression ($\sigma_{22} + \sigma_{33} < 0$).

In equations (4-3) - (4-7):

α and β are coefficients related to shear contribution (respectively in the planes (1; 2) and (1; 3)) to fiber damage initiation in tension. The fibers are assumed to be uniaxially oriented along direction 1 (warp).

$X_{(+/-)}$ are tensile and compressive failure strength in longitudinal direction – warp (0°), respectively,

$Y_{(+/-)}$ are respectively maximum tensile and compressive stress in transverse direction – weft (90°),

S_{12} and S_{23} = S_{13} are shear failure strength for in-plane and out-of-plane direction, respectively.

The values of listed parameters were determined through the experimental tests and presented in Tables 2-4 and 2-6 (Chapter 2).

The global damage variables d_m and d_f, respectively for the matrix and fibers (warp and weft) are defined in the following way:

$$d_m = 1 - (1 - d_{m+})(1 - d_{m-})$$
$$d_f = 1 - (1 - d_{f+})(1 - d_{f-})$$

(4-8)

They are responsible for the failure modes which were implemented in Abaqus/Explicit software as a user subroutine VUMAT in order to carried out the simulation. Algorithm of the numerical procedure to solve elastic case is shown in Figure 4-15.
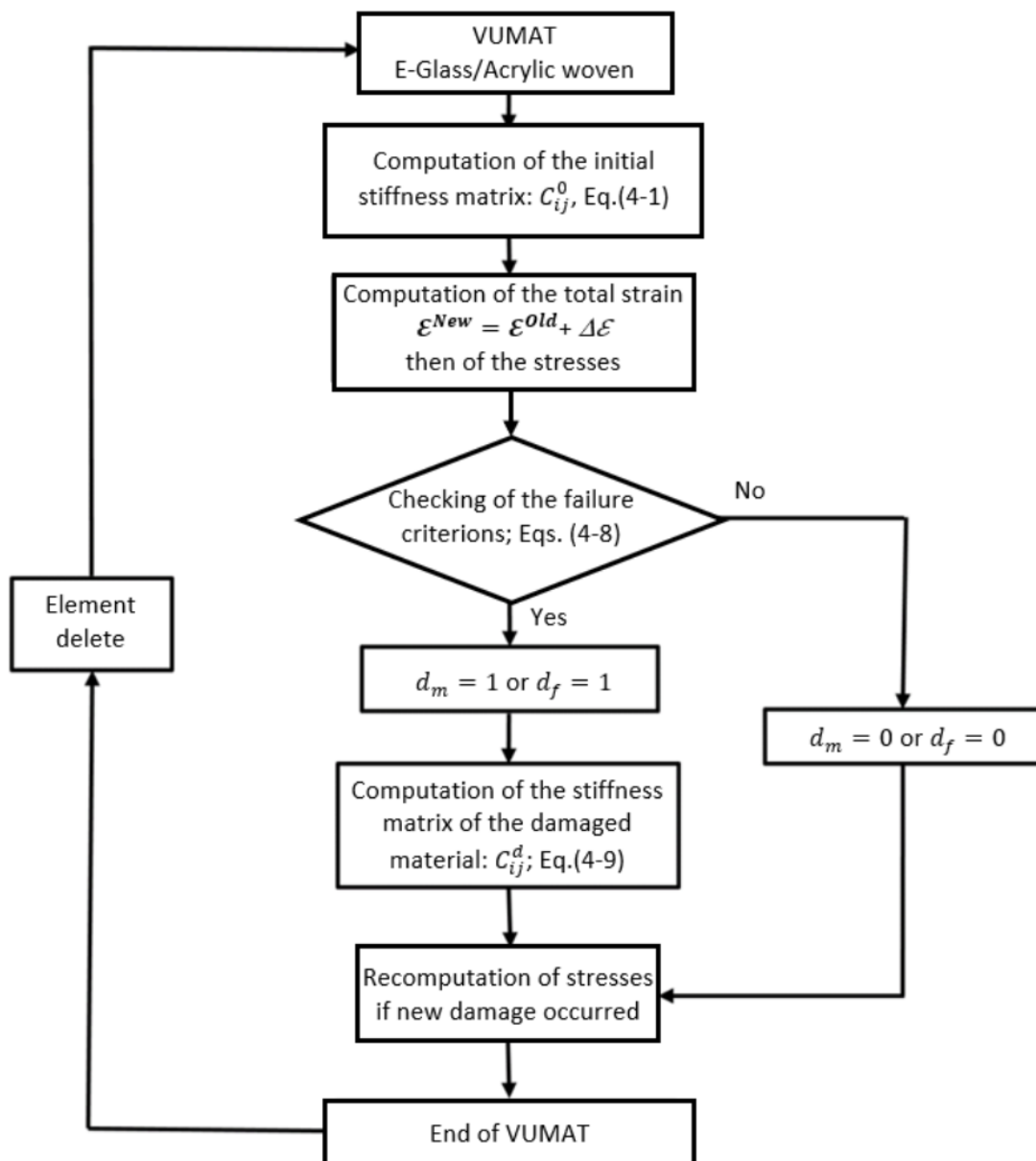
Fig. 4-15. Scheme of the numerical procedure to reflect elastic behaviour of GFRE $[0°/90°]_4$ individual plies.

A scheme indicates that failure initiates when any of the presented damage variables (Eqs. (4-3) - (4-7)) reached value of 1. This condition leads to the reduction of the stiffness, which can be represented as:

$$
\begin{pmatrix} \sigma_{11} \\ \sigma_{22} \\ \sigma_{33} \\ \sigma_{12} \\ \sigma_{31} \\ \sigma_{23} \end{pmatrix} = \begin{bmatrix} C_{11}^d & C_{12}^d & C_{13}^d & & & \\ C_{12}^d & C_{22}^d & C_{23}^d & & 0 & \\ C_{13}^d & C_{23}^d & C_{33}^d & & & \\ & & & C_{44}^d & 0 & 0 \\ & 0 & & 0 & C_{55}^d & 0 \\ & & & 0 & 0 & C_{66}^d \end{bmatrix} \begin{pmatrix} \varepsilon_{11} \\ \varepsilon_{22} \\ \varepsilon_{33} \\ \varepsilon_{12} \\ \varepsilon_{31} \\ \varepsilon_{23} \end{pmatrix}
$$

(4-9)

where:

$$C_{11}^d = (1 - d_f)C_{11}^0$$

$$C_{22}^d = (1 - d_f)(1 - d_m)C_{22}^0$$

$$C_{33}^d = (1 - d_f)(1 - d_m)C_{33}^0$$

$$C_{12}^d = (1 - d_f)(1 - d_m)C_{12}^0$$

$$C_{13}^d = (1 - d_f)(1 - d_m)C_{13}^0$$

$$C_{23}^d = (1 - d_f)(1 - d_m)C_{23}^0$$

$$C_{44}^d = 2(1 - d_f)(1 - S_{m+} d_{m+})(1 - S_{m-} d_{m-})G_{12}$$

$$C_{55}^d = 2(1 - d_f)(1 - S_{m+} d_{m+})(1 - S_{m-} d_{m-})G_{13}$$

$$C_{66}^d = 2(1 - d_f)(1 - S_{m+} d_{m+})(1 - S_{m-} d_{m-})G_{23}$$

(4-10)

$S_{m(+/-)}$ is a factor that controls the shear modulus loss caused by matrix failure in tension or compression. Empirically [130], these parameters are set as S_{m+}= 0.8 and S_{m-}= 0.5. A variable is introduced to facilitate elimination of elements from the stiffness matrix if their values become to be 0.

Usually, delamination between layers is simulated using a cohesive zone method. In some papers the behaviour of the cohesive element used in simulation is controlled by a traction-separation law as described by [131]. Therefore, this method was initially applied to simulate the behaviour of the cohesive layer in the laminated composite tested. However, despite many trials the characteristics of the impacted force vs time were inconsistent with the results of experiment. In order to describe more properly the inelastic behaviour of the acrylic matrix and correlate the fracture initiation either in simulation or experiment - a continuum damage law was applied. The fracture strain at damage initiation was chosen

empirically, and its value for the impact energies from 10 J to 50 J was equal to 0.08. In the same way, the initial displacement of 1.5 mm was determined for the description of failure evolution related to the damage propagation stage. Such solution enabled to provide a good agreement between the experimental force-time characteristic and its numerical prediction.

4.3.2 Numerical model

The experimental setup used for low impact velocity tests (see Figure 4-1) were applied for the modeling. A laminated composite consisted of four homogeneous layers of GFRE[0°/90°]₄ identically oriented. The plies with dimensions of 100 mm × 100 mm × 1.8 mm were placed perpendicularly to the axis of the impactor, Figure 4-16. Between the plies, the cohesive zones of the same lateral dimension and thickness (0.001 mm) were introduced (see Figure 4-14).
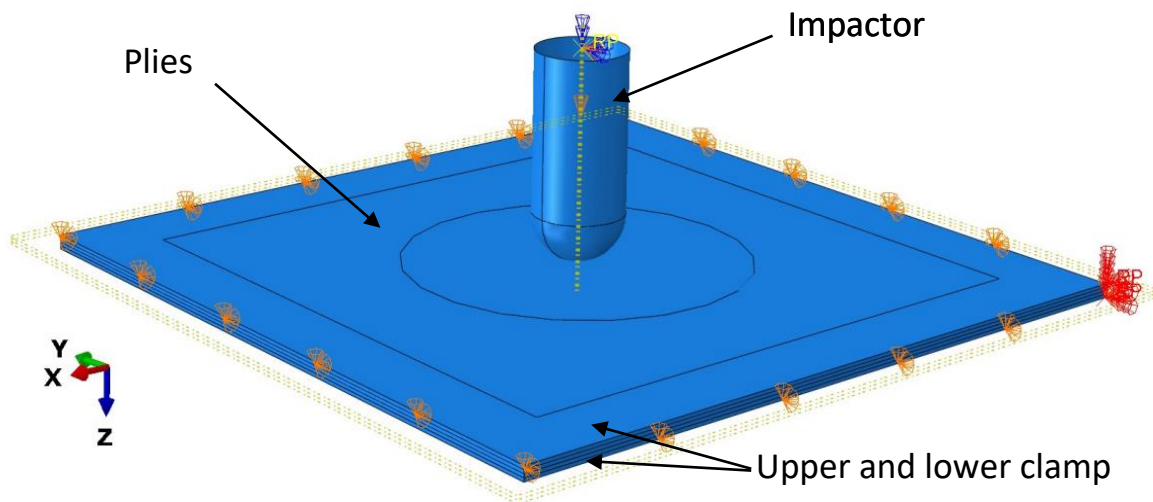
Fig. 4-16. General view of the macroscopic model: setup and boundary conditions.

The impactor has a mass equal to 5.762 kg and the diameter of 16 mm. The projectile, bottom and upper support are treated as the rigid bodies. The mesh was divided into two regions. A finer mesh was located in the central zone and cover area of diameter equal 50 mm with elements of size 0.5 mm. Reduced integration solid elements were used (Abaqus C3D8R) to simulate the plies. In turn, the cohesive zones with a thickness of 0.001 mm placed between plies were meshed with cohesive elements (Abaqus COH3D8). Impact

energy levels equal to 10 J, 30 J and 50 J were applied during impact tests. Numerical simulations were performed for a time period of 12 ms on the computer with 24 cores (in parallel on Intel(R) Xeon(R) Gold 6136 CPU, 2 × 3.00 GHz and 128 GB RAM). Due to high complexity of the geometry modelled, only small finite elements were chosen. They enable to generate stable time increment of 10^{-9} s^{-1}.

4.3.3 Macroscopic response to the low velocity impacts - results and discussion

Figure 4-17 shows a comparison of the results obtained numerically for impact energy equal to 10 J and 30 J with the experimental data presented in section 4.2.1 of this chapter.
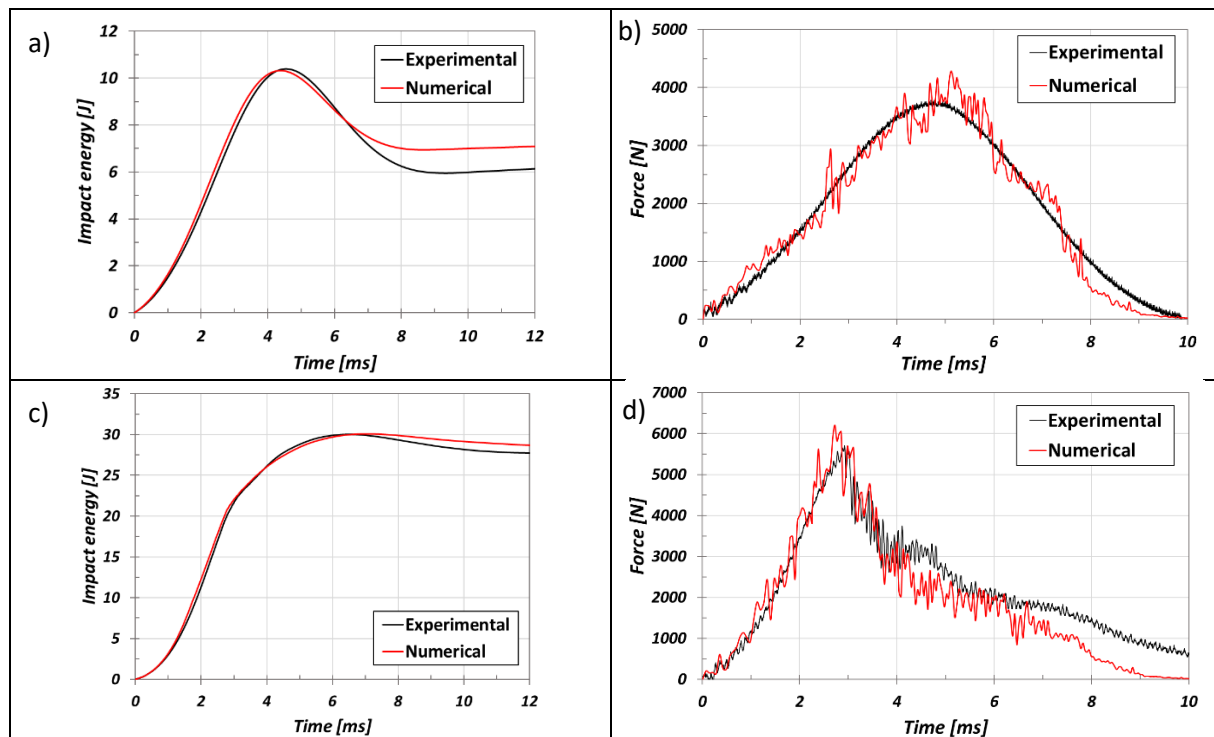
Fig. 4-17. Energy and force evolution for the acrylic laminated composites for the impact energy of: 10 J (a)–(b), 30 J (c)–(d).

One can notice the same tendency either for the experimental data or numerical predictions. However, it is worth noting a little overestimation of the critical force during numerical simulations. In both cases (10 J and 30 J) it is about 10% higher than that in the experiments obtained. Moreover, the force drops more rapidly in the numerical model. This could be related to the loss of stiffness due to damage development. A certain scatter can be

observed between experimental and numerical results presenting energy variations (Fig. 4-17. (a) and (c)).

Figure 4-18 shows a distribution of the displacement values around the impactor. One can notice that the displacement is equal to zero at the fixed nodes and significantly increases in the impacted zone.
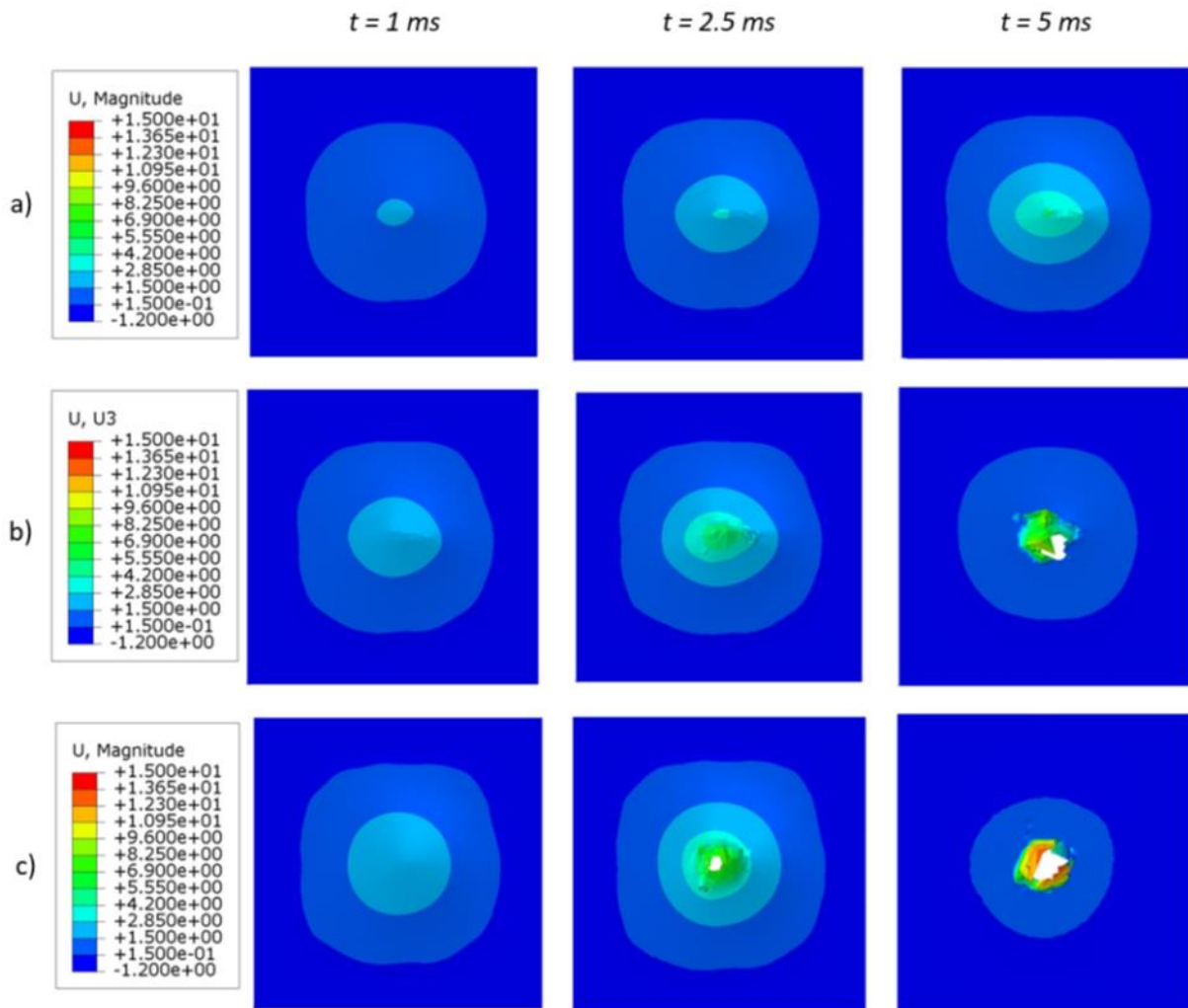
Fig. 4-18. Maps of displacement distribution profiles during impact for energy equal to: 10J (a), 30 J (b), and 50 J (c).

At 30 J and t = 5 ms, a partial penetration of the plate can be observed (see Figure 4-18 (b)). Damage appears to be slightly larger than that shown in Fig. 4-11, during real experiment. In turn, at 50 J and for t = 5 ms, a total penetration of the plate was obtained. It is easy to

noticed that perforation occurred at $t = 2.5\ ms$. It corresponds to the sudden drop of force, clearly shown in Figure 4-19 (b) and (c).
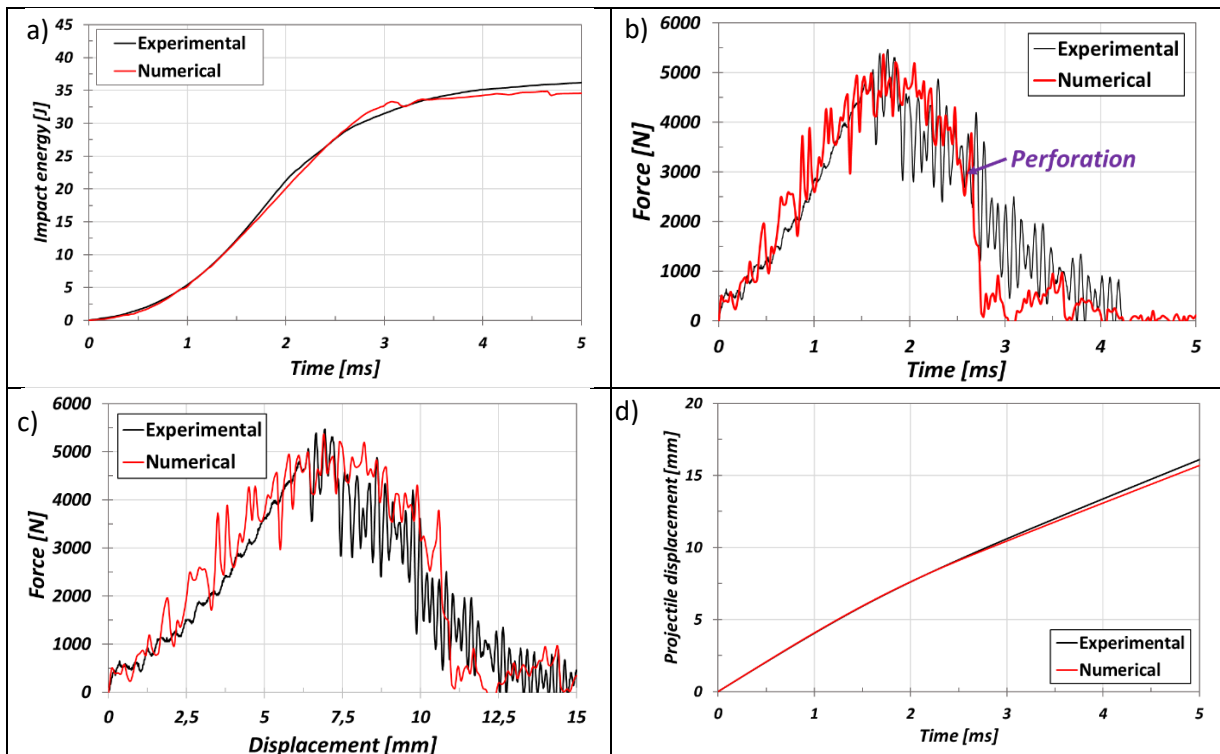
Fig. 4-19. Comparison of the results for impact energy of 50 J. (a) Energy-time, (b) Force-time, (c) Force-displacement and (d) Displacement-time.

The maximum force in the experiment and simulation remained at the same level. However, its value in the simulation after exceeding the maximum peek drops more significantly than in the test. This may result from the fact that, the deleted elements in the model no longer contributed to the stiffness of the composite plate tested, or from the friction conditions between the plate and impactor. The values of energy and force shown in Figures 4-17 and 4-19 were overestimated or underestimated. It might be the result of the fact that all the simulations were carried out by considering the same values of limits at failure. Since the strain rate is not the same for the analyzed impact energies, some errors would be introduced into the numerical results.

4.4 Conclusions

The low velocity impact tests at the range of energy levels were conducted on the aged and non-aged glass fiber/acrylic specimens for two fiber orientations of the laminated composites. The force-displacement and energy-time responses were analysed for both materials. The non-aged specimens impacted at energy of 5 J, 10 J and 30 J were not perforated and exhibited a great ability to rebound the impactor. The composites subjected

to fatigue aging demonstrated the greatest decrease of the initial slope in the force-displacement diagrams. It results from the significant reduction of stiffness due to the matrix cracking and interface debonding taking place between the fibers and matrix. The maximum force reduction for tests carried out at the impact energy of 50 J for GFRE $[0°/90°]_4$ and GFRE $[45°/45°]_4$ was equal to 11% and 19%, respectively.

Analysis of the absorbed energy during impact tests, confirmed that the aged materials containing the woven fabric oriented at the angle of 45° exhibited the weakest impact resistance. Therefore, it can be concluded that the fibers orientation, fatigue aging, and glass fibers concentration significantly affect the elastic properties and lead to a decrease of the stiffness reduction and increase of the energy absorbed. These results represent novel and original value of this work since so far, no data exist on impact tests performed on the aged Elium laminates. These results are in agreement with the analyses of damage phenomena. The acrylic matrix allows energy to be dissipated by plastic deformation. The flexibility of the composite based on acrylic resin is linked to the fact that its molecular chains are long but chemically separated, which is particularly visible for the specimens with the fibers oriented with an angle of 45 degree (richer in resin).

In this part of the study the macroscopic modelling approach was applied. In order to simulate the low impact velocity behaviour of the glass fiber/acrylic laminates, the modified 3D Hashin's criteria were applied. The developed three-dimensional intralaminar damage model based on the computational algorithm, that was successful in predicting damage character of the materials in question. Impact responses of the laminates subjected to impact energy equal to 10 J, 30 J and 50 J, were quantified using the approach developed for predicting intralaminar damage. The matrix cracking features and delamination are discussed. A negligible small difference was observed between the slope of the numerical and experimental characteristics and the levels of energy absorbed. However, when using the proposed model, it was clearly observed, that the maximum displacement was very similar to those captured in experiments.

Chapter 5. Dynamic behaviour of glass fibers/Elium acrylic laminated composites subjected to perforation

The previous chapter was devoted to the analysis of the impact properties for the aged and non-aged GFRE subjected to the low impact velocity with its maximum value of 4.16 m/s. The main purpose of this chapter was to evaluate the high velocity impact resistance of the same laminated composites. Therefore, impacts on GFRE $[0°/90°]_4$ and GFRE $[45°/45°]_4$ specimens were carried out to estimate the ballistic limit and energy absorption. Thus, an experimental work was performed in order to evaluate the effect of damage due to fatigue aging on the process of perforation of the thin laminated composite plates using a hemispherical projectile. Numerical analysis of ballistic behaviour of the non-aged plates with the $[0°/90°]_4$ fiber orientation was also carried out. To predict the performance of laminates under high-velocity impacts, the same model as that proposed in section 4.3 was applied.

5.1 High-velocity impact resistance of the glass woven fabric laminated composites

The main disadvantage of the fiber reinforced polymer matrix composites is their poor impact resistance. They are susceptible to failure in the form of delamination when subjected to impact loading. Damage of metals due to impact is easily detected as it starts at the impacted surface; however, damage in composites often begins on the non-impacted surface or in the form of an internal delamination. The behaviour of fiber reinforced composites when impacted by a solid object has been investigated by many research teams either experimentally or numerically. The penetration and perforation of targets by the projectile involve highly complex processes, which have been investigated experimentally for more than two last decades [132,133].

Fiber reinforced laminates are particularly important for armour applications. There are many types of fibers. Glass fibers are especially popular nowadays, even much often used than the kevlar, because of its high cost [134]. Cantwell and Morton [135] studied the influence of projectile mass on CFRP laminates under low and high velocity impact. They found, that the low velocity impact leads to global deformation, whereas the high velocity impact results in a localized deformation. Fatt and Lin [136] studied the perforation of

woven E-glass polyester panels. They proposed the analytical solutions to predict deformation and damage of fully clamped, woven E-glass/polyester panels subjected to indentation by a blunt cylindrical indenter, whose radius is small compared to the lateral extent of the panel. The estimated energy absorbed by plate deflection, matrix cracking, delamination and fiber failure, enabled to identify a reduction of the panel bending stiffness, and thus, allowed higher transverse deformations. The analytical predictions of ballistic limit were within 13% of the test data, while the analytical predictions of total energy dissipated at the ballistic limit were within 25% of the test results.

Wen [137] investigated the penetration and perforation of FRP laminates using different shape of projectiles. Analytical equations were developed for predicting the penetration and perforation by projectiles with different nose shapes. It was based on the assumption that the deformation is localized and that the mean pressure offered by the laminate targets to resist the projectiles can be decomposed into two parts. One part is a cohesive quasi-static resistive pressure due to the elastic plastic deformation of the laminate materials. The second part represents a dynamic resistive pressure arising from velocity effects. Zhu et al. [138] studied the response of kevlar/polyester laminate to quasi-static and dynamic penetration by cylindro-conical projectiles. Ballistic limit and terminal velocity were determined.

As described, many researchers have studied high velocity impact properties of the composite target. However, until today the impact resistance of non-aged and aged glass fiber/Elium acrylic woven laminates was not determined.

5.1.1 Specimens and experimental setup

The experimental device consists of a pneumatic gas gun, two laser measuring velocity sensors, target, target holder, and projectile catcher box, Figure 5-1. The projectile incident velocity V_0 can be adjusted by changing the pneumatic gas pressure P_0. The diameter of the gun barrel is 13 mm, and it is roughly equal to the diameter of the projectile. The device is equipped with two velocity sensors: the first one is to measure the initial impact velocity V_0 and the second one is used to measure the velocity of the projectile after perforation allowing to define the residual velocity V_R, Figure 5-2.

During the impact and perforation of polymer targets, there was often plug ejections and debris for all materials tested. In this case the residual velocity sensor can define not only the residual velocity of the projectile V_R, but also the plug velocity. Knowing the projectile length, it is possible to distinguish between the velocity signals due to the projectile displacement from those due to the plug displacement. The residual velocity is mainly affected by the projectile initial impact velocity V_0 and its shape, mechanical properties and thickness of the target.
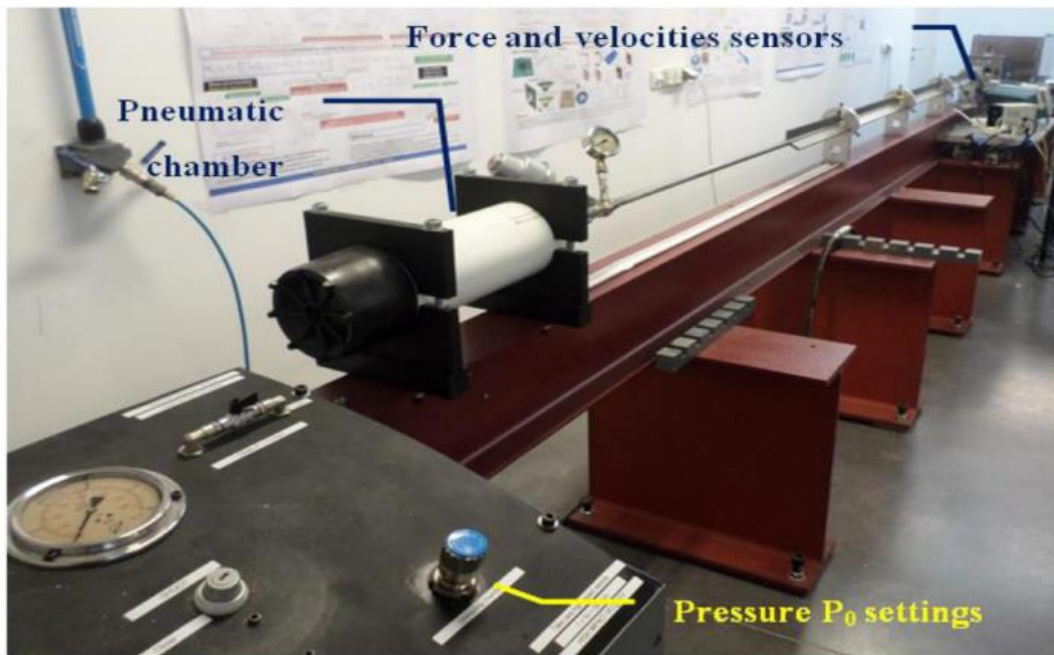
Fig. 5-1. Pneumatic gas gun chamber and control panel to define the initial impact velocity [49].
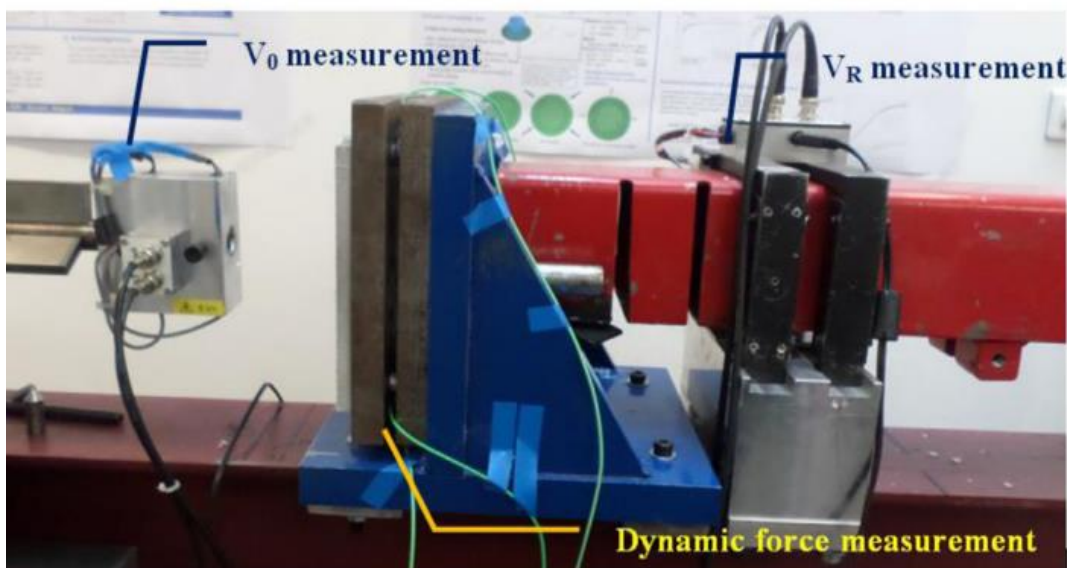
Fig. 5-2. Position of the velocity sensors [49].

Besides of the velocity sensors, the ballistic impact device is equipped with the force measuring system. This system consists of four piezoelectric sensors, Figure 5-3, fixed on the target fixation device in order to measure the global resistance force versus time.
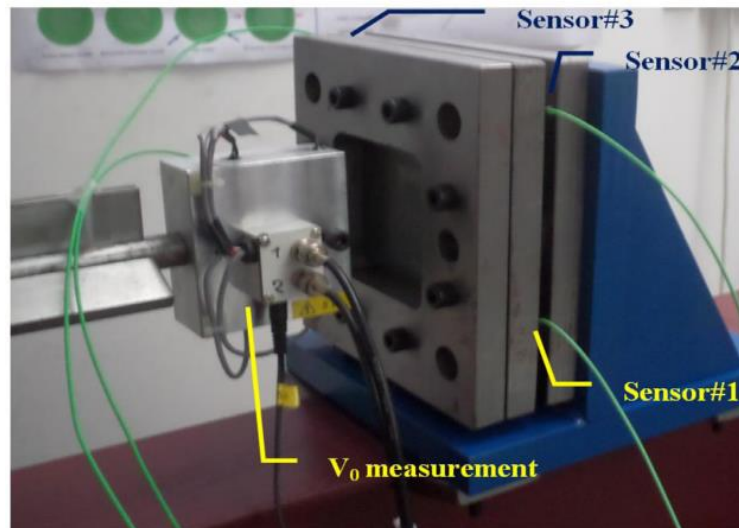
Fig. 5-3. Illustration of the force sensors [49].

The force sensors measure the resistance force induced by the projectile on the target during impact and perforation. Thus, the global instantaneous force can be estimated for each incident velocity V_0. The four sensors are used to measure uniaxial dynamic forces along the impact direction. The four piezoelectric sensors can measure a maximum force of about 20kN.

The projectile for impact tests had a hemispherical shape with a diameter of 12.8 mm, and total mass of 29.1 g, approximately. It was made of Maraging steel subjected to heat treatment enabling the yield stress to be around 2 GPa. Therefore, the projectile had no visible permanent deformation during the penetration. All perforation tests were carried out at room temperature for the impact velocities up to 180 m/s. The polymer plate is a square of 100×100 mm^2. The active part is 80×80 mm^2 with average thickness equal to 1.8 mm.

5.1.2 Influence of fatigue aging on dynamic properties

Using the gas gun testing setup, four series of perforation tests were carried out. The first two were executed on the specimens cut out along the fiber GFRE $[0°/90°]_4$, while the next two tests with a fiber orientation of 45 degree with regard to that of the fibers, GFRE $[45°/45°]_4$. Half of the tested specimens in each mentioned group was prior aged by

cyclic loading with the value of stress below the yield point, while in the rest of them were prior aged due to cycles under stress above the yield point.

In order to analyze the influence of the fatigue aging, the results were compared with the ballistic limit of non-aged impacted specimens. As is shown in Figures 5-4 and 5-5, the experimental ballistic curves are fitted using the Recht and Ipson (1963) model (Eq. 1-10), for GFRE [0°/90°]4 and GFRE [45°/45°]4 plates, respectively.
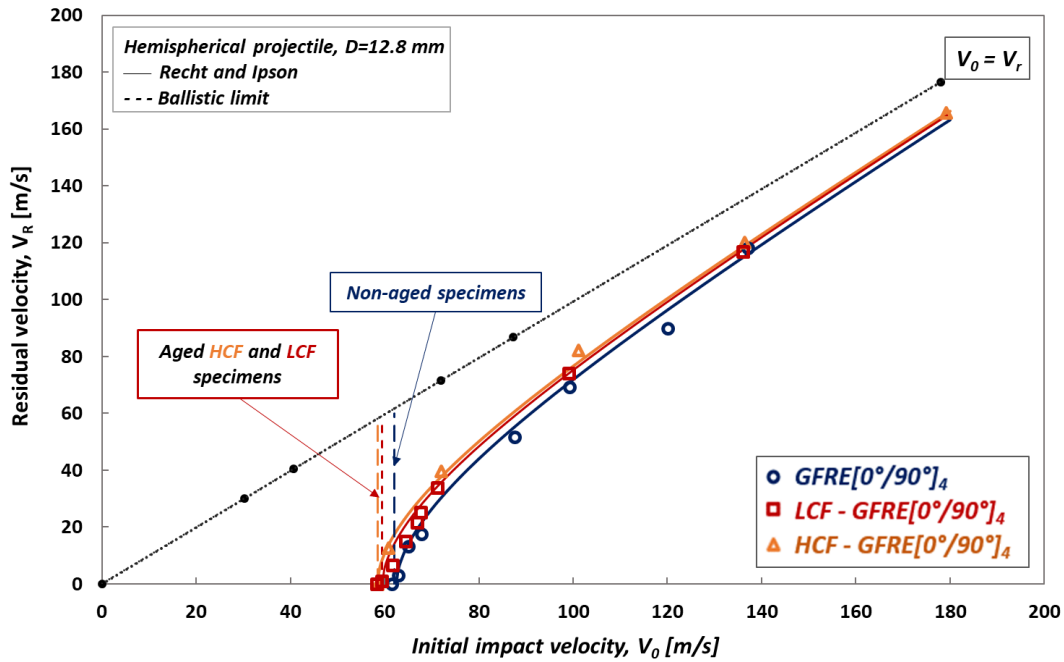
Fig. 5-4. The ballistic impact response of non-aged and aged GFRE[0°/90°]4.
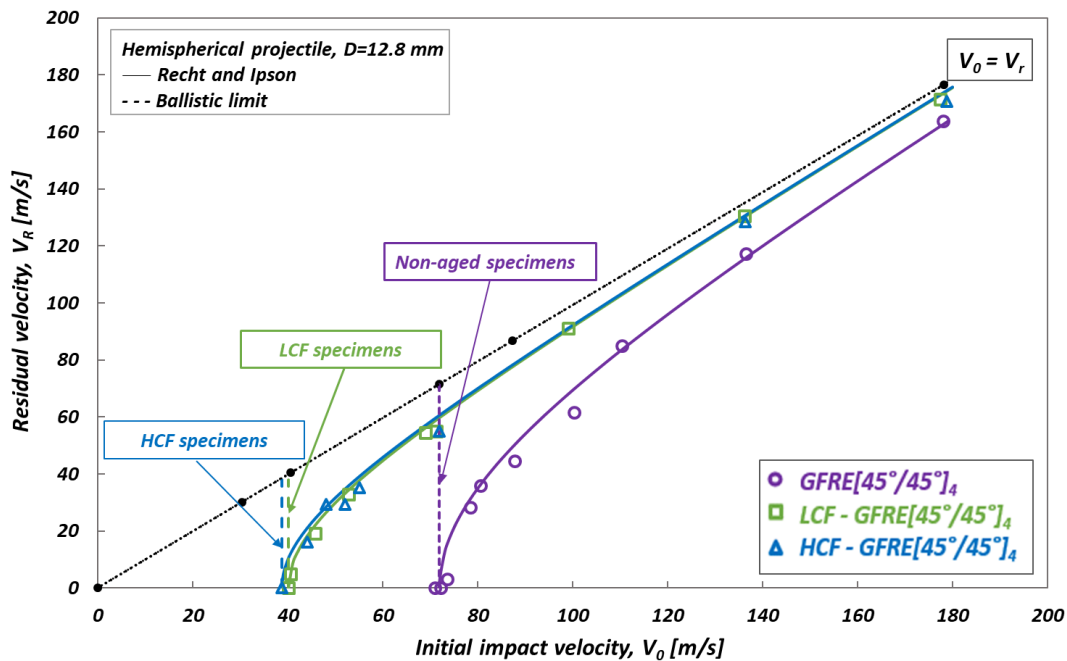
Fig. 5-5. The ballistic curves of non-aged and aged GFRE [45°/45°]4.

It is worth to notice that the ballistic limit for non-aged GFRE [45°/45°]$_4$ specimens was about 8.4 m/s higher than that observed for non-aged GFRE [0°/90°]$_4$ specimens. However, comparing to the fatigue aged GFRE [45°/45°]$_4$, the drop of the impact resistance of the aged GFRE [0°/90°]$_4$ was minimal and did not exceed 3.6 m/s. Moreover, it can be observed that specimens aged by cyclic loading - both LCF and HCF - GFRE [45°/45°]$_4$ have 23 m/s lower ballistic limit than that obtained for GFRE [0°/90°]$_4$, and 31 m/s for GFRE [45°/45°]$_4$.
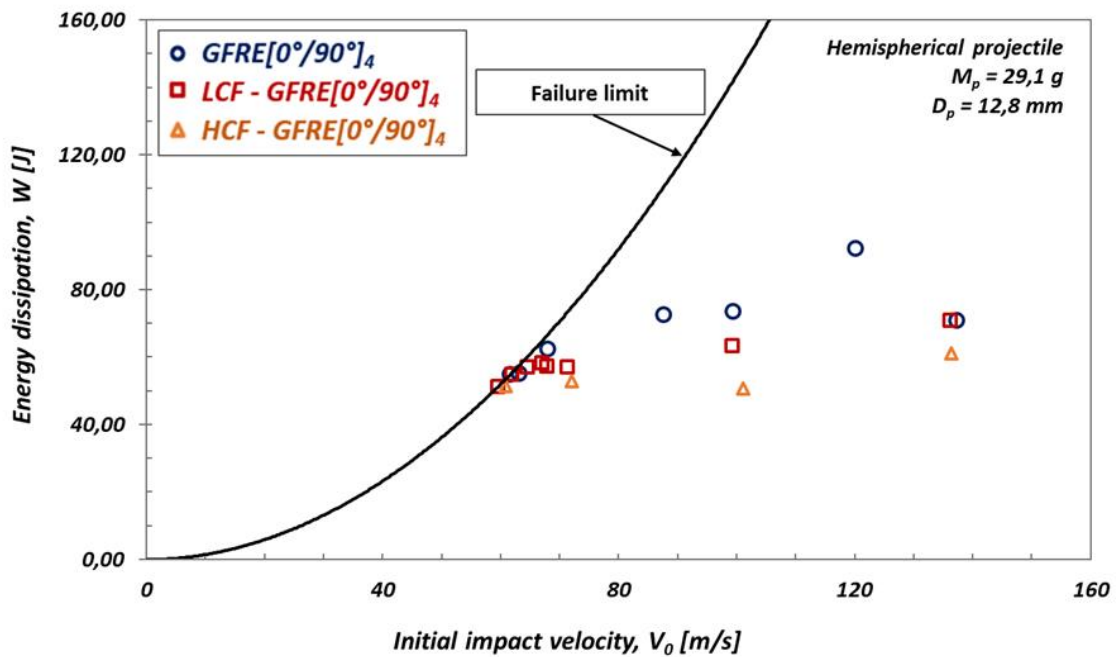
Fig. 5-6. Energy dissipation in 4 layers GFRE [0°/90°]$_4$ targets.
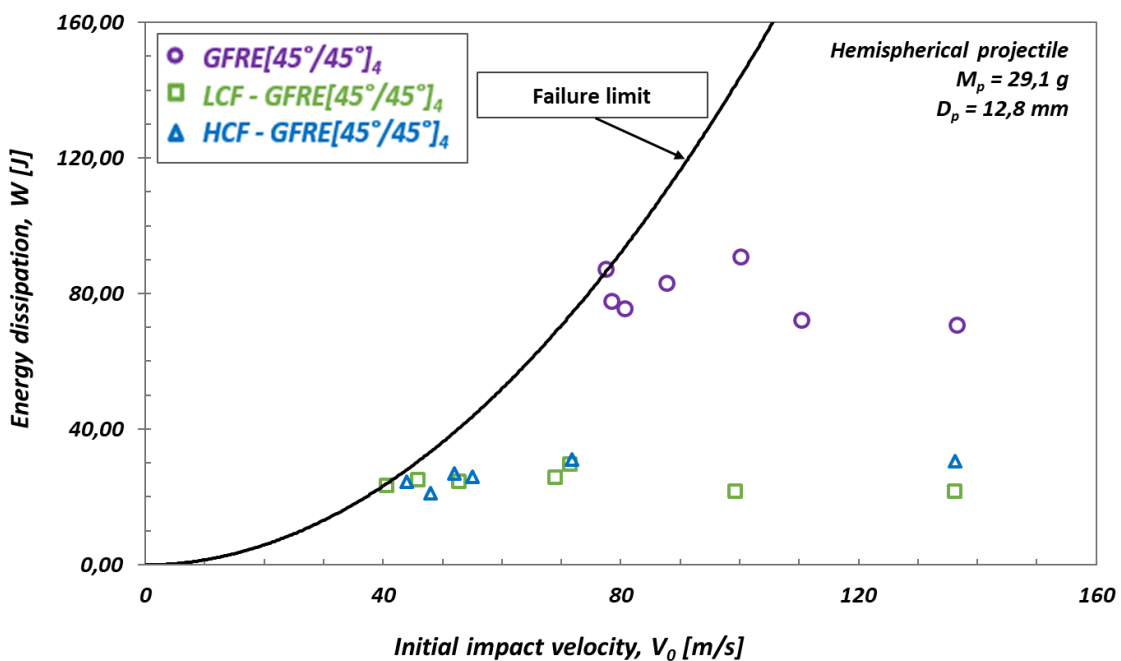
Fig. 5-7. Energy dissipation in 4 layers GFRE [45°/45°]$_4$ targets.

The energy absorbed by the composite targets during perforation at different initial impact velocities was computed using the initial and residual velocities according to Eq. (1-11). Having these results the absorbed energy vs initial impact velocity plots were established for GFRE [0°/90°]$_4$ and GFRE [45°/45°]$_4$, Figures 5-6 and 5-7, respectively. As shown in Figures 5-6 and 5-7, the average energy absorbed by non-aged and aged GFRE [0°/90°]$_4$ is about 78 J, while for non-aged GFRE [45°/45°]$_4$ targets, the energy dissipation reaches 82 J. In turn, the average energy dissipated by aged GFRE [45°/45°]$_4$ targets is only about 30 J, while for the aged GFRE[0°/90°]$_4$ its value is much higher and reach 65 J. The results shown that the GFRE[0°/90°]$_4$ specimens subjected to uniaxial fatigue loading have better ballistic performance and higher energy dissipation than for GFRE [45°/45°]$_4$ targets.

The evolution of force as a function of time was the next mechanical quantity analyzed during ballistic impact tests. The four piezoelectric force sensors were calibrated in the range of 20 kN. Three experiments for each considered groups of laminated composites were performed to confirm the test results repeatability. The relationship between the value of recorded force and impact velocity for all impacted laminates are illustrated in Figure 5-8.
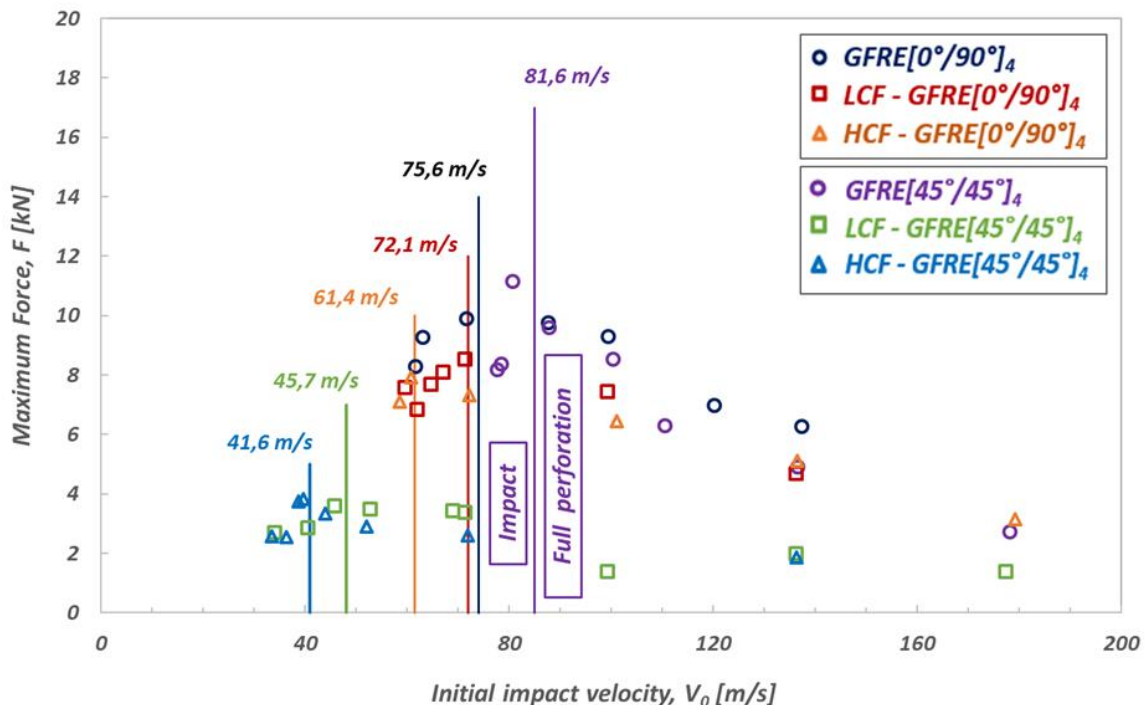
Fig. 5-8. Maximum force evolution versus initial impact velocity for laminates tested.

As it is observed in Figure 5-8, the maximal resistance force, about 12 kN, was obtained for non-aged GFRE [45°/45°]$_4$ plates. In turn, for aged GFRE [45°/45°]$_4$ plates its maximal value

dropped up to 4 kN. The results of tests carried out on the non-aged and aged GFRE [0°/90°]$_4$ laminates do not exhibit such large differences in the measured force as in the case of GFRE [45°/45°]$_4$ plates. The maximum value of the force for the non-aged GFRE [0°/90°]$_4$ laminate was 10 kN and for the aged laminate 8 kN. This observation leads to the conclusion that the decrease of analysed force depends on both factors, fibers direction and stiffness loss due to fatigue. It can be easily noticed, that damage at high impact velocities was characterized by the low force for the projectile velocity close to the ballistic limit. Subsequently, the force reached the peak, and then slowly dropped as the initial impact velocity increased. Such tendency was similar for all tested composites. It resulted from the fracture mechanism typical for the laminated composites subjected to the perforation tests.

5.1.3 Damage analysis of perforated plates

The uniaxial cyclic loading of laminated composites leads to intralaminar and/or interlaminar mechanism of damage. Intralaminar damage is characterized by interface decohesion between the fiber and resin, which leads to matrix cracking. The formation of cracks in the matrix depends on rigidity and strength. Also voids in matrix, and stress concentrations induced by fibers may have influence of this type of damage. Interlaminar damage is characterized by debonding of individual layers of the laminated composite. Their form and size strongly depend on existing geometric diversity of singular plies and their orientations. In order to understand proliferation of the internal changes and characterize the damage phenomenon of perforated specimens for both tested orientations, the external surfaces of GFRE [0°/90°]$_4$ and GFRE [45°/45°]$_4$ were examined.

Figures 5-9 and 5-10 show the back face of the tested plates subjected to high impact velocity, before and after fatigue aging, for the composite laminates oriented at [0° /90°]$_4$ and, [45°/ 45°]$_4$ respectively.

It is easy to notice, that the non-aged composites are least damaged for both orientations of the laminated composites considered. At the critical state (Threshold), the damage was localized mainly in the matrix and took the form of numerous matrix cracks accompanied by small delamination area and fibers breakage.
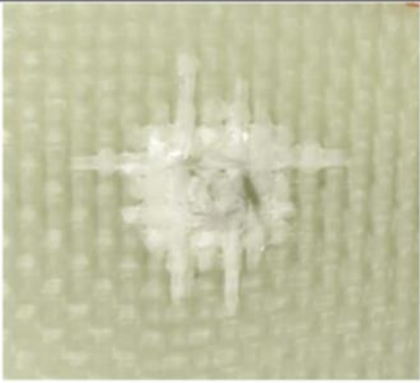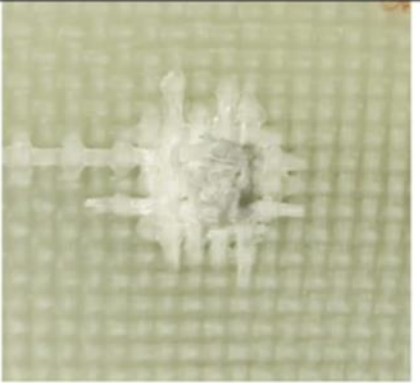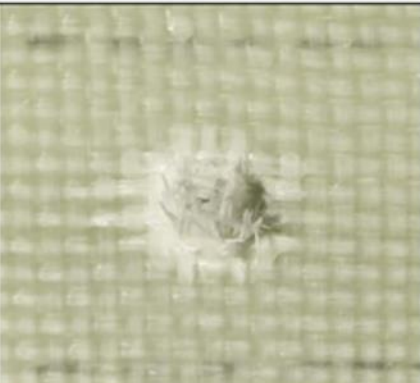
	Critical perforation	Complete perforation
GFRE [0°/90°]₄		
HCF GFRE [0°/90°]₄		
LCF GFRE [0°/90°]₄		

Fig. 5-9. Damage back face view of GFRE [0°/90°]₄ targets perforated at 20 °C.

For tests carried out at high impact velocity, the area of damage increased significantly, thus revealing an occurrence of more severe forms of damages, i.e. delamination and fibers breakage for example. When the composite laminates were subjected to prior fatigue aging, the degree of damage generated by that process underwent further development due to impact introducing more severe forms of damage. One can indicate, that the composites prestressed due to fatigue aging under the stress amplitude below the elastic limit were more damaged than those subjected to the same process, however, under stress amplitudes

higher that the elastic limit. As a consequence, the mechanisms of plastic deformation were activated, which might induce some cavities and contribute to arrest propagation of cracks when the plate is subjected to impact. This effect is more obvious for the GFRE [45°/45°]$_4$ composite laminate.
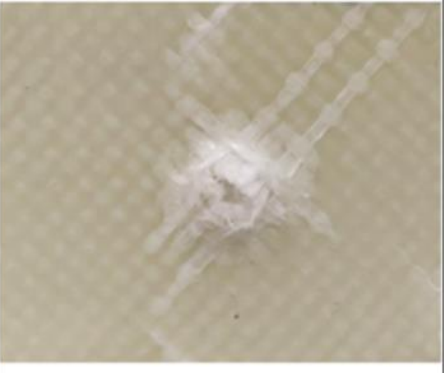
	Critical perforation	Complete perforation
GFRE [45°/45°]$_4$		
HCF GFRE [45°/45°]$_4$		
LCF GFRE [45°/45°]$_4$		

Fig. 5-10. Damage back face view of GFRE[45°/45°]$_4$ plates perforated at 20 ℃.

In Figure 5-11, a comparison between the perforated non-aged and aged plates is presented. The microtomography analysis showed that the area of matrix cracks of the non-aged laminate was smaller than that for the aged laminate plate observed. The results confirmed that the cyclic loading (aging) of the laminated composite leads to the decohesion of the

fibers/matrix interface and promotes a generation of the severe delamination and matrix cracking when both tested composite laminates were impacted.
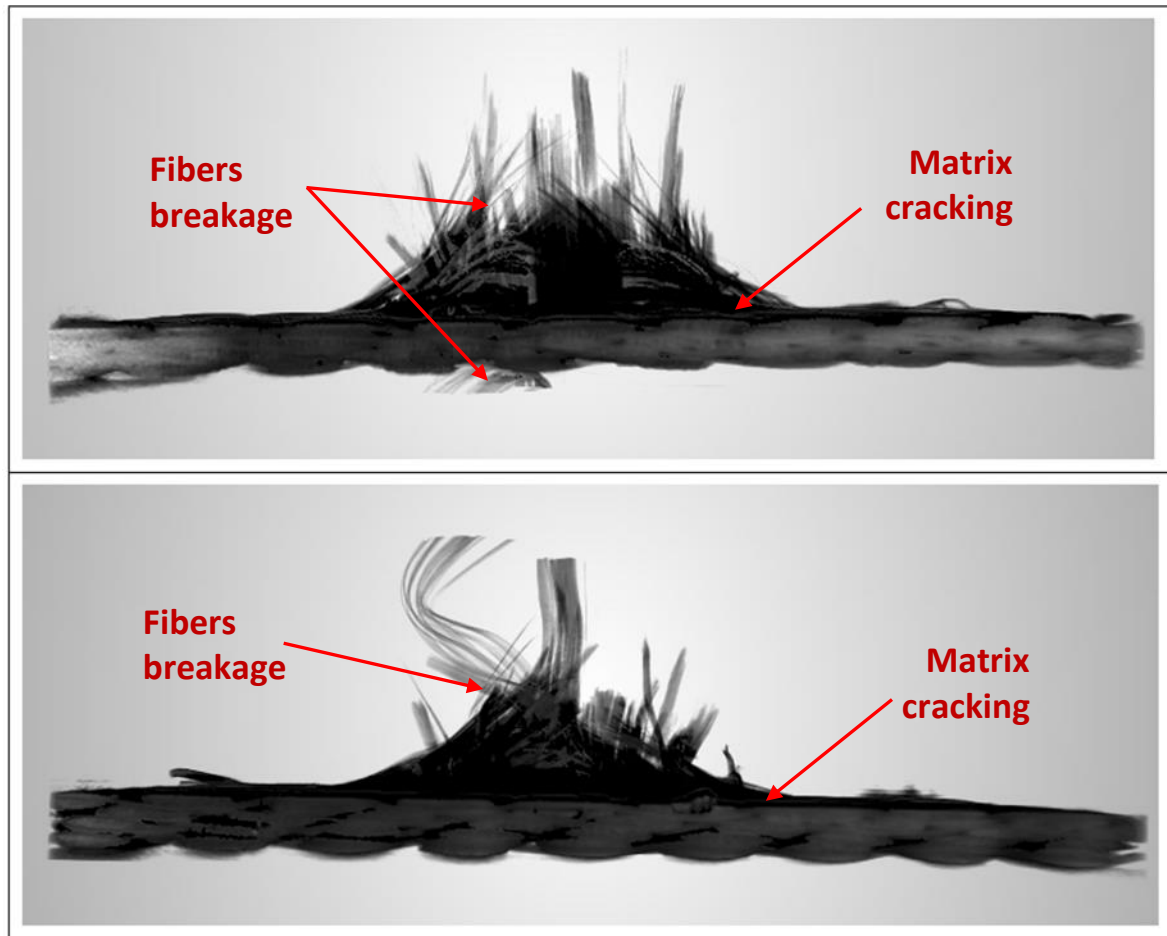
Fig. 5-11. Tomographic analysis of the perforated GFRE[0°/90°]₄ for: (a) non-aged; and (b) aged composites.

5.2 Numerical analysis of high velocity impact for thin woven GFRE laminates

Various approaches based on the finite element method (FEM), which are used to simulate laminate penetration mechanics, are already discussed in the Section 3 of Chapter 4. Based on this knowledge, a new model was developed, and subsequently successfully applied to simulate the impact behaviour of non-aged GFRE[0°/90°]₄ under low velocity impact. Since the strain rate sensitivity is not the same during the perforation test at high and low velocity impact, one should take into account the inelastic viscoplastic behaviour of the acrylic matrix, which occurs under dynamic loading. Such viscoplastic behaviour of the PMMA matrix, described by the model proposed by Nasraoui [109] was already used into the numerical simulation of impact by Kinvi-Dossou et al. [54]. Since this model is not available in the

Abaqus, they introduced an appropriate equation through the VUMAT subroutine. In order to capture rate dependent behaviour and isotropic hardening of acrylic matrix (Elium) the viscoplastic part was reproduced using the Johnson Cook model. The parameters used to simulate behaviour of cohesive layers of the model are presented in the next section.

5.2.1 Material description

Figure 5-12 shows the dimensions of effective area of impacted specimen and the projectile. As can be seen, the shape of the projectile, as well as dimensions of the upper and lower clamp and the target are the same as those used for the low energy impact tests. However, the mass of projectile in the high velocity impact was changed. The projectile of a mass equal to 0.0291 kg was used in the numerical simulation. Since the maximal available projectile velocity is 180 m/s, the impact resistance of the GFRE[0°/90°]$_4$ was studied in the range of impact energies from 10 J up to 470 J.
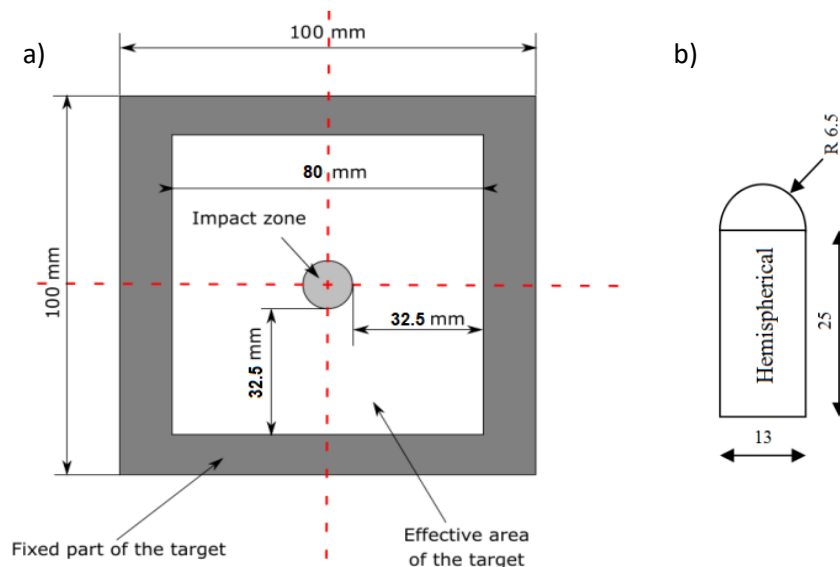
Fig. 5-12. (a) Dimensions of the specimen, and (b) projectile.

The dynamic properties of non-aged GFRE[0°/90°]$_4$ at high strain rates used in the numerical model were estimated by application of the relations proposed by [139] and [140]. The high-strain rate correction factors for the Young's and shear moduli as well as for the failure limits were estimated at 1.5 and 3, respectively [125]. As suggested in the works [141,142], a value of the Poisson's ratio and the material density used for the simulation was constant. The summary of the dynamic properties of woven E-glass fiber/Elium laminate is shown in Table 5-1.

Table 5-1. Summary of the dynamic properties of the non-aged GFRE[0°/90°]₄.

Laminate density ρ [kg/m³]	1960
Young's modulus along fiber direction: $E_{11} = E_{22}$ [GPa]	40.5
Young's modulus in the transversal direction: E_{33} [GPa]	20,4
In-plane shear modulus: G_{12} [GPa]	13.9
Out of plane shear modulus: $G_{13} = G_{23}$ [GPa]	10.6
Poisson's ratio: ν_{12}	0.192
Poisson's ratio: $\nu_{13} = \nu_{23}$	0.315
Failure stress in directions X_+ and Y_+ [MPa]	1270
Failure stress in directions X_- and Y_- [MPa]	1460
Failure shear stress in directions S_1 [MPa]	482
Failure shear stress in directions S_{23} and S_{13} [MPa]	461

For the simulation of high velocity impact, the fracture strain at damage initiation was equal to 0.02 and the initial displacement 5 mm. In order to consider the inelastic behaviour over a wide range of strain rate, the plastic part of acrylic Elium (applied in the model as the cohesive layer) was described using the Johnson Cook parameters. The identified parameters are listed in the Table 5-2. A good agreement between the experiment and model is obtained, Figure 5-13.
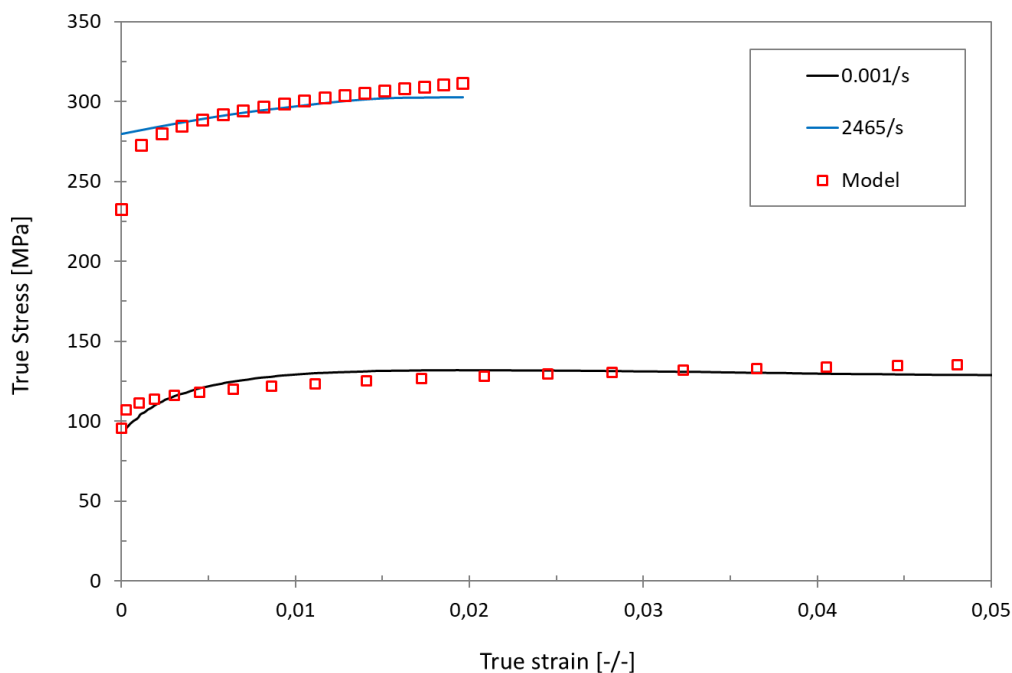
Fig. 5-13. Dynamic compressive behaviour of ELIUM 150.

Table 5-2. The parameters controlling the development of plastic deformation of pure Elium.

Density ρ [kg/m3]	1200
Initial yield of the material, A [MPa]	95.6
Strain hardening coefficient, B [MPa]	83.3
Strain hardening exponent, n	0.24
Strain rate sensitivity, C	0.097

In order to simulate a behaviour of the non-aged GFRE[0°/90°]$_4$ under dynamic loading, the several impact velocity tests were performed in the range from 59 to 180 m/s. Numerical simulations were performed for a time period of 20 ms on a computer equipped with 24 cores (in parallel on Intel(R) Xeon(R) Gold 6136 CPU, 2 × 3.00 GHz and 128 GB RAM). Due to the complexity of the modelled geometry, only small finite elements that generate an initial stable time increment of 10^{-8} s^{-1} were considered.

5.2.2 Results and discussion

The ballistic response predicted by the finite element model and the experimental results from Section 5.1.2 of this chapter are shown in Fig. 5-14.
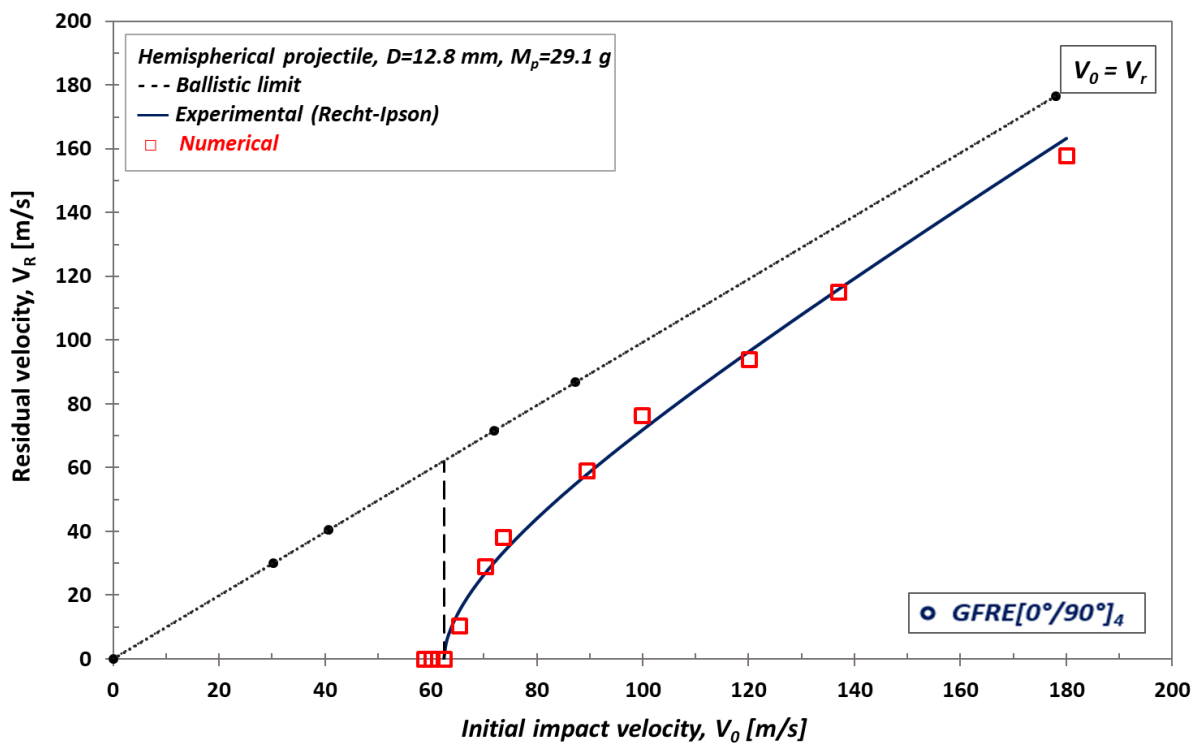
Fig. 5-14. Plots of experimental and finite element ballistic limits.

In order to obtain the experimental ballistic limit, the experimental curve was adjusted using

the analytical law proposed by Recht-Ipson (Eq. ([1-10](#))) discussed in previous section. Good agreement can be observed between the experimental data and the finite element results for both the ballistic limit and the residual velocities. A small discrepancy between experimental and numerical residual velocity for the high impact velocity could be due to possible variations in the specimen's thickness. The highest error is reached at the maximum impact velocity, V_I = 180 m/s, but it is below the 6 %.

In order to validate the model, it is necessary to compare the energy dissipation predicted by the numerical model with the results coming from the experiments.
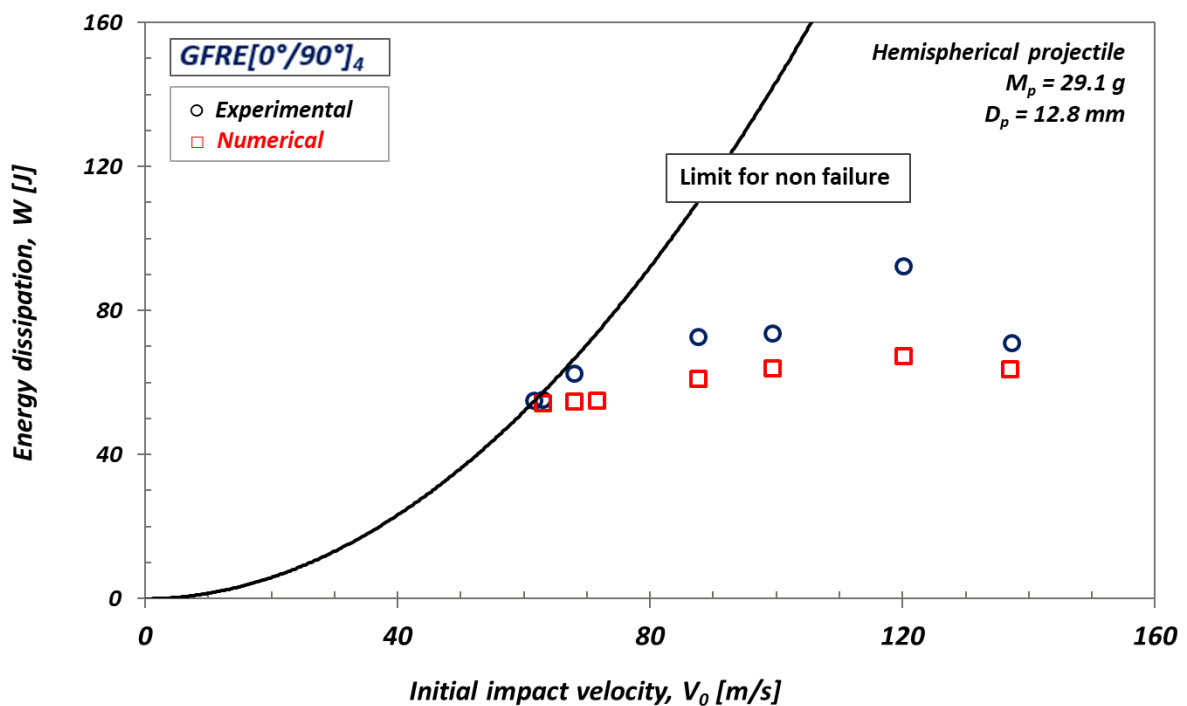
Fig. 5-15. Energy dissipation in 4 layers non-aged GFRE[0°/90°]₄ targets.

In Figure 5-15 it is clearly seen that the values of the energy dissipation obtained from the simulation are much lower than the experimental one. The average difference of the analyzed energy does not exceed 8%. However, for the initial impact velocity of 120 m/s, the energy dissipation value is almost three times higher. Analysis of damage surfaces shown in Figure 5-9, confirmed that in case of the thin laminates, a dominant energy absorption mechanism is the breakage and deformation of glass woven fibers. Considering that these are thin laminates, it is logical that significant energy is absorbed by this mechanism since other authors assume that the behavior is similar to a membrane [143,144]. Therefore, the deformation of fibers plays the most important role and in our case reach a maximal value

before the failure at the impact velocity of about 120 m/s. Observed discrepancy of the results appears presumably due to imperfectly selected dynamic values of correction factors.

5.3 Conclusions

Two groups of glass fibers/Elium acrylic based composite laminates with shapes and dimensions adapted for the impact resistance testing after prior fatigue aging, were prepared by means of the infusion process. The effect of damage induced by fatigue aging was investigated through analysis of the impact resistance properties.

High impact velocity tests carried-out on the non-aged plates at different levels of impact energy exhibited their good impact resistance. The ballistic limit of non-aged specimens cut with an angle 45 degree is higher than those cut along the fiber. In this case the difference was equal almost 8.4 m/s. However, it has been observed that specimens aged by cyclic loading - both with the value of stress below and above the yield point - cut out with an angle of 45 degree (GFRE $[45°/45°]_4$) have 20 m/s lower ballistic limits compared to aged GFRE $[0°/90°]_4$. A drop of the impact resistance of the aged $[0°/90°]_4$ GFRE specimens was minimal and did not exceed 3.6 m/s. In general, the composites subjected to LCF loading for both fiber orientations demonstrated the highest decrease of the ballistic limit. It results from the significant reduction of stiffness caused by the matrix cracking and interface debonding taking place between the fibers and matrix. Detailed analysis of the energy dissipation and evolution of impact force during perforation tests, confirmed that the aged materials containing the woven fabric oriented at the angle of 45° exhibited the weakest impact resistance. Therefore, one can conclude that the fibers orientation, fatigue aging, and glass fibers concentration significantly affect the elastic properties and lead to decrease of stiffness and increase of the energy absorbed.

The high-velocity impact phenomenon of non-aged GFRE$[0°/90°]_4$ laminated composite was studied by means of a finite element model. A finite element model was implemented in a VUMAT user sub-routine in Abaqus/Explicit. Experimental and numerical ballistic limits and residual velocities were compared for 1.8 mm thick specimens. An analysis of the energy absorption has also been carried out. Good agreement was observed with maximum differences being lower than 6 %. The results showed that the use of plastic damage model gives consistent results for all impact velocities.

Summary and Perspective

General summary

International emission standard concerning carbon dioxide requires from car manufacturers a reduction of fuel consumption. Every 10% vehicle weight reduction decreases battery or gasoline consumption roughly by 8%. Therefore, the main goal of the automotive industry today is to diminish the weight of the car structure. The use of composite materials, on the one hand, reduces the mass, and, on the other hand, does not diminish the safety of the construction. In addition, to protect the environment, the currently used thermosetting matrices are being replaced by fully recyclable thermoplastic resins. For this purpose, ARKEMA and IRTm2p proposed ELIUM, a liquid thermoplastic resin compatible with a large number of existing ancillaries, mold constructions and mixing machines for high performance composite structures. The work of the engineers and scientists conducted in this field contributed to the development of thermoplastic resins by improving their physicochemical and thermomechanical properties and facilitates the manufacturing processes of laminated composites, as well. This research offers a contribution to deepening the knowledge regarding the influence of fatigue aging on the low and high impact resistance of new thermoplastic acrylic resin ELIUM reinforced by the glass woven fabric.

Four layers laminated glass fiber/acrylic woven composite was fabricated by vacuum infusion. Two orientations, representing two different cases were selected in this study. The first group of tested material, named GFRE $[0°/90°]_4$ was cut out along the fibers direction. The second one, GFRE $[45°/45°]_4$ was cut along direction inclined by an angle of 45° with respect to the fiber direction.

Based on the stress-strain tensile curves two stress levels were chosen for the fatigue aging of both types of specimens (GFRE $[0°/90°]_4$ and GFRE $[45°/45°]_4$). The response of the materials on cyclic fatigue loading was evaluated in terms of the stiffness variation analysis. Therefore, the elastic modulus was measured using an extensometer during tensile tests carried out between subsequent blocks of the fatigue loading cycles. The fatigue aging program was interrupted prior to the specimen failure at a given value of the stiffness drop.

The initial stiffness was reduced by about 17 % for the GFRE $[0°/90°]_4$, after either LCF or HCF tests. Such reduction was much more pronounced in the case of GFRE $[45°/45°]_4$. It was equal to 48 %. Subsequently, the aged specimens were dismounted from the testing machine and subjected to low and high velocity impact tests.

In order to understand the influence of fatigue aging on low impact properties, the force-displacement and energy-time responses were analyzed for both materials. The non-aged specimens impacted at energy of 5 J, 10 J and 30 J were not perforated and showed a great ability to rebound the impactor. The composites subjected to low cyclic fatigue (LCF) loading demonstrated the greatest decrease of the initial slope of the force-displacement characteristics. It results from the significant reduction of stiffness caused by the matrix cracking and interface debonding, taking place between the fibers and matrix. The maximum force reduction for tests carried out at the impact energy of 50 J for GFRE $[0°/90°]_4$ and GFRE $[45°/45°]_4$ was equal to 11% and 19%, respectively. Analysis of the absorbed energy during impact tests, confirmed that the aged materials containing the woven fabric oriented at the angle of 45° exhibited the weakest impact resistance.

In turn, the effects of fatigue aging on the impact behavior at high impact velocity were assessed by comparing ballistic limits and the amount of dissipated energy of aged and non-aged plates. It is worth to notice that the ballistic limit of non-aged specimens cut with an angle 45 degree is higher than those cut along the fiber. In this case the difference was equal almost 8.4 m/s. However, it was observed that specimens aged by cyclic loading - both with the value of stress below and above the yield point - cut out with an angle of 45 degree (GFRE $[45°/45°]_4$) had 20 m/s lower ballistic limits compared to aged GFRE $[0°/90°]_4$. A drop of the impact resistance of the aged GFRE $[0°/90°]_4$ specimens was minimal and did not exceed 3.6 m/s. Similarly to the tests at low velocity impact, through analysis of the energy dissipation and evolution of the impact force during perforation tests, confirmed that GFRE $[0°/90°]_4$ plates subjected to uniaxial fatigue loading had better ballistic performance and higher energy dissipation than GFRE $[45°/45°]_4$ targets. Therefore, one can conclude that the fibers orientation, fatigue aging, and glass fibers concentration significantly affect the elastic properties and lead to stiffness reduction and decrease of the energy absorbed. The results are in agreement with the analyzes of damage phenomena. The acrylic matrix allows energy to be dissipated by plastic deformation. The flexibility of the composite based on

acrylic resin is linked to the fact that its molecules are long but chemically separated, which is particularly visible for the specimens with the fibers oriented with an angle of 45 degree (richer in resin).

Finally, for GFRE $[0°/90°]_4$ composite a numerical model was proposed to simulate the impact behaviour of non-aged woven laminated composite plates subjected to low and high velocity impact. The elastic properties and the failure limits used in simulation were estimated through the in-plane static and out-of-plane dynamic experimental tests. The proposed 3D model was implemented in an explicit FEM framework for Abaqus/Explicit by a VUMAT material user-subroutine. The model consisted of four layers of glass fiber/Elium acrylic woven which represent the laminate as a homogeneous material. The phenomenon of damage, both for in-plane and out-of-plane failure modes, are simulated using modified Hashin's failure criteria [54]. Applied damage model is based on the degradation of elastic properties of homogenized layers until a maximum stress failure criterion is verified. Thin layers of the cohesive zone (pure Elium) were introduced between the woven plies in order to account for interlayer damage. To capture rate dependent effects and isotropic hardening of acrylic matrix (Elium) the viscoplastic part was reproduced using the Johnson-Cook model.

In order to validate the proposed numerical models, the results of the impact simulation were compared with the experimental data. Impact response of laminates subjected to impact energy equal to 10 J, 30 J and 50 J, was quantified using the developed approach for predicting intralaminar damage. The experimental and numerical results of the ballistic limits, residual velocities as well as the analysis of the energy absorption were then compared for 1.8 mm thick specimens. A negligible small difference was observed between the slope of the numerical and experimental curve and the energy levels absorbed. However, it was clearly demonstrated that the maximum displacement and response obtained using the proposed micromechanical model were very similar to the experimental findings.

Perspective

The work presented herein was focused on the influence of uniaxial cyclic loading on low and high velocity impact resistance of the glass fiber/Elium acrylic woven laminates.

However, in order to account for various exploitation conditions, it would be extremely important also to investigate that in the near future:

- an influence of the possible softening effect caused by multiaxial cyclic loading, and then to analyse its influence on impact resistance of material,
- an effect of cyclic bending on stiffness reduction, and as a consequence, decrease of impact properties of the laminated composites.

Besides, it would be necessary to define the damage resistance and residual strength of the impacted plates through the compression tests after impact (CAI).

It is also planned to understand the influence of low velocity impact, i.e. up to 1.32 m/s (5 J), on fatigue properties of the laminated composites. Such a situation often takes place during assembly of the vehicle structure elements or their exploitation. Due to the low impact energy damage in the form of matrix cracks and delamination is often invisible on the surface. During exploitation such defects may grow, and in consequence, lead to a decrease of the strength and lifetime of the composites in question. Taking into account the product liability of car manufacturers, the fatigue analysis of the previously damaged due to impact material should be considered in the further more thorough research. Subsequently, an effect of fatigue aging of the prestrained laminated composites on low and high velocity impact resistance could be compared to the results of the same tests carried out on the laminates tested in this study.

The results of perforation tests showed that the ballistic limit of the non-aged plates with on-axis reinforcement orientation is characterized by higher value than that of the non-aged specimens with off-axis reinforcement orientation. In turn, the aged laminates based on thermoplastic resin with yarns oriented in on-axis direction exhibit higher fatigue and impact resistance than that with yarns oriented in off-axis direction. Therefore, it would be worth to carry out the perforation tests on the aged and non-aged specimens consisting several layers of the glass woven fabric that are stacked alternatively in the on- and off-axis directions. Such study would enable a development of the optimal composition of the laminate that could provide both, a good fatigue resistance and high velocity impact resistance.

The 3D numerical model proposed in this work can be further developed. Based on the out-of-plane dynamic properties of pure acrylic resin determined for various levels of strain rate

and temperature, the viscoplastic behaviour of cohesive zone introduced between the woven plies, could be reproduced using Nasraoui parameters instead of the Johnson-Cook ones. Therefore, one could also consider an implementation of the second material as a user subroutine in VUMAT, and as a consequence, provides better description of the dynamic response of the impacted fiber/Elium acrylic woven laminates.

In the next step it is planned to develop the fatigue stiffness degradation model for the proposed 3D geometry of the laminated composite tested. A suitable UMAT subroutine for a prediction of the effective elastic properties of aged laminate for a given number of the loading cycles and various stress levels could be based on damage parameter D and accompanying evolution of the stiffness loss determined in the present work. Resulting stiffness matrix tensor could be subsequently exported to Abaqus/Explicit and used as an input for simulations of the low and high velocity impact resistance. It would enable a comparison of the results of impact tests carried out on the aged specimens predicted by the model with presented data.

References

1. Thermoplastic composites and advanced composites with outstanding properties – Arkema.com. https://www.arkema.com/en/arkema-group/innovation/lightweight-materials-and-design/thermoplastic-composites/.

2. Feldmann, J. Kunststoffe – Werkstoffe der Energieeffizienz. Kunststoffe im Automobilbau 2008. VDI- Verlag, 2008.

3. EU-Kommission begrenzt PKW-Emissionen auf 95g CO2/km. https://www.klimaktiv.de (2020).

4. Automotive Plastics Market: Industry Analysis, Market Size, Share, Trends, Application Analysis, Growth And Forecast 2022-2027 – Industry ARC. https://www.industryarc.com. Report Code: CMR 15574.

5. Boufaida, Z.; Farge, L.; André, S.; Meshaka, Y. Influence of the fiber/matrix strength on the mechanical properties of a glass fiber/thermoplastic-matrix plain weave fabric composite. Composites: Part A. 2015, 75, 28–38. DOI: https://doi.org/10.1016/j.compositesa.2015.04.012.

6. Kinvi-Dossou, G.; Matadi Boumbimba, R.; Bonfoh, N.; Koutsawa, Y.; Eccli, D.; Gerard, P. A numerical homogenization of E- glass/acrylic woven composite laminates: Application to low velocity impact. Compos. Struct. 2018, 200, 540-554. DOI: https://doi.org/10.1016/ j.compstruct. 2018.05.137.

7. Obande, W.; Ray, D.; Brádaigh, C.M.Ó. Viscoelastic and drop-weight impact properties of an acrylic-matrix composite and a conventional thermoset composite – A comparative study. Mater. Lett. 2019, 238, 38-41. DOI: https://doi.org/10.1016/j.mat-let.2018.11.137.

8. Cadieu, L.; Kopp, J.B.; Jumel, J.; Bega, J.; Froustey, C. Strain rate effect on the mechanical properties of a glass fibre reinforced acrylic matrix laminate. An experimental approach. Compos. Struct. 2019, 223, 110952. DOI: https://doi.org/ 10.1016/j.comp-struct.2019.110952.

9. Matadi Boumbimba, R.; Coulibaly, M.; Khabouchi, A; Kinvi-Dossou, G.; Bonfoh, N.; Gerard, P. Glass fibres reinforced acrylic thermoplastic resin-based tri-block copolymers composites: Low velocity impact response at various temperatures. Compos. Struct. 2017, 160, 939-951. DOI: https://doi.org/10.1016/j.compstruct. 201610.127.

10. Freund, L. Study of the hygrothermal aging of natural fibers reinforced composites: an experimental and numerical approach, HAL CCSD 2018-06-20, https://tel.archives-ouvertes.fr/tel-01870255/document.

11. Boissin, E.; Bois, C.; Wahl, J.-C.; Palin-Luc, T. Effect of temperature on damage mechanisms in an acrylic-matrix and glass-fiber-reinforced composite under monotonic tensile and fatigue loadings, ECCM18 - 18th European Conference on Composite Materials Athens, Greece, 24-28 June 2018.

12. Azouaoui, K.; Azari, Z.; Pluvinage, G. Evaluation of impact fatigue damage in glass/epoxy composite laminate. Int. J. Fatigue 2010, 32(2), 443-452. DOI: https://doi.org/10.1016/ j.ijfatigue.2009.09.005.

13. Recht, R.F. ; Ipson, T.W. Ballistic perforation dynamics. J. Appl. Mech. 1963, 30, 384-390.

14. Nivon, M. Techniques de l'Ingénieur Sécurité dans la transformation des plastiques. 2014. 33.

15. Aiman, D.P.C.; Yahya, M. F.; Salleh, J. Impact properties of 2D and 3D woven composites : A review. AIP Conference Proceedings. 2016, 1774, 020002. https://doi.org/10.1063/1.4965050.

16. Berthelot, J.M. Matériaux composites. Comportement mécanique et analyse des structures. Lavoisier, 2012.

17. Pini, T. ; Caimmi, F.; Briatico-Vangosa, F.; Frassine, R.; Rink, M. Fracture initiation and propagation in unidirectional CF composites based on thermoplastic acrylic resins. Engineering Fracture Mechanics. 15 October 2017, 184, 51-58. https://doi.org/10.1016/j.engfracmech. 2017.08.023.

18. Ahmad, H .; Markina, A. A.; Porotnikov, M. V.; Ahmad, F. A review of carbon fiber materials in automotive industry. 2020 IOP Conf. Ser.: Mater. Sci. Eng. 971 032011. DOI: https://doi.org/ 10.1088/ 1757-899X/971/3/032011.

19. Advanced lightweight composites transform industries – MTS.com.

20. Hovorun, T.P.; Berladir, K.V.; Pererva, V.I.; Rudenko, S.G.; Martynov, A. Modern materials for automotive industry. Journal of Engineering Sciences. 2017, 4(2).

21. Carlson, E.; Nelson, K. Nylon under the hood: history of innovation. Automotive Engineering 1996;104:84-89.

22. Boufaida, Z., Analyse des propriétés mécaniques de composites taffetas verre/matrice acrylique en relation avec les propriétés d'adhésion des fibres sur la matrice. 2015.

23. Steeves, C.A.; Fleck, N.A. In-plane properties of composite laminates with through-tickness pin reinforcement, Int. J. Solids Struct. 2006, 43(10), 3197-3212.

24. Chyanbin, Hwu.; Tan, C.J. In-plane/out-of-plane concentrated forces and moments on composite laminates with elliptical elastic inclusions. International Journal of Solids and Structures. 1 October 2007, 44(20), 6584-6606.

25. Kaminski, M. ; Maire, J. ; Laurin, F. ; Rakotoarisoa, C.; Hemon, H. Méthodologies de prévision de durée de vie des composites, ONERA.

26. Rice, R.C.; Leis, B.N.; Berns, H.D.; Nelson, D.V; Lingenfleser, D.; Mitchell, M.R. Fatigue Design Handbook, Warrendale, SAE, 1988.

27. Plumtree, A.; Abdel-Raouf, H.A. Cyclic stress–strain response and substructure. Int. J. Fatigue 2001, 23(9), 799-805. DOI: https://doi.org/10.1016/S0142-1123(01)00037-8.

28. Lee, L.J.; Yang, J.N.; Sheu, D.Y. Prediction of fatigue life for matrix-dominated composite laminates. Compos. Sci. Technol. 1993, 46(1), 21-28. DOI: https://doi.org/ 10.1016/0266-3538(93)90077-T.

29. Kattan, P.I.; Voyiadjis, G.Z. Overall Damage and Elasto-Plastic Deformation in Fibrous Metal Matrix Composites. International Journal of Plasticity, 1993, 9(8), 931-949.

30. Yang, J.N.; Lee, L.J.; Sheu, D.Y. Modulus reduction and fatigue damage of matrix dominated composite laminates. Compos. Struct. 1992, 21(2), 91-100. DOI: https://doi.org/10.1016/ 0263-8223(92)90044-D.

31. Kachanov, L.M. Time of the rupture process under creep conditions. Izvestiya Akademii Nauk SSR, Otd Tekh Nauk. 1958, 8, 26-31.

32. Voyiadjis, G.Z.; Venson, A.R.; Kattan, P.I. Experimental Determination of Damage Parameters in Uniaxially-Loaded Metal Matrix Composites Using the Overall Approach. International Journal of Plasticity. 1995, 11(8), 895-926.

33. Kattan, P.I.; Voyiadjis, G.Z. A Coupled Theory of Damage Mechanics and Finite Strain Elasto-Plasticity, Part I: Damage and Elastic Deformations. International Journal of Engineering Science. 1990, 28(5), 421-435.

34. Voyiadjis, G.Z.; Echle, R. High Cycle Fatigue Damage Evolution in Uni-Directional Metal Matrix Composites Using a Micro-Mechanical Approach. Mechanics of Materials Journal. 1998, 30, 91-110.

35. Kattan, P. I.; Voyiadjis, G.Z. Damage-Plasticity in a Uniaxially-Loaded Composite Lamina: Overall Analysis. International Journal of Solids and Structures. 1996, 33(4), 555-576.

36. Voyiadjis, G.Z. Degradation of Elastic Modulus in Elasto-Plastic Coupling with Finite Strains. International Journal of Plasticity. 1988, 4(4), 335-353.

37. Pandita, D.; Huysmans, G.; Wevers, M.; Verpoest, I. Tensile Fatigue Behaviour of Glass Plain-Weave Fabric Composites in on- and off-Axis Directions. Composites Part A: Applied Science and Manufacturing. 2001, 32, 1533-1539.

38. Lou, X.; Cai, H.; Yu, P.; Jiao, F.; Han, X. Failure analysis of composite laminate under low-velocity impact based on micromechanics of failure. Composite Structures. 2017, 163, 238-247.

39. Yu, G.-C.; Wu, L-Z.; Ma, L; Xiong, J. Low Velocity Impact of Carbon Fiber Aluminum Laminates. Composite Structures. 2014, 119, 757-766.

40. Bouvet, C. Dommages d'impact sur stratifié composite/Impact damages on composite laminate. Journées Nationales sur les Composites (JNC17). 2011, 1-10.

41. Xu, Z.; Yang, F; Guan, Z.W.; Cantwell, W.J. An Experimental and Numerical Study on Scaling Effects in the Low Velocity Impact Response of CFRP Laminates. Composite Structures. 2016, 154, 69-78.

42. Suresh Kumar, C.; Arumugam, V.; Dhakal, H.N.; Risil, J. Effect of temperature and hybridisation on the low velocity impact behavior of hemp-basalt/epoxy composites. Composite Structures. 2015, 125, 407-416.

43. Dhakal, H.N.; Zhang, Z.; Bennett, N.; Reis, P. Low-velocity impact response of non-woven hemp fibre reinforced unsaturated polyester composites: Influence of impactor geometry and impact velocity. Composite Structures. 2012, 94(9), 2756-2763.

44. Dhakal, H.N.; Arumugam, V.; Aswinraj, A.; Santulli, C.; Zhang, Z.Y.; Lopez-Arraiza, A. Influence of temperature and impact velocity on the impact response of jute/UP composites. Polymer Testing. 2014, 35, 10-19.

45. Shi, Y.; C. Pinna.; Soutis, C. Modelling impact damage in composite laminates: A simulation of intra- and inter-laminar cracking. Composite Structures. 2014, 114, 10-19.

46. Farooq, U.; Myler, P. Prediction of load threshold of fibre-reinforced laminated composite panels subjected to low velocity drop-weight impact using efficient data filtering techniques. Results in Phys. 2015, 5, 206-221. DOI: https://doi.org/10.1016/j.rinp.2015.07.007.

47. Greenhalgh, G.; Hiley, M. The assessment of novel materials and processes for the impact tolerant design of stiffened composite aerospace structures. Composites Part A: Applied Science and Manufacturing. February 2003, 34(2), 151-161.

48. Cochrane, A.D.; Serra, J.; Lander, J.K.; Partridge, I.K.; Böhm, H.; Wollmann, T.; Hornig, A.; Gude, M.; Hallett, S.R. Experimental investigation of large-scale high-velocity soft-body impact on composite laminates. International Journal of Impact Engineering. March 2022, 61, 104089.

49. Mbarek, I.; Matadi, Boumbimba, R.; Rusinek, A.; Voyiadjis, G.Z.; Gerard, P.; Samadi-Dooki, A. The dynamic behavior of poly 716 (methyl methacrylate) based nano-rubbers subjected to impact and perforation: Experimental investigations. Mech. Mater. 2018, 717 122, 9-25. DOI: https://doi.org/10.1016/j.mechmat.2018.03.011.

50. Lambert, J.; Jonas, G. Towards standarization of in terminal ballistic testing: velocity representation. Ballistic research laboratories 1976.

51. Ganesh Babu, M.; Vemurugan, R.; Gupta, N. K. Energy absorption and ballistic limit of targets struck by heavy projectile. Latin American Journal of Solids and Structures. 2006, 3, 21-39.

52. Davis, G.A.O.; Zang, X. Impact damage prediction in carbon composite structures. Int. J. of Impact Engineering. 1995, 16 (1), 149-170.

53. Zhou, J.; Guan, Z.; Cantwell, W. Numerical modelling of perforation impact damage of fibre metal laminates. 2014, 1–1.

54. Kinvi-Dossou, G; Bonfoh, N.; Matadi Boumbimba, R.; Koutsawa, Y.; Lachaud, F.; Nyoungue, A.; Gerard, P. A mesoscale modelling approach of glass fibre/Elium acrylic woven laminates for low velocity impact simulation. Composite Structures. 15 November 2020, 252, 112671.

55. Voyiadjis, G.Z.; Deliktas, B. Multi-scale Analysis of Multiple Damage Mechanisms Coupled with Inelastic Behavior of Composite Materials. Mechanics Research Communications Journal. 2000, 27(3), 295-300.

56. Hoffman, O. The brittle strength of orthotropic materials. J Compos Mater. 1967, 1(2), 200-206. https://doi.org/10.1177/002199836700100210.

57. Tsai, S. W.; Wu, E.M. A General Theory of Strength for Anisotropic Materials. Journal of Composite Material. 1971, 5, 58-80. https://doi.org/10.1177/002199837100500106.

58. Liu, K.S.; Tsai, S.W. A progressive quadratic failure criterion for a laminate. Compos Sci Technol. 1998, 58 (7),1023-1032.

59. Hill, R. Theory of mechanical properties of fiber-strengthened materials. III. Self-consistent model. J Mech Phys Solids. 1965, 13, 189-198.

60. Hashin, Z.; Rotem, A. A Fatigue Failure Criterion for Fiber Reinforced Materials. Journal of Composite Materials. 1973, 7, 448-464.

61. Chang, F-K.; Chang, K-Y. A Progressive Damage Model for Laminated Composites Containing Stress Concentrations. Journal of Composite Material. 1987, 21, 834-855.

62. Christensen, R.M. Stress Based Yield: Failure Criteria for Fiber Composites. Journal of Solid and Structures. 1997, 34, 529-543.

63. Puck, A.; Schürmann, H. Failure Analysis of FRP Laminates by means of Physical Based Phenomenological Models. Composites Science and Technology. 1998, 58, 1045-1067.

64. Hashin, Z. Failure Criteria for Unidirectional Fiber Composites. Journal of Applied Mechanics. 1980, 74, 329-334.

65. Xiao, J.R.; Haque, B.Z.; Gillespie, J.W. Progressive damage and delamination in plain weave S-2 glass/SC-15 composites under quasi-static punch-shear loading. Composite Structures. 2007, 78(2), 182-196.

66. Juhasz, J.; Rolfes, R.; Rohwer, K. A new strength model for application of a physically based failure criterion to orthogonal 3D fiber reinforced plastics. Composites Science and Technology. 2001, 61(13), 1821-1832.

67. Matzenmiller, A.; Lubliner, J.; Taylor, R.L. A constitutive model for anisotropic damage in fiber-composites. Mechanics of Materials. 1995, 20(2), 125-152.

68. Kattan, P.I.; Voyiadjis, G.Z. Damage Mechanics. In: Damage Mechanics with Finite Elements, (2002). Springer, Berlin, Heidelberg. https://doi.org/10.1007/978-3-642-56384-3_1.

69. Ladeveze, P.; LeDantec, E. Damage modelling of the elementary ply for laminated composites. Composites Science and Technology. 1992, 43(3), 257-267.

70. Maire, J.F.; Lesne, P.M. An explicit damage model for the design of composites structures. Composites Science and Technology. 1998, 58(5), 773-778.

71. Talreja, R. A Continuum Mechanics Characterization of Damage in Composite Materials. Proceedings of the Royal Society of London. Series A, Mathematical and Physical Sciences. 1985, 399(1817), 195-216.

72. Böhm, R.; Gude, M.; Hufenbach, W. A phenomenologically based damage model for 2d and 3d-textile composites with non-crimp reinforcement. Mater Des. 2011, 32, 2532-2544.

73. Randles, P.W.; Nemes, J.A. Continuum Damage Model for Thick Composite Materials. Mechanics of Materials. 1992, 13, 1-13.

74. Griffith, A.A. The Phenomena of Rupture and Flow in Solids. Philosophical Transactions of the Royal Society of London. 1921, (A221), 163-198.

75. Alfano, G.; Crisfield, M.A. Finite element interface models for the delamination analysis of laminated composites: mechanical and computational issues. International Journal for Numerical Methods in Engineering. 2001, 50(7), 1701-1736.

76. Allix, O.; Corigliano, A. Modeling and simulation of crack propagation in mixed-modes interlaminar fracture specimens. Journal of Fracture. 1996, 77, 111-140.

77. Allix, O.; Ladeveze, P.; Corigliano, A. Damage analysis of interlaminar fracture specimens. Composite Structures. 1995, 31, 61-74.

78. Campilho, R.; Moura, M.; Ramantani, D.; Gonçalves, J. Obtaining the cohesive laws of a trapezoidal mixed-mode damage model using an inverse method. Cięncia e Tecnologia dos Materiais. 2008, 20, 1-2.

79. Jules, E.J. Couplage entre propriétés thermiques, réactivité chimique et viscosité des matériaux composites thermodurcissables en relation avec les conditions de leur élaboration fondée sur l'hystérésis diélectrique. , in Ecole National Supérieure d'Arts et Métiers. 2001.

80. Dereims, A. Industrial simulation of composite part manufacturing processes by resin infusion : interaction between fluid and low permeability porous solid undergoing large deformations. 2013, Ecole Nationale Supérieure des Mines de Saint-Etienne.

81. Vinson, J.R. Plate and Panel Structures of Isotropic, Composite and Piezoelectric Materials, Including Sandwich. Springer Science & Business Media, 30 mar 2006-424.

82. Kpobie, W. Modélisation 3D d'assemblages flip chip pour la fiabilisation des composants électroniques à haute valeur ajoutée de la famille "More than Moore. 2014.

83. ASTM D638 – 14: Standard Test Method for Tensile Properties of Plastics.

84. ASTM D3039: Standard Test Method for Tensile Properties of Polymer Matrix Composite Materials.

85. Gilat, A.; Goldberg, R.K.; Roberts, G.D. Experimental study of strain-rate-dependent behavior of carbon/epoxy composite. Composites Science and Technology. 2002, 62(10), 1469-1476.

86. Taniguchi, N.; Nishiwaki, T.; Kawada, H. Tensile strength of unidirectional CFRP laminate under high strain rate. Advanced Composite Materials. 2007, 16(2), 167-180.

87. ASTM D4255M: Standard Test Method for In-Plane Shear Properties of Polymer Matrix Composite Materials by the Rail Shear Method.

88. Couégnat, G. Approche multi échelle du comportement mécanique de matériaux composites à renfort tissé. 2008.

89. Mbacke, M.A. Caractérisation et modélisation du comportement mécanique des composites tressés 3D : Application à la conception de réservoirs GNV. 2013.

90. ASTM D5528: Standard Test Method for Mode I Interlaminar Fracture Toughness of Unidirectional Fiber-Reinforced Polymer Matrix Composites.

91. Yoshihara, H.; Kawamura, T. Mode I fracture toughness estimation of wood by DCB test. Composites Part A: Applied Science and Manufacturing. 2006, 37, 2105-2113.

92. ASTM D7905: Standard Test Method for Determination of the Mode II Interlaminar Fracture Toughness of Unidirectional Fiber-Reinforced Polymer Matrix Composites.

93. Walley S.M.; Field, J.E. Strain Rate Sensitivity of Polymers in Compression from low to high rates, DYMAT journal 1. 1994, 3, 211-227.

94. Proud, W. G.; Porter, D.; Gould, P.J.; Williamson, D.M.; Walley, S.M. The Mechanical Performance of Polymers and Polymer Composites at High Strain-Rates, Proceedings of the IMPLAST 2010 Conference, October 12-14, 2010 Providence, Rhode Island USA.

95. Ochola, R.O.; Marcus, K.; Nurick, G.N.; Granz, T. Mechanical behaviour of glass and carbon fiber reinforced composites at varying strain rates, Composite Structures. 2004, 63, 455-467.

96. Rusinek, A.; Bernier, R.; Matadi Boumbimba, R.; Klosak, M.; Jankowiak, T.; Voyiadjis, G.Z. New devices to capture the temperature effect under dynamic compression and impact perforation of polymers, application to PMMA. Polymer Testing. February 2018, 65, 1-9.

97. Bernard, C.A.; Bahlouli, N.; George, D.; Rémond, Y.; Ahzi, S. Identification of the dynamic behavior of epoxy material at large strain over a wide range of temperatures. Mechanics of Materials. April 2020, 143, 103323.

98. Voyiadjis, G.Z., Doktor Honoris Causa Politechniki Poznanskiej: Constitutive Modeling and Simulation of Materials/Structures under Extreme Loadings due to Impact Loading at High Strain Rates. Poznan, Poland. 2017. ISBN 978-83-7775-458-0.

99. Richeton, J.; Ahzi, S.; Daridon, L.; Rémond, Y. A formulation of the cooperative model for the yield stress of amorphous polymers for a wide range of strain rates and temperatures. Polymer. 2005, 46(16):6035–6043.

100. Huang, Z.M. Micromechanical strength formulae of unidirectional composites, Materials Letters. August 1999, 40(4), 164-169.

101. Goldberg, R.K.; Roberts, G.D.; Gilat, A. Implementation of an associative flow rule including hydrostatic stress effects into the high strain rate deformation analysis of polymer matrix composites. Journal of Aerospace Engineering. 2005, 18(1), 18-27.

102. Tay, T.E.; Ang, H.G.; Shim, V.P.W. An Empirical Strain Rate–Dependent Constitutive Relationship for Glass-Fibre Reinforced Epoxy and Pure Epoxy, Composite Structures. 1995, 33, 201–210.

103. Wang, Y.; Xia, Y.M. Experimental and theoretical study on the strain rate and temperature dependence of mechanical behavior of Kevlar fiber, Composite Part A. 1999, 30, 1251-1257.

104. Thiruppukuzhi, S.V.; Sun, C.T. Models for the Strain-Rate-Dependent Behavior of Polymer Composites, Composites Science and Technology. 2001, 61, 1–12.

105. Weeks, C.A.; Sun, C.T. Modeling Non-linear Rate-Dependent Behavior in Fiber Reinforced Composites, Composites Science and Technology. 1998, 58, 603–611.

106. Gates, T.S.; Sun, C.T. Elastic/Viscoplastic Constitutive Model for Fiber Reinforced Thermoplastic Composites, AIAA Journal. 1991, 29, 457–463.

107. Yoon, K.J; Sun, C.T. Characterization of Elastic-Viscoplastic Properties of an AS4/ PEEK Thermoplastic Composite, Journal of Composite Materials. 1991, 25, 1277–1313.

108. Thiruppukuzhi, S.V.; Sun, C.T. Testing of Modelling High Strain Rate Behaviour of Polymeric Composites, Composites. 1998, 29B, 535–546.

109. Nasraoui, M.; Forquin, P.; Siad, L.; Rusinek, A. Influence of strain rate, temperature and adiabatic heating on the mechanical behaviour of poly-methyl-methacrylate: experimental and modelling analyses. Mater Des. 2012, 37, 500–9.

110. G'sell, C.; Jonas, J.J. Determination of the plastic behaviour of solid polymers at constant true strain rate. J Mater Sci. 1979, 14(3), 583–91. DOI: https://doi.org/ 10.1007/ BF00772717.

111. Yuan, F.; Prakash, V.; Tullis. T. Origin of pulverized rocks during earthquake fault rupture. Journal of geophysical research. 2011, 116. (B06309). https://doi.org/ 10.1029/2010JB007721

112. Lennon, A.M.; Ramesh, K.T. A technique for measuring the dynamic behavior of materials at high temperatures. Int. J. Plast. 1998, 14, 1279-1292.

113. Skelton, R.P.; Maier, H.J.; Christ, H-J. The Bauschinger effect, Masing model and the Ramberg–Osgood relation for cyclic deformation in metals. Mater SciEng A. 1997, 238, 377–90.

114. Gao, X.; Tao, N.; Chen, S.; Wang, L.; Wu, W. Tensile-tensile fatigue behavior of multi-axial warp-knitted reinforced composite. Fibres Text. East. Eur. 2018, 1, 73–80, DOI: https://doi.org/10.5604/01.3001.0010.7800.

115. Yan, Y.J.; Yam, L.H. Online detection of crack damage in composite plates using embedded piezoelectric actuators/sensors and wavelet analysis. Compos. Struct. 2002, 58(1), 29–38, DOI: https://doi.org/10.1016/S0263-8223(02)00043-0.

116. Selver, E.; Potluri, P.; Hogg, P.; Soutis, C. Impact damage tolerance of thermoset composites reinforced with hybrid com-mingled yarns. Compos. Part B Eng. 2016, 91, 522–538, DOI: https://doi.org/10.1016/j.compositesb.2015.12.035.

117. Matadi Boumbimba, R.; Froustey, C.; Viot, P.; Gerard, P. Low velocity impact response and damage of laminate composite glass fibre/epoxy based tri-block copolymer.

Compos. Part B Eng. 2015, 76, 332–342, DOI: https://doi.org/10.1016/j.compositesb.2015.02.007.

118. García-Moreno, I.; Caminero, M.Á.; Rodríguez, G.P.; López-Cela, J.J. Effect of thermal ageing on the impact damage resistance and tolerance of carbon fibre-reinforced epoxy laminates. Polymers. 2019, 11, 160, DOI: https://doi.org/10.3390/polym11010160.

119. Reis, P.N.B.; Ferreira, J.A.M.; Zhang, Z.Y.; Benameur, T.; Richardson, M.O.W. Impact response of Kevlar composites with nanoclay enhanced epoxy matrix. Compos. Part B Eng. 2013, 46, 7–14, DOI: https://doi.org/10.1016/j.compositesb.2012.10.028.

120. Aktaş, M.; Atas, C.; Içten, B.M.; Karakuzu, R. An experimental investigation of the impact response of composite laminates. Compos. Struct. 2009, 87, 307–313, DOI: https://doi.org/10.1016/j.compstruct.2008.02.003.

121. Yang, X.; Yi, F.; Xin, Z.; Zheng, S. Morphology and mechanical properties of nanostructured blends of epoxy resin with poly(ε-caprolactone)-block-poly(butadiene-co-acrylonitrile)-block-poly(ε-caprolactone) triblock copolymer. Polymer. 2009, 50, 4089–4100, DOI: https://doi.org/10.1016/j.polymer.2009.06.030.

122. Yee, A.F.; Pearson, R.A. Toughening mechanisms in elastomer-modified epoxies. J. Mater. Sci. 1986, 21, 2462–2474, DOI: https://doi.org/10.1007/BF01114293.

123. Erkendirci, Ö.F.; Haque, B.Z. Quasi-static penetration resistance behavior of glass fiber reinforced thermoplastic composites. Composites Part B: Engineering. December 2012, 43(8), 3391-3405.

124. García-Castillo, S.; Sánchez-Sáez, S.; Santiuste, C.; Barbero, E.; Navarro, C. Perforation of Composite Laminate Subjected to Dynamic Loads. Netherlands: Springer, 978-94-007-5329-7. 2013. 291–337.

125. Alonso, L.; Martínez-Hergueta, F.; Garcia-Gonzalez, D.; Navarro, C.; García-Castillo, S.K.; Teixeira-Dias, F. A finite element approach to model high-velocity impact on thin woven GFRP plates. International Journal of Impact Engineering. August 2020, 142, 103593.

126. Iannucci, L.; Dechaene, R.; Willows, M.; Degrick, J. A failure model for the analysis of thin woven glass composite structures under impact loadings. Computers & Structures. 2001, 79(8), 785–99.

127. Davila, C.; Camacho, P.; Rose, C. Failure criteria for FRP laminates. Journal of Composite Materials. 2005, 39(4), 323–45. https://doi.org/10.1177/0021998305046452.

128. Gower, H.; Cronin, D.; Plumtree, A. Ballistic impact response of laminated composite panels. International Journal of Impact Engineering. 2008, 35(9), 1000–8.

129. Iannucci, L.; Willows, M. An energy based damage mechanics approach to modelling impact onto woven composite materials part i: Numerical models. Composites Part A: Applied science and manufacturing. 2005, 37(11), 2041–56.

130. Nie, Z. Advanced meso mechanical modeling of triaxially braided composites for dynamic impact analysis with failure. 2014.

131. Turon, A.; Dávila, C.; Camaho, P.; Coste, J. An engineering solution for mesh size effects in the simulation of delamination using cohesive zone models. Engineering Fracture Mechanics. 2007, 74(10), 1665–82.

132. Abrate, S. Impact on laminated composite materials. Applied Mech Review. 1991, 44(4), 155–90.

133. Backman, M.E.; Goldsmith, W. The mechanics of penetration of projectiles into targets. Int Jof. Engineering Science. 1978, 16, 1–99.

134. Zukus, J.A. Penetration and perforation of solids. In Zukus JA et al., editors, Impact dynamics. Newyork: Wiley, 1982, 155–214.

135. Cantwell, W. J.; Morton, J. The influence of varying projectile mass on the impact response of cfrp. Composite Structures. 1989, 13, 101–114.

136. Hoo Fatt M.S.; Revilock Jr, D.M.; Lin, C.; Hopkins, D.A. Ballistic impact of glare fiber metal laminates. Composite Structures. 2003, 61, 73–88.

137. Wen, H.M. Predicting the penetration and perforation of frp laminates struck normally by projectiles with different nose shapes. Composite Structures. 2000, 49, 321–329.

138. Zhu, G.; Goldsmith, W.; Dharan, C.K.H. Penetration of laminated kevlar by projectiles-I. Experimental investigation. Int. J. of Solids and Structures. 1992, 29(4), 399–420.

139. Harding, J.; Ruiz, C. The mechanical behaviour of composite materials under impact loading. Key Engineering Materials 1998, 143, 2, 403–26. http://www.scientific.net/KEM.141-143.403

140. García-Castillo, S.; López-Puente, J.; Sánchez Sáez, S.; Barbero, E.; Navarro, C. Analytical model for energy absorption capabilities of glass/polyester panels subjected to ballistic impact. Conference in Developments in Theoretical and Applied Mechanics 2006.

141. Corigliano, A.; Rizzi, E.; Papa, E. Experimental characterization and numerical simulations of a syntactic-foam/glass-fibre composite sandwich. Composites Science and Technology. 2000, 60, 2169–80.

142. Dayou, M.; Manes, A.; Campos-Amico, S.; Giglio, M. Ballistic strain-rate-dependent material modelling of glass-fibre woven composite based on the prediction of a meso-heterogeneous approach. Composite Structures. 2019, 210, 840–57.

143. Moyre, S.; Hine, P.; Duckett, R.; Carr, D.; Ward, I. Modelling of the energy absorption by polymer composites upon ballistic impact. Composites Science and Technology. 2000, 60(14), 2631–42.

144. Naik, N.; Shrirao, P. Composite structures under ballistic impact. Composite Structures. 2004, 66(1–4), 579–90.

Appendix

The following code is the VUMAT material subroutine used in the numerical simulations.

```fortran
      subroutine vumat (
c Read only -
     1 nblock, ndir, nshr, nstatev, nfieldv, nprops, lanneal,
     2 stepTime, totalTime, dt, cmname, coordMp, charLength,
     3 props, density, strainInc, relSpinInc,
     4 tempOld, stretchOld, defgradOld, fieldOld,
     5 stressOld, stateOld, enerInternOld, enerInelasOld,
     6 tempNew, stretchNew, defgradNew, fieldNew,
c Write only -
     7 stressNew, stateNew, enerInternNew, enerInelasNew )
c
      include 'vaba_param.inc'
c
c 3D Orthotropic Elasticity with Hashin 3d Failure criterion
c
c The state variables are stored as:
c   state(*,1)   = material point status
c   state(*,2:7) = damping stresses
c
c User defined material properties are stored as
c  * First line:
c    props(1) --> Young's modulus in 1-direction, E1
c    props(2) --> Young's modulus in 2-direction, E2
c    props(3) --> Young's modulus in 3-direction, E3
c    props(4) --> Poisson's ratio, nu12
c    props(5) --> Poisson's ratio, nu13
c    props(6) --> Poisson's ratio, nu23
c    props(7) --> Shear modulus, G12
c    props(8) --> Shear modulus, G13
c
c  * Second line:
c    props(9)  --> Shear modulus, G23
c    props(10) --> beta damping parameter
c    props(11) --> "not used"
c    props(12) --> "not used"
c    props(13) --> "not used"
c    props(14) --> "not used"
c    props(15) --> "not used"
c    props(16) --> "not used"
c
c  * Third line:
c    props(17) --> Ultimate tens stress in 1-direction, sigu1t
c    props(18) --> Ultimate comp stress in 1-direction, sigu1c
c    props(19) --> Ultimate tens stress in 2-direction, sigu2t
c    props(20) --> Ultimate comp stress in 2-direction, sigu2c
c    props(21) --> Ultimate tens stress in 2-direction, sigu3t
c    props(22) --> Ultimate comp stress in 2-direction, sigu3c
```

```
c    props(23) --> "not used"
c    props(24) --> "not used"
c
c  * Fourth line:
c    props(25) --> Ultimate shear stress, sigu12
c    props(26) --> Ultimate shear stress, sigu13
c    props(27) --> Ultimate shear stress, sigu23
c    props(28) --> "not used"
c    props(29) --> "not used"
c    props(30) --> "not used"
c    props(31) --> "not used"
c    props(32) --> "not used"
c

     dimension props(nprops), density(nblock),
    1 coordMp(nblock,*),
    2 charLength(*), strainInc(nblock,ndir+nshr),
    3 relSpinInc(nblock,nshr), tempOld(nblock),
    4 stretchOld(nblock,ndir+nshr), defgradOld(nblock,ndir+nshr+nshr),
    5 fieldOld(nblock,nfieldv), stressOld(nblock,ndir+nshr),
    6 stateOld(nblock,nstatev), enerInternOld(nblock),
    7 enerInelasOld(nblock), tempNew(*),
    8 stretchNew(nblock,ndir+nshr), defgradNew(nblock,ndir+nshr+nshr),
    9 fieldNew(nblock,nfieldv), stressNew(nblock,ndir+nshr),
    1 stateNew(nblock,nstatev),
    2 enerInternNew(nblock), enerInelasNew(nblock)
*
     character*80 cmname
*
     parameter( zero = 0.d0, one = 1.d0, two = 2.d0, half = .5d0 )
*
     parameter(
    *   i_svd_DmgFiberT   = 1,
    *   i_svd_DmgFiberC   = 2,
    *   i_svd_DmgMatrixT  = 3,
    *   i_svd_DmgMatrixC  = 4,
    *   i_svd_statusMp    = 5,
    *   i_svd_dampStress  = 6,
c   *   i_svd_dampStressXx = 6,
c   *   i_svd_dampStressYy = 7,
c   *   i_svd_dampStressZz = 8,
c   *   i_svd_dampStressXy = 9,
c   *   i_svd_dampStressYz = 10,
c   *   i_svd_dampStressZx = 11,
    *   i_svd_Strain    = 12,
c   *   i_svd_StrainXx = 12,
c   *   i_svd_StrainYy = 13,
c   *   i_svd_StrainZz = 14,
c   *   i_svd_StrainXy = 15,
c   *   i_svd_StrainYz = 16,
c   *   i_svd_StrainZx = 17,
    *   n_svd_required = 17 )
```

```
*
      parameter(
*     i_s33_Xx = 1,
*     i_s33_Yy = 2,
*     i_s33_Zz = 3,
*     i_s33_Xy = 4,
*     i_s33_Yz = 5,
*     i_s33_Zx = 6 )
*
* Structure of property array
      parameter (
*     i_pro_E1   = 1,
*     i_pro_E2   = 2,
*     i_pro_E3   = 3,
*     i_pro_nu12 = 4,
*     i_pro_nu13 = 5,
*     i_pro_nu23 = 6,
*     i_pro_G12  = 7,
*     i_pro_G13  = 8,
*     i_pro_G23  = 9,
*
*     i_pro_beta  = 10,
*
*     i_pro_sigu1t = 17,
*     i_pro_sigu1c = 18,
*     i_pro_sigu2t = 19,
*     i_pro_sigu2c = 20,
*     i_pro_sigu3t = 21,
*     i_pro_sigu3c = 22,
*     i_pro_sigu12 = 25,
*     i_pro_sigu13 = 26,
*     i_pro_sigu23 = 27 )
* Temporary arrays
      dimension eigen(maxblk*3)
*
* Read material properties
*
      E1 = props(i_pro_E1)
      E2 = props(i_pro_E2)
      E3 = props(i_pro_E3)
      xnu12 = props(i_pro_nu12)
      xnu13 = props(i_pro_nu13)
      xnu23 = props(i_pro_nu23)
      G12 = props(i_pro_G12)
      G13 = props(i_pro_G13)
      G23 = props(i_pro_G23)
*
      xnu21 = xnu12 * E2 / E1
      xnu31 = xnu13 * E3 / E1
      xnu32 = xnu23 * E3 / E2
*
*
```

```fortran
* Compute terms of stiffness matrix
      gg = one / ( one - xnu12*xnu21 - xnu23*xnu32 - xnu31*xnu13
     *     - two*xnu21*xnu32*xnu13 )
      C11  = E1 * ( one - xnu23*xnu32 ) * gg
      C22  = E2 * ( one - xnu13*xnu31 ) * gg
      C33  = E3 * ( one - xnu12*xnu21 ) * gg
      C12  = E1 * ( xnu21 + xnu31*xnu23 ) * gg
      C13  = E1 * ( xnu31 + xnu21*xnu32 ) * gg
      C23  = E2 * ( xnu32 + xnu12*xnu31 ) * gg
*
      f1t = props(i_pro_sigu1t)
      f1c = props(i_pro_sigu1c)
      f2t = props(i_pro_sigu2t)
      f2c = props(i_pro_sigu2c)
      f3t = props(i_pro_sigu3t)
      f3c = props(i_pro_sigu3c)
      f12 = props(i_pro_sigu12)
      f13 = props(i_pro_sigu13)
      f23 = props(i_pro_sigu23)
*
      beta = props(i_pro_beta)
*
* Assume purely elastic material at the beginning of the analysis
*
      if ( totalTime .eq. zero ) then
        if (nstatev .lt. n_svd_Required) then
          call xplb_abqerr(-2,'Subroutine VUMAT requires the '//
     *        'specification of %I state variables. Check the '//
     *        'definition of *DEPVAR in the input file.',
     *        n_svd_Required,zero,' ')
          call xplb_exit
        end if
        call OrthoEla3dExp ( nblock,
     *      stateOld(1,i_svd_DmgFiberT),
     *      stateOld(1,i_svd_DmgFiberC),
     *      stateOld(1,i_svd_DmgMatrixT),
     *      stateOld(1,i_svd_DmgMatrixC),
     *      C11, C22, C33, C12, C23, C13, G12, G23, G13,
     *      strainInc,
     *      stressNew )
        return
      end if
*
*  Update total elastic strain
      call strainUpdate ( nblock, strainInc,
     *    stateOld(1,i_svd_strain), stateNew(1,i_svd_strain) )
*
* Stress update
      call OrthoEla3dExp ( nblock,
     *    stateOld(1,i_svd_DmgFiberT),
     *    stateOld(1,i_svd_DmgFiberC),
     *    stateOld(1,i_svd_DmgMatrixT),
```

```
     *       stateOld(1,i_svd_DmgMatrixC),
     *       C11, C22, C33, C12, C23, C13, G12, G23, G13,
     *       stateNew(1,i_svd_strain),
     *       stressNew )
*
* Failure evaluation
*
      call copyr ( nblock,
     *     stateOld(1,i_svd_DmgFiberT), stateNew(1,i_svd_DmgFiberT) )
      call copyr ( nblock,
     *     stateOld(1,i_svd_DmgFiberC), stateNew(1,i_svd_DmgFiberC) )
      call copyr ( nblock,
     *     stateOld(1,i_svd_DmgMatrixT), stateNew(1,i_svd_DmgMatrixT) )
      call copyr ( nblock,
     *     stateOld(1,i_svd_DmgMatrixC), stateNew(1,i_svd_DmgMatrixC) )
      nDmg = 0
      call eig33Anal ( nblock, stretchNew, eigen )
      call Hashin3d  ( nblock, nDmg,
     *    f1t, f2t, f3t, f1c, f2c, f3c, f12, f23, f13,
     *    stateNew(1,i_svd_DmgFiberT),
     *    stateNew(1,i_svd_DmgFiberC),
     *    stateNew(1,i_svd_DmgMatrixT),
     *    stateNew(1,i_svd_DmgMatrixC),
     *    stateNew(1,i_svd_statusMp),
     *    stressNew, eigen )
*     -- Recompute stresses if new Damage is occurring
      if ( nDmg .gt. 0 ) then
        call OrthoEla3dExp ( nblock,
     *      stateNew(1,i_svd_DmgFiberT),
     *      stateNew(1,i_svd_DmgFiberC),
     *      stateNew(1,i_svd_DmgMatrixT),
     *      stateNew(1,i_svd_DmgMatrixC),
     *      C11, C22, C33, C12, C23, C13, G12, G23, G13,
     *      stateNew(1,i_svd_strain),
     *      stressNew )
      end if
*
* Beta damping
      if ( beta .gt. zero ) then
        call betaDamping3d ( nblock,
     *      beta, dt, strainInc,
     *      stressOld, stressNew,
     *      stateNew(1,i_svd_statusMp),
     *      stateOld(1,i_svd_dampStress),
     *      stateNew(1,i_svd_dampStress) )
      end if
*
* Integrate the internal specific energy (per unit mass)
*
      call EnergyInternal3d ( nblock, stressOld, stressNew,
     *   strainInc, density, enerInternOld, enerInternNew )
*
```

```fortran
      return
      end


*****************************************************
*  OrthoEla3dExp: Orthotropic elasticity - 3d       *
*****************************************************
      subroutine OrthoEla3dExp ( nblock,
     *    dmgFiberT, dmgFiberC, dmgMatrixT, dmgMatrixC,
     *    C11, C22, C33, C12, C23, C13, G12, G23, G13,
     *    strain, stress )
*
      include 'vaba_param.inc'

* Orthotropic elasticity, 3D case -
*
      parameter( zero = 0.d0, one = 1.d0, two = 2.d0)
      parameter(
     *    i_s33_Xx = 1,
     *    i_s33_Yy = 2,
     *    i_s33_Zz = 3,
     *    i_s33_Xy = 4,
     *    i_s33_Yz = 5,
     *    i_s33_Zx = 6,
     *    n_s33_Car = 6 )
*
      dimension  strain(nblock,n_s33_Car),
     *    dmgFiberT(nblock), dmgFiberC(nblock),
     *    dmgMatrixT(nblock), dmgMatrixC(nblock),
     *    stress(nblock,n_s33_Car)
*    -- shear fraction in matrix tension and compression mode
      parameter ( smt = 0.9d0, smc = 0.5d0 )
*
      do k = 1, nblock
*    -- Compute damaged stiffness
        dft = dmgFiberT(k)
        dfc = dmgFiberC(k)
        dmt = dmgMatrixT(k)
        dmc = dmgMatrixC(k)
        df = one - ( one - dft ) * ( one - dfc )
*
        dC11 = ( one - df ) * C11
        dC22 = ( one - df ) * ( one - dmt ) * ( one - dmc ) * C22
        dC33 = ( one - df ) * ( one - dmt ) * ( one - dmc ) * C33
        dC12 = ( one - df ) * ( one - dmt ) * ( one - dmc ) * C12
        dC23 = ( one - df ) * ( one - dmt ) * ( one - dmc ) * C23
        dC13 = ( one - df ) * ( one - dmt ) * ( one - dmc ) * C13
        dG12 = ( one - df )
     *      * ( one - smt*dmt ) * ( one - smc*dmc ) * G12
        dG23 = ( one - df )
     *      * ( one - smt*dmt ) * ( one - smc*dmc ) * G23
        dG13 = ( one - df )
```

```fortran
*         * ( one - smt*dmt ) * ( one - smc*dmc ) * G13
*    -- Stress update
      stress(k,i_s33_Xx) = dC11 * strain(k,i_s33_Xx)
*         + dC12 * strain(k,i_s33_Yy)
*         + dC13 * strain(k,i_s33_Zz)
      stress(k,i_s33_Yy) = dC12 * strain(k,i_s33_Xx)
*         + dC22 * strain(k,i_s33_Yy)
*         + dC23 * strain(k,i_s33_Zz)
      stress(k,i_s33_Zz) = dC13 * strain(k,i_s33_Xx)
*         + dC23 * strain(k,i_s33_Yy)
*         + dC33 * strain(k,i_s33_Zz)
      stress(k,i_s33_Xy) = two * dG12 * strain(k,i_s33_Xy)
      stress(k,i_s33_Yz) = two * dG23 * strain(k,i_s33_Yz)
      stress(k,i_s33_Zx) = two * dG13 * strain(k,i_s33_Zx)
      end do
*

      return
      end


***************************************************************
*   strainUpdate: Update total strain              *
***************************************************************
      subroutine strainUpdate ( nblock,
*      strainInc, strainOld, strainNew )
*
      include 'vaba_param.inc'
*
      parameter(
*     i_s33_Xx = 1,
*     i_s33_Yy = 2,
*     i_s33_Zz = 3,
*     i_s33_Xy = 4,
*     i_s33_Yz = 5,
*     i_s33_Zx = 6,
*     n_s33_Car = 6 )
*
      dimension strainInc(nblock,n_s33_Car),
*      strainOld(nblock,n_s33_Car),
*      strainNew(nblock,n_s33_Car)
*
      do k = 1, nblock
      strainNew(k,i_s33_Xx)= strainOld(k,i_s33_Xx)
*              + strainInc(k,i_s33_Xx)
      strainNew(k,i_s33_Yy)= strainOld(k,i_s33_Yy)
*              + strainInc(k,i_s33_Yy)
      strainNew(k,i_s33_Zz)= strainOld(k,i_s33_Zz)
*              + strainInc(k,i_s33_Zz)
      strainNew(k,i_s33_Xy)= strainOld(k,i_s33_Xy)
*              + strainInc(k,i_s33_Xy)
      strainNew(k,i_s33_Yz)= strainOld(k,i_s33_Yz)
*              + strainInc(k,i_s33_Yz)
      strainNew(k,i_s33_Zx)= strainOld(k,i_s33_Zx)
```

```fortran
*                     + strainInc(k,i_s33_Zx)
      end do
*
      return
      end


************************************************************
*   Hashin3d w/ Modified Puck: Evaluate Hashin 3d failure  *
*   criterion for fiber, Puck for matrix            *
************************************************************
      subroutine Hashin3d ( nblock, nDmg,
     *    f1t, f2t, f3t, f1c, f2c, f3c, f12, f23, f13,
     *    dmgFiberT, dmgFiberC, dmgMatrixT, dmgMatrixC,
     *    statusMp, stress, eigen )
*
      include 'vaba_param.inc'

      parameter( zero = 0.d0, one = 1.d0, half = 0.5d0, three =3.d0 )
      parameter(
     *    i_s33_Xx = 1,
     *    i_s33_Yy = 2,
     *    i_s33_Zz = 3,
     *    i_s33_Xy = 4,
     *    i_s33_Yz = 5,
     *    i_s33_Zx = 6,
     *    n_s33_Car = 6 )
*
      parameter(i_v3d_X=1,i_v3d_Y=2,i_v3d_Z=3 )
      parameter(n_v3d_Car=3 )
*
      parameter ( eMax = 1.00d0, eMin = -0.8d0 )
*
      dimension  dmgFiberT(nblock), dmgFiberC(nblock),
     *    dmgMatrixT(nblock), dmgMatrixC(nblock),
     *    stress(nblock,n_s33_Car),
     *    eigen(nblock,n_v3d_Car),
     *    statusMp(nblock)
*
      f1tInv = zero
      f2tInv = zero
      f3tInv = zero
      f1cInv = zero
      f2cInv = zero
      f3cInv = zero
      f12Inv = zero
      f23Inv = zero
      f13Inv = zero
*
      if ( f1t .gt. zero ) f1tInv = one / f1t
      if ( f2t .gt. zero ) f2tInv = one / f2t
      if ( f3t .gt. zero ) f3tInv = one / f3t
```

```
      if ( f1c .gt. zero ) f1cInv = one / f1c
      if ( f2c .gt. zero ) f2cInv = one / f2c
      if ( f3c .gt. zero ) f3cInv = one / f3c
      if ( f12 .gt. zero ) f12Inv = one / f12
      if ( f23 .gt. zero ) f23Inv = one / f23
      if ( f13 .gt. zero ) f13Inv = one / f13
*
      do k = 1, nblock
        if ( statusMp(k) .eq. one ) then
*
        nDmk = 0
*
        s11 = stress(k,i_s33_Xx)
        s22 = stress(k,i_s33_Yy)
        s33 = stress(k,i_s33_Zz)
        s12 = stress(k,i_s33_Xy)
        s23 = stress(k,i_s33_Yz)
        s13 = stress(k,i_s33_Zx)
*
*   Evaluate Fiber modes in warp direction
        if ( s11 .gt. zero ) then
*     -- Tensile Fiber Mode
          rft = (s11*f1tInv )**2 + (s12*f12Inv )**2 + (s13*f13Inv )**2
          if ( rft .ge. one ) then
            lDmg = 1
            dmgFiberT(k) = one
          end if
        else if ( s11 .lt. zero ) then
*     -- Compressive Fiber Mode
          rfc = abs(s11) * f1cInv
          if ( rfc .ge. one ) then
            lDmg = 1
            dmgFiberC(k) = one
          end if
        end if
*   Evaluate Fiber modes in weft direction
        if ( s22 .gt. zero ) then
*     -- Tensile Fiber Mode
          rft = (s22*f2tInv )**2 + (s12*f12Inv )**2 + (s23*f23Inv )**2
          if ( rft .ge. one ) then
            lDmg = 1
            dmgFiberT(k) = one
          end if
        else if ( s22 .lt. zero ) then
*     -- Compressive Fiber Mode
          rfc = abs(s22) * f2cInv
          if ( rfc .ge. one ) then
            lDmg = 1
            dmgFiberC(k) = one
          end if
        end if
*
```

```
*    Evaluate Matrix Modes
       if ( s22 + s33 .gt. zero ) then
*    -- Tensile Matrix mode
         rmt = ( s11 * half * f1tInv )**2
*          + ( (s22 + s33)**2 * abs(f2tInv * f2cInv) )
*          + ( s12 * f12Inv )**2
*          + ( (s22 + s33) * (f2tInv + f2cInv) )
         if ( rmt .ge. one ) then
           lDmg = 1
           dmgMatrixT(k) = one
         end if
       else if ( s22 + s33 .lt. zero ) then
*    -- Compressive Matrix Mode
         rmc = ( s11 * half * f1tInv )**2
*          + ( (s22 + s33)**2 * abs(f2tInv * f2cInv) )
*          + ( s12 * f12Inv )**2
*          + ( (s22 + s33) * (f2tInv + f2cInv) )
         if ( rmc .ge. one ) then
           lDmg = 1
           dmgMatrixC(k) = one
         end if
       end if
*
       eigMax=max(eigen(k,i_v3d_X),eigen(k,i_v3d_Y),eigen(k,i_v3d_Z))
       eigMin=min(eigen(k,i_v3d_X),eigen(k,i_v3d_Y),eigen(k,i_v3d_Z))
       enomMax = eigMax - one
       enomMin = eigMin - one
*
       if ( enomMax .gt. eMax .or.
*          enomMin .lt. eMin .or.
*          dmgFiberT(k) .eq. one ) then
         statusMp(k) = zero
       end if
*
       nDmg = nDmk + lDmg
*
       end if
*
     end do
*
     return
     end


***********************************************************
*  betaDamping: Add beta damping                    *
***********************************************************
   subroutine betaDamping3d ( nblock,
*    beta, dt, strainInc, sigOld, sigNew,
*    statusMp, sigDampOld, sigDampNew )
*
   include 'vaba_param.inc'
```

```
*

      parameter(
*     i_s33_Xx = 1,
*     i_s33_Yy = 2,
*     i_s33_Zz = 3,
*     i_s33_Xy = 4,
*     i_s33_Yz = 5,
*     i_s33_Zx = 6,
*     n_s33_Car = 6 )
*

      dimension  sigOld(nblock,n_s33_Car),
*     sigNew(nblock,n_s33_Car),
*     strainInc(nblock,n_s33_Car),
*     statusMp(nblock),
*     sigDampOld(nblock,n_s33_Car),
*     sigDampNew(nblock,n_s33_Car)
*

      parameter ( zero = 0.d0, one = 1.d0, two=2.0d0,
*     half = 0.5d0, third = 1.d0/3.d0 )
      parameter ( asmall = 1.d-16 )
*

      betaddt =  beta / dt
*

      do k =1 , nblock
        sigDampNew(k,i_s33_Xx) = betaddt * statusMp(k) *
*         ( sigNew(k,i_s33_Xx)
*         - ( sigOld(k,i_s33_Xx) - sigDampOld(k,i_s33_Xx) ) )
        sigDampNew(k,i_s33_Yy) = betaddt * statusMp(k) *
*         ( sigNew(k,i_s33_Yy)
*         - ( sigOld(k,i_s33_Yy) - sigDampOld(k,i_s33_Yy) ) )
        sigDampNew(k,i_s33_Zz) = betaddt * statusMp(k) *
*         ( sigNew(k,i_s33_Zz)
*         - ( sigOld(k,i_s33_Zz) - sigDampOld(k,i_s33_Zz) ) )
        sigDampNew(k,i_s33_Xy) = betaddt * statusMp(k) *
*         ( sigNew(k,i_s33_Xy)
*         - ( sigOld(k,i_s33_Xy) - sigDampOld(k,i_s33_Xy) ) )
        sigDampNew(k,i_s33_Yz) = betaddt * statusMp(k) *
*         ( sigNew(k,i_s33_Yz)
*         - ( sigOld(k,i_s33_Yz) - sigDampOld(k,i_s33_Yz) ) )
        sigDampNew(k,i_s33_Zx) = betaddt * statusMp(k) *
*         ( sigNew(k,i_s33_Zx)
*         - ( sigOld(k,i_s33_Zx) - sigDampOld(k,i_s33_Zx) ) )
*

        sigNew(k,i_s33_Xx) = sigNew(k,i_s33_Xx)+sigDampNew(k,i_s33_Xx)
        sigNew(k,i_s33_Yy) = sigNew(k,i_s33_Yy)+sigDampNew(k,i_s33_Yy)
        sigNew(k,i_s33_Zz) = sigNew(k,i_s33_Zz)+sigDampNew(k,i_s33_Zz)
        sigNew(k,i_s33_Xy) = sigNew(k,i_s33_Xy)+sigDampNew(k,i_s33_Xy)
        sigNew(k,i_s33_Yz) = sigNew(k,i_s33_Yz)+sigDampNew(k,i_s33_Yz)
        sigNew(k,i_s33_Zx) = sigNew(k,i_s33_Zx)+sigDampNew(k,i_s33_Zx)
*

      end do
*
```

```fortran
      return
      end


***********************************************************
*  EnergyInternal3d: Compute internal energy for 3d case  *
***********************************************************
      subroutine EnergyInternal3d(nblock, sigOld, sigNew ,
     *   strainInc, curDensity, enerInternOld, enerInternNew)
*
      include 'vaba_param.inc'
*
      parameter(
     *   i_s33_Xx = 1,
     *   i_s33_Yy = 2,
     *   i_s33_Zz = 3,
     *   i_s33_Xy = 4,
     *   i_s33_Yz = 5,
     *   i_s33_Zx = 6,
     *   n_s33_Car = 6 )
*
      parameter( two = 2.d0, half = .5d0 )
*
      dimension sigOld (nblock,n_s33_Car), sigNew (nblock,n_s33_Car),
     *    strainInc (nblock,n_s33_Car), curDensity (nblock),
     *    enerInternOld(nblock), enerInternNew(nblock)
*
      do k = 1, nblock
        stressPower  = half * (
     *      ( sigOld(k,i_s33_Xx) + sigNew(k,i_s33_Xx) )
     *      * ( strainInc(k,i_s33_Xx) )
     *      +    ( sigOld(k,i_s33_Yy) + sigNew(k,i_s33_Yy) )
     *      * ( strainInc(k,i_s33_Yy))
     *      +    ( sigOld(k,i_s33_Zz) + sigNew(k,i_s33_Zz) )
     *      * ( strainInc(k,i_s33_Zz))
     *      + two * ( sigOld(k,i_s33_Xy) + sigNew(k,i_s33_Xy) )
     *      * strainInc(k,i_s33_Xy)
     *      + two * ( sigOld(k,i_s33_Yz) + sigNew(k,i_s33_Yz) )
     *      * strainInc(k,i_s33_Yz)
     *      + two * ( sigOld(k,i_s33_Zx) + sigNew(k,i_s33_Zx) )
     *      * strainInc(k,i_s33_Zx) )
*
        enerInternNew(k) = enerInternOld(k) + stressPower/curDensity(k)
      end do
*
      return
      end


***********************************************************
*  CopyR: Copy from one array to another              *
***********************************************************
      subroutine CopyR(nCopy, from, to )
```

```
*
      include 'vaba_param.inc'
*
      dimension from(nCopy), to(nCopy)
*
      do k = 1, nCopy
        to(k) = from(k)
      end do
*
      return
      end


***********************************************************************
* eig33Anal: Compute eigen values of a 3x3 symmetric matrix analytically *
***********************************************************************
      subroutine eig33Anal( nblock, sMat, eigVal )
*
      include 'vaba_param.inc'
*
      parameter(i_s33_Xx=1,i_s33_Yy=2,i_s33_Zz=3 )
      parameter(i_s33_Xy=4,i_s33_Yz=5,i_s33_Zx=6 )
      parameter(i_s33_Yx=i_s33_Xy )
      parameter(i_s33_Zy=i_s33_Yz )
      parameter(i_s33_Xz=i_s33_Zx,n_s33_Car=6 )
*
      parameter(i_v3d_X=1,i_v3d_Y=2,i_v3d_Z=3 )
      parameter(n_v3d_Car=3 )
*
      parameter ( zero = 0.d0, one = 1.d0, two = 2.d0,
     *    three = 3.d0, half = 0.5d0, third = one / three,
     *    pi23 = 2.094395102393195d0,
     *    fuzz = 1.d-8,
     *    preciz = fuzz * 1.d4 )
*
      dimension eigVal(nblock,n_v3d_Car), sMat(nblock,n_s33_Car)
*
      do k = 1, nblock
        sh  = third*(sMat(k,i_s33_Xx)+sMat(k,i_s33_Yy)+sMat(k,i_s33_Zz))
        s11 = sMat(k,i_s33_Xx) - sh
        s22 = sMat(k,i_s33_Yy) - sh
        s33 = sMat(k,i_s33_Zz) - sh
        s12 = sMat(k,i_s33_Xy)
        s13 = sMat(k,i_s33_Xz)
        s23 = sMat(k,i_s33_Yz)
*
        fac  = max(abs(s11), abs(s22), abs(s33))
        facs = max(abs(s12), abs(s13), abs(s23))
        if( facs .lt. (preciz*fac) ) then
          eigVal(k,i_v3d_X) = sMat(k,i_s33_Xx)
          eigVal(k,i_v3d_Y) = sMat(k,i_s33_Yy)
          eigVal(k,i_v3d_Z) = sMat(k,i_s33_Zz)
        else
```

```
      q = third*((s12**2+s13**2+s23**2)+half*(s11**2+s22**2+s33**2))
      fac = two * sqrt(q)
      if( fac .gt. fuzz ) then
        ofac = two/fac
      else
        ofac = zero
      end if
      s11 = ofac*s11
      s22 = ofac*s22
      s33 = ofac*s33
      s12 = ofac*s12
      s13 = ofac*s13
      s23 = ofac*s23
      r = s12*s13*s23
*         + half*(s11*s22*s33-s11*s23**2-s22*s13**2-s33*s12**2)
      if( r .ge. one-fuzz ) then
        cos1 = -half
        cos2 = -half
        cos3 = one
      else if( r .le. fuzz-one ) then
        cos1 = -one
        cos2 = half
        cos3 = half
      else
        ang = third * acos(r)
        cos1 = cos(ang)
        cos2 = cos(ang+pi23)
        cos3 =-cos1-cos2
      end if
      eigVal(k,i_v3d_X) = sh + fac*cos1
      eigVal(k,i_v3d_Y) = sh + fac*cos2
      eigVal(k,i_v3d_Z) = sh + fac*cos3
     end if
    end do
*
    return
    end
```

Résume

Encouragée par les dernières normes européennes sur les émissions de dioxyde de carbone et les exigences de recyclage actuelles, l'utilisation des composites à matrices organiques dans l'industrie des transports a connu un essor considérable ces dernières années. Outre la réduction de la masse des structures, ces matériaux possèdent d'excellentes propriétés mécaniques et s'adaptent facilement aux éléments structurels à géométrie complexe, sans pourtant perdre leurs propriétés. Parmi ces matériaux composites, les nouveaux composites stratifiés à matrice thermoplastique, Elium acrylique connaissent de nos jours un intérêt de plus en plus grandissant.

L'un des principaux avantages des résines thermoplastiques liquides, est leur compatibilité avec un large panel de procédés de préparation, qui étaient jusque-là réservés aux composites à matrices thermodurcissables. Cela permet une réduction significative du coût de leur utilisation dans des domaines tels que le génie civil et l'industrie automobile.

En 2015, l'entreprise chimique ARKEMA a développé dans son laboratoire une nouvelle résine thermoplastique liquide et recyclable, appelée ELIUM. Elle offre la possibilité de fabriquer les composites en un temps record, ce qui diminue le prix final des composites stratifiés résultants. Afin d'augmenter la résistance des composites stratifiés, Elium est utilisé en combinaison avec des fibres de verre ou de carbone uni ou bidirectionnelles. Les stratifiés avec des fibres de verre bidirectionnelles ou à armure taffetas bénéficient d'une répartition plus ou moins équilibrée de leurs propriétés mécaniques suivant les directions principales du plan. Ils sont les plus avantageux pour les constructeurs automobiles. Par conséquent, dans cette thèse, un composite stratifié à base de résine Elium acrylique et de quatre couches de tissu en fibres de verre à armure taffetas, a été étudié.

Différentes études sur les composites à matrice Elium acrylique ont été publiées à ce jour [5-11]. Elles montrent que les propriétés thermomécaniques des composites stratifiés fibres de verre/ Elium acrylique sont similaires, voir meilleurs que celles des composites à base de résines thermodurcissables.

Il va de soi que la résistance à l'impact est l'une des caractéristiques les plus importantes que les fabricants de pièces automobiles envisagent. Elle détermine la durée de vie de l'élément ainsi que sa sécurité. Il est donc très important de comprendre comment les

propriétés à l'impact peuvent être affectées par l'endommagement et la cinétique de rupture qui se produisent lors de l'exploitation des structures. Dans cette thèse (suivant les objectifs du projet COACH), le vieillissement en fatigue a été identifié comme processus pouvant affecter la structure interne du CFRA et, par conséquent, détériorer ses propriétés à l'impact. Etant donné que les composites contenant des tissus de fibres à armure taffetas possèdent des propriétés quasi identiques dans le sens chaîne et trame, nous avons uniquement retenu deux orientations dans le cadre de cette étude. Dans le premier cas, les fibres sont disposées suivant les axes principaux. Dans le second cas, elles forment un angle de 45 degrés par rapport à ces derniers. Appelés « dans l'axe » (GFRE$[0°/90°]_4$) et « hors axe » (GFRE$[45°/45°]_4$), ces deux cas sont respectivement associés à la ténacité la plus forte et la plus faible du matériau étudié. La force appliquée aux composites stratifiés « hors axes » lors de leur vieillissement par fatigue n'est pas transmise à travers la fibre, si bien que leur réponse dépend principalement de la rigidité et de la résistance de la matrice elle-même ainsi que de la qualité de l'interface fibre/matrice. A l'inverse, le chargement cyclique est effectué le long des fibres pour les stratifiés « dans l'axe ». Les fibres ayant un module d'élasticité beaucoup plus élevé que celui de la matrice, l'endommagement par fatigue se produit généralement dans les fibres transversales, ce qui n'entraîne pas de diminution significative de la rigidité et de la résistance à l'impact qui en dépend. ***Ainsi, l'objectif principal de cette thèse est consacré à la vérification des hypothèses suivantes :***

- les stratifiés à matrice thermoplastique renforcés par des fibres de verre « dans l'axe », d'abord soumis à un vieillissement en fatigue puis soumis à un impact basse vitesse, au moyen d'un puit de chute, conservent leur excellente tenue à l'impact. Ceci est valable surtout pour les composites stratifiés vieillis à un niveau de contrainte inférieur à la limite d'élasticité.

- les stratifiés contenant de l'Elium, sensible à la vitesse de déformation, ont une réponse balistique après vieillissement supérieure lorsqu'ils sont renforcés « dans l'axe » plutôt que « hors axe ».

Trois types d'expériences ont été menés afin d'analyser l'effet du vieillissement par fatigue sur le comportement à l'impact des stratifiés fibres de verre/Elium acrylique :

La première expérience (i) consiste en un chargement cyclique uni-axial (vieillissement par fatigue), qui est suivi soit d'un essai d'impact basse vitesse (ii) ou soit d'un essai de perforation (iii), (impact à grande vitesse). La perte de ténacité et donc de la capacité de dissipation d'énergie sont ainsi quantifiées en fonction de la vitesse d'impact. De plus, un modèle éléments finis 3D simple basé sur les critères de rupture de Hashin modifiés permettant de comparer les données expérimentales et numériques a été proposé.

1.1 Caractéristiques des matériaux de l'étude

La méthode d'infusion sous vide, décrite dans [9] (Figs. 2-2 et 2-3), a été utilisée pour la production des plaques composites. Le matériau testé était un composite stratifié à matrice Elium acrylique. La formulation de la résine utilisée dans cette thèse est de l'Elium 150 (de viscosité ϑc = 150 cPs), développée par le groupe ARKEMA. Sa température de transition vitreuse se situe autour de 105°C (Tg = 105°C). Cette résine contient en plus du monomère acrylique, un agent accélérateur ((Luperox®) ~ 2,5 %) permettant d'activer le catalyseur qui provoque la réaction de polymérisation. Le renfort utilisé est un tissu bidirectionnel en fibres de verre fourni par la société Chomarat. Il est constitué de files (ou mèches) entrecroisés dans les sens chaine et trame (Fig. 2-1). La période de répétition du motif du tissu est T = 7.8 mm et sa densité surfacique vaut d_s = 600 g/m^2.

Il est communément admis que l'orientation des fibres a un effet indéniable sur les propriétés des composites stratifiés. C'est pourquoi les éprouvettes composées d'une matrice acrylique et de quatre couches de tissé ont été découpées à l'aide d'une machine à jet d'eau (Fig. 2-5), la découpe s'effectuant soit :

- le long des fibres, GFRE[0°/90°]$_4$.
- avec un angle de 45 degrés par rapport à celui des fibres, GFRE[45°/45°]$_4$.

Afin de déterminer les limites de rupture ainsi que les modules de cisaillement et d'Young des matériaux étudiés suivant des directions ans le plan et hors du plan, quatre types d'expériences mécaniques ont été réalisées :

- l'essai de traction uni-axiale dans le sens des fibres (détermination de E_{11} ou E_{22} ainsi que du coefficient de Poisson v_{12}).
- l'essai de cisaillement dans le plan (G_{12}).
- l'essai de flexion trois points faisceau court (valeurs pour la détermination de G_{23}),

- le test de compression hors plan (pour estimer E_{33} et v_{13} ou v_{23}).

Tous les tests ont été effectués conformément aux normes, à l'aide de la machine hydraulique servo uni-axiale MTS 810 visible sur la Figure 2-9 (a). Les essais de traction avec déplacement contrôlé ont été réalisés à température ambiante avec un extensomètre couvrant une plage de déformation de ± 0.2. La cellule de chargement a été calibrée dans la plage de ±250 kN. De plus, afin de déterminer le coefficient de Poisson, un système de corrélation d'images numériques (DIC) a été employé.

Les propriétés en traction et en cisaillement du GFRE [0°/90°]$_4$ testé, sont répertoriées dans les Tableaux 2-4 et 2-6, tandis que celles du GFRE [45°/45°]$_4$ dans les Tableaux 2-5 et 2-7. Concernant les propriétés de compression du stratifié tissé en fibre de verre/acrylique Elium, le Tableau 2-8 regroupe, entre autre, le module de Young hors du plan E_{33}, la contrainte maximale σ_{33} et la déformation maximale ε_{33}, ainsi que les coefficients de Poisson v_{13}. L'étude expérimentale du comportement mécanique sous chargements quasi-statiques a permis d'élaborer les courbes « contrainte nominale – déformation nominale » pour toutes les directions de chargement considérées. Le composite stratifié a un comportement anisotrope qui est fortement lié aux directions de chargement. La non-linéarité du comportement des plis a donc été clairement observée dans tous les cas de chargement. Le comportement élasto-viscoplastique constaté avec la résine acrylique est également bien connu, puisqu'il concerne la plupart des polymères. Un tel comportement a notamment été mis en évidence par Couegnat [88] sur un composite tissé carbone/époxy lors de la relaxation de la déformation résiduelle après déchargement. Il faut souligner que les écoulements visqueux et plastiques ne sont pas les seuls processus responsables de la non-linéarité des stratifiés, qui peut également être due à des mécanismes d'endommagement [89].

Les composites soumis à des chocs à basse et à haute vitesse étant très sensibles au délaminage, les paramètres de la loi cohésive ont été déterminés par la suite. Dans ce travail, la méthode la plus courante basée sur la théorie des faisceaux a été utilisée [91] afin de quantifier le taux de restitution d'énergie en Mode I. Sur la base de cette théorie, la valeur de la ténacité avant amorçage de fissure en mode I pur a été estimée à G_{IC} = 2.1 N/mm, comme présenté à la Fig. 2-25. La valeur de la ténacité avant amorçage de fissure en

mode II pur, a quant à elle été tirée de la littérature [54], et vaut E_{IIC} = 3.84 N/mm pour le matériau testé.

Ensuite, les propriétés dynamiques de la résine Elium acrylique pure, d'une part, et renforcée en fibres de verre, d'autre part, ont été quantifiées pour différentes températures et vitesses de déformation au moyen des barres de Hopkinson [111]. La Fig.2-29 montre les éprouvettes testées et leur orientation dans le système XYZ. Afin d'étudier la sensibilité à la vitesse de déformation de ces matériaux et l'influence des renforts alignés perpendiculairement à la direction d'impact, des expériences de chargement dynamique ont été menées pour des vitesses de déformation allant de 1000/s à ≈2500/s pour les composites, et de 750/s à ≈2000/s pour la résine pure. La Fig. 2-31 présente les courbes contrainte – déformation de l'acrylique Elium 150 étudiée, pour différentes températures et différentes vitesses de déformation. À leur tour, les Fig. 2-33 et 2-34 présentent respectivement les propriétés hors plan de l'Elium acrylique renforcée et de l'Epoxy (pour comparaison). A des températures de 50 et 80 degrés Celsius, le composite Elium renforcé de fibres de verre semble être légèrement plus sensible aux effets de la vitesse de déformation que l'époxy renforcée en fibres de verre. Cependant, les deux matériaux ont presque la même déformation dans des conditions dynamiques. Sur la base de ces résultats, on peut conclure que l'Elium150 pur est plus sensible à la température que les deux composites. De plus, sa sensibilité à la vitesse de déformation apparaît plus élevée à température ambiante qu'à 50°C ou 80°C. Par conséquent, l'ajout de la phase renforçant augmente significativement la résistance et réduit l'effet de la température du composite testé, ceci est particulièrement visible à 50°C.

Enfin, les données expérimentales de compression dynamique pour l'Elium pur ont été comparées aux prédictions du modèle de Nasraoui [109], (Figs. 2-30 et 2-32). Le Tableau 2-9 regroupe les paramètres identifiés pour ce modèle.

1.2 Vieillissement en fatigue

La fatigue est le changement structurel progressif, localisé et irréversible, qui se produit dans les matériaux soumis à des contraintes et des déformations cycliques, lesquelles entraînent un endommagement interne du matériau après un nombre donné de cycles. L'endommagent en fatigue est l'un des types de dommages matériels les plus dangereux car il peut se produire à de faibles valeurs de contraintes (même bien en dessous de la limite

d'élasticité du matériau). Généralement, la fatigue a été divisée en deux catégories, selon que le niveau de contrainte est inférieur ou supérieur à la limite d'élasticité. Dans le premier cas, la fatigue est dite polycyclique (HCF). Principalement élastique, elle nécessite plus de 10^4 cycles pour atteindre la rupture. Dans le second cas, la fatigue est oligocyclique (LCF), et se caractérise par une plasticité importante.

L'endommagement en fatigue dans les composites stratifiés évolue différemment de celui des métaux. La Fig. 1-7 montre le comportement typique des deux matériaux en fonction du nombre de cycles jusqu'à la rupture. En ce qui concerne le composite tissé, les principaux dommages par fatigue sont la fissuration de la matrice, le délaminage, le décollement de l'interface fibre/matrice et la rupture des fibres. Selon leur degré d'évolution, la résistance à la fatigue et la rigidité des composites stratifiés est diminuée [5]. Il est donc très important d'étudier les propriétés de fatigue des composites dans une large plage de conditions de chargement.

La forme et les dimensions des éprouvettes utilisées pour les essais de vieillissement en fatigue sont présentées à la Fig. 3-1(a). La dimension de la zone utile (ligne rouge pointillée) est de 100 mm × 100 mm et correspond à la dimension des éprouvettes utilisées lors des essais d'impact ultérieurs. La forme et les dimensions des éprouvettes ont été étudiées pour assurer une bonne homogénéité et concentration de la distribution des contraintes dans la zone d'impact. Elle a été vérifiée par les nombreux essais de fatigue à différent niveaux de contrainte. La Fig. 3-1(b) montre l'emplacement des dommages résultant des chargements en fatigue.

La machine d'essai servo-hydraulique uni-axiale MTS 810 d'une capacité de charge allant jusqu'à 250 kN a été utilisée dans toutes les expériences de vieillissement par fatigue. Un système de préhension spécial a été élaboré pour fixer les éprouvettes dans les mâchoires de la machine d'essai (Fig. 3-9 (a)). Afin de déterminer les variations de rigidité au cours des essais, un extensomètre de déformation MTS de la plage de ± 0.2 a été appliqué. Le chargement cyclique a été effectué en faisant varier la force entre une valeur maximale (F_{max}) et une valeur minimale (F_{min}) et à une fréquence de 2 Hz. Le mode de chargement sinusoïdal a été caractérisé par $R = F_{min}/F_{max} = 0,1$. Le programme de fatigue a été divisé en deux types de blocs repérés par des couleurs bleues et rouges sur la Fig. 3-9 (b). Dans les blocs du premier type, le module d'élasticité a été déterminé sur la base d'un simple essai de

traction. La force maximale pendant chaque essai de traction était inférieure à celle correspondant au niveau de chargement moyen pendant le processus de vieillissement par fatigue exécuté dans le deuxième bloc. Pour le deuxième type de blocs, un nombre donné de chargements cycliques de traction uni-axiale a été appliqué. Les conditions détaillées de vieillissement par fatigue pour les deux composites stratifiés testés sous LCF et HCF sont présentées dans le Tableau 3-3.

Tous les essais de fatigue ont commencé par la détermination du module de Young (E_0), puis les blocs de cycles de chargement sélectionnés ont été exécutés. Après le dernier cycle, l'éprouvette a été démontée à force nulle et le module d'élasticité résiduel E_i a été déterminé. Les variations du module d'élasticité sous chargement cyclique pour les essais LCF et HCF sont présentées dans les Fig. 3-10 et 3-11, respectivement.

Les niveaux de contrainte des tests LCF étaient supérieurs à la limite d'élasticité. Pour les éprouvettes orientées à [0°/90°]$_4$, le niveau de contrainte était égal à 250 MPa, c'est-à-dire 35 MPa au-dessus de la limite d'élasticité, (voir Tableau 3-3). Dans le cas des éprouvettes orientées [45°/45°]$_4$, elle était de 80 MPa, soit 22 MPa au-dessus de la limite d'élasticité (Tableau 3-3). Chaque bloc utilisé pour la réduction de la rigidité du matériau testé contenait n_i = 500 cycles. Comme observé sur la Fig. 3-10, la variation de rigidité en fonction du nombre de cycles présente trois zones bien distinctes, pour les deux matériaux testés. Dans la première partie des courbes (jusqu'au point B), sa valeur chute rapidement, en raison du comportement en fatigue typique des matériaux composites, qui entraîne une certaine perte de rigidité (endommagement en fatigue précoce, se développant principalement dans la matrice) [27,28]. Dans la seconde partie (zone BC sur la Fig. 3-10), une dégradation de la matrice et un processus de délaminage se développent encore, mais beaucoup plus lentement que durant la phase précédente. Cependant, le module d'élasticité diminue presque linéairement pour le GFRE [45°/45°]$_4$, ce qui est moins le cas pour le GFRE [0°/90°]$_4$. Dans la dernière partie du processus, au-delà du point C, il y a le module d'élasticité qui chute brutalement, et descend en dessous du point D, ce qui conduit à la rupture des fibres.

Un protocole similaire a été mis en place pour les essais HCF. Les niveaux de contrainte sont cependant inférieurs à la limite d'élasticité, les contraintes maximales valant 80 et 55 MPa pour les orientations [0°/90°]$_4$ et [45°/45°]$_4$ des composites stratifiés, respectivement (Fig. 3-11). Le nombre total de cycles à la rupture N_f était d'environ 500 000 pour les deux

orientations considérées. Chacun des blocs de chargement appliqués dans le programme expérimental comprenait n_i = 50 000 cycles.

De manière analogue à la Fig. 3-10, la Fig. 3-11 montre l'évolution de la rigidité résiduelle durant les essais HCF, où trois zones sont une fois de plus visibles : *AB*, *BC* et *CD*. On peut cependant remarquer que la raideur initiale décroît un peu plus lentement que lors des essais LCF (zone *AB)*. Par conséquent, la transition est plus douce à la deuxième étape (zone *BC*), où le processus de ramollissement est pratiquement le même que celui des éprouvettes soumises au LCF, et ce pour les deux orientations des armures taffetas. Enfin, au-delà du point *C*, une variation similaire des courbes pour les deux orientations considérées est observée. Comme le montrent les Figs. 3-10 et 3-11, près de 17 % de réduction de la raideur initiale est obtenue pour le GFRE [0°/90°]$_4$, indépendamment de la nature des tests (LCF ou HCF). Dans le cas du GFRE [45°/45°]$_4$, la réduction de raideur est beaucoup plus nette et s'élève environ à 48 %. Les résultats sont cohérents avec une autre étude [30] du comportement en fatigue des composites stratifiés à armure taffetas dans les directions « sur axe » et « hors axe », bien que de la résine thermoplastique Elium ait été utilisée comme matrice en lieu et place de l'époxy (matrice thermodurcissable) dans cette étude.

Sur la base de l'évolution du module élastique enregistrée et de la perte de rigidité qui l'accompagne, par analogie à la définition de l'endommagement introduite par Khachanov [31] ou Azouaoui, et al. [12] (Eq. (1-5)), un paramètre d'endommagement D_E a été défini, comme le montre la Fig. 1-10. Ses valeurs pour les éprouvettes soumises à des charges LCF et HCF sont présentées dans les Figs. 3-12 et 3-13, respectivement. Compte tenu des évolutions du paramètre d'endommagement présentées dans les Figs. 3-12 et 3-13, trois stades de d'endommagements peuvent être facilement identifiés. Lors de la première étape, représentée par une partie de caractéristique notée *O-B*, le paramètre d'endommagement présente une augmentation significative et prend les valeurs à la fin de cette étape de D_E = 0,085 ÷ 0,100 et D_E = 0,035 ÷ 0,040 pour les tests LCF et HCF, respectivement. Durant la deuxième étape, les défauts sous forme de microfissures et de délaminage générés par le vieillissement en fatigue se propagent beaucoup plus rapidement pour les composites stratifiés orientés GFRE [45°/45°]$_4$ que pour les GFRE [0°/90°]$_4$. Pour ces derniers, le paramètre D_E augmente avec le nombre de cycles seulement jusqu'à 0,15 et 0,10 pour les tests LCF et HCF, respectivement. Dans le cas de GFRE [45°/45°]$_4$, le même

paramètre au même stade d'endommagement prend une valeur égale à 0.6 indépendamment d'un type de chargement (LCF ou HCF). La troisième étape, qui correspond à la phase finale pour atteindre la rupture, est en comparaison très courte. Cette rupture apparaît à N_f = 500,000 pour le HCF et à N_f = 6,000 pour le LCF.

Par la suite, les états pré-critiques ont été établis pour tous les groupes de stratifiés composites testés à partir des évolutions de la rigidité résiduelle E_i et du paramètre d'endommagement D_E. Leurs plages sont marquées par les lignes noires en pointillés représentées sur les Fig. 3-12 et 3-13.

L'identification des états pré-critiques a permis d'interrompre les processus de vieillissement, induits par le chargement cyclique uni-axial, lorsqu'une valeur donnée de la perte de rigidité est atteinte, assurant un endommagement interne (microfissures dans la matrice et décollement inter-plis) pour comparaison entre les deux orientations étudiées et les niveaux de contraintes appliqués. Par conséquent, les éprouvettes en GFRE [45°/45°]$_4$ ont été vieillies jusqu'à ce que le paramètre d'endommagement D_E atteigne la valeur de 0.45 avant les essais d'impact. Cette valeur correspond à σ_{max} = 80 MPa et N_f = 4,500 cycles pour les essais LCF et à σ_{max} = 55 MPa et N_f = 350,000 cycles pour les essais HCF. Par ailleurs, les composites GFRE [0°/90°]4 ont été vieillies jusqu'à ce que le paramètre d'endommagement D_E atteigne la valeur 0.15 et 0.11, ce qui correspond à σ_{max} = 250 MPa et σ_{max} = 80 MPa pour les essais LCF et HCF, respectivement. Par conséquent, pour atteindre la valeur attendue de la perte de rigidité, il était nécessaire d'avoir un nombre de cycles N_f = 4,000 cycles pour les essais de fatigue au-dessus de la limite élastique LCF et N_f = 400,000 cycles pour ceux effectués en dessous de la limite élastique HCF.

Enfin, afin d'étudier l'effet de l'adoucissement généré par le vieillissement en fatigue sur la résistance à un impact basse et grande vitesse(perforation), 80 éprouvettes de tailles 100 mm × 100 mm ont été vieillies par chargement cyclique uni-axial (soit 20 pour chaque groupe testé).

1.3 Effet du vieillissement en fatigue sur la résistance à l'impact basse vitesse des stratifiés fibres de verre/Elium acrylique

Les tests d'impact basse vitesse ont été effectués au moyen d'une tour de chute Instron DYNATUP 9250HV, Fig. 4-1. L'impacteur utilisé pour ces essais avait une forme

hémisphérique de 16 mm de diamètre. La masse totale, incluant celle du chariot et de l'impacteur, était égale à 5762 ± 100 g. Trois groupes d'éprouvettes de composites stratifiés fibres de verre/Elium acrylique ont été testés : (i) non vieillis, (ii) vieillis à la contrainte inférieure à la limite d'élasticité (HCF), et (iii) vieillis à la contrainte supérieure à la limite d'élasticité (LCF). Pour ces essais d'impact basses vitesses, les énergies d'impact retenues étaient de 5, 10, 30 et 50 J, ce qui correspond à des vitesses respectives de 1,32, 1,86, 3,23 et 4,16 m/s. Les tests ont été répétés cinq fois pour chaque condition afin de vérifier la répétabilité des résultats. La résistance à l'impact a été quantifiée sur la base de l'analyse de la force d'impact maximale F_i et du déplacement correspondant U, ainsi que de l'énergie absorbée E_a et du seuil de pénétration. Les résultats des essais d'impact basse vitesse sont rapportés dans les Tableaux 4-1 et 4-2.

La résistance à l'impact basse vitesse a été présenté au moyen des caractéristiques force-déplacement, énergie-temps (Figs. (4-2)-(4-7)), et par la détermination du seuil de pénétration (Figs. 4-8 et 4-9). Les premières étapes des courbes force - déplacement pour les composites stratifiés soumis à une énergie d'impact de 10 J (pente de la courbe sur la Fig. 4-2), ne sont pas les mêmes pour GFRE $[0°/90°]_4$, indiquant que le processus de vieillissement par fatigue a affecté la rigidité du composite stratifié. On observe également, quelques petites oscillations lorsque la force augmente, ce qui témoigne de la présence des fissures dans la matrice [118]. Cet effet est surtout visible pour le GFRE $[45°/45°]_4$, car une contribution de la résine dans la transmission de la force est plus importante pour ce type de composites. Elle a lieu pour une valeur de force d'environ 2200 N. Au-delà de 3000 N, une stagnation de la force est observée. Cela est dû à la réduction de la rigidité en flexion. Elle résulte du comportement fragile des dommages par impact du GFRE ainsi que du développement du processus de délaminage. L'intensité du processus de stagnation de la force est plus claire pour les éprouvettes vierge (non vieillies) que pour les composites stratifiés vieillis. La force d'impact maximale (F_i) diminue pour les deux orientations du renfort considéré par rapport au composite non vieilli. Elle est associée à une augmentation de la déflexion, indiquant la capacité du matériau à dissiper plus d'énergie. Les résultats de la Fig. 4-3 permettent à leur tour de mettre en évidence une perte significative de rigidité causée par la fissuration de la matrice et le décollement de l'interface entre les fibres et la matrice. Les résultats du GFRE $[0°/90°]_4$ soumis à un impact à basse vitesse à 10 J montrent

qu'il est moins sujet au délaminage que le GFRE [45°/45°]$_4$ et conserve une meilleure résistance à l'impact après vieillissement en fatigue. Cependant, il faut remarquer que les composites stratifiés soumis à une charge LCF préalable présentent une capacité de dissipation d'énergie beaucoup plus faible.

Par la suite, tous les groupes de matériaux ont été soumis aux tests d'impact à 30 J et 50 J. Les Figs. 4-4 et 4-5 montrent l'évolution de la force en fonction du déplacement des matériaux. Les valeurs d'énergie d'impact de 30 J et 50 J sont suffisantes pour provoquer une fracture visible avec de nombreuses fissures internes. Les éprouvettes vieillies et non vieillies ne résistent pas à l'impact à 50 J, et toutes ont atteint le seuil de pénétration. Il convient de noter, qu'à nouveau, les éprouvettes vieillies d'orientation GFRE [45°/45°]$_4$ sont les moins résistantes aux impacts. La fissuration de leur matrice se produit pour une force inférieure à celle du GFRE [0°/90°]$_4$. De plus, le délaminage apparaissant lors de l'impact conduit à des réductions importantes de la force transmise, d'où les oscillations de la force maximale qui atteignent 1000 et 1200 N environ pour les essais d'impact de 30 et 50 J, respectivement. Les Figs. 4-6 et 4-7 montrent les résultats pour ces deux niveaux d'énergie, respectivement. Elles permettent de conclure qu'une énergie d'impact de 30 J peut être vue comme la quantité d'énergie proche de la limite de résistance à l'impact pour les composites testés. Toutes les caractéristiques énergétiques présentent un pic d'énergie, puis, leurs courbes commencent à descendre, ce qui est une preuve claire de la pénétration et de la perforation subséquente des échantillons testés. De plus, les différences entre les courbes de l'énergie d'impact observées pour les éprouvettes non vieillies et vieillies témoignent clairement d'un effet du vieillissement par fatigue sur sa résistance à l'impact. Ceci confirme les observations précédentes, à savoir que le matériau GFRE [45°/45°]$_4$ vieilli est présente la résistance à l'impact la plus faible parmi tous ceux considérés dans cette étude. En analysant la réponse à l'impact du GFRE non vieilli et vieilli soumis à une énergie d'impact de 50 J (Fig. 4-7), l'initiation de la perforation des plaques est identifiée. Dans le cas d'un matériau non vieilli, cette pénétration commence lorsque le niveau d'énergie atteint respectivement 40 J et 38 J, environ, pour le GFRE [0°/90°]$_4$ et le GFRE [45°/45°]$_4$. De plus, il est clair que les groupes d'éprouvettes après chargement de fatigue ont une résistance à l'impact significativement plus faible. La perforation est apparue dans le cas le plus indésirable (HCF-GFRE [45°/45°]$_4$).

Le seuil de pénétration fait partie des caractéristiques les plus utilisées pour la quantification de la résistance à l'impact d'un composite des stratifiés [117]. Ce paramètre détermine l'énergie nécessaire à la pénétration du composite stratifié. Dans cette étude, une méthode définie par Reis et al. [119] et Aktas et al. [120] a été appliquée. La première consiste à représenter l'énergie absorbée en fonction de l'énergie d'impact. La pénétration a lieu lorsque l'énergie absorbée est égale à l'énergie d'impact (points situés sur la droite représentant la ligne d'égal énergie). Lorsque les points sont situés en dessous de cette ligne, cela témoigne du fait que la pénétration n'a pas encore eu lieu. Le deuxième critère quant à lui est une représentation de l'énergie élastique en fonction de l'énergie d'impact. Le seuil de pénétration dans ce cas est donné par la racine non nulle de l'approximation polynomiale du second degré de l'énergie élastique en fonction de l'énergie d'impact. Afin d'évaluer la résistance à l'impact des composites stratifiés à base d'acrylique Elium, les courbes de seuil de pénétration ont été construites pour les différents matériaux testés. La Fig. 4-8 résume les résultats obtenus pour les échantillons non vieillis et vieillis soumis à un impact à basse vitesse, c'est-à-dire pour des niveaux d'énergie égaux à 5, 10 et 30 J. Les valeurs pour les stratifiés non vieillis et vieillis sont situées sous la ligne d'égal énergie. Cela signifie que le seuil de pénétration n'a pas été atteint. Pour l'énergie d'impact la plus élevée (50 J), toutes les éprouvettes ont été perforées. Les résultats pour l'énergie d'impact de 10 J et 30 J montrent clairement combien la différence de capacité d'absorption d'énergie change suivant le type d'orientation des renforts et des conditions de vieillissement en fatigue. Le seuil de pénétration est évidemment atteint pour les stratifiés vieillis, préalablement soumis à des sollicitations LCF, quelle que soit l'orientation l'armure taffetas. Les valeurs d'énergie absorbée les plus élevées sont obtenues pour le GFRE $[45°/45°]_4$ après vieillissement suite aux tests LCF. Cela signifie que, par rapport aux autres configurations considérées, cette orientation est le moins adaptée aux applications où la charge d'impact est dominante. A l'inverse, les valeurs d'énergie absorbée les plus basses sont atteintes après vieillissement grâce aux tests HCF pour le GFRE $[0°/90°]_4$.

De plus, pour mieux comprendre l'effet du vieillissement par fatigue sur la faible résistance aux chocs, le diagramme de l'énergie élastique en fonction de l'énergie absorbée est élaboré (Fig. 4-9). On peut observer que les seuils de pénétration calculés à 20 °C pour des énergies d'impact de 5 J, 10 J et 30 J dépendent fortement de l'endommagement interne

introduit par le vieillissement en fatigue. Comme prévu, les composites non vieillis représentent les matériaux avec les meilleures propriétés de résistance à l'impact. Les valeurs estimées de l'énergie d'impact aux seuils de pénétration sont égales à 35,8 J pour le GFRE $[45°/45°]_4$ et 35,1 J pour le GFRE $[0°/90°]_4$, respectivement. Dans le cas des mêmes matériaux après vieillissement dû aux essais HCF, les énergies d'impact aux seuils de pénétration sont respectivement égales à 33,2 et 33,5 J et pour les mêmes matériaux après vieillissement dû au LCF: 31,9 J et 32,6 J respectivement. On remarque que la différence maximale entre les seuils de pénétration n'est que de 3,9 J. La principale raison d'une si petite différence résulte directement du nombre limité de points représentés dans le diagramme (seuls 3 niveaux d'énergie ont été utilisés pour l'approximation polynomial). Malgré ce nombre limité, on peut conclure que l'historique de la variation de l'énergie élastique due à l'augmentation de l'énergie d'impact fournit un paramètre efficace pour l'analyse de la réponse à l'impact des composites renforcés par des fibres de verre avec différentes orientations de tissu. On observe que la différence d'énergie élastique entre le GFRE non vieilli et vieilli $[45°/45°]_4$ augmente avec l'énergie d'impact. Un effet inverse se produit dans le cas du GFRE $[0°/90°]_4$, notamment si des essais sont réalisés à des énergies proches de celle correspondant au seuil de pénétration.

En conclusion, le processus de vieillissement par fatigue diminue la réponse élastique exprimée par la réduction de la rigidité des deux composites testés et, par conséquent, affecte leur ténacité. Elle est fortement dépendante des mécanismes se développant lors de la traction d'une part, et d'une réduction des forces de cohésion entre fibres et résine due au vieillissement en fatigue d'autre part. Elle conduit à la génération de fissures dans les files (torons) transversaux pour le GFRE$[0°/90°]_4$, et soit dans le sens chaîne ou trame pour le GFRE$[45°/45°]_4$.

Afin de bien comprendre les endommagements internes, la microscopie électronique à balayage (MEB) et la tomographie ont été utilisés. La Fig. 4-12 montre les dommages intra-plis (Figs. 4-12 (b), (c), (d)) et inter-plis (Figs. 4-12 (e), (f)) des composites stratifiés dans le sens chaîne et trame. Il y a clairement des fissures visibles dans le toron sélectionné (trame), ainsi qu'un délaminage entre les plis adjacents. Les fissures dans le sens chaîne et trame ont été induites en raison des charges LCF ou HCF, entraînant le ramollissement de toute la structure du composite. En conséquence, la rigidité et la résistance à l'impact ont

été affectées. Ces observations sont en accord avec celles obtenues dans l'étude de Pandita et al. [37], qui montrent l'endommagement induit par le chargement de fatigue en traction dans les composites stratifiés. Ensuite, les plaques vieillies ou non sont comparées à l'issue d'un impact avec une énergie de 50 J (Fig. 4-13). L'analyse par micro-tomographie révèle que l'étendue de la fissuration matricielle du stratifié est plus petite en l'absence de vieillissement. Ce constat confirme que le chargement cyclique provoque la décohésion de l'interface fibres/matrice, favorisant ainsi un délamination sévère et une fissuration de la matrice lors de l'impact du stratifié composite.

1.4 Résistance à l'impact grandes vitesses des stratifiés tissés fibre de verre/Elium acrylique vieillis et non vieillis en fatigue

Afin de comprendre la résistance à la perforation des composites stratifiés fibres de verre/Elium acrylique, ayant subi un vieillissement en fatigue, des essais de perforation au moyen d'un canon à gaz ont été effectués.

Comme le montre la Fig. 5-1, le dispositif expérimental se compose d'une partie pneumatique, de deux capteurs de vitesse, d'une cible, d'un support et de la boîte de récupération des projectiles. Ce dispositif d'impact balistique est également équipé d'un système de mesure de force. Il permet de mesurer les forces dynamiques uni-axiales dans la direction d'impact. Le projectile utilisé a une forme hémisphérique avec un diamètre de 12,8 mm et une masse totale d'environ 29,1 g. La plaque de polymère, c'est-à-dire la cible, mesure 100 mm × 100 mm, dont une partie utile (en dehors de la zone de bridage) est de 80 mm × 80 mm avec une épaisseur moyenne de 1,8 mm. Trois cas de figure sont observés à l'issue de cette expérience : une perforation complète suite au passage du projectile (i), une perforation critique où l'impacteur reste coincé dans la plaque (ii) et enfin, l'absence de perforation (iii). Afin d'évaluer la tenue à la perforation, la vitesse initiale V_0 (avant l'impact)et la vitesse résiduelle V_R (après perforation) ont été mesurées, et ont servi à tracer les l'évolution de la vitesse résiduelle en fonction de la vitesse d'impact (courbe balistique).

Quatre séries de tests de perforation ont été effectuées sur des éprouvettes préalablement vieillies par chargement cyclique. Les deux premières concernent les éprouvettes GFRE [0°/90°]$_4$, tandis que les deux autres portent sur le cas où l'orientation des fibres fait un angle de 45° avec les directions principales du plan GFRE [45°/45°]$_4$. Pour chaque série, les éprouvettes sont divisées en deux groupes égaux, l'un vieilli avec un niveau de contrainte

inférieur à la limite élastique et l'autre avec un niveau supérieur à cette dernière. Afin d'analyser l'influence de ce vieillissement par fatigue, les résultats sont comparés à la limite balistique des éprouvettes non vieillies. Les courbes balistiques pour les plaques GFRE [0°/90°]$_4$ et GFRE [45°/45°]$_4$ sont illustrées aux Fig. 5-4 et 5-5, respectivement. Elles ont été ajustées en utilisant le modèle de Recht et Ipson (1963) (Eq. (1-10)). Par rapport au GFRE [45°/45°]$_4$ vieilli en fatigue, la chute de la résistance à l'impact du GFRE [0°/90°]$_4$ vieilli est minime et ne dépasse pas 3.6 m/s. De plus, on note que les éprouvettes vieillies dans le domaine LCF et HCF – GFRE [45°/45°]$_4$ ont des limites balistiques de 20 m/s plus petite que celles des composites stratifiés GFRE [0°/90°]$_4$.

L'énergie absorbée par les cibles composites lors de la perforation est calculée à partir de la vitesse initiale et la résiduelle du projectile en utilisant l'Eq. (1-11). A partir de ces calculs, les diagrammes d'énergie absorbée en fonction de la vitesse d'impact initiale ont pu être établis pour les composites GFRE [0°/90°]$_4$ et GFRE [45°/45°]$_4$ (Figs. 5-6 et 5-7, respectivement). Comme le montrent ces figures, l'énergie moyenne absorbée par le composite GFRE[0°/90°]$_4$ vieilli ou non est d'environ 78 J, tandis que la dissipation d'énergie atteint 82 J pour les cibles de GFRE [45°/45°]$_4$ non vieillies. En ce qui concerne l'énergie moyenne dissipée par les cibles GFRE [45°/45°]$_4$ vieillies, elle n'est que d'environ 30 J, tandis que pour les cibles GFRE [0°/90°]$_4$ vieilli, elle est beaucoup plus élevée et atteint une valeur d'environ 65 J. Les résultats montrent que les éprouvettes GFRE [0°/90°]$_4$ soumises à une charge de fatigue cyclique uni-axiale ont de meilleures performances balistiques et une dissipation d'énergie plus élevée que les cibles GFRE [45°/45°]$_4$.

L'autre aspect étudié est l'évolution de la force en fonction du temps, au cours des essais d'impact balistique. Les courbes représentatives de la force en fonction de la vitesse d'impact pour tous les stratifiés testés, est illustrée à la Fig. 5-8. Une force de résistance maximale d'environ 12 kN est observée pour des plaques GFRE [45°/45°]$_4$ non vieillies. Concernant les plaques GFRE [45°/45°]$_4$ vieillies, cette valeur maximale chute jusqu'à 4 kN. Les résultats des tests effectués sur les stratifiés GFRE [0°/90°]$_4$ vieillis et non vieillis ne présentent pas de différences aussi importantes au niveau de la force mesurée en comparaison avec les plaques GFRE [45°/45°]$_4$. La valeur maximale de la force pour le stratifié GFRE [0°/90°]$_4$ non vieilli était de 10 kN et pour le stratifié vieilli de 8 kN. Cette observation nous a permis de conclure que la diminution de la force dépend de deux

facteurs : la direction des fibres et la perte de rigidité due à la fatigue. On observe également que les dommages à des vitesses d'impact élevées sont caractérisés par une faible force lorsque la vitesse du projectile est proche de la limite balistique. Par la suite, la force atteint son maximum, puis chute lentement à mesure que la vitesse d'impact initiale augmente. Ce comportement est similaire pour tous les composites testés. Il résulte du mécanisme de rupture typique des composites stratifiés soumis aux tests de perforation.

Afin d'analyser les endommagements consécutives aux essais de perforation sur les composites GFRE [0°/90°]$_4$ et GFRE [45°/45°]$_4$ vieillis et non vieillis, un examen des surfaces externes a été effectué. Les Figs. 5-9 et 5-10 montrent la face arrière des plaques testées , avant et après vieillissement en fatigue, pour les composites stratifiés GFRE [45°/45°]$_4$ et GFRE [0°/90°]$_4$, respectivement. On remarque de manière évidente que les composites non vieillis sont les moins endommagés pour les deux orientations considérées. Dans le cas où la vitesse d'impact avoisine la limite balistique, les endommagements sont localisés principalement dans la matrice et se présentent sous la forme de nombreuses fissurations matricielles, accompagnées d'une petite zone de délaminage, avec quelques ruptures des fibres. Pour les essais réalisés à haute vitesse d'impact, la surface d'endommagement augmente significativement, révélant ainsi l'apparition de formes d'endommagement plus sévères, c'est-à-dire le délaminage et la rupture des fibres par exemple. Lorsque les stratifiés composites sont soumis à un vieillissement par fatigue préalable, le degré d'endommagement généré par ce processus a subi une évolution supplémentaire en raison de l'impact introduisant des formes d'endommagement plus graves. On peut indiquer, que les composites précontraints du fait du vieillissement en fatigue sous une amplitude de contrainte inférieure à la limite d'élasticité ont été plus endommagés que ceux soumis au même processus, avec des amplitudes supérieures. En conséquence, les mécanismes de déformation plastique ont été activés, ce qui pourrait induire des cavités et contribuer à arrêter la propagation des fissures lorsque la plaque est soumise à un impact. Cet effet est plus évident pour le stratifié composite GFRE [45°/45°]$_4$.

De plus, pour bien comprendre la prolifération des changements internes causés les essais de perforation une analyse par micro-tomographie a été effectuée. La comparaison entre les plaques perforées non vieillies et vieillies est présentée à la Fig. 5-11. L'analyse par micro-tomographie montre que l'étendue des fissurations matricielles du stratifié non vieilli est

plus petite que celle de la plaque de stratifié vieilli. Les résultats confirment que le chargement cyclique (vieillissement) du composite stratifié conduit à la décohésion de l'interface fibres/matrice et favorise la génération de délaminage sévère et de la fissuration matricielle au cours du processus d'impact.

1.5 Simulation numérique de l'impact basse et de la perforation des plaques GFRE[0°/90°]$_4$ non vieillies

Dans ce travail, les simulations numériques de la réponse à l'impact basse et haute vitesse des composites stratifiés fibres de verre/Elium acrylique ont été réalisées à l'échelle macroscopique et comparées aux résultats expérimentaux. L'approche de modélisation macroscopique retenue permet de décrire la dégradation intra et inter-plis se produisant dans les plis . Le modèle 3D proposé a été implémenté dans un code de calculs par éléments finis (MEF) explicite pour Abaqus/Explicit, à l'aide d'une sous-routine utilisateur de matériau VUMAT. Le modèle se compose de quatre couches de tissé fibres de verre/Elium acrylique qui représentent le stratifié comme un matériau homogène. Le phénomène d'endommagement, à la fois dans le plan et hors du plan, est simulé à l'aide d'un critère de rupture de Hashin modifié [54]. En général, les stratifiés qui contiennent des matrices plus fragiles sont capables de transférer toute leur ténacité dans le composite alors que, dans le cas de matrices plus ductiles, seule une partie de la ténacité de la matrice contribue réellement à la résistance à la rupture du composite [17]. Ainsi, afin de modéliser le délaminage des couches du tissé fibres de verre/Elium acrylique, de fines couches de zones cohésives (Elium pur)ont été introduites à l'interface entre les différents plis, Fig. 4-14. Elles permettent de décrire le comportement inélastique de la matrice acrylique. Il convient de noter que le modèle est basé sur les hypothèses selon lesquelles les fibres doivent être parfaitement alignées par rapport aux torons dans le sens chaîne et trame, et de plus leur ondulation est négligée. Afin de réduire le nombre d'éléments du modèle numérique, le matériau a été remplacé par un équivalent homogène ayant les mêmes propriétés, Fig. 4-14. Les propriétés élastiques du GFRE [0°/90°]$_4$ non vieilli utilisées pour la simulation de l'impact basse vitesse sont répertoriés dans le Tableau 4-3. Concernant les limites de rupture, c'est-à-dire la contrainte de traction maximale dans les directions longitudinale, transversale et de cisaillement obtenues à partir d'essais expérimentaux sur des échantillons macroscopiques, ont été extraites des Tableaux 2-4 et 2-6, respectivement. La contrainte de compression

maximale pour la direction perpendiculaire a été extraite des Tableau 2-8. Afin de prédire l'endommagement intra-laminaire de chaque pli, le critère de rupture de Hashin [60] modifié par Puck [63] (pour la matrice) a été retenu. Le modèle d'endommagement est basé sur la dégradation des propriétés élastiques des couches homogénéisées. Pour simuler l'endommagement du tissu à armure taffetas, le critère de rupture prend en compte six variables d'endommagement: deux pour le toron dans le sens chaîne, deux pour le toron dans le sens trame et deux pour la matrice, (Eqs. (4-3)-(4-7)). Les variables d'endommagement responsables des modes de défaillance ont été implémentées dans le logiciel Abaqus/Explicit en tant que sous-programme utilisateur VUMAT afin de réaliser les simulations. L'algorithme de la procédure numérique pour résoudre le cas élastique est illustré à la Fig. 4-15. Cela indique que la rupture commence lorsque l'une des variables d'endommagement atteint la valeur de 1. Cette condition conduit à une réduction de la rigidité, représentée par l'Eq. (4-8). Afin de décrire plus précisément le comportement inélastique de la matrice acrylique et de corréler l'amorçage de la rupture entre la simulation et les données expérimentales, une loi d'endommagement continu a été appliquée. La déformation à la rupture au début de l'endommagement a été choisie empiriquement et sa valeur pour les énergies d'impact de 10 J à 50 J a été fixée à 0,08. De même, le déplacement initial de 1,5 mm, pour la description de l'évolution de la défaillance liée à l'étape de propagation de l'endommagement a été retenu. Une telle solution a permis de fournir un bon accord entre les caractéristiques force-temps expérimentales et ses prédictions numériques.

Une vue générale du modèle macroscopique: la configuration et les conditions aux limites sont illustrées à la Fig. 4-16. Les plis de dimensions 100 mm x 100 mm x 1.8 mm ont été placés perpendiculairement à l'axe de l'impacteur. L'impacteur a une masse de 5.762 kg et un diamètre de 16 mm. Le projectile, le support inférieur et supérieur ont été traités comme des corps rigides. Le maillage est divisé en deux régions. Il est plus fin au niveau de la centrale pour laquelle une zone de diamètre 50 mm est maillée avec des éléments de taille 0.5 mm. Des éléments massifs à intégration réduite ont quant à eux été utilisés (Abaqus C3D8R) pour simuler les plis. Concernant les zones cohésives d'une épaisseur de 0.001 mm placées entre les plis, elles ont été maillées avec des éléments cohésifs (Abaqus COH3D8). Des niveaux d'énergie d'impact égaux à 10 J, 30 J et 50 J ont été appliqués lors des essais

d'impact. Des simulations numériques ont été effectuées pendant une période de 12 ms au moyen d'une station de calculs à 24 cœurs (en parallèle sur le processeur Intel(R) Xeon(R) Gold 6136, 2 × 3,00 GHz et 128 Go de RAM). En raison de la grande complexité de la géométrie modélisée, seuls de petits éléments finis ont été choisis. Ils permettent de générer un incrément de temps stable de 10^{-9} s^{-1}.

Une comparaison des résultats obtenus numériquement pour une énergie d'impact égale à 10 J et 30 J avec les données expérimentales est présentée à la Fig. 4-17. On observe la même tendance que pour les données expérimentales. Cependant, il convient de noter une légère surestimation de la force critique lors des simulations numériques. Dans les deux cas (10 J et 30 J) elle est supérieure d'environ 10 % à celle des expériences obtenues. De plus, la force chute plus rapidement dans le modèle numérique. Cela pourrait être lié à la perte de rigidité due au développement des dommages. Une certaine dispersion a été observée entre les résultats expérimentaux et numériques pour les courbes décrivant l'évolution de l'énergie absorbée en fonction du temps (Fig. 4-17. (a) et (c)). Par la suite, une distribution des champs de déplacement autour de l'impacteur a été analysée, Fig. 4-18. On peut remarquer que le déplacement est égal à zéro aux nœuds fixes et augmente significativement dans la zone impactée. A 30 J et t = 5 ms, une pénétration partielle de la plaque peut être observée (voir Fig. 4-18 (b)). Les dommages semblent être légèrement plus importants que ceux illustrés à la Fig. 4-11, lors d'une expérience réelle. A 50 J et pour t = 5 ms, une pénétration totale de la plaque a été obtenue. On peut remarquer que la perforation s'est produite à t = 2,5 ms. Elle correspond à la chute brutale de force clairement représentée sur les Fig. 4-19 (b) et (c). Il est clairement visible que la force maximale obtenue par la simulation est en accord avec celle issue de l'expérience. Cependant, sa valeur dans la simulation, après avoir dépassé le pic maximal, chute plus significativement que dans le test. Cela peut résulter du fait que les éléments supprimés dans le modèle ne contribuent plus à la raideur de la plaque composite testée, ou aux conditions de frottement entre la plaque et l'impacteur. D'autre part, la valeur d'énergie indiquée sur la Fig. 4-19 n'atteint pas le niveau observé au cours de l'expérience. Cela pourrait être le résultat du fait que toutes les simulations ont été réalisées en considérant les mêmes valeurs de limites à la rupture. Étant donné que la vitesse de déformation n'est pas le même pour les énergies d'impact analysées, cela pourrait introduire des écarts dans les résultats numériques.

Pour prédire les performances du composite GFRE [0°/90°]$_4$ non vieilli à l'impact grande vitesse, le même modèle que celui proposé pour les impacts basse vitesse a été utilisé.

Les dimensions de la surface utile des échantillons et du projectile sont illustrées à la Fig. 5-12. Il apparait clairement que la forme du projectile, ainsi que les dimensions du système de bridage et de la cible sont les mêmes que celles utilisées pour les essais d'impact à basse énergie. Cependant, la masse du projectile lors de l'impact à grande vitesse a été modifiée. Le projectile de masse égale à 0.0291 kg a été utilisé dans la simulation numérique. Comme la vitesse maximale disponible du projectile est de 180 m/s, la résistance à l'impact du GFRE [0°/90°]$_4$ a été étudiée dans la gamme des énergies d'impact allant de 10 J à 470 J.

Les propriétés dynamiques du composite GFRE [0°/90°]$_4$ non vieilli à des vitesses de déformation élevées utilisées dans le modèle numérique ont été estimées par application des relations proposées par Harding et al. [139] et [140]. Les facteurs de correction de l'effet de la vitesse de déformation élevée sur les modules d'Young ,de cisaillement ainsi que sur les contraintes à la rupture ont été estimés à 1,5 et 3, respectivement [125]. Comme suggéré dans plusieurs travaux [141,142], des valeurs constantes du coefficient de Poisson et de la densité du matériau ont été utilisées pour la simulation. Le résumé des propriétés dynamiques du composite GFRE[0°/90°]$_4$ non vieilli est présenté dans le Tableau 5-1.

Pour la simulation d'un impact à haut vitesse, la déformation à la rupture au début de l'endommagement est égale à 0.02 et le déplacement initial à 5 mm. Étant donné que la sensibilité à la vitesse de déformation n'est pas la même lors de l'essai de perforation et l'impact basse vitesse, il convient de prendre en compte le comportement viscoplastique de la matrice acrylique qui se produit sous chargement dynamique. Afin d'en tenir compte sur une large gamme de vitesse de déformation, le comportement plastique de l'Elium acrylique (appliquée dans le modèle en tant que couche cohésive) a été décrit à l'aide des paramètres de Johnson Cook. Un bon accord entre l'expérience et le modèle a ainsi été obtenu, Fig. 5-13. Les paramètres identifiés sont répertoriés dans le Tableau 5-2.

Afin de simuler le comportement du composite GFRE [0°/90°]$_4$ non vieilli sous chargement dynamique, plusieurs simulations pour des vitesses d'impact allant de 59 à 180 m/s ont été réalisés. Ces simulations numériques ont été réalisées pendant une durée de 20 ms sur une station de calculs équipé de 24 cœurs (en parallèle sur processeur Intel(R) Xeon(R) Gold 6136, 2 × 3,00 GHz et 128 Go de RAM). En raison de la complexité de la

géométrie modélisée, seuls les petits éléments finis qui génèrent un incrément de temps initial stable de 10^{-8} s^{-1} ont été pris en compte.

La réponse balistique prédite par le modèle éléments finis et les résultats expérimentaux ont été comparés à la Fig. 5-14. Un bon accord peut être observé entre les données expérimentales et les prédiction des simulations à la fois pour la limite balistique et les vitesses résiduelles. Un petit écart entre la vitesse résiduelle expérimentale et numérique pour les vitesses d'impact élevées pourrait être dû à d'éventuelles variations de l'épaisseur de l'échantillon. L'erreur la plus élevée est atteinte lorsque la vitesse d'impact maximale (V_I = 180 m/s), mais demeure néanmoins inférieure à 6 %.

Afin de valider le modèle, la dissipation d'énergie prédite par le modèle numérique et les résultats issus des tests ont été comparés. On voit clairement que les valeurs numériques de la dissipation d'énergie sont bien inférieures aux données expérimentales, Fig. 5-15. La différence moyenne de l'énergie analysée ne dépasse pas 8%. Cependant, pour la vitesse d'impact initiale de 120 m/s, la valeur de dissipation d'énergie est presque trois fois plus élevée. L'analyse des surfaces endommagées illustrée à la Fig. 5-9 confirme que dans le cas des composites stratifiés à faible épaisseur, le mécanisme d'absorption d'énergie dominant est la rupture des fibres de verre. Considérant qu'il s'agit de stratifiés minces, il est logique qu'une énergie importante soit absorbée par ce mécanisme puisque d'autres auteurs supposent que le comportement est similaire à celui d'une membrane [143,144]. Par conséquent, la déformation des fibres joue le rôle le plus important et dans notre cas atteint une valeur maximale avant la rupture à la vitesse d'impact d'environ 120 m/s. On peut donc supposer dans notre cas que cet écart résulte d'un facteur de correction de propriété dynamique imparfaitement sélectionné.

Conclusion

Deux groupes de composites stratifies à matrice Elium acrylique GFRE, de formes et de dimensions adaptées pour le test de résistance aux chocs après vieillissement en fatigue, ont été préparés au moyen du procédé d'infusion de résine.

Afin de déterminer les paramètres nécessaires à la simulation de la tenue à l'impact des plaques composites, des essais thermomécaniques quasi-statique et dynamiques ont été réalisés, avant l'étude de l'influence du vieillissement en fatigue sur la résistance à l'impact des composites stratifiés fibres de verre/Elium acrylique. Tout d'abord, les limites à la

rupture et les modules d'Young et de cisaillement obtenus dans le plan et hors plan ont été définis. Ensuite, le comportement mécanique de la matrice Elium acrylique et des composites stratifiés à base d'Elium acrylique, a été étudié sur une large plage de températures et de vitesses de déformation.

Ensuite, l'effet des endommagements induits par le vieillissement en fatigue a été étudié. Une variation du module d'élasticité et l'apparition des endommagements au sein des composites stratifiés ayant subi au préalable un vieillissement en fatigue ont été observées. Les deux groupes de composites stratifiés testés GFRE [0°/90°]$_4$ et GFRE [45°/45°]$_4$ présentaient de manière manifeste une perte de rigidité. La rigidité initiale a été réduite d'environ 17 % pour le GFRE [0°/90°]$_4$, après les tests LCF ou HCF. Cette réduction était beaucoup plus prononcée dans le cas du composite GFRE [45°/45°]$_4$, elle était d'environ 48 %.

Sur la base de l'évolution de la rigidité résiduelle ou du paramètre d'endommagement au cours du vieillissement par fatigue dû au LCF et au HCF, les états précritiques ont été identifiés avec succès. Elle a permis de déterminer le paramètre d'endommagement D_E qui définit un nombre de cycles nécessaires pour atteindre l'état pré-critique pour chaque groupe d'éprouvettes vieillies sous le niveau de contrainte appliqué. La réduction de rigidité introduite par la fatigue a été évaluée. Pour les deux composites stratifiés, elle était égale à 12 % pour les éprouvettes soumises aux essais LCF et d'environ 40 % pour les essais HCF.

Des tests d'impact à basse vitesse effectués sur les plaques non vieillies, pour différents niveaux d'énergie d'impact ont montré leur bonne résistance à l'impact. Par conséquent, les échantillons non vieillis impactés à une énergie de 5 J, 10 J et 30 J n'ont pas été perforés et ont montré une grande capacité à faire rebondir le projectile. Les composites soumis au chargement LCF ont affiché la plus grande diminution du module dynamique (pente initiale des courbes force-déplacement). Cette réduction de de la rigidité est causée par la fissuration de la matrice et le décollement de l'interface entre les fibres et la matrice. La réduction de force maximale pour les essais effectués à une énergie d'impact de 50 J pour les composites GFRE [0°/90°]$_4$ et GFRE [45°/45°]$_4$ est égale à 11 % et 19 %, respectivement. L'analyse de l'énergie absorbée lors de l'essai d'impact basse vitesse, a permis de confirmer que les composites vieillis GFRE [45°/45°]$_4$ présentaient la plus faible résistance à l'impact.

Des tests de perforation effectués sur les composites non vieillies à différents niveaux d'énergie d'impact ont montré leur bonne résistance à l'impact. La limite balistique des

composites non vieillis GFRE [45°/45°]$_4$ est plus élevée celle des composites non vieillis GFRE [0°/90°]$_4$. Il a cependant été observé que les composites GFRE [45°/45°]$_4$, vieillis en fatigue, on une limite balistique inférieure de 23 m/s, lorsqu'on les compare aux composites GFRE [45°/45°]$_4$, non vieillis. Cette diminution de la limite balistique semble moins significative pour les composites GFRE [0°/90°]$_4$ vieillis.

De manière générale, les composites GFRE [0°/90°]$_4$ ou GFRE [45°/45°]$_4$ soumis à une charge LCF arborent la plus forte diminution de la limite balistique. La réduction significative de la rigidité est causée par la fissuration de la matrice et le décollement de l'interface entre les fibres et la matrice. Une analyse détaillée de la dissipation d'énergie et de l'évolution de la force d'impact lors des tests de perforation a confirmé que les matériaux vieillis GFRE [45°/45°]$_4$ présentaient la plus faible résistance aux chocs.

Pour finir, un modèle numérique a été proposé pour simuler le comportement à l'impact (impact basse vitesse et perforation) des composites stratifiées non vieillies GFRE [0°/90°]$_4$ Le modèle 3D proposé a été implémenté dans un code de calculs par éléments finis Abaqus/Explicit au moyen d'une sous-routine utilisateur VUMAT. Dans ce modèle, le composite stratifié est considéré comme une superposition de quatre couches homogènes, séparées par des zones cohésives (ce qui permet de prendre en compte le délaminage). Le phénomène d'endommagement, à la fois pour les modes de défaillance dans le plan et hors du plan, est simulé à l'aide des critères de défaillance de Hashin modifiés. Le modèle d'endommagement appliqué est basé sur la dégradation des propriétés élastiques des couches homogénéisées jusqu'à ce qu'un critère de rupture en contrainte maximale soit vérifié. Afin de prendre en compte la dépendance en vitesse de déformation et la écrouissage de la matrice acrylique, une partie viscoplastique a été reproduite à l'aide du modèle de Johnson-Cook.

Afin de valider les modèles numériques proposés, les résultats de la simulation d'impact ont été comparés aux données expérimentales. La réponse à l'impact des stratifiés soumis à une énergie d'impact égale à 10 J, 30 J et 50 J a été quantifiée à l'aide de l'approche développée pour prédire les dommages intra-laminaires. Ensuite, les résultats expérimentaux et numériques des limites balistiques, des vitesses résiduelles ainsi que l'analyse de l'absorption d'énergie ont été comparés pour des éprouvettes de 1.8 mm d'épaisseur. Une différence négligeable a été observée entre la pente de la courbe

numérique et expérimentale et les niveaux d'énergie absorbés. Cependant, il a été clairement démontré que le déplacement maximal et la réponse obtenus à l'aide du modèle proposé étaient très similaires aux résultats expérimentaux.